SAKARYA ÜNİVERSİTESİ

FEN BİLİMLERİ ENSTİTÜSÜ DERGİSİ

Sakarya University Journal of Science (SAUJS)

SAKARYA ÜNİVERSİTESİ

e-issn: 2147-835X

SAÜ Fen Bil Der/SAUJS

Cilt/Volume: 27

Sayı/Issue: 3

Haziran/June 2023

Sakarya Üniversitesi Fen Bilimleri Enstitüsü Dergisi
(Sakarya University Journal of Science)
Cilt/Volume: 27 No/ Issue:3 Haziran/June 2023

Editör Kurulu/Editorial Boards

Managing Editor

Statistical Editor

English Language Editor

SAKARYA ÜNİVERSİTESİ FEN BİLİMLERİ ENSTİTÜSÜ DERGİSİ
(SAKARYA UNIVERSITY JOURNAL OF SCIENCE)
İÇİNDEKİLER/CONTENTS
Cilt/Volume: 27 – No/Issue3: (HAZİRAN/JUNE-2023)

RESEARCH ARTICLES

SAKARYA ÜNİVERSİTESİ
FEN BİLİMLERİ ENSTİTÜSÜ DERGİSİ

Sakarya University Journal of Science
SAUJS

ISSN 1301-4048 e-ISSN 2147-835X Period Bimonthly Founded 1997 Publisher Sakarya University
http://www.saujs.sakarya.edu.tr/

Title: Aortic Regeneration is Promoted by Intermittent Fasting in Aged Rats

Authors: Taha CEYLANİ, Hikmet Taner TEKER

Recieved: 2022-11-25 00:00:00

Accepted: 2023-02-18 00:00:00

Article Type: Research Article

Volume: 27
Issue: 3
Month: June
Year: 2023
Pages: 504-511

How to cite
Taha CEYLANİ, Hikmet Taner TEKER; (2023), Aortic Regeneration is Promoted by Intermittent Fasting in Aged Rats. Sakarya University Journal of Science, 27(3), 504-511, DOI: 10.16984/saufenbilder.1209954
Access link
https://dergipark.org.tr/en/pub/saufenbilder/issue/78131/1209954

Sakarya University Journal of Science 27(3), 504-511, 2023

Aortic Regeneration is Promoted by Intermittent Fasting in Aged Rats

Hikmet Taner TEKER[1], Taha CEYLANİ*[2]

Abstract

Intermittent fasting (IF) plays important role in health. The regeneration that starts at the cellular level is reflected in all tissues and organs. In this study, molecular changes in the aortic tissue of 12-month-old male Wistar rats that underwent intermittent fasting for 18 hours a day for 35 days were determined by spectrochemical analysis and machine learning algoritm. While IF did not significantly affect body weights or blood glucose levels, it led to increased food and water consumption. Spectrochemical analysis revealed significant differences in the forms of DNA, specifically an increase in the A-DNA form in aortic samples. This form of DNA plays an essential role in cellular defense systems and biological processes. There was also an increase in the Amid I band, providing information about hydration status and lipid molecule interactions. Notably, a significant decrease was observed in protein phosphorylation markers, which could impact a wide range of cellular activities. IF also led to reductions in protein carbonylation, a marker of oxidative damage, and changes in the acyl chain length of fatty acids, impacting membrane fluidity. These findings suggest that IF may offer several health benefits, including improved membrane dynamics, reduced oxidative stress, and potential cellular regeneration through autophagy. Further research is needed to confirm these observations and understand their implications for human health.

Keywords: Intermittent fasting, aorta, ATR-FTIR, wistar rat, support vector machine

1. INTRODUCTION

Cardiovascular diseases are one of the leading causes of morbidity and mortality worldwide [1]. The key pathophysiology for cardiovascular diseases is atherosclerosis, which is characterized by lipid and cholesterol metabolic abnormalities and chronic inflammation. Atherosclerotic plaques can form, worsen, and eventually burst due to a number of different reasons. One of the most important of these variables is hypercholesterolemia, and specifically an elevated low-density lipoprotein cholesterol level [2]. Also the aging promote the development of atherosclerotic lesions and calcifications. The aorta is the largest artery in the human body and arguably one of the most important it receives oxygen-rich blood from the left ventricle of the heart and supplies it to the body via the systemic circulation [3]. Aortic atherosclerosis is well recognized as a significant risk factor for atheroembolic

* Corresponding author: t.ceylani@alparslan.edu.tr (T. CEYLANI)
[1]Ankara Medipol Uniersity
[2] Muş Alparslan University
E-mail: h.tanerteker@gmail.com
ORCID: https://orcid.org/0000-0002-6621-3071, https://orcid.org/0000-0002-3041-6010

events, particularly stroke, following cardiac surgery [4].

Intermittent fasting (IF) is an essential non-pharmaceutical technique for overweight and obese patients. Alternate-day fasting, modified fasting regimens, and time-restricted feeding (TRF) are three types of IF approaches that have been used to reduce body weight in people and rodent models [5]. Standard intermittent fasting, often known as TRF (consisting of 16 hours of fasting and 8 hours of eating), is beneficial for both the maintenance of physical fitness and the amelioration of metabolic disorders [6]. Recently, it was observed that intermittent fasting for 18 hours a day for 35 days increased the species diversity in the gut microbiota, changed the presence of these species towards healthy microbiota criteria, and played a role in the recovery of the dysbiotic structure [7]. When the molecular profiles of the colon, ileum and liver tissues of the rats belonging to the same application were evaluated, it was seen that the intermittent fasting program provided significant rejuvenation in these tissues [8]. Significant molecular improvements were also determined in the study with heart tissue [9].

With its ability to detect molecular vibrations and generate molecular spectral bands in the mid-infrared region, Fourier Transform Infrared (FTIR) Spectroscopy is a useful tool in biological investigations because it can collect broad-spectrum data rapidly, easily, and without causing any damage to the sample [10]. The FTIR spectroscopic mode of attenuated total reflection (ATR) is effective for examining biological substances [11]. Chemometrics is a discipline of chemistry that deals with computer-assisted chemical data processing as well as statistics and mathematics. Chemometric techniques (machine learning approaches) are used to analyze data from a wide range of analytical processes in fields like analytical chemistry, clinical and forensic medicine, biology, and archaeology [12]. In this study, significant changes in the aortic tissue at the molecular level after intermittent fasting for 18 hours a day for 35 days were determined by ATR-FTIR. Using the FTIR data collected, it was also evaluated with the machine learning-based Support Vector Machine learning algorithm.

2. MATERIAL METHOD

2.1. Animal Studies

In the study, the male Wistar rat (12-month-old) was used. For 35 days, rats (n = 7) in the study's experimental group were subjected to intermittent fasting. While the rats in the experimental group could always drink water, their access to food was limited for 18 hours, and they could only feed for 6 hours. The experimental group's meal access period was determined to be between $9:^{00}$ a.m. and $3:^{00}$ p.m. For 24 hours, the control group (n = 7) had access to water and food. Ad libitum, the mice were fed a conventional rat diet [13]. For 35 days, the animals' body weight, feed, and water consumption were tracked. When the application process was complete, blood glucose levels were also assessed. One day after the end of the 35-day intermittent fasting program, the rats in the experimental and control groups were lightly stunned with ether, then sacrificed, and aortic tissues were removed. The excised aorta tissues were shocked on dry ice and stored in a -80^{o}C deep freezer until further study. Aorta samples from the descending aorta were used. All of the animals were kept in conventional animal care conditions.

2.2. Attenuated Total Reflectance Fourier Transform Infrared (ATR-FTIR) Spectroscopy for Sample Analysis

To examine the aorta samples, an ATR-FTIR spectrometer (PerkinElmer) was used, with a resolution of 4 cm-1 and a scan number of 32, after compressing all of the samples (2x24=48) on the Zn/Se crystal of the ATR unit. The spectra were obtained from 4000-

650 cm-1 using a Spectrum One (PerkinElmer). [5].

2.3. Studies of Prediction Utilizing a Variety of Machine Learning Techniques, All Driven by Massive Amounts of Spectral Data

Pattern recognition uses spectral data. For the most unbiased results from the FTIR spectrometers, spectra were preprocessed using The Unscrambler® X 10.3 (CAMO Software AS, Norway) by applying a baseline offset transformation in the 4000-650 cm1 region to each spectrum. Spectra were initially submitted to unsupervised Principal Component Analysis (PCA). Standard deviation normalization and leverage or full-cross random validation passed spectra. The spectra were then studied in lipid (3000-2700 cm-1), protein (1700-1500 cm-1), nucleic acid (1200-650 cm1), and complete (4000-650 cm-1) areas [5].

Support Vector Machine (SVM) is a popular machine learning approach. The Unscrambler® X 10.3 (CAMO Software AS, Norway) performed SVM classification. After preprocessing all spectra, distinct sample categories were utilized to create a training set. Nu-SVC was chosen as SVM type with a linear Kernel. Nu=0.5, weights=1.00. Training and cross-validation accuracies employed 9 cross-validation segments. The training dataset was used to all sample datasets to create an SVM classification model. [5].

2.4. FTIR Spectral Band Quantification Studies

OPUS 5.5 (Bruker) program analyzed spectral data. Before band quantification analysis, each sample's average spectrum was baseline adjusted using 128 baseline points. In thorough band studies, the bands with the greatest absorbance values in different spectral areas were picked and their beginning and ending frequencies were calculated. Using OPUS 5.5 (Bruker) software, the integral regions of biomolecule-specific frequency ranges were investigated. A virtual line was created from the band's midway to its top, and its length was measured with a virtual ruler. Bandwidth values were then calculated by drawing a horizontal line down the band at the location where 0.75 times the length of the line corresponded with the line [5].

2.5. Statistics

GraphPad Prism 6.01 was used for all statistical analyses and graphical representation of the findings (GraphPad, USA). Statistical significance was determined using an unpaired t-test, and results were indicated as $P \leq 0.05$ *. The results are shown as a mean standard error of the mean (standard error of the mean).

3. RESULTS AND DISCUSSION

IF didn't affect rats' body weights ($p \leq 0.7950$). However, rats in the control group significantly gained weight ($p \leq 0.001$). Also significant ($p \leq 0.0001$) was the difference between the experimental and control groups. Additionally, there was a significant difference in food consumption ($p \leq 0.0001$) and water ($p \leq 0.0001$). In the days following the application, the rats in the experimental group tended to consume more food and water. There was no significant difference in blood glucose ($p \leq 0.250$). [5].

Changes in various spectrochemical bands, each linked with different functional groups of biomolecules, are clearly apparent in the average spectra (whole infrared range /4000-650 cm-1) of aorta samples from the control and IF groups. A comparable classification was obtained with the SVM method with 100% accuracy, for the whole content of aorta tissues (Table 1). The PO2 antisymmetric band from the absorbance spectrum located in between 1242–1238 cm^{-1} that is assigned to total nucleic acids [14]. The absorbance of the main B and A-forms of DNA are located at 1221 cm^{-1} and 1240 cm^{-1}, respectively [15]. It is seen that intermittent fasting caused a

significant increase in A-DNA form in samples taken from the aorta Figure 1a. Double-stranded DNA may have many forms, including A-, B-, and Z-DNA. Despite the fact that the B-form DNA is the most often seen structure in solution under physiological settings, the A-form DNA serves an important biological function in the context of cellular defense systems under hard conditions [16].

Table 1 Intermittent fasting modifies the gross biomolecules in rat aorta tissues. Support Vector Machine classification for aorta samples in full (4000-650 cm-1) infrared spectral region. CA (control rats), FA (rats on intermittent fasting). Support Vector Machine type: Classification (nu-SVC). Method: Linear.

Accuracy (%)	100	
Classification		
Samples		**Class**
CA1	1	CA
CA2	2	CA
CA3	3	CA
CA4	4	CA
CA5	5	CA
CA6	6	CA
FA1	7	FA
FA2	8	FA
FA3	9	FA
FA4	10	FA
FA5	11	FA
FA6	12	FA
FA7	13	FA
FA8	14	FA

The A-form of DNA is not only involved in cellular defense systems, but also has a striking presence in many other biological processes. For certain proteins to bind to DNA, the sugar phosphate backbone of the DNA must be unprotected so that direct recognition processes may take place. Local B-DNA to A-DNA transition is triggered by proteins like polymerases, endonucleases, etc., which execute cutting and sealing actions. The B-A transition widens the main groove and narrows the minor groove, exposing previously inaccessible regions of DNA. During transcription, some transcription factors use an indirect readout method by looking for an A-form in the genome to bind to [17]. Keeping A-DNA "hydrated" is another benefit of local B-A transition, which occurs when water molecules establish bridges between the different hydrophilic atoms of DNA bases in the A-form [18].

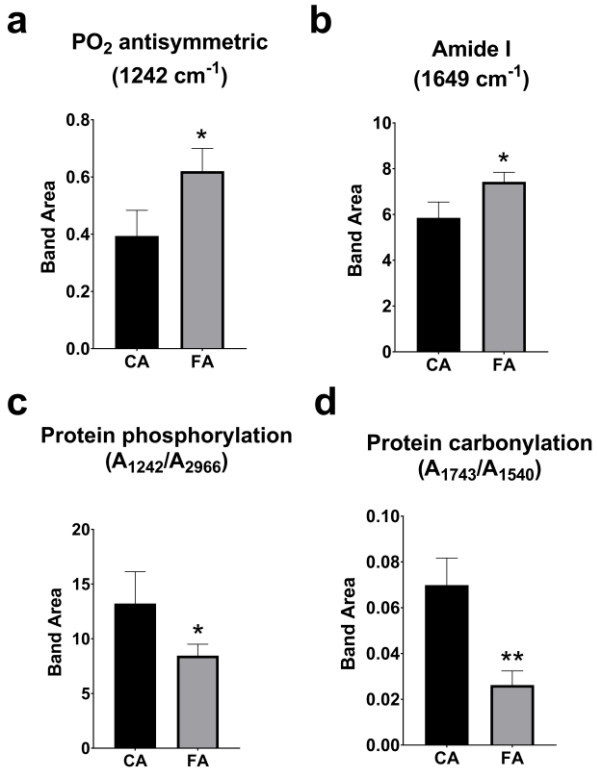

Figure 1 The changes in the FTIR spectral band areas for aorta samples. The area values of a) PO2 antisymmetric (1242 cm-1), b) Amide I (1649 cm-1), c) protein phosphorylation (A1242/A2966), and d) protein carbonylation (A1743/A1540). CA (control rats), FA (rats on intermittent fasting).

There was also a significant increase in the Amid I band in aortic tissue samples after intermittent fasting Figure 1b. Amide I (1649 cm−1) which associated with C=O stretching The SVM method revealed 100% training and 100% cross-validation accuracies for the whole content of aorta tissue vibration [19]. This is a particularly useful band for evaluating environmental changes, hydrogen bonding of lipid molecules, and differentiating ligand interactions [20]. As a result, the location and intensity of the carbonyl band provide useful information about the hydration status of lipid molecules

near the water interface. Water content varies as lipid density changes. As the lipid layer thickens, the headgroup becomes less hydrated, causing the carbonyl bands to shift to higher wavenumbers [21].

Phosphorylation of proteins is the most significant post-translational modification, with effects on a wide range of cellular activities including gene expression, metabolism, cell cycle control, differentiation, and death [22]. In this study, after intermittent fasting, there was a significant decrease in the bands area ratio A_{1242}/A_{2966} that is markers of protein phosphorylation in the aortic tissue Figure 1c. Proteins serve diverse purposes depending on the specific alteration state they are in, such as after acetylation, methylation, or phosphorylation. A protein's function may respond quite differently to the same change made at two distinct locations. Some protein phosphorylation sites may activate the protein's activities, whereas other phosphorylation sites can inhibit them. So, the functional regulation of a protein can be changed in many ways, such as by adding or removing residues in certain places [23].

Protein oxidation plays a crucial role in the pathophysiology of aging and the regulation of physiological processes, limiting tissue injury. According to the oxidative stress hypothesis of aging, senescence is primarily governed by an advanced accumulation of oxidized molecules that disrupt biotic homeostasis and cause a functional deterioration in cellular physiology. High amounts of protein carbonylation, known as a marker of protein oxidative damage [24]. The protein carbonylation bands area ratio A_{1743}/A_{1540} was also significantly reduced after intermittent fasting Figure 1d. With the application of intermittent fasting, damage to age-related oxidative stress mechanisms may be improved. However, recent proteomic studies revealed opposite findings on the key doctrine of oxidative stress theory were identified in the soluble cell portions from the exceptionally long-living rodent (naked-mole rats) compared to short-living mice [25].

The acyl chain length of fatty acids can be calculated by band area ratio A_{2922}/A_{2966}. In this study, it was observed that there was a significant decrease in the acyl chain length band area ratio after intermittent fasting Figure 2a. The length of the fatty acid tail influences membrane fluidity. This is due to the intermolecular interactions of the phospholipid tails, which provide membrane rigidity. Longer phospholipid tails allow for tail-to-tail interactions while decreasing membrane fluidity. At physiological temperatures, saturated lipid acyl chains tend to produce non-fluid, closely packed gel phases, while unsaturated lipid acyl chains fluidize the bilayer [26]. When the stiffness of the aorta and other blood vessels due to age is taken into account, it is clear that intermittent fasting can help get rid of this problem.
Membranes, which are composed of lipids and proteins, are very complex structures that perform several functions in living organisms. By separating cells and cell compartments from their environment, they serve as an effective barrier against a variety of chemicals. The membranes, on the other hand, must permit contact with the same environment by actively or passively transporting things into and out of the cell. The cell surface receives external signals, and the membranes' role is to transfer them to the cell's internal machinery. Cells may adapt to their constantly changing surroundings by doing so. To execute all of these functions, a biological membrane must maintain dynamic equilibrium between its components and with their surroundings [27]. The band area ratio $A_{2922}/_{2966}$ of membrane dynamics increased significantly after intermittent fasting Figure 2b. One of the most important features of intermittent fasting applications exceeding 16 hours is that they provide regeneration at the cellular level by activating autophagy mechanisms [28]. A significant increase in membrane dynamics may indicate this renewal.

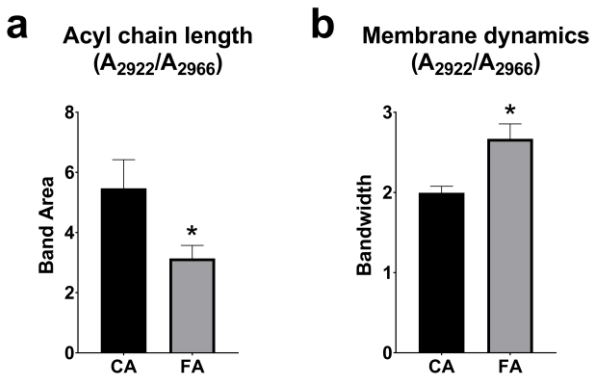

Figure 2 The changes in the FTIR spectral band areas for aorta samples. The area values of **a)** Acyl chain lenght (A2922/A2966), **b)** Membrane dynamics (A2922/A2966). CA (control rats), FA (rats on intermittent fasting).

3. CONCLUSIONS

In this study, the effects of intermittent fasting on aortic tissue were evaluated with ATR-FTIR spectroscopy. The practice of intermittent fasting caused significant molecular changes. When the significant increase in membrane dynamics was evaluated together with the other results obtained, it was determined that the application of intermittent fasting supported the regeneration of the aortic tissue. In this respect, intermittent fasting may be considered an effective therapeutic approach for age-related aortic deformations.

Funding
This research received no specific grant from any funding agency in the public, commercial, or not-for-profit sectors.

Authors' Contribution
The authors contributed equally to the study.

The Declaration of Conflict of Interest/ Common Interest
No conflict of interest or common interest has been declared by the authors.

The Declaration of Ethics Committee Approval
The study was carried out with the approval of the Ethics Committee (approval number: 2021/05) from the Saki Yenilli Experimental Animal Production and Practice Laboratory.

The Declaration of Research and Publication Ethics
The authors of the paper declare that they comply with the scientific, ethical and quotation rules of SAUJS in all processes of the paper and that they do not make any falsification on the data collected. In addition, they declare that Sakarya University Journal of Science and its editorial board have no responsibility for any ethical violations that may be encountered, and that this study has not been evaluated in any academic publication environment other than Sakarya University Journal of Science.

REFERENCES

[1] S. S, Virani, A. Alonso, E. J. Benjamin, M. S. Bittencourt, C. W. Callaway, A. P. Carson, A. M. Chamberlain, A. R. Chang, S. Cheng, F. N. Delling, L. Djousse, M. S. V. Elkind, J. F. Ferguson, M. Fornage, S. S. Khan, B. M. Kissela, K. L. Knutson, T. W. Kwan, D. T. Lackland, T. T. Lewis, J. H. Lichtman, C. T. Longenecker, M. S. Loop, P. L. Lutsey, S. S. Martin, K. Matsushita, A. E. Moran, M. E. Mussolino, A. M. Perak, W. D. Rosamond, G. A. Roth, U. K. A. Sampson, G. M. Satou, E. B. Schroeder, S. H. Shah, C. M. Shay, N. L. Spartano, A. Stokes, D. L. Tirschwell, L. B. VanWagner, C. W. Tsao, "Heart disease and stroke statistics-2020 update: A report from the American Heart Association: A report from the American Heart Association," Circulation, vol. 141, no. 9, pp. e139–e596, 2020.

[2] A. C. Milin, G. Vorobiof, O. Aksoy, R. Ardehali, "Insights into aortic sclerosis and its relationship with coronary artery disease," Journal of the American Heart Association, vol. 3, no. 5, p. e001111, 2014.

[3] A. D. Caballero, S. Laín, "A review on computational fluid dynamics modelling in human thoracic aorta," Cardiovascular Engineering and Technology, vol. 4, no. 2, pp. 103–130, 2013.

[4] A. Harloff, J. Simon, S. Brendecke, D. Assefa, T. Helbing, A. Frydrychowicz, J. Weber, M. Olschewski, C. Strecker, J. Hennig, C. Weiller, M. Markl, "Complex plaques in the proximal descending aorta: an underestimated embolic source of stroke: An underestimated embolic source of stroke," Stroke, vol. 41, no. 6, pp. 1145–1150, 2010.

[5] G. Li, C. Xie, S. Lu, R. G. Nichols, Y. Tian, L. Li, D. Patel, Y. Ma, Brocker, N. C. T. Yan, K. W. Krausz, R. Xiang, O. Gavrilova, A. D. Patterson, F. J. Gonzalez, "Intermittent fasting promotes white adipose browning and decreases obesity by shaping the gut Microbiota," Cell Metabolism, vol. 26, no. 4, pp. 672-685.e4, 2017.

[6] C. A. Rynders, E. A. Thomas, A. Zaman, Z. Pan, V. A. Catenacci, E. L. Melanson, "Effectiveness of intermittent fasting and time-restricted feeding compared to continuous energy restriction for weight loss," Nutrients, vol. 11, no. 10, p. 2442, 2019.

[7] H. T. Teker, T. Ceylani, "Intermittent fasting supports the balance of the gut microbiota composition," International Microbiology, vol. 26, no. 1, pp. 51-57, 2022.

[8] T. Ceylani, H. T. Teker, G. Samgane, R. Gurbanov, "Intermittent fasting-induced biomolecular modifications in rat tissues detected by ATR-FTIR spectroscopy and machine learning algorithms," Analitical Biochemistry, vol. 654, no. 114825, p. 114825, 2022.

[9] İ. Ardahanlı, H. İ. Özkan, F. Özel, R. Gurbanov, H. T. Teker, T. Ceylani, "Infrared spectrochemical findings on intermittent fasting-associated gross molecular modifications in rat myocardium," Biophysical Chemistry, vol. 289, no. 106873, p. 106873, 2022.

[10] R. Gurbanov, F. Yıldız, "Molecular Profile of Oral Probiotic Bacteria To Be Used With Functional Foods," Journal of Food and Health Science, vol. 12, no. 11, pp. S117-31, 2017.

[11] C. Aksoy, F. Severcan, "Infrared spectroscopy and imaging in stem cells and aging research," Methods in Molecular Biology, vol. 2045, pp. 201–215, 2019.

[12] E. Dinç, "Kemometri Çok Değişkenli Kalibrasyon Yöntemleri," Hacettepe Üniversitesi Eczac Fakültesi Dergisi, vol. 39, pp. 46–58, 2007.

[13] M. P. Mattson, V. D. Longo, M. Harvie, "Impact of intermittent fasting on health and disease processes," Ageing Research Reviews, vol. 39, pp. 46–58, 2017.

[14] M. Banyay, M. Sarkar, A. Gräslund, "A library of IR bands of nucleic acids in solution," Biophysical Chemistry, vol. 104, no. 2, pp. 477–488, 2003.

[15] D. R. Whelan, K. R. Bambery, P. Heraud, M. J. Tobin, M. Diem, D. McNaughton, B. R. Wood, "Monitoring the reversible B to A-like transition of DNA in eukaryotic cells using Fourier transform infrared spectroscopy," Nucleic Acids Research, vol. 39, no. 13, pp. 5439–5448, 2011.

[16] T. Liu, T. Yu, S. Zhang, Y. Wang, W. Zhang, "Thermodynamic and kinetic properties of a single base pair in A-

DNA and B-DNA," Physical Review, vol. 103, no. 4–1, p. 042409, 2021.

[17] M. Kulkarni, A. Mukherjee, "Understanding B-DNA to A-DNA transition in the right-handed DNA helix: Perspective from a local to global transition," Progress İn Biophysics And Molecular Biology, vol. 128, pp. 63–73, 2017.

[18] N. Pastor, "The B- to A-DNA transition and the reorganization of solvent at the DNA surface," Biophysical Journal, vol. 88, no. 5, pp. 3262–3275, 2005.

[19] N. S. Mehanna, Z. M. R. Hassan, H. M. F. El-Din, A. A. E. Ali, R. Amarowicz, T. M. El-Messery, "Effect of interaction phenolic compounds with milk proteins on cell line," Food and Nutrition Science, vol. 05, no. 22, pp. 2130–2146, 2014.

[20] L. B. Dreier, M. Bonn, E. H. G. Backus, "Hydration and orientation of carbonyl groups in oppositely charged lipid monolayers on water," The Journal Of Physical Chemistry, vol. 123, no. 5, pp. 1085–1089, 2019.

[21] A. Dicko, H. Bourque, M. Pézolet, "Study by infrared spectroscopy of the conformation of dipalmitoylphosphatidylglycerol monolayers at the air–water interface and transferred on solid substrates," Chemistry and Physics of Lipids, vol. 96, no. 1–2, pp. 125–139, 1998.

[22] C.-R. Lee, Y. H. Park, H. Min, Y. R. Kim, Y. J. Seok, "Determination of protein phosphorylation by polyacrylamide gel electrophoresis," Journal Of Microbiology, vol. 57, no. 2, pp. 93–100, 2019.

[23] R. Wang, G. Wang, "Protein modification and autophagy activation," Advances In Experimental Medicine And Biology, vol. 1206, pp. 237–259, 2019.

[24] M. L. R. Paraboni, J. Kalinoski, B. G. Braciak, A. E. Wilk, L. S. Santos, E. G. Schmitt, V. Manfredini, I.L. Gonçalves, "Protein carbonyl products, malondialdehyde, glutathione and vitamins C/E of breast cancer patients subjected to chemotherapy," Brazilian Journal of Oncology, vol. 18, e20220302, 2022.

[25] E. M. De Waal, H. Liang, A. Pierce, R. T. Hamilton, R. Buffenstein, A. R. Chaudhuri, "Elevated protein carbonylation and oxidative stress do not affect protein structure and function in the long-living naked-mole rat: a proteomic approach," Biochemical And Biophysical Research Communications, vol. 434, no. 4, pp. 815–819, 2013.

[26] S. Ballweg, E. Sezgin, M. Doktorova, R. Covino, J. Reinhard, D. Wunnicke, I. Hänelt, I. Levental, G. Hummer, R. Ernst, "Regulation of lipid saturation without sensing membrane fluidity," Nature Communications, vol. 11, no. 1, p. 756, 2020.

[27] B. Szalontai, Y. Nishiyama, Z. Gombos, N. Murata, "Membrane dynamics as seen by Fourier transform infrared spectroscopy in a cyanobacterium, Synechocystis PCC 6803," Biochimica Et Biophysica Acta, vol. 1509, no. 1–2, pp. 409–419, 2000.

[28] A. Paoli, G. Tinsley, A. Bianco, and T. Moro, "The influence of meal frequency and timing on health in humans: The role of fasting," Nutrients, vol. 11, no. 4, p. 719, 2019.

SAKARYA ÜNİVERSİTESİ
FEN BİLİMLERİ ENSTİTÜSÜ DERGİSİ

Sakarya University Journal of Science
SAUJS

ISSN 1301-4048 e-ISSN 2147-835X Period Bimonthly Founded 1997 Publisher Sakarya University
http://www.saujs.sakarya.edu.tr/

Title: Application of Classical Fenton Process and Advanced Photo Electro Fenton Process for the Degradation of COD from Wood Processing Wastewater: A Comparative Study

Authors: Murat SOLAK

Recieved: 2022-09-09 00:00:00

Accepted: 2023-02-20 00:00:00

Article Type: Research Article

Volume: 27
Issue: 3
Month: June
Year: 2023
Pages: 512-522

How to cite
Murat SOLAK; (2023), Application of Classical Fenton Process and Advanced Photo Electro Fenton Process for the Degradation of COD from Wood Processing Wastewater: A Comparative Study. Sakarya University Journal of Science, 27(3), 512-522, DOI: 10.16984/saufenbilder.1173306
Access link
https://dergipark.org.tr/en/pub/saufenbilder/issue/78131/1173306

Sakarya University Journal of Science 27(3), 512-522, 2023

Application of Classical Fenton Process and Advanced Photo Electro Fenton Process for the Degradation of COD from Wood Processing Wastewater: A Comparative Study

Murat SOLAK*[1]

Abstract

In this study, Chemical Oxygen Demand (COD) removal efficiency from wood processing wastewaters by Fenton Process (FP) and Photo Electro Fenton Process (PEFP) were examined. Important operating parameters such as pH, Fe^{+2} concentration/(amper for PEFP), H_2O_2 concentration and reaction time were optimized. Optimum operation conditions of the FP were pH 3.5, 1.4 gr/L Fe^{2+} concentration and 50 gr/L H_2O_2 concentration and 150 min. reaction time while they were pH 3.00, 9.99 mA/cm^2 current density and 70 gr/L H_2O_2 concentration and 150 min reaction time in PEFP. At the optimum conditions, COD removal efficiency of FP and PEFP was 91% and 99%, respectively. Sludge production of FP was 20% higher than PEFP at the optimum conditions.

Keywords: Wood processing wastewater, Fenton process, photo electro Fenton process

1. INTRODUCTION

Depending on rapid developments in organic material demand due to the increasing demands in home usages, the number of the wood processing industries has increased in recent years. The amount of wastewater generated by this sector, which uses high amounts of water in production processes, has also increased. In the process of manufacturing wood products, trees brought to the factory as billets are peeled from their shells. It is then processed by immersing in water at high temperatures. The wood is held in water at high temperature for about one day. This process is the source of wastewater. Finally, the logs are converted into smaller wood products by various processes. This wastewater generated in production processes has high organic pollutant as COD, BOD and colour. In the treatment of these kind of wastewaters conventional methods such as coagulation-flocculation are not enough. Therefore, it would be more appropriate to apply advanced treatment techniques as oxidation [1], membrane filtration [2], biological processes [3] to such wastewaters. The Fenton oxidation process is one of the processes where the organic pollutants are effectivley removed from wastewaters at low pH values with Fe(II) reagent and H_2O_2 oxidant [4]. The formation of the

* Corresponding author: Murat SOLAK (M. SOLAK)
[1] Düzce University
E-mail: muratsolak@duzce.edu.tr, musolak26@gmail.com
ORCID: https://orcid.org/0000-0003-1542-1599

homogeneous hydroxyl radicals (OH) is the main reaction for the Fenton processes and hydroxyl radicals play important role in this process, oxidizing the organic pollutants into CO_2, H_2O and inorganic ions by dehydrogenating or hydroxylating reaction Eq. (5) or Eq. (6), respectively. Fenton reactions are given in Equation 1 to 7 [5].

$$Fe^{2+} + H_2O_2 \rightarrow Fe^{3+} + OH^- + OH^{\cdot} \quad (1)$$

Fe (II) is oxidized to Fe (III) by another reaction of hydroxyl radicals in the environment.

$$OH^{\cdot} + Fe^{2+} \rightarrow OH^- + Fe^{3+} \quad (2)$$

Fe^{3+} decomposes H_2O_2 with a mechanism that involves hydroxyl and hydroperoxyl radicals.

$$Fe^{+3} + H_2O_2 \leftrightarrow Fe - OOH^{2+} + H^+ \quad (3)$$

$$Fe - OOH^{2+} \rightarrow HO_2^{\cdot} + Fe^{2+} \quad (4)$$

$$Fe^{2+} + HO_2^{\cdot} \rightarrow Fe^{+3} + HO_2^- \quad (5)$$

$$Fe^{+3} + HO_2^{\cdot} \rightarrow Fe^{2+} + H^+ + O_2 \quad (6)$$

$$OH^{\cdot} + H_2O_2 \rightarrow H_2O + HO_2^{\cdot} \quad (7)$$

Photo Electro Fenton process is an advanced Fenton process which is used in a wide scope of wastewaters as landfill leachate [6], coking industry [7], dairy industry [8], dye production industry [9]. The difference of the Fenton process from the electro-Fenton process is the method of addition of Fe(II) to the wastewater. In the Fenton process, Fe(II) is added externally, but in Electro-Fenton process Fe(II) ions are produced by electrolysis. In addition, to enhance the effectiveness of electro Fenton process, and to oxidize the organic materials effectively a UV lamp can be added to this process. Photo Electro Fenton process, is the wastewater treatment technique that UV and electro Fenton processes are used together [10], [11]. The Photo Electro Fenton process takes place in two ways. i) production of hydroxyl radicals by photo reduction of $Fe(OH)^{2+}$ (Eq. (8)) and (ii) production of Fe (II) by photolysis of Fe (III) (Eq.(9)).

$$Fe(OH) \xrightarrow{2+h\upsilon(k_4)} Fe^{2+} + {}^{\cdot}OH \quad (8)$$

$$R(CO_2) - Fe(III) + h\upsilon \rightarrow R({}^{\cdot}CO_2) + Fe(II) \rightarrow {}^{\cdot}R + CO_2 \quad (9)$$

In the present study, the performance of Fenton process (FP) and photo electro-Fenton (PEF) process for the removal of high COD from wood processing wastewater was compared. The effects of operating parameters such as pH, Fe^{2+} concentration/current, H_2O_2 concentration and reaction time on COD removal were investigated.

2. MATERIALS AND METHODS

2.1 Wastewater samples

Characterization of wood processing wastewater is given in Table 1. Raw wastewater is supplied from a wood processing company that produces wood products in Düzce, Türkiye.

Table 1 Raw wastewater characterization

Parameter	Value/Concentration
pH	5.52 ± 0,21
Conductivity	4.16 ± 0,1 mS/cm
COD	3850 ± 150 mg/L
SS	1500 ± 120 mg/L
TDS	2.07 ± 0.02 g/L
Colour	
460nm	12 m^{-1}
525nm	15 m^{-1}
620nm	17 m^{-1}

2.2 FP experiments

Fenton process experiments were performed with a volume of 400 mL wood processing wastewater by Jar Tests (Fig. 1). $FeSO_4.7H_2O$ (Ferrous sulfate - heptahydrate) as a Fe^{2+} source and H_2O_2 (hydrogen peroxide, 50% W/W) as an oxidant were used in the experiments. Since Fenton process is efficient

at low pH, pH was adjusted by adding H_2SO_4, $FeSO_4.7H_2O$ was initially added to the pH-adjusted sample, and H_2O_2 was added in the second step. After the addition of $FeSO_4.7H_2O$ and H_2O_2, the samples were mixed at 150 rpm with rapid mixing for 5 minutes and at 50 rpm with slow mixing for 45 minutes. When the determined reaction times were completed, the pH of the wastewater sample was increased to 7.5-8.0. Then the pollutants in the wastewater were allowed to settle for 1 hour. The supernatants were filtered with using 0.45 μm filter papers and soluble COD and colour analysis were conducted. pH adjustment was done by using 1 N H_2SO_4 and 1 N NaOH solutions.

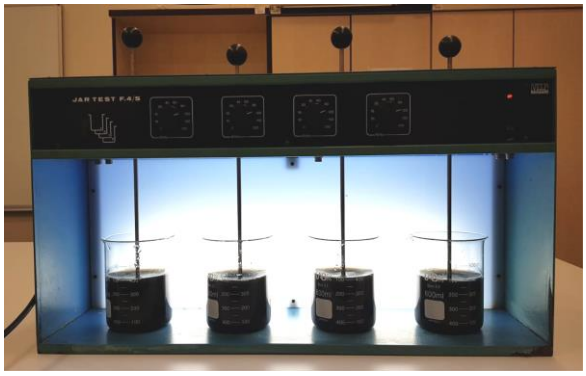

Figure 1 Jar test

2.3 PEFP experiments

PEFP experiments were performed with a volume of 750 mL of wood processing wastewater by the PEF reactor (Fig. 2). Reactor dimensions were as 20 cm x 10 cm x 10 cm (HxLxB). 40 W (254 nm) UV lamp was used for the UV light source in PEFP. 10 iron electrodes with dimensions of 1 cm x 20 cm were used for the electro Fenton process in the reactor (Fig. 3). 10 mL H_2O_2 oxidant was added as soon as the electrolysis process was started in the reactor. Then the oxidant was added to the reactor with an interval of 10 min. 3A-30V DC Power Supply was used to give an electricity to the electrodes.

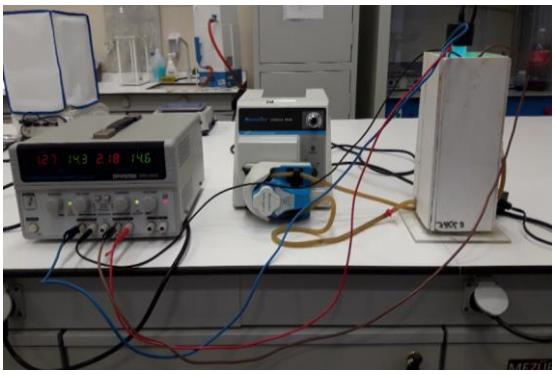

Figure 2 PEFP experimental design

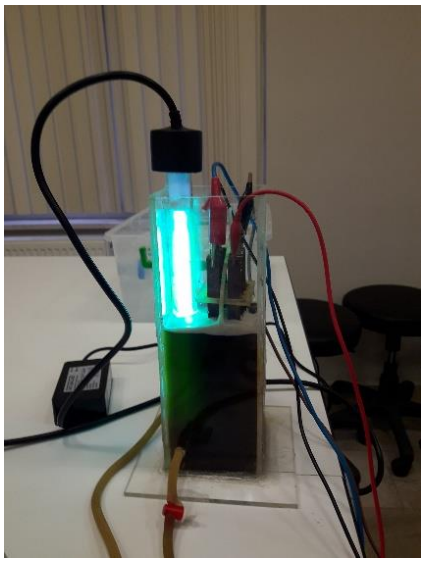

Figure 3 PEFP reactor

2.4 Analytical methods

In experimental studies, Standard Method (5220 D) was used for the determination of COD concentrations in inlet and outlet water samples. pH measurements were performed by electrometric method with Hanna HI 2211 pH meter, conductivity and TDS measurements were performed by electrometric method with Hach Conductivity-TDS meter [12].

3. RESULTS AND DISCUSSION

3.1 Effect of pH on FP and amper on PEFP

pH is one of the most important parameters affecting the efficiency of Fenton processes. Especially, the wastewater medium should be acidic for removing organic contaminants

such as COD, BOD and color [13]. Because, at higher pH values, free iron species ferric oxyhydroxide decreases due to precipitation [14], while efficiency of the electro Fenton decreases under pH 3 through complex formation of H_2O_2 and Fe^{3+} [15].

In the experimental conditions, where Fe^{2+} concentration was 0.8 g/L, H_2O_2 concentration was 40 g/L and reaction time was 75 minutes, optimum pH was determined as 3.0, COD removal efficiency was 59% and sludge volume was 3.45 kg/m^3 in Fenton process (Fig. 4.). A similar result for the effect of pH was observed in a study by Çetinkaya et al. In PEFP, in the conditions of 1.25 A of current, 40 g/L of H_2O_2, 75 min of reaction time, optimum pH was determined as 3.5, COD removal efficiency was determined as 74% and sludge volume was 0.48 kg/m^3. Also, low pH value was effective on removal of COD by Fenton processes. Sludge volume was decreased while pH increased in all Fenton processes in the study. Similar results were observed in the study of Su et al. 2019 [16]. In FP, sludge volume was 14 times larger, and COD removal efficiency was approximately 15 % less than PEFP, in optimum pH values.

EF processes have been preferred over other electrochemical and oxidation other methods due to the high mineralization rates and treatment efficiency of organic pollutants. This high efficiency is partly due to the continuous regeneration of Fe^{2+} at the cathode. EF process thus avoids Fe^{3+} accumulation in the medium and minimizes the production of iron sludge [17, 18] At the same time another reason why the sludge volume is less than the classical Fenton process is that ultraviolet light can increase the catalytic capacity of the catalysts, increasing the degradation efficiency of organic pollutants and reducing iron sludge production [19, 18].

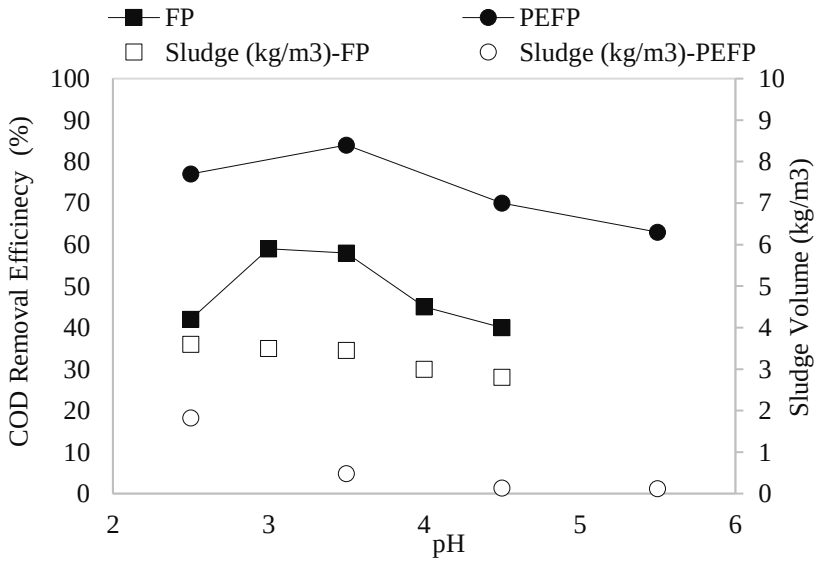

Figure 4 Effect of pH parameter on FP and PEFP
(FP: Fe^{2+} =0.8 g/L, H_2O_2 = 40 g/L, Reaction Time= 75 min),
(PEFP: I=1.25A-8.33 mA/cm^2, H_2O_2 = 40 g/L, Electrolysis Time= 75 min)

3.2 Effect of Fe^{2+} concentration on FP and amper on PEFP

Ferrous ion is an important parameter which influences the Fenton processes. Because while the concentration of Fe^{2+} increases, more hydroxyl radicals produces in the solution [20]. In the study same trends were observed. At the conditions of pH 3.5, H_2O_2 40 g/L, reaction time 75 min, optimum Fe^{+2} concentration was determined as 1.4 g/L, COD removal efficiency was determined as 75%, and sludge volume was 4.5 kg/m^3, in Fenton process. At the conditions of pH 3, 40

g/L of H_2O_2, 75 min of reaction time, optimum current was determined as 1.5 A-9.99 mA/cm^2, COD removal efficiency was determined as 88% and sludge volume was 0.88 kg/m^3, in PEFP (Fig. 5.). At the optimum conditions, sludge volume was 4 times larger, and COD removal efficiency was approximately 13% less than PEFP. Increasing of the Fe^{+2} concentration from 0.6 to 1.4 g/L, COD removal efficiency was enhanced from 28% to 75%. When current increased from 1 to 2 A, the COD removal efficiency was increased from 73% to 89% in PEFP.

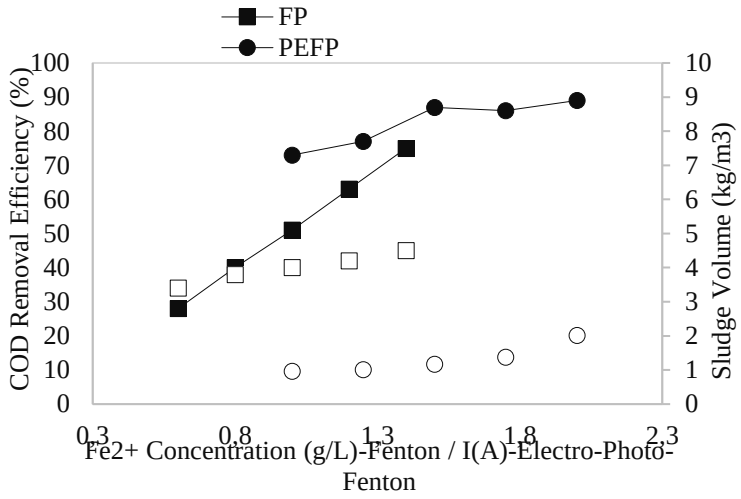

Figure 5 Effect of Fe^{2+} Concentration on FP and Effect of Amper on PEFP
(FP: pH 3.5, H_2O_2 = 40 g/L, Reaction Time= 75 min)
(PEFP: pH 3, H_2O_2 = 40 g/L, Electrolysis Time= 75 min
(1A-6.66mA/cm^2, 1.25A-8.33 mA/cm^2, 1.5A-9.99 mA/cm^2, 1.75A-11.66 mA/cm^2, 2A-13.32 mA/cm^2)

3.3 Effect of H_2O_2 concentration on FP and PEFP

H_2O_2 is a main parameter affecting the degradation efficiency of organic pollutants. Because of that in order to determine the maximum removal efficiency of organic pollutants, the optimal H_2O_2 concentration should be examined. Generally, the removal efficiency of organic pollutants increases with the increasing of H_2O_2 concentration [21, 22]. However, H_2O_2 has to be given in an optimal dose, otherwise, the excessive H_2O_2 not only increases the operating costs, but also increases the scavenging effect of OH by H_2O_2 [23, 24], which has a negative effect on the degradation of organic pollutants. At the conditions of pH 3.5, 1.4 g/L of Fe^{+2}, 75 min of reaction time, optimum H_2O_2 concentration was determined as 50 g/L, COD removal efficiency was determined as 82%, and sludge volume was 3.3 kg/m^3, in FP. At the conditions of pH 3, 1.5 A of current, 75 min of reaction time, optimum H_2O_2 concentration was determined as 70 g/L, COD removal efficiency was determined as 95% and sludge volume was 2.96 kg/m^3, in PEFP (Fig. 6.). In optimum conditions, sludge volume of FP was 1.1 times larger, and COD removal efficiency was approximately 13% less than PEFP.

Increasing of H_2O_2 concentration from 30 to 60 g/L, COD removal efficiency was enhanced from 36% to 82% in FP. Increasing of H_2O_2 concentration from 30 to 70 g/L, COD removal efficiency was enhanced from 79% to 95% in PEFP.

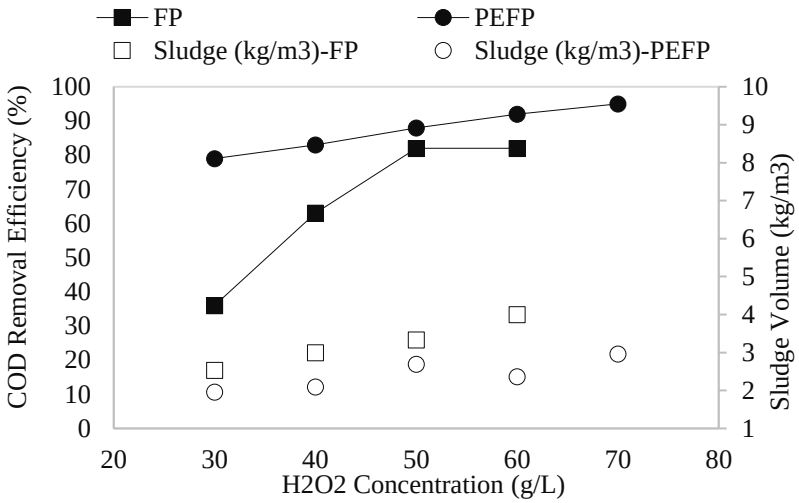

Figure 6 Effect of H_2O_2 concentration on FP and PEFP
(FP: pH 3.5, Fe^{2+} =1.4 g/L, Reaction Time= 75 min)
(PEFP: pH 3, I=1.5A-9.99 mA/cm^2, Electrolysis Time= 75 min)

3.4 Effect of reaction time on FP and PEFP

In Fenton processes, the reaction time has to be optimized for effective COD removal. While iron ions are added at the beginning of the reaction in the Fenton process, the reaction begins with the dissolution of the iron electrodes in the electrochemical Fenton process. For this reason, reaction time and optimization of the electrochemical Fenton process is more important than the classical Fenton process. At the conditions of pH 3.5, 1.4 g/L of Fe^{+2}, 50 g/L of H_2O_2, optimum reaction time was determined as 150 min, COD removal efficiency was determined as 91 %, and sludge volume was 10 kg/m^3, in FP. In the conditions of 3 of pH, 1.5 A of current, 75 min of reaction time, optimum H_2O_2 concentration was determined as 1.5 A, COD removal efficiency was determined as 99 % and sludge volume was 8.3 kg/m^3, in PEFP (Fig. 7.). At the optimum conditions, sludge volume of FP was 1.1 times higher, and COD removal efficiency was approximately 13% less than PEFP. In a study, COD removal efficiency was determined as 97% in an initial concentration of 2000 mg/L from landfill leachate wastewater by photo electro Fenton process [6].

Fenton reaction is seen in Eq. 10. Fe^{2+} oxidizes to Fe^{3+} to formation of hydroxyl radicals [10].

$$Fe^{2+} + H_2O_2 \rightarrow Fe^{3+} + OH^- + OH^{\cdot} \qquad (10)$$

This reaction is propagated by ferrous ion regeneration, which is mainly due to the reduction of the produced ferric species with hydrogen peroxide.

$$H_2O_2 + Fe^{3+} \rightarrow Fe^{2+} + {}^{\cdot}H_2O + H^+ \qquad (11)$$

The rate constant of Eq. (1) varies between 63 and 76 L mol^{-1}s^{-1} whereas the rate constant of Eq. (2) is in the order of 0.01–0.02 L mol^{-1}s^{-1} [25-26-11]. This means that the consumption of ferrous ions is more rapid than the regeneration. This results in the formation of large amount of ferric hydroxide sludge during the process, which occurs additional sludge disposal problems [27, 28, 11]. In the study FP was produced more sludge than PEFP. It is thought that sufficient iron dissolution in the electrochemical Fenton process and also the support of this process with UV causes less sludge formation compared to the FP.

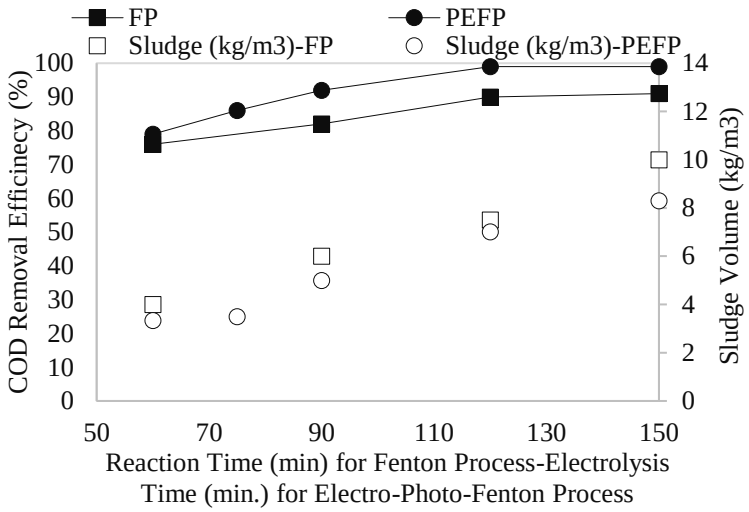

Figure 7 Effect of reaction time on FP and PEFP
(FP: pH 3.5, Fe^{2+} =1.2 g/L, H_2O_2 = 50 g/L)
(PEFP: pH 3, I=1.5A-9.99 mA/cm^2, H_2O_2 = 70 g/L)

Raw wood processing wastewater, sludge occurred in PEFP after neutralization (after 60 min) and sludge occurred in FP after neutralization (after 60 min) was given in Fig. 8a, 8b and 8c., respectively. The obtained sludge of Fenton processes is seen as a reddish-brown color.

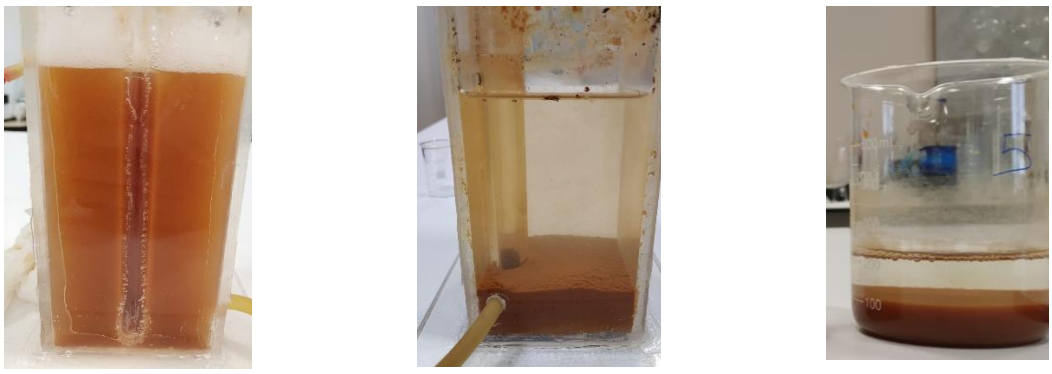

a) b) c)

Figure 8 a) Raw wood processing wastewater, b) Sludge occurred in PEFP after neutralization (after 60 min), c) Sludge occurred in FP after neutralization (after 60 min)

In the neutralization phase ferric hydroxide occurs as the main chemical in Fenton sludge. In pH 3.7-7.0 ferrihydrite occurs and in high pH values as >7.0 the Fenton sludge was transformed to goethite. The chemical compounds formed in the precipitate can be explained in Eq. 10-11 [16]. Since the precipitation process was carried out at the pH of 7.5-8 range in the study, it is thought that the fenton sludge obtained may be goethite.

i) Schwertmannite

$$Fe_8O_8(OH)_{8-2x}(SO_4)_x + 2XOH^- \rightarrow 8FeOOH + xSO_4^{2-} \quad (10)$$

ii) Ferrihydrite

$$Fe_5HO_8.4H_2O \rightarrow 5FeOOH + 2H_2O \quad (11)$$

3.5 Reaction kinetics of FP and PEFP

The oxidation of organic pollutants by Fenton processes are commonly considered as a single-stage process that conforms to pseudo first-order kinetics [29]. In this study, all of the Fenton processes showed the same trend. R^2 values of 0, 1. and 2. order reaction kinetics of FP and PEFP processes are given in Table 2 and Equations are given in Figure

9. It was determined that FP and PEFP were compatible with the 1st order kinetic.

Table 2 R^2 values of the kinetic models

Process	0.	1st	2nd
FP	0.80	0.95	0.72
PEFP	0.78	0.96	0.95

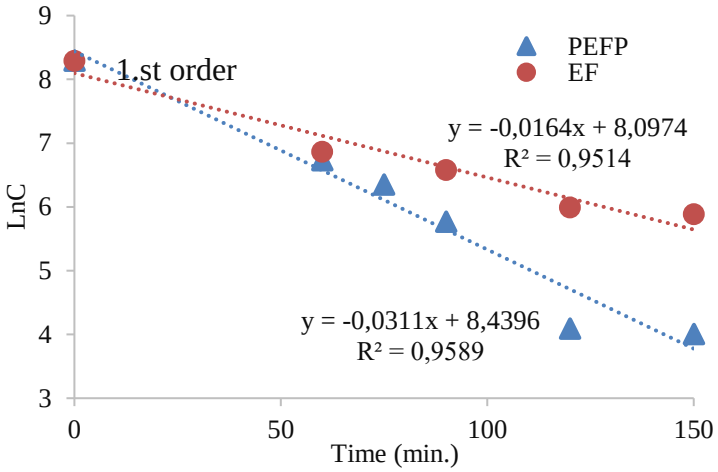

Figure 9 1st order kinetic model of EF and PEFP

4. CONCLUSION

Fenton and Photo Electro Fenton Processes have high removal efficiency in the removal of COD from wood processing industry. In acidic medium conditions all Fenton processes are effective. Optimum values for FP were determined as 1.4 mg/L of Fe concentration, 50 g/L of H_2O_2 concentration and 150 min of reaction time; for PEFP were determined as 1.5 A of amper, 70 g/L of H_2O_2 concentration and 150 min of reaction time. At the optimum conditions, Fenton process and electro-photo-Fenton process discharge COD concentration was 360 mg/L and 40 mg/L, respectively. And sludge production of Fenton process was 20% greater than PEFP.

PEFP can be an effective approach improving the wastewater quality for recovery and/or reuse of the wood processing wastewater due to its higher COD removal efficiency and lower discharge COD concentration and sludge volume when compared to FP.

Acknowledgments
The author would like to acknowledge the reviewers and editors of Sakarya University Journal of Science.

Funding
The author has no received any financial support for the research, authorship or publication of this study.

Authors' Contribution
The first author contributed 100%.

The Declaration of Conflict of Interest/ Common Interest
No conflict of interest or common interest has been declared by the authors.

The Declaration of Ethics Committee Approval
This study does not require ethics committee permission or any special permission.

The Declaration of Research and Publication Ethics
The authors of the paper declare that they comply with the scientific, ethical and quotation rules of SAUJS in all processes of the paper and that they do not make any falsification on the data collected. In addition, they declare that Sakarya University Journal of Science and its editorial board have no responsibility for any ethical violations that may be encountered, and that this study has not been evaluated in any academic

publication environment other than Sakarya University Journal of Science.

REFERENCES

[1] S. Y. Güvenç, "Optimization of COD removal from leachate nanofiltration concentrate using H_2O_2/Fe^{+2}/heat–Activated persulfate oxidation processes", Process Safety and Environmental Protection vol. 126 pp. 7, 2019.

[2] R. Lafi, L. Gzara, R. H. Lajimi, A. Hafiane, "Treatment of textile wastewater by a hybrid ultrafiltration/electrodialysis process", Chemical Engineering & Processing: Process Intensification, vol. 132, pp. 105-113, 2018.

[3] S. C. Azimi, F. Shirini, A. Pendashteh, "Evaluation of cod and turbidity removal from woodchips wastewater using biologically sequenced batch reactor", Process Safety and Environmental Protection, vol. 128, pp. 211-227, 2019.

[4] N. Abedinzadeh, M. Shariat, S. M. Monavari, A. Pendashteh, "Evaluation of color and COD removal by Fenton from biologically (SBR) pre-treated pulp and paper wastewater", Process Safety and Environmental Protection vol. 116, pp. 82-91, 2018.

[5] E. Neyens, J. Baeyens, "A review of classic Fenton's peroxidation as an advanced oxidation technique", Journal of Hazardous Materials, vol. B98 pp. 33–50, 2003.

[6] P. Asaithambi, R. Govindarajan, M. B. Yesuf, E. Alemayehun, "Removal of color, COD and determination of power consumption from landfill leachate wastewater using an electrochemical advanced oxidation processes", Separation and Purification Technology, vol. 233, pp. 115935, 2020.

[7] G. Meng, N. Jiang, Y. Wang, H. Zhang, Y. Tang, Y. Lv, J. Bai, "Treatment of coking wastewater in a heterogeneous electro-Fenton system: Optimization of treatment parameters, characterization, and removal mechanism", Journal of Water Process Engineering, vol. 45, pp. 102482, 2022.

[8] D. E. G. Trigueros, L. Braun, C. L. Hinterholz, "Environmental and economic feasibility of the treatment of dairy industry wastewater by photo-Fenton and electrocoagulation process: Multicriteria optimization by desirability function", Journal of Photochemistry and Photobiology, A: Chemistry vol. 427, pp. 113820, 2022.

[9] E. Can-Güven, "Advanced treatment of dye manufacturing wastewater by electrocoagulation and electro-Fenton processes: Effect on COD fractions, energy consumption, and sludge analysis", Journal of Environmental Management, vol. 300, 113784, 2021.

[10] W. P. Ting, M. C. Lu, Y. H. Huang, "The reactor design and comparison of Fenton, electro-Fenton and photoelectron-Fenton processes for mineralization of benzene sulfonic acid (BSA)", Journal of Hazardous Materials., vol. 156, pp. 421-427, 2008.

[11] A. Babuponnusami, K. Muthukumar, "Advanced oxidation of phenol: A comparison between Fenton, electro-Fenton, sono-electro-Fenton and photo-electro-Fenton processes", Chemical Engineering Journal, vol. 183, pp. 1-9, 2012.

[12] American Public Health Association (APHA), Standard Methods for the Examination of Waste and Wastewater (19th ed.), Washington, 2005.

[13] S. G. Çetinkaya, M. H. Morcali, S. Akarsu, C.A. Ziba, M. Dolaz, "Comparison of classic Fenton with ultrasound Fenton processes on industrial textile wastewater", Sustainable Environment Research, vol. 28, pp. 165-170, 2018.

[14] Oliveira, R., Almeida, M. F., Santos, L., Madeira, L.M., "Experimental design of 2, 4- dichlorophenol oxidation by Fenton's reaction", Industrial Engineering Chemistry Research, Vol. 45, pp. 1266–1276, 2006.

[15] Torrades, F., Garcia-Montano, J., "Using central composite experimental design to optimize the degradation of real dye wastewater by Fenton and photo-Fenton reactions", Dyes Pigments, vol. 100, pp. 184–189, 2014.

[16] X. Su, X. Li, L. Ma, J. Fan, "Formation and transformation of schwertmannite in the classic Fenton process", Journal of Environmental Sciences, vol. 82, pp. 145-154, 2019.

[17] E. Brillas, E. Mur, J. Casado, "Iron (II) catalysis of the mineralization of aniline using a Carbon-PTFE O 2-Fed cathode", Journal of the Electrochemical Society, vol. 143, no. 3, pp. L49-L53, 1996.

[18] J. Casado, "Towards industrial implementation of Electro-Fenton and derived technologies for wastewater treatment: A review", Journal of Environmental Chemical Engineering vol. 7, pp. 102823, 2019.

[19] M. H. Zhang, H. Dong, L. Zhao, De-xi Wang, Di Meng, "A review on Fenton process for organic wastewater treatment based on optimization perspective", Science of the Total Environment, vol. 670, pp. 110–121, 2019.

[20] M. Muruganandham, M. Swaminathan, "Decolourisation of Reactive Orange 4 by Fenton and photo-Fenton oxidation technology", Dyes and Pigments, vol. 63, pp. 315-321, 2004.

[21] F. J. Rivas, F. J. Beltran, J. Frades, P. Buxeda, "Oxidation of p-hydroxybenzoic acid by Fenton's reagent", Water Research vol. 35, pp. 387–396, 2001.

[22] X. H. Li, S. Chen, I. Angelidaki, Y. F. Zhang, "Bio-electro-Fenton processes for wastewater treatment: advances and prospects", Chemical Engineering Journal, vol. 354, pp. 492–506, 2008.

[23] N. Borràs, R. Oliver, C. Arias, E. Brillas, "Degradation of atrazine by electrochemical advanced oxidation processes using a boron-doped diamond anode", Journal of Physical Chemistry A, 114, pp. 6613–6621, 2010.

[24] Hu, C. J., Huang, D. L., Zeng, G. M., Cheng, M., Gong, X. M., Wang, R. Z., Xue, W. J., Hu, Z. X., Liu, Y. N., "The combination of Fenton process and phanerochaete chrysosporium for the removal of bisphenol A in river sediments: mechanism related to extracellular enzyme, organic acid and iron", Chemical Engineering Journal No. 338, pp. 432–439, 2018.

[25] N. Kang, D. S. Lee, J. Yoon, "Kinetic modeling of Fenton oxidation of phenol and monochlorophenols", Chemosphere, vol. 47, pp. 915-924, 2002.

[26] H. Kusic, N. Koprivanac, A. L. Bozic, I. Selanec, "Photo-assisted Fenton type processes for the degradation of phenol: A kinetic study", Journal of Hazardous Materials, no. B136, pp. 632-644, 2006.

[27] E. Brillas, I Sires, M. A. Oturan, “Electro-Fenton Process and Related Electrochemical Technologies Based on Fenton’s Reaction Chemistry”, Chemistry, vol. 109 no. 12, pp. 6570-6631, 2009.

[28] S. Chon, Y. H. Huang, S. N. Lee, G. H. Huang, “Treatment of high strength hexaminecontaining wastewater by electro-Fenton method”, Water Research, no. 33, pp. 751-759, 1999.

[29] Y. Li, H. Cheng, “Chemical kinetic modeling of organic pollutant degradation in Fenton and solar photo-Fenton processes”, Journal of the Taiwan Institute of Chemical Engineers, no. 123, pp. 175-184, 2021.

SAKARYA ÜNİVERSİTESİ
FEN BİLİMLERİ ENSTİTÜSÜ DERGİSİ

Sakarya University Journal of Science
SAUJS

ISSN 1301-4048 e-ISSN 2147-835X Period Bimonthly Founded 1997 Publisher Sakarya University
http://www.saujs.sakarya.edu.tr/

Title: Comparison of Essential Oils and Secretion Structures of Rosa damascena Mill. Grown in Iğdır and Isparta (Turkey)

Authors: Songül KARAKAYA, Hafize YUCA, Enes TEKMAN, Ayşe CİVAŞ, Gözde ÖZTÜRK, Betül DEMİRCİ, Allahverdi KARACA, Zuhal GÜVENALP

Recieved: 2022-11-01 00:00:00

Accepted: 2023-02-20 00:00:00

Article Type: Research Article

Volume: 27
Issue: 3
Month: June
Year: 2023
Pages: 523-529

How to cite
Songül KARAKAYA, Hafize YUCA, Enes TEKMAN, Ayşe CİVAŞ, Gözde ÖZTÜRK, Betül DEMİRCİ, Allahverdi KARACA, Zuhal GÜVENALP; (2023), Comparison of Essential Oils and Secretion Structures of Rosa damascena Mill. Grown in Iğdır and Isparta (Turkey) . Sakarya University Journal of Science, 27(3), 523-529, DOI: 10.16984/saufenbilder.1197825
Access link
https://dergipark.org.tr/en/pub/saufenbilder/issue/78131/1197825

Sakarya University Journal of Science 27(3), 523-529, 2023

Comparison of Essential Oils and Secretion Structures of *Rosa damascena* Mill. Grown in Iğdır and Isparta (Turkey)

Hafize YUCA[1], Enes TEKMAN[2], Ayşe CİVAŞ[3], Songül KARAKAYA[2*], Gözde ÖZTÜRK[4], Betül DEMİRCİ[4], Allahverdi KARACA[5], Zühal GÜVENALP[1]

Abstract

The paper aims to compare the chemical compositions of essential oils and anatomical properties of secretory structures differences between *R. damascena* which is cultivated in Iğdır and Isparta (EOI1, EOI2, and EOIg). GC/ MS and GC-FID were utilized for essential oils analysis. Nonadecane (31.0%), heneicosane (21.1%), citronellol (16.8%), and 1-nonadecene (6.2%) were primal constituents of EOI1. Nonadecane (29.3%), heneicosane (17.6%), citronellol (18.6%), 1- and nonadecene (5.4%) were primal constituents of EOI2. Heneicosane (15.2%), nonadecane (14.1%), γ-muurolene (13.0%), citronellol (7.8%), and tricosane (8.5%) were primal constituents of EOIg. Both Isparta and Iğdır sepal cross-section anatomies glandular and non-glandular trichomes were observed.

Keywords: Rosa damascena, Iğdır, Isparta, essential oil, anatomy

1. INTRODUCTION

Rosa L. species is known as one of the most popular types of ornamental plants with its pleasant smell and beautiful appearance, belonging to the Rosoideae subfamily, which is in the Rosaceae family. The genus *Rosa* has 200 species and more than 18,000 varieties. The rose plant is one of the most cultivated ornamental plants in the world today. The history of the rose, which is considered the queen of flowers, dates back to prehistoric times. Rose is an important ornamental plant with economic, cultural and symbolic value. In addition to being used as a garden plant, roses also have economic importance in terms of their petals, which are a natural source of fragrance, colour and sweetener. The rose

* Corresponding author: songul.karakaya@atauni.edu.tr (S. KARAKAYA)
[1] Atatürk University, Faculty of Pharmacy, Department of Pharmacognosy, Erzurum, Turkey.
[2] Atatürk University, Faculty of Pharmacy, Department of Pharmaceutical Botany, Erzurum, Turkey.
[3] Igdir University, Department of Pharmacy and Pharmaceutical Services, Igdir, Turkey.
[4] Anadolu University, Faculty of Pharmacy, Department of Pharmacognosy, Eskişehir, Turkey.
[5] Avos Organics Tarım Sanayi ve Ticaret Limited Şirketi.
E-mail: hafize.yuca@atauni.edu.tr, enes.tekman@atauni.edu.tr, ayse.civas@igdir.edu.tr, gozde_ozturk@anadolu.edu.tr, bdemirca@anadolu.edu.tr, avosorganics@hotmail.com, guvenalp@atauni.edu.tr
ORCID: https://orcid.org/0000-0002-3268-721X, https://orcid.org/0000-0002-0857-4776, https://orcid.org/0000-0002-1226-7218, https://orcid.org/0000-0002-8838-3856, https://orcid.org/0000-0002-3998-8859, https://orcid.org/0000-0003-2343-746X, https://orcid.org/0000-0002-7708-3583, https://orcid.org/0000-0002-8803-8147

plant originated mostly in Western Asia and partly in Europe. It is widely seen in European and Middle Eastern countries, especially Iran, Afghanistan and Turkey. It is grown in Bulgaria, Russia, Egypt, France, India and Morocco. It has been reported by many botanists that around 200 rose species have been described in the world. The most important and most used of these rose species are Isparta rose (*Rosa damascena* Mill.) and rosehip (*Rosa canina* L.) [1].

The natural distribution area of *R. damascena*, whose homeland is Iran, is the Northern Hemisphere, and it is cultivated in France, Lebanon, India, Russia, China, Morocco, Mexico, Italy and other European countries, especially in Turkey and Bulgaria. *R. damascena* is a plant with very thorny, and pink flowers, which is formed by the hybridization of *R. gallica* L. and *R. phoenicia* Boiss. [2].

R. damascena (Rosaceae) is known as "Yağ gülü, Yağlık gül, Isparta gülü, Reçellik gül, Pembe gül, Katmer gül, Yalınkat gül, Şam gülü, Güla Muhammedi, Peygamber kokusu, Ölü gülü, Kazanlık gül" in Turkey. It is the only type of rose cultivated for industrial purposes. It is accepted that rose oil helps to relieve the pain, sadness and stress caused by mental problems, helps to provide mental balance and facilitates the birth psychologically during childbirth. In the Ottoman period, the essential oil obtained by fermenting (sourcing) different rose flowers by steam distillation (retort system) was called "sega oil" and this oil was used as an elixir in the treatment of many diseases (pharyngitis, tonsillitis, etc. in the treatment of throat and respiratory tract diseases). It is known that the scent of rose is used in the treatment of psychiatric and neurological disorders through aromatherapy. In the research, it has been determined that the child of the mother who has used rose oil since birth is more advanced than her peers in distinguishing odours. Memory-enhancing effects in other living things it has been experienced. It is believed that those who are busy with roses strengthen their memories. Rose oil has been used for solving skin problems since it is known as an accelerator of new tissue formation and wound healing since ancient times. Massage can be done by adding rose oil to fixed oils. It is added to the water in the aroma diffuser as one drop per square meter of room area in the aromatherapy lamp and can be used by inhalation [3].

Approximately 15.000 tons of rose flowers are produced annually worldwide, and Turkey ranks first among the essential countries producing rose flowers. According to the 2014 Rose Flower Report data, it has been determined that Turkey's rose flower planted area is 2.200 ha, its production is 6.750 tons and its yield is 4.250 kg ha^{-1}. The report also states that Turkey exported 3.443 kg of rose oil with a total return of $13.961,163 in 2014 is reported. 50% of the world's rose oil demand is met by Turkey, 40% by Bulgaria and the remaining 10% from other countries such as Iran, India, Morocco and Afghanistan [4].

The paper aims to compare the chemical compositions of essential oils and anatomical properties of secretory structures differences between *R. damascena* which is cultivated in Iğdır and Isparta.

2. MATERIALS AND METHODS

2.1. Plant materials and obtaining essential oils

Isparta samples were collected in May 2022 and they were identified by authors Assoc. Prof. Dr Songul Karakaya (Department of Pharmaceutical Botany) and Asst. Prof. Dr Hafize Yuca (Department of Pharmacognosy). Fresh flowers of *Rosa damascena* were obtained from two different regions of Isparta. The crushed dried flowers (300 g and 300 g) of *R. damascena* from Isparta (EOI1 and EOI2) were placed in hydrodistillation for 3 h through a Clevenger-type apparatus in reference to the method suggested at the European Pharmacopoeia.

In November 2020, 1500 red rose (qızıl gül) seedlings grown in gardens in Iğdır were planted in the field. The roses grown in the field at the foot of Mount Ağrı (850 m, Karakoyunlu district, Zülfikar village, latitude: 39.9849, longitude: 44.1597) were collected in May 2022. The crushed fresh flowers (750 kg) of *Rosa damascena* from Iğdır (EOIg) were placed in a copper boiler and hydrodistillated for 2 h. 60 mL of rose oil and 1125 L rose water were obtained in reference to the method suggested at the European Pharmacopoeia. Voucher specimens have been stored at Atatürk University, Biodiversity Application and Research Center with the numbers of EOI1, EOI2, and EOIg AUEF 1397, 1398, and 1399, respectively

Isparta roses were taken from two different regions to fully understand the difference or similarity of the content of the rose grown in Iğdır with Isparta roses.

Obtained oils were dried over anhydrous sodium sulfate and held in sealed vials at +4°C temperature in the dark up to the analysis.

2.2. GC-FID and GC-MS analyses of essential oils

GC/MS and GC analysis were established with Agilent 5975 GC-MSD and Agilent 6890N GC systems, in turn. An Innowax FSC column (60 m x 0.25 mm, 0.25 μm film thickness) in helium (0.8 mL/min) was taken as the carrier gas. The GC oven temperature for 10 minutes was 60°C and programmed to 220°C at a rate of 4°C/min and was 220°C for 10 minutes at a rate of 240°C at a rate of 1°C/min. The division proportion was set to 40:1. The injector temperature was 250°C. Mass spectra were enlisted at 70 eV and the mass range was m/z 35 to 450. The FID detector temperature was 300°C. To get the same elution order as GC/MS, a contemporaneous automated injection was carried on a replicate of the same column, applying the same operating conditions. Relative percent sums of partitioned compounds were calculated from the FID chromatograms.

2.3. Microscopic Analysis

For anatomical properties of secretory structures, sections were made manually from the flower of *Rosa damascena* from Isparta and Iğdır (EOI1, EOI2, and EOIg). Plants materials were fixed in 70% alcohol. Sartur and tusche reagents were used. Images were registered with a Zeiss 51425 camera engaged to a light microscope (Zeiss 415500-1800-000, Carl Zeiss Microscopy, GmbH Konigsallee 9-21, 37081 Gottingen GERMANY). An average of 8-12 samples were used for the sections. In this study, only where the essential oils are produced in the plant and their chemical similarities and differences were tried to be revealed.

3. RESULTS

The colour of the EOI1, EOI2, and EOIg were yellow, yellow and greenish and the essential oil % yields were 0.001, 0.001, and 0.008 w/v, respectively. A total of 33, 26, and 32 compounds found 99.1%, 97.5%, and 87.6% of the essential oils were identified in the EOI1, EOI2, and EOIg. Nonadecane (31.0%), heneicosane (21.1%), citronellol (16.8%), 1-nonadecene (6.2%), and tricosane (5.2%) were the main constituents of the EOI1. Nonadecane (29.3%), heneicosane (17.6%), citronellol (18.6%), 1-nonadecene (5.4%), and tricosane (4.1%) were the main constituents of the EOI2. Heneicosane (15.2%), nonadecane (14.1%), γ-muurolene (13.0%), citronellol (7.8%), tricosane (8.5%), and (2E,6Z)-farnesol (5.5%) were the main constituents of the EOIg. The chemical compositions of essential oils were given in Table 1.

Both Isparta and Iğdır sepal cross-section anatomies glandular and non-glandular trichomes were observed (Figures 1-2).

Table 1 The chemical compositions of essential oils

RRI	Component	EOI1 %	EOI2 %	EOIg %
1362	*cis*-Rose oxide	-	0.3	-
1377	*trans*-Rose oxide	-	0.1	-
1500	Pentadecane	0.1	0.2	0.5
1544	α-Guaijane	0.3	0.9	-
1600	Hexadecane	tr	tr	0.1
1612	*β*-Caryophyllene	0.6	1.5	2.3
1661	Alloaromadendrene	-	-	0.4
1668	Citronellyl acetate	tr	0.3	1.2
1687	*α*-Humulene	0.4	0.8	1.0
1700	Heptadecane	-	-	1.7
1704	γ-Muurolene	-	-	13.0
1726	Germacrene D	3.4	2.5	-
1730	*δ*- Guaijane	1.3	4.0	-
1772	Citronellol	16.8	18.6	7.8
1808	Nerol	tr	tr	1.3
1857	Geraniol	0.4	0.5	2.0
1800	Octadecane	0.9	1.0	0.7
1852	1-Octadecene	-	-	tr
1900	Nonadecane	31.0	29.3	14.1
1915	1-Nonadecene	6.2	5.4	1.4
1937	Phenylethyl alcohol	-	tr	-
1973	1-Dodecanol	-	-	0.2
2000	Eicosane	5.0	3.0	3.0
2016	9-Eicosene	0.4	2.1	tr
2050	(*E*)-Nerolidol		tr	0.1
2071	Humulene epoxide II	-	0.4	-
2096	Elemol	-	-	tr
2100	Heneicosane	21.1	17.6	15.2
2185	*β*- Eudesmol	-	-	0.2
2200	Docosane	0.9	-	0.5
2209	Citronellyl caprylate	tr	tr	-
2214	Phenylethy tiglate		0.7	-
2250	γ-Eudesmol		-	0.4
2278	(*2E,6E*)-Farnesal	-	-	tr
2300	Tricosane	5.2	4.1	8.5
2330	(*2E,6Z*)-Farnesol	-	-	5.5
2337	9- Tricosene	0.7	0.5	-
2369	(*2E,6E*)-Farnesol	-	-	4.3
2396	Citronellyl nonanoate	0.5	0.4	-
2400	Tetracosane	0.4	0.3	0.4
2500	Pentacosane	1.7	1.2	1.8
2512	Citronellyl benzoate	0.4	0.3	-
2600	Hexacosane	-	0.5	-
2700	Heptacosane	1.4	-	tr
2931	Hexadecanoic acid	-	1.0	tr
	Total	**99.1**	**97.5**	**87.6**

RRI Relative retention indices calculated against n-alkanes
% calculated from FID data, tr for Trace (< 0.1 %)

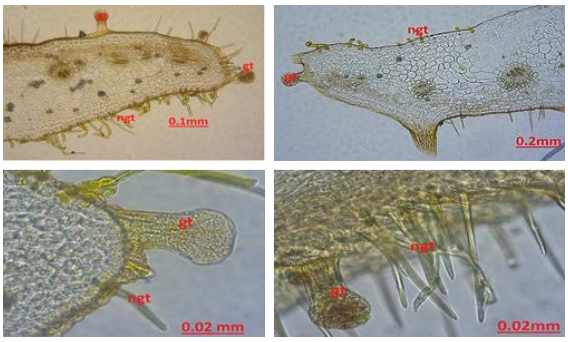

Figure 1 *Rosa damascena* (Isparta) sepal cross-section anatomy; gt: glandular trichome, ngt: non-glandular trichome with Sartur reagent

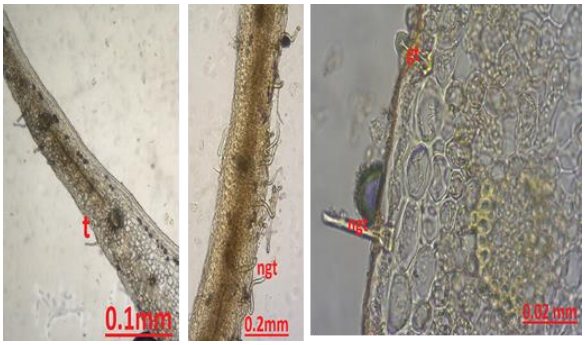

Figure 2 *Rosa damascena* (Iğdır) sepal cross-section anatomy; t: trichome, gt: glandular *trichome, ngt: non-glandular trichome with Sartur reagent*

Secretory structures were found in Isparta and Iğdır petal adaxial surface anatomies (Figures 3-4). The presence of essential oils in papillae was also seen in Isparta and Iğdır petal adaxial surface anatomies with tusche reagent (Figures 3-4).

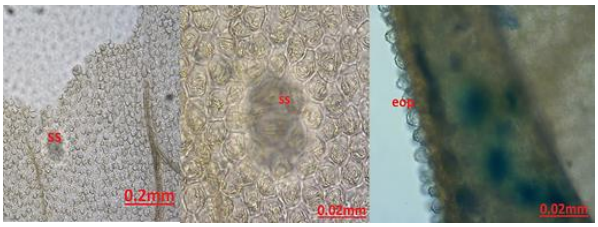

Figure 3 *Rosa damascena* (Isparta) petal adaxial surface anatomy; ss: secretory structure, eop: essential oil in papillae with Sartur and tusche reagents-glandular *trichome with Sartur reagent*

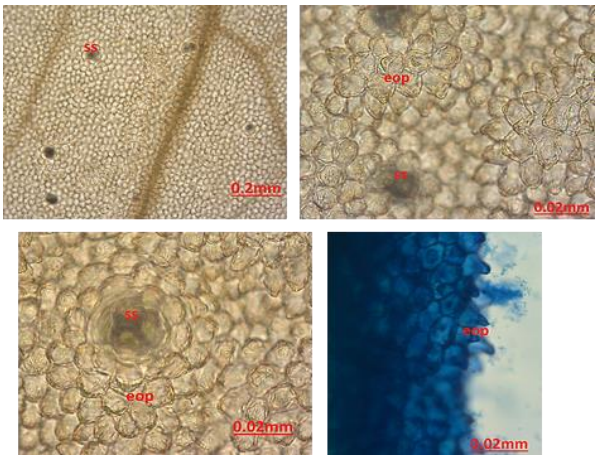

Figure 4 *Rosa damascena* (Iğdır) petal adaxial surface anatomy; ss: secretory structure, eop: essential oil in papillae with Sartur and tusche reagents

4. DISCUSSION

The rose oil's basic character is dependent on geraniol (9 to 24%) and citronellol (31 to 44%). It is changed by nerol (5 to 11%) and farnesol (0.2 to 1.4%). If farnesol content is higher, it causes to the potent floral character. Nerol adds both rosaceous character and freshness. In cases when the geraniol content is low, the freshness of nerol manifests itself as a bit citrusy. However, when geraniol content is high, the mixture of geraniol, farnesol, citronellol, and nerol results in a potent, sweet, fresh, and floral character. The rose oil's other characteristic constituents are geranyl acetate, citronellyl formate, nonanal, eugenol, methyl eugenol, cis-rose oxide, citronellyl acetate, α-terpineol, linalool, and phenylethyl alcohol. The other natural compounds of rose oil are stearoptenes (mainly nonadecane). If they are present, they cause the solidification of rose oil at room temperature and when cooled [5]. In our study, the geraniol content of EOIg (2.0%) was higher than others while the citronellol content of EOI2 is the highest one (18.6%). Farnesol and nerol had only been found in EOIg. Therefore, the floral, rosaceous and fresh scents are more dominant in this sample. The nonadecane contents were higher in Isparta samples (EOI1 and EOI2), so they can solidify more easily than the Iğdır sample (EOIg).

There are many studies on the essential oil the content of *Rosa damascena*. In a study about content of rose oil obtained from roses cultivated in Turkey, citronellol (30.9 to 43.9%), geraniol (9.3 to 14.1%), nonadecane (8.3 to 14.7%), and nerol (5.2 to 7.6%) were found as major compounds [6]. For Bulgarian two rose oil samples, the main compounds were found as citronellol (30.24-31.15%), geraniol (20.62-21.24%), *n*-heneicosane (8.79-9.05%), and *n*-nonadecane (8.51-8.77%) [7]. For Iranian rose oil, according to the GC-MS results, citronellol (14.5-47.5%), nonadecane (10.5-40.5%), geraniol (5.5-18%), and henicosane (7-14%) were the major compounds [8]. Our research when compared to the previous studies, the major compounds were similar, but the nonadecane and heneicosane were found as higher than geraniol and citronellol in all samples.

When previous anatomy studies were evaluated, as, in our study, glandular and non-glandular trichomes were observed in sepals [9, 10]. The glandular trichomes in the Isparta samples were more numerous than in the Iğdır sample (Figures 1, and 2). In other studies, it was observed that papillae from the adaxial surface of the petals had residue of dried secretion as in our study [11, 12, 13]. To our knowledge, it is the first time that the secretory structures were shown clearly in all samples. Additionally, they were figured on the Iğdır sample more than others (Figures 3, and 4).

5. CONCLUSION

The results of original comparable research on essential oils components of Isparta and Iğdır samples. Their secretory structures are not different, they differ only in their size and number. The essential oil is also similar in content, but there is variation in quantities. These essential oils could be used in cosmetics, perfumery, pharmacy and industry owing to their chemical compositions.

The Declaration of Conflict of Interest/ Common Interest

The authors have declared no conflict of interest.

Authors' Contribution

Concept: H.Y, E.T, A.C., S.K., B.D., A.K., Z.G., Design: H.Y, S.K., Data Collection or Processing: H.Y, E.T, A.C., S.K., B.D., A.K., Analysis or Interpretation H.Y, E.T, A.C., S.K., B.D., Literature Search: H.Y, S.K., B.D., Writing: H.Y, S.K., B.D., A.K.

The Declaration of Ethics Committee Approval

This study does not require ethics committee permission or any special permission

Acknowledgement

We would like to thank Pharm. Volkan Zülaloğlu and Özgür Cem Can, co-founders with Pharm. Allahverdi Karaca of AVOS Organics Company, for their contributions. We would like to thank Ata Technocity for supporting us. Enes TEKMAN would like to thank the scholarship along with his postgraduate program supported by the Turkish Scientific and Technical Research Council (TUBITAK).

The Declaration of Research and Publication Ethics

The authors of the paper declare that they comply with the scientific, ethical and quotation rules of SAUJS in all processes of the paper and that they do not make any falsification of the data collected. In addition, they declare that Sakarya University Journal of Science and its editorial board have no responsibility for any ethical violations that may be encountered, and that this study has not been evaluated in any academic publication environment other than Sakarya University Journal of Science.

REFERENCES

[1] G. B. Torusdağ, "Van ilinde yetişen *Rosa* × *damascena* Miller'in bazı fiziksel ve kimyasal özellikleri ile

antosiyanin ekstraksiyon koşullarının belirlenmesi", Master's thesis, Dept. Food Eng., Van Yüzüncü Yıl Univ., Van, Turkey, 2020.

[2] O. T. Ağar, "*Rosa damascena* Mill. farmakope standartlarının belirlenmesi, matriks metalloproteinaz (MMP) inhibitör etkinliklerinin araştırılması", Ph.D. dissertation, Dept. Pharmacogn., Hacettepe Univ., Ankara, Turkey, 2018.

[3] H. Özçelik, B. Yıldırım, B. Muca, "*Rosa damascena* Mill.'nın Türkiye'de varyasyonu", Süleyman Demirel Üniversitesi Fen Bilimleri Enstitüsü Dergisi, vol. 17, no 2, pp. 52-60, 2014.

[4] R. Dilmen, N. G. Baydar, "Yağ gülü (*Rosa damascena* Mill.)'nde doku kültürü uygulamaları", Ziraat Fakültesi Dergisi, vol. 11, no 2, pp. 134-141, 2016.

[5] European Medicines Agency, Committee on Herbal Medicinal Products (HMPC). (2014, July 1), Assessment report on *Rosa gallica* L., *Rosa centifolia* L., *Rosa damascena* Mill., flos [Online]. Available: https://www.ema.europa.eu/en/documents/herbal-report/final-assessment-report-rosa-gallica-l-rosa-centifolia-l-rosa-damascena-mill-flos_en.pdf

[6] K. H. C. Baser, M. Kurkcuoglu, T. Ozek, "Turkish rose oil research recent results", Perfumer and Flavorist, vol. 28, no 2, pp. 34-43, 2003.

[7] T. Atanasova, M. Kakalova, L. Stefanof, M. Petkova, A. Stoyanova, S. Damyanova, S., M. Desyk, "Chemical composition of essential oil from *Rosa damascena* mill., growing in new region of Bulgaria", Ukrainian Food Journal, vol. 5, no 3, pp. 492-498, 2016.

[8] H. Loghmani-Khouzani, "Essential oil composition of *Rosa damascena* Mill cultivated in central Iran", Scientia Iranica, vol. 14, no 4, pp. 316-319, 2007.

[9] J. C. Caissard, V. Bergougnoux, M. Martin, M. Mauriat, S. Baudino, "Chemical and histochemical analysis of 'Quatre Saisons Blanc Mousseux', a moss rose of the *Rosa* x *damascena* group", Annals of Botany, vol. 97, no 2, pp. 231-238, 2006.

[10] G. Kendir, A. Köroğlu, "Morphological and anatomical evaluation of herbal drugs sold under the name of Gül (*Rosa damascena* Mill.) in Turkey", Journal of Research in Pharmacy, vol. 25, no 1, 63-71, 2021.

[11] Z. H. Abudayeh, U. Karpiuk, N. Armoon, Q. Abualassal, E. Mallah, L. K. Hassouneh, Y. Aldalahmeh, "Phytochemical, physiochemical, macroscopic, and microscopic analysis of *Rosa damascena* flower petals and buds", Journal of Food Quality, vol. 2022, pp. 1-10, 2022.

[12] S. N. Fathima, S. V. Murthy, "Pharmacognostic study of petals *Rosa damascene*", Asian Journal of Pharmacy and Pharmacology, vol. 5, pp. 779-785, 2019.

[13] B. Zuraw, A. Sulborska, E. Stawiarz, E. Weryszko-Chmielewska, "Flowering biology and pollen production of four species of the genus *Rosa* L.", Acta Agrobotanica, vol. 68, no 3, pp. 267-278, 2015.

SAKARYA ÜNİVERSİTESİ
FEN BİLİMLERİ ENSTİTÜSÜ DERGİSİ

Sakarya University Journal of Science
SAUJS

ISSN 1301-4048 e-ISSN 2147-835X Period Bimonthly Founded 1997 Publisher Sakarya University
http://www.saujs.sakarya.edu.tr/

Title: Facile Synthesis And Characterization Of gCN, gCN-Zn And gCN-Fe Binary Nanocomposite And Its Application As Photocatalyst For Methylene Blue Degradation

Authors: Mustafa KAVGACI, Hasan ESKALEN

Recieved: 2022-10-28 00:00:00

Accepted: 2023-02-23 00:00:00

Article Type: Research Article

Volume: 27
Issue: 3
Month: June
Year: 2023
Pages: 530-541

How to cite
Mustafa KAVGACI, Hasan ESKALEN; (2023), Facile Synthesis And Characterization Of gCN, gCN-Zn And gCN-Fe Binary Nanocomposite And Its Application As Photocatalyst For Methylene Blue Degradation. Sakarya University Journal of Science, 27(3), 530-541, DOI: 10.16984/saufenbilder.1195934
Access link
https://dergipark.org.tr/en/pub/saufenbilder/issue/78131/1195934

Sakarya University Journal of Science 27(3), 530-541, 2023

Facile Synthesis and Characterization of gCN, gCN-Zn and gCN-Fe Binary Nanocomposite and Its Application as Photocatalyst for Methylene Blue Degradation

Mustafa KAVGACI [*1,3], Hasan ESKALEN [2,3]

Abstract

The combustion method to obtain for pure graphitic carbon nitride (gCN) and two binary nanocomposites, gCN-Zn - gCN-Fe have been used in the present study. The structural, morphological, thermal and optical characterizations of the syhtesized samples were characterized with X-ray diffraction, scanning electron microscopy, thermogravimetric analysis (TGA) and UV-Vis spectroscopy. The intensity of characteristic gCN peak at (002) crystalline plane decrease with formation of binary nanocomposites was observed. The EDX spectra supports presents of Zn and Fe element in binary nanocomposites. The bandgap of pristine gCN is calculated as 2.75 eV and it decreases to 2.58 eV and 2.50 eV for Zn and Fe addition. The degradation capacity of pristine gCN and synthesized binary nanocomposites showed an enhanced photodegradation performance for binary composite relative to pristine gCN was observed. The maximum degradation performance was observed at gCN-Zn binary composite. The obtained composites with this simple synthesis method and cost effective raw materials used for the photodegradation of methylene blue dye detail.

Keywords: Degradation, Zn, Fe, methylene blue (MB), graphitic carbon nitride (gCN)

1. INTRODUCTION

Environmental pollution is one of the significant problems for humans and other living organisms. Unfortunately, pollution increases in parallel to industrialization, which might result in pollution of water sources and unhealthy drinking water. To overcome this problem, some scientists focused on water treatment, especially pollution originating from dyestuff. Since the wastewater from dye can contaminate not only freshwater sources but also sands, that may magnify the risk [1–5]. Some of the organics dyes are toxic, carcinogenic, and have mutagenic potential [6]. Considering the current situation of dyes, especially their types (more than 100,000 varied structured) and different application areas (textile, medicine, pharmaceutic, cosmetics, food,

* Corresponding author:mkavgaci@gmail.com (M. KAVGACI)
[1] Elbistan Vocational School of Health Services, Department of Opticianry, Kahramanmaraş Istiklal University, Kahramanmaraş, Turkey.
[2] Vocational School of Health Services, Department of Opticianry, Kahramanmaraş Sutcu Imam University, Kahramanmaras, Turkey.
[3] Department of Material Science and Engineering, Graduate School of Natural and Applied Sciences, Kahramanmaraş Sutcu Imam University, Kahramanmaras, Turkey.
E-Mail: heskalen@gmail.com
ORCID: https://orcid.org/0000-0001-8747-0635, https://orcid.org/0000-0002-4523-6573

printing), the importance of treatment of wastewater originating from dyes may become more evident [7–9]. Different methods have been utilized to degrade wastewater, including physiochemical and biological approaches; photodegradation has massive potential for dealing with wastewater since its a clean and cost-effective method [10–12].

Graphitic carbon nitride (gCN) is defined as nitrogen substituted graphane with anisotropic 2D geometry, and aromatic conjugate structure [13]. gCN has been considered as a promotion material due to its original preparation methods, high stability, band gap and low cost [14–16]. Moreover, the earth abundant nature, suitable electronic band position, nontoxic characteristic, outstanding physicochemical stability and admirable optical properties has considered as novel specifications of the gCN [17, 18]. Triurea, melamine, cyanamide, urea, ammonium thiocyanate and dicyandiamide are some examples of gCN precursors that are inexpensive and high nitrogen content generally used in synthesis of gCN [17]. Fast charge carrier recombination, small particle size and poor absorption coefficient of the gCN negatively affect the photoactivity of pure gCN [19–21]. Different methods have been utilized to overcome this shortcoming like fabricating nano/mesoporous structures, coupling with other semiconductors, noble metal deposition and impurity doping [22–24]. Among them doping different elements like metal, metal oxide and nonmetals to the bulk structure results in a decrease in band gap and lead to enhancement of absorption of visible light [25]. Flower like copper/zinc bedecked gCN composite (gCN-CuO/ZnO) was fabricated and methylene blue dye (MB) degradation was investigated. The enhancement of the photocatalytic activity of gCN-CuO/ZnO relative to pure gCN has been observed [26]. H_2 release of P doped gCN - TiO_2 catalyst was used for hydrogen (H_2) release from the sodium borohydride ($NaBH_4$) methanolysis [27]. The photocatalytic degradation of Rhodamine B dye of gCN/nano zero valent iron doped bismuth ferrite nanoparticle composite demonstrated the degradation performance better than previously reported $BiFeO_3$ composite [28]. The photocatalytic performance of silver iodide- gCN nanocomposite was exhibited better behavior than pristine silver iodide and gCN over rhodamine B and methyl orange dye was reported [29]. Enhanced photocatalytic behavior observed with the addition of reduced graphene oxide and gCN to zinc oxide over methylene blue dye was investigated [30].

The present work has employed the combustion method to obtain two binary nanocomposites, gCN-Zn and gCN-Fe. The structural, morphological, thermal and optical characterizations were performed in detailly. The degradation capacity of pristine gCN and synthesized binary nanocomposites showed an enhanced photodegradation performance for binary composite relative to pristine gCN was observed. The obtained composites with this simple synthesis method and cost effective raw materials used for the photodegradation of methylene blue dye detail.

2. MATERIALS AND METHOD

2. 1. Materials

Ultra pure water was used in the studies. Ultra pure water was obtained from Kahramanmaras Sutcu Imam University University-Industry-Public Cooperation Development Application and Research Center (USKIM). All chemicals were used in tests and syntheses without purification. Thiourea (98%) was purchased from Merck, zinc nitrate (98%) was from Acros Organics, and iron nitrate (99%) was from Sigma Aldrich.

2. 2. Synthesis of gCN, gCN-Fe and gCN-Zn

gCN was produced using a the combustion method. Thiourea (10 g) in a ceramic crucible was heated to 550 °C at a heating rate of 10 °C/min in an muffle furnace. It was then calcined at 550 °C for 5 hours. gCN-Fe and gCN-Zn were synthesized under the same conditions. Briefly, 10 g of thiorue was dissolved in 50 mL of ultra water. Iron nitrate and zinc nitrate were then added to this solution in a weight ratio of 0.25:10. It was mixed on a magnetic stirrer for 1 hour. It was then dried at 90 °C for 48 hours. The obtained powder sample was heated to 550 °C at a heating rate of 5 °C/min and calcined at the same temperature for 5 hours. The synthesized samples were ground in a mortar for experiments. The graphitic carbon nitride gCN synthesized in a weight ratio of 0.25:10 was named as iron-doped graphitic carbon nitride gCN-Fe and zinc-doped graphitic carbon nitride gCN-Zn. Figure 1 shows a graphical representation of the gCN samples synthesis.

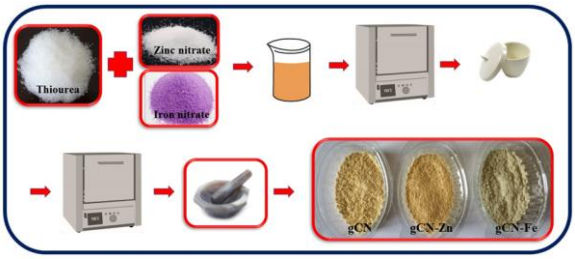

Figure 1 Scheme showing synthesis of gCN, gCN-Fe and gCN-Zn samples

2.3.Characterization

The X-ray diffraction (XRD) pattern of the gCN samples was obtained using a Philips brand X'Pert PRO model XRD instrument with Cu Ka radiation (λ=0.154056 nm, 40 kV and 30 mA). Scanning Electron Microscope (SEM) images and EDX measurements were taken with the FEI brand Quanta 650 Field Emission SEM model electron microscope available at Çukurova University Central Research Laboratory (CUMERLAB). Thermogravimetric analysis (TGA) was performed using a thermal analyzer (Perkin-Elmer Diamond) in a nitrogen atmosphere with a heating rate of 20 °C/min in the temperature range of 20 to 750 °C. FT-IR spectrum measurements were taken with the Perkin Elmer Spectrum 400 device in the range of 4000–400 cm^{-1}. UV–Vis absorption measurements were obtained with a Shimadzu-1800 UV spectrometer. XRD, TGA, FTIR and UV measurements were obtained in the USKIM laboratory.

2.4. Photocatalytic test

The photocatalytic performance of the produced gCN, gCN-Fe and gCN-Zn structures was tested with methylene blue (MB) dye. 20 mg of the photocatalyst gCN, 5 ppm was dropped into 50 mL MB solution (with water). First of all, the solutions to which the catalyst was added were kept in the dark for 30 minutes, taking into account the absorption-desorption balance. It was then tested by irradiation under a Xeon lamp light source (300 W Luzchem). Photocatalytic performances of the samples were investigated with a Shimadzu UV1800 spectrometer in 10-minute time [.

3. RESULTS AND DISCUSSION

Graphically showing the XRD patterns of gCN, gCN-Fe and gCN-Zn are presented (Figure 2). Two characteristic peaks of pure gCN appear prominently at 12.8° and 27.3° both (100) and (002) peaks can be attributed to interplanetary structural stacking of conjugated aromatic systems indexed for graphite materials. These peaks are consistent with the XRD data of the reported studies available in the literature for the gCN structure [31, 32]. It is clearly seen in the XRD graph that the intensity of the (002) peak decreases with the doping of Zn and Fe. This suggests that adding Zn and Fe can limit the crystal growth of gCN. The decrease in peak intensity can be attributed to an interaction between Zn/Fe and gCN. This effect deforms the nitride pore structure and changes the distance between the holes [33]. In addition,

the decrease in crystallinity in the (002) crystal planes can be attributed to the effects of Fe and Zn additions on the thermal condensation of urea/thiourea [34]. When the XRD graph was examined, no diffraction peak was observed for Zn and Fe structures.

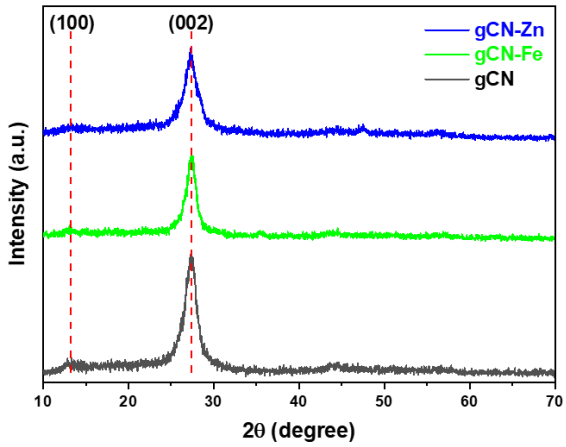

Figure 2 XRD pattern of gCN, gCN-Fe and gCN-Zn

SEM images illuminating the SEM surface morphologies of gCN, gCN-Fe and gCN-Zn are given in Figure 3. Characteristic plate-like structures are seen and the construction of pronounced 2D layered bulk sheets that remain grouped together is celarly seen from this figure. Fe and Zn additives did not affect gCN morphology [35]. This demonstrates that introducing Fe to gCN does not modify its sheet structure. According to result of similar research related to 5% Fe doped gCN that obtained composite not contain any iron nanoparticles, proving that Fe was ionically added to the gCN framework [36]. The addition of Fe to the carbon nitride structure does not alter the stacking of chain layers, implying that Fe-gCN preserves the original crystal structure of gCN [37]. The morphology of ZnO incorporated gCN was observed by SEM and the images reveal its 2-D layered nanosheet structures without much variation in its morphology upon incorporating zinc metal into gCN.

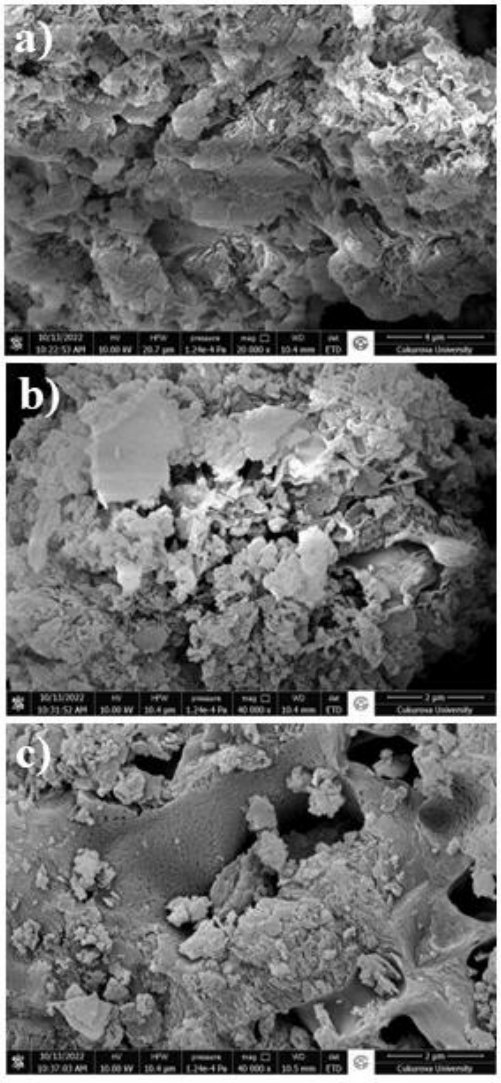

Figure 3 SEM images of gCN (a) gCn-Fe (b) and gCN-Zn (c)

EDX analysis was performed to determine the chemical composition of gCN, gCN-Fe and gCN-Zn nanocatalysts (Figure 4). The EDX spectra of the samples confirm the presence of C, N, O, Fe and Zn elements.

Optical band gap energies of the synthesized samples were determined by using optical absorption spectra. Optical band gaps were obtained with the Tauc plot. $(\alpha h\nu)^2$ for samples as a function of photon energy is plotted graphically in Figure 5. The band gap energy for gCN was found to be 2.75 eV. In the literature, some researchers found the same result for gCN [38, 39]. The addition of Zn and Fe decreased the band gap energy. Band gap energies for gCN-Zn and gCN-Fe

were found to be 2.58 eV and 2.50 eV, respectively. The results found are in agreement with previous studies. In the literature, some studies found that the forbidden energy gap decreases with the addition of Zn and Fe to gCN [33, 40, 41].

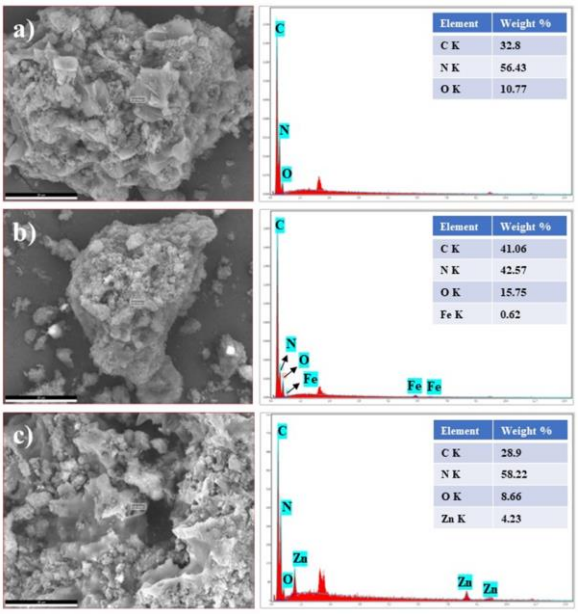

Figure 4 EDX spectra of gCN (a) gCn-Fe (b) and gCN-Zn (c)

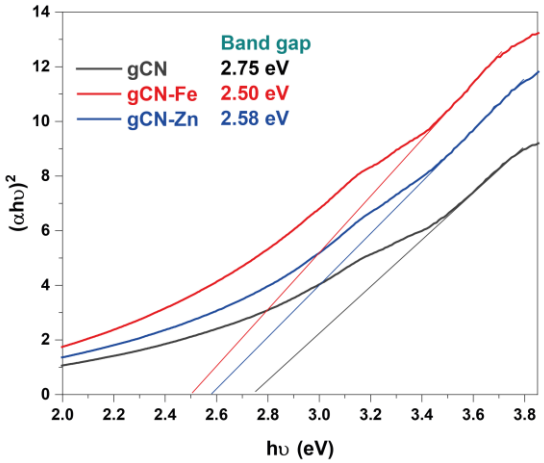

Figure 5 Bandgap graph gCN, gCN-Fe and gCN-Zn

The TGA pattern of gCN, gCN-Fe and gCN-Zn are presented in Figure 6. It is observed that the remarkable thermal decomposition of the samples starts around 400 °C. It is clearly seen that the samples show a tendency to decompose at temperatures higher than 600 °C. This result indicates that thermally gCN structures are one of the highly stable organic materials [42]. The degree of condensation seriously affects thermal stability. Complete degradation of the synthesized gCN sample takes place at 620 °C and no material remains. However, complete degradation does not occur in Zn and Fe doped gCN samples.

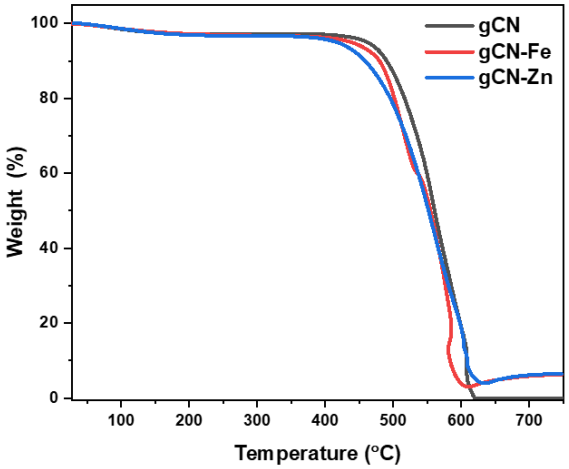

Figure 6 TG thermograms for the gCN, gCN-Fe and gCN-Zn

FTIR spectroscopy is used to detect tensile and bending vibrational bands of synthesized gCN structures and to examine the functional groups and types of chemical bonds of gCN structures. Figure 7 shows the FT-IR spectra of the synthesized gCN constructs. Measurements in the range of 450–4000 cm^{-1} were taken for the FTIR analysis. The broad absorption peak centered at 3150 cm^{-1} is attributed to the tensile vibration of the N–H group. The peaks seen in the 1000-1750 cm^{-1} range indicate the characteristic stretching modes of C-N heterocycles. The sharp peak observed at 805 cm^{-1} can be assigned to the respiratory mode typical of triazine units [43, 44]. As a result of the addition of Zn and Fe, the intensity of the peaks observed between 3150 cm^{-1} and 1000-1750 cm^{-1} decreased. This indicates that the crystallization of Fe and Zn can affect the thermal polymerization of Thiourea. It is consistent with the result of the XRD analysis, which shows that the addition of Fe and Zn can lead to the deterioration of the graphite structure of gCN [33].

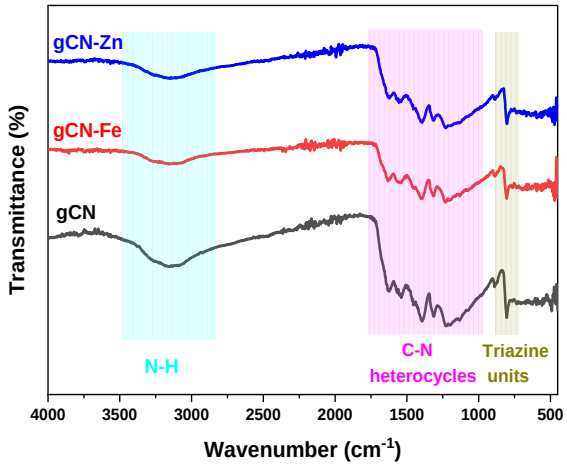

Figure 7 FTIR pattern of obtained samples

Optical absorptions of synthesized gCN samples were measured between 450-750 nm wavelengths using UV-vis spectroscopy. All samples were kept in the dark for 30 minutes and then measurements were taken with a UV-Vis spectrophotometer every 10 minutes for 60 minutes. The photocatalytic degradation of the catalyst-free and gCN-catalyzed dyestuff solutions with respect to time was investigated under normal conditions under 300 W Xenon light. In Figure 8, absorption graphs of gCN, gCN-Fe and gCN-Zn samples are given. The maximum peak in the UV-Vis absorption spectra of the dyestuffs was determined as 664 nm for methylene blue. 50 ml of 5 ppm methylene blue solution was taken and kept under xenon and room light for 60 minutes without a catalyst. The degradation rates under room conditions (called day in Figure 9) and under a xenon lamp (called sim in Figure 9) were determined as 2.7% and 5.4%, respectively (Figure 9).

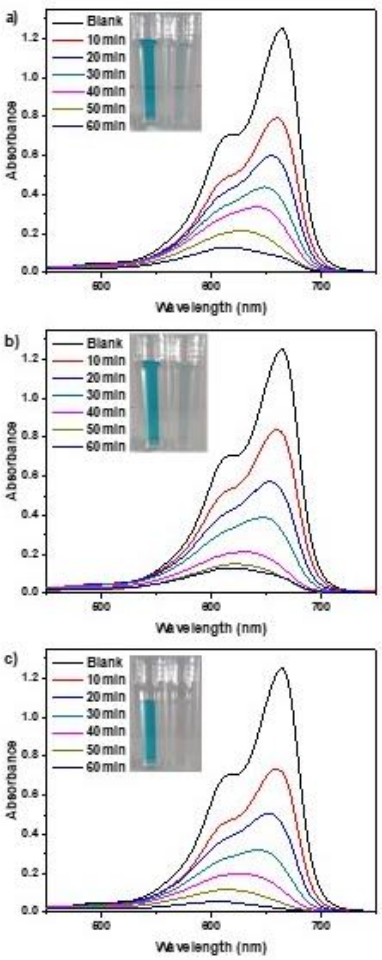

Figure 8 UV-visible absorption spectra for MB in a) gCN, b) gCN-Fe and c) gCN-Zn

In Figure 9, the graph of the decay rates with respect to time is given. In Figure 9, the degradation rates of gCN samples on MB after 60 minutes were determined as 92.7% for gCN, 93.3% for gCN-Fe and 98.4% for gCN-Zn.

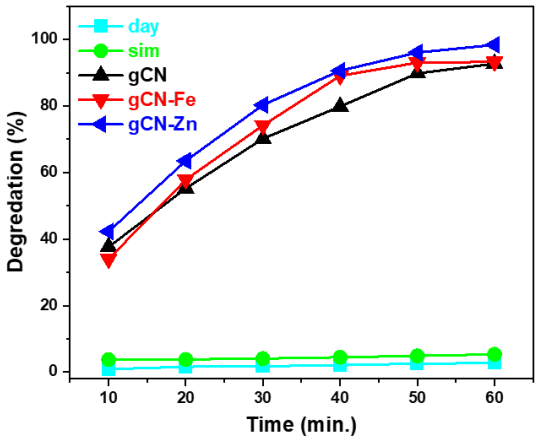

Figure 9 The degradation graph of MB in all samples

It was observed that the synthesized Zn-doped gCN sample was more effective on MB. Figure 10 presents the graph of ln (C_0/C_t) versus time. k (min^{-1}) rate constants (pseudo-first order) were calculated using the slope of the graphs [45]. As can be seen from the graph, the gCN-Zn sample with the highest degradation rate has the largest k value (k=0,06839 min^{-1}).

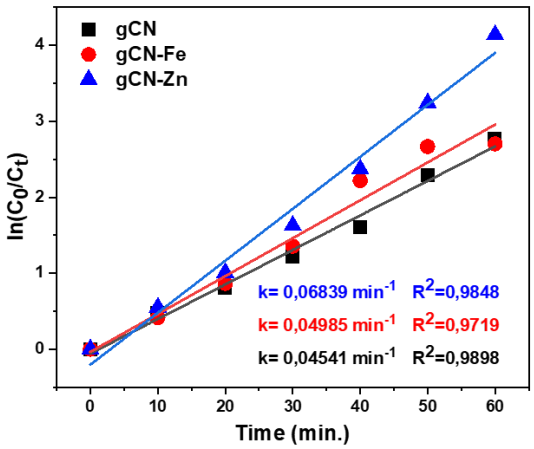

Figure 10 Graph of ln(C_0/C_t) to time gCN, gCN-Fe and gCn-Zn

Photocatalytic evaluation of prepared gCN, gCN-Fe and gCN-Zn samples was investigated through the degradation of MB. gCN-Fe and gCN-Zn were found to exhibit better photocatalytic activity compared to pure gCN. The primary factors of photocatalytic activity are light-absorption capacity, surface composition, and photogenerated charge-separation efficiency [46]. The improvement in photocatalytic activity of gCN-Fe and gCN-Zn composites can be attributed to (i) gCN-Fe and gNC-Zn have a well-developed synergistic interaction in the obtained structure, (ii) a reduction in the bandgap energy of a binary composite can increase the transfer of photo-induced electrons while decreasing electron-hole pair recombination [47, 48]. Zinc oxide absorbe more light quanta than iron oxide and this may the reason of the syhtesized gNC-Zn shows better performance than the gCN-Fe sample [49]. This can increase photocatalytic activity. In addition, the development of photocatalytic activity can be attributed to the promotion of hydroxyl radical formation [40, 41, 50–52].

4. CONCLUSION

In summary, the prisitne gCN, gCN-Zn and gCN-Fe structures were successfully synthesized by the combustion method. The structural properties of the obtained samples were detailly characterized with X-Ray diffraction, SEM-EDX, FTIR and UV-Vis spectroscopy. The bandgap value of pure gCN was found as 2.75 eV and the band gap values of gCN-Zn and gCN-Fe syhtesized binary composites decrease to 2.58 eV and 2.50 eV respectively. The results of the elemental analysis show the apparent differences between the pure forms of gCN, gCN-Zn, and gCN-Fe indicating that syhtesized binary composites have different composition. The obtained FTIR results are comparable with the XRD study, which reveals that the addition of Fe and Zn can cause the graphite structure of gCN to deteriorate. The photocatalytic performances of the synthesized materials were investigated. The degradation effect of synthesized nanocomposites on MB was enhanced with metal ion doping. The obtained results also demonstrated that adding a zinc and iron elements increased the photocatalytic activity remarkably. Among the samples examined, gCN-Zn exhibited the highest photocatalytic performance. The degradation effect of gCN-Zn sample on MB was found to be 98.4% after 60 minutes. The results showed strong photocatalytic effects of Fe and Zn doped gCN structures. Therefore, the prepared gCN-Zn nanocomposite has significant potential and a promising candidate for the destruction of environmental pollutants.

Funding
This work was financially supported by Kahramanmaraş Sütçü İmam University, (KSU) Scientific Research Projects Coordination Department, under Project No. 2021/1-7 YLS and 2020/3-7 YLS.

Authors' Contribution
The authors contributed equally to the study.

The Declaration of Conflict of Interest/ Common Interest
No conflict of interest or common interest has been declared by the authors.

The Declaration of Ethics Committee Approval
This study does not require ethics committee permission or any special permission.

The Declaration of Research and Publication Ethics
The authors of the paper declare that they comply with the scientific, ethical and quotation rules of SAUJS in all processes of the paper and that they do not make any

REFERENCES

[1] S. Kerli, H. Eskalen, "Synthesis of titanium oxide thin films by spray pyrolysis method and its photocatalytic activity for degradation of dyes and ciprofloxacin," Physics and Chemistry of Solid State, vol. 21, no. 3, pp. 426–432, 2020.

[2] H. Eskalen, S. Uruş, Ş. Özgan, "Microwave-Assisted Synthesis of Mushrooms Like MWCNT/SiO2@ZnO Nanocomposite: Influence on Nematic Liquid Crystal E7 and Highly Effective Photocatalytic Activity in Degradation of Methyl Blue," Journal of Inorganic and Organometallic Polymers and Materials, vol. 31, no. 2, pp. 763–775, 2021.

[3] H. Eskalen, H. Yaykaşlı, M. Kavgacı, A. Kayış, "Investigating the PVA/TiO2/CDs polymer nanocomposites: effect of carbon dots for photocatalytic degradation of Rhodamine B," Journal of Materials Science: Materials in Electronics, vol. 33, no. 7, pp. 4643–4658, 2022.

[4] S. Uruş, M. Çaylar, H. Eskalen, Ş. Özgan, "Synthesis of GO@Fe3O4@TiO2 type organic–inorganic nanohybrid material: Investigation of the effect of nanohybrid doped liquid crystal E7 and the photocatalytic degradation of ciprofloxacin," Journal of Materials Science: Materials in Electronics, vol. 33, no. 7, pp. 4314–4329, 2022.

[5] H. Eskalen, S. Kerli, "Synthesis of Gd Doped Tio2 Thin Film for Photocatalytic Degradation of Malachite Green," Sakarya University Journal of Science, vol. 24, no. 6, pp. 1210–1215, 2020.

[6] M. Ikram, F. Jamal, A. Haider, S. Dilpazir, T. Shujah, M. Naz, M. Imran, A. Ul-Hamid, I. Shahzadi, H. Ullah, W. Nabgan, S. Ali, "Efficient Photocatalytic Dye Degradation and Bacterial Inactivation by Graphitic Carbon Nitride and Starch-Doped Magnesium Hydroxide Nanostructures," ACS Omega, p. 2022.

[7] S. Kerli, Ü. Alver, H. Eskalen, S. Uruş, A.K. Soğuksu, "Structural and Morphological Properties of Boron Doped V2O5 Thin Films: Highly Efficient Photocatalytic Degradation of Methyl Blue," Russian Journal of Applied Chemistry 2019 92:2, vol. 92, no. 2, pp. 304–309, 2019.

[8] C. Kursun, M. Gogebakan, H. Eskalen, S. Uruş, J.H. Perepezko, "Microstructural Evaluation and Highly Efficient Photocatalytic Degradation Characteristic of Nanostructured Mg65Ni20Y15−xLax (X = 1, 2, 3) Alloys," Journal of Inorganic and Organometallic Polymers and Materials, vol. 30, no. 2, pp. 494–503, 2020.

[9] H. Eskalen, S. Uruş, H. Yaykaşlı, M. Gögebakan, "Microstructural Characterization of Ball Milled Co60Fe18Ti18Nb4 Alloys and Their Photocatalytic Performance," Alloy Materials and Their Allied Applications, pp. 91–103, 2020.

[10] N. Venkatesh, G. Murugadoss, A.A.A. Mohamed, M.R. Kumar, S.G. Peera, P. Sakthivel, "A Novel Nanocomposite Based on Triazine Based Covalent Organic Polymer Blended with Porous g-C3N4 for Photo Catalytic Dye Degradation of Rose Bengal and Fast Green," Molecules 2022, Vol. 27, Page 7168, vol. 27, no. 21, p. 7168, 2022.

[11] H. Özlü Torun, R. Kırkgeçit, F. Kılıç Dokan, E. Öztürk, "Preparation of La-Dy-CeO2 ternary compound: Examination of photocatalytic and photoluminescence properties," Journal of Photochemistry and Photobiology A: Chemistry, vol. 418, p. 113338, 2021.

[12] M. Atashkadi, A. Mohadesi, M.A. Karimi, S.Z. Mohammadi, V. Haji Aghaei, "Synthesis and characterization of Black Au nanoparticles deposited over g-C_3N_4 nanosheets: enhanced photocatalytic degradation of methylene blue," Environmental Technology, pp. 1–17, 2022.

[13] V. Ugraskan, F. Karaman, "Enhanced thermoelectric properties of highly conductive poly (3,4-ethylenedioxy thiophene)/exfoliated graphitic carbon nitride composites," Synthetic Metals, vol. 287, p. 117070, 2022.

[14] S. Yılmaz, E.G. Acar, G. Yanalak, E. Aslan, M. Kılıç, İ. Hatay Patır, Ö. Metin, "Enhanced hydrogen evolution by using ternary nanocomposites of mesoporous carbon nitride/black phosphorous/transition metal nanoparticles (m-gCN/BP-M; M = Co, Ni, and Cu) as photocatalysts under visible light: A comparative experimental and theoretical study," Applied Surface Science, vol. 593, p. 153398, 2022.

[15] A. Sudhaik, P. Raizada, S. Thakur, A.K. Saini, P. Singh, A. Hosseini-Bandegharaei, "Metal-free photo-activation of peroxymonosulfate using graphene supported graphitic carbon nitride for enhancing photocatalytic activity," Materials Letters, vol. 277, p. 128277, 2020.

[16] G. K. Dutta, N. Karak, "Bio-based waterborne polyester supported oxygeneous graphitic carbon nitride nanosheets as a sustainable photocatalyst for aquatic environment remediation," Journal of Cleaner Production, vol. 285, p. 124906, 2021.

[17] M. S. Khan, F. Zhang, M. Osada, S. S. Mao, S. Shen, "Graphitic Carbon Nitride-Based Low-Dimensional Heterostructures for Photocatalytic Applications," Solar RRL, vol. 4, no. 8, p. 1900435, 2020.

[18] W. Xu, S. Lai, S. C. Pillai, W. Chu, Y. Hu, X. Jiang, M. Fu, X. Wu, F. Li, H. Wang, "Visible light photocatalytic degradation of tetracycline with porous Ag/graphite carbon nitride plasmonic composite: Degradation pathways and mechanism," Journal of Colloid and Interface Science, vol. 574, pp. 110–121, 2020.

[19] V. Balakumar, R. Manivannan, C. Chuaicham, S. Karthikeyan, K. Sasaki, "A simple tactic synthesis of hollow porous graphitic carbon nitride with significantly enhanced photocatalytic performance," Chemical Communications, vol. 57, no. 55, pp. 6772–6775, 2021.

[20] J. Tan, Z. Li, J. Li, Y. Meng, X. Yao, Y. Wang, Y. Lu, T. Zhang, "Visible-light-assisted peroxymonosulfate activation by metal-free bifunctional oxygen-doped graphitic carbon nitride for enhanced degradation of imidacloprid: Role of non-photochemical and photocatalytic activation pathway," Journal of Hazardous Materials, vol. 423, p. 127048, 2022.

[21] D. Gogoi, A. K. Shah, M. Qureshi, A. K. Golder, N. R. Peela, "Silver grafted graphitic-carbon nitride ternary hetero-junction Ag /gC3N4(Urea) -gC3N4 (Thiourea) with efficient charge transfer for enhanced visible-light photocatalytic green H2 production," Applied Surface Science, vol. 558, p. 149900, 2021.

[22] R. Kavitha, P. M. Nithya, S. Girish Kumar, "Noble metal deposited graphitic carbon nitride based heterojunction photocatalysts," Applied Surface Science, vol. 508, p. 145142, 2020.

[23] N. Rono, J. K. Kibet, B. S. Martincigh, V. O. Nyamori, "A comparative study between thermal etching and liquid exfoliation of bulk graphitic carbon nitride to nanosheets for the photocatalytic degradation of a model environmental pollutant, Rhodamine B," Journal of Materials Science: Materials in Electronics, vol. 32, no. 1, pp. 687–706, 2021.

[24] H. Lin, X. Tang, J. Wang, Q. Zeng, H. Chen, W. Ren, J. Sun, H. Zhang, "Enhanced visible-light photocatalysis of clofibric acid using graphitic carbon nitride modified by cerium oxide nanoparticles," Journal of Hazardous Materials, vol. 405, p. 124204, 2021.

[25] A. Hayat, A. G. Al-Sehemi, K. S. El-Nasser, T. A. Taha, A. A. Al-Ghamdi, Jawad Ali Shah Syed, M. A. Amin, T. Ali, T. Bashir, A. Palamanit, J. Khan, W. I. Nawawi, "Graphitic carbon nitride (g–C3N4)–based semiconductor as a beneficial candidate in photocatalysis diversity," International Journal of Hydrogen Energy, vol. 47, no. 8, pp. 5142–5191, 2022.

[26] S. Sivasakthi, K. Gurunathan, "Graphitic carbon nitride bedecked with CuO/ZnO hetero-interface microflower towards high photocatalytic performance," Renewable Energy, vol. 159, pp. 786–800, 2020.

[27] C. Saka, "Phosphorus decorated g-C3N4-TiO2 particles as efficient metal-free catalysts for hydrogen release by NaBH4 methanolysis," Fuel, vol. 322, p. 124196, 2022.

[28] M. U. Rahman, U. Y. Qazi, T. Hussain, N. Nadeem, M. Zahid, H. N. Bhatti, I. Shahid, "Solar driven photocatalytic degradation potential of novel graphitic carbon nitride based nano zero-valent iron doped bismuth ferrite ternary composite," Optical Materials, vol. 120, p. 111408, 2021.

[29] Y. Orooji, M. Ghanbari, O. Amiri, M. Salavati-Niasari, "Facile fabrication of silver iodide/graphitic carbon nitride nanocomposites by notable photo-catalytic performance through sunlight and antimicrobial activity," Journal of Hazardous Materials, vol. 389, p. 122079, 2020.

[30] U. Saeed, A. Jilani, J. Iqbal, H. Al-Turaif, "Reduced graphene oxide-assisted graphitic carbon nitride@ZnO rods for enhanced physical and photocatalytic degradation," Inorganic Chemistry Communications, vol. 142, p. 109623, 2022.

[31] L. Ge, "Synthesis and photocatalytic performance of novel metal-free g-C3N4 photocatalysts," Materials Letters, vol. 65, no. 17–18, pp. 2652–2654, 2011.

[32] H. Zou, X. Yan, J. Ren, X. Wu, Y. Dai, D. Sha, J. Pan, J. Liu, "Photocatalytic activity enhancement of modified g-C3N4 by ionothermal copolymerization ," Journal of Materiomics, vol. 1, no. 4, pp. 340–347, 2015.

[33] D. R. Paul, S. Gautam, P. Panchal, S. P. Nehra, P. Choudhary, A. Sharma, "ZnO-Modified g-C3N4: A Potential Photocatalyst for Environmental Application," ACS Omega, vol. 5, no. 8, pp. 3828–3838, 2020.

[34] J. Hu, P. Zhang, W. An, L. Liu, Y. Liang, W. Cui, "In-situ Fe-doped g-C3N4 heterogeneous catalyst via photocatalysis-Fenton reaction with enriched photocatalytic performance for removal of complex wastewater," Applied Catalysis B: Environmental, vol. 245, pp. 130–142, 2019.

[35] M. Piri, M. M. Heravi, A. Elhampour, F. Nemati, "Silver nanoparticles supported on P, Se-codoped g-C3N4 nanosheet as a novel heterogeneous catalyst for reduction of nitroaromatics to their corresponding amines," Journal of Molecular Structure, vol. 1242, p. 130646, 2021.

[36] J. Hu, P. Zhang, W. An, L. Liu, Y. Liang, W. Cui, "In-situ Fe-doped g-C3N4 heterogeneous catalyst via photocatalysis-Fenton reaction with enriched photocatalytic performance for removal of complex wastewater," Applied Catalysis B: Environmental, vol. 245, pp. 130–142, 2019.

[37] Y. Oh, J.O. Hwang, E.S. Lee, M. Yoon, V.D. Le, Y.H. Kim, D.H. Kim, S.O. Kim, "Divalent Fe Atom Coordination in Two-Dimensional Microporous Graphitic Carbon Nitride," ACS Applied Materials and Interfaces, vol. 8, no. 38, pp. 25438–25443, 2016.

[38] C. Liu, H. Huang, W. Cui, F. Dong, Y. Zhang, "Band structure engineering and efficient charge transport in oxygen substituted g-C3N4 for superior photocatalytic hydrogen evolution," Applied Catalysis B: Environmental, vol. 230, pp. 115–124, 2018.

[39] M. A. Mohamed, M. F. M. Zain, L. Jeffery Minggu, M. B. Kassim, N. A. Saidina Amin, W. N. W. Salleh, M. N. I. Salehmin, M. F. Md Nasir, Z. A. Mohd Hir, "Constructing bio-templated 3D porous microtubular C-doped g-C3N4 with tunable band structure and enhanced charge carrier separation," Applied Catalysis B: Environmental, vol. 236, pp. 265–279, 2018.

[40] S. Babar, N. Gavade, H. Shinde, A. Gore, P. Mahajan, K. H. Lee, V. Bhuse, K. Garadkar, "An innovative transformation of waste toner powder into magnetic g-C3N4-Fe2O3 photocatalyst: Sustainable e-waste management," Journal of Environmental Chemical Engineering, vol. 7, no. 2, p. 103041, 2019.

[41] S. Liu, S. Wang, Y. Jiang, Z. Zhao, G. Jiang, Z. Sun, "Synthesis of Fe2O3 loaded porous g-C3N4 photocatalyst for photocatalytic reduction of dinitrogen to ammonia," Chemical Engineering Journal, vol. 373, pp. 572–579, 2019.

[42] C. Daikopoulos, Y. Georgiou, A. B. Bourlinos, M. Baikousi, M. A. Karakassides, R. Zboril, T. A. Steriotis, Y. Deligiannakis, "Arsenite

remediation by an amine-rich graphitic carbon nitride synthesized by a novel low-temperature method," Chemical Engineering Journal, vol. 256, pp. 347–355, 2014.

[43] Y. Yang, J. Chen, Z. Mao, N. An, D. Wang, B. D. Fahlman, "Ultrathin g-C 3 N 4 nanosheets with an extended visible-light-responsive range for significant enhancement of photocatalysis," RSC Advances, vol. 7, no. 4, pp. 2333–2341, 2017.

[44] H. Leelavathi, R. Muralidharan, N. Abirami, S. Tamizharasan, A. Kumarasamy, R. Arulmozhi, "Exploration of ZnO decorated g-C3N4 amphiphilic anticancer drugs for antiproliferative activity against human cervical cancer," Journal of Drug Delivery Science and Technology, vol. 68, p. 103126, 2022.

[45] A. K. Soğuksu, S. Kerli, M. Kavgacı, A. Gündeş, "Electrochemical Properties, Antimicrobial Activity and Photocatalytic Performance of Cerium-Iron Oxide Nanoparticles," Russian Journal of Physical Chemistry A, vol. 96, no. 1, pp. 209–215, 2022.

[46] F. Shi, L. Chen, C. Xing, D. Jiang, D. Li, M. Chen, "ZnS microsphere/g-C3N4 nanocomposite photo-catalyst with greatly enhanced visible light performance for hydrogen evolution: synthesis and synergistic mechanism study," RSC Advances, vol. 4, no. 107, pp. 62223–62229, 2014.

[47] S. Iqbal, A. Bahadur, S. Ali, Z. Ahmad, M. Javed, R. M. Irfan, N. Ahmad, M. A. Qamar, G. Liu, M. B. Akbar, M. Nawaz, "Critical role of the heterojunction interface of silver decorated ZnO nanocomposite with sulfurized graphitic carbon nitride heterostructure materials for photocatalytic applications," Journal of Alloys and Compounds, vol. 858, p. 158338, 2021.

[48] S. Le, T. Jiang, Y. Li, Q. Zhao, Y. Li, W. Fang, M. Gong, "Highly efficient visible-light-driven mesoporous graphitic carbon nitride/ZnO nanocomposite photocatalysts," Applied Catalysis B: Environmental, vol. 200, pp. 601–610, 2017.

[49] S. Sakthivel, B. Neppolian, M. v. Shankar, B. Arabindoo, M. Palanichamy, V. Murugesan, "Solar photocatalytic degradation of azo dye: comparison of photocatalytic efficiency of ZnO and TiO2," Solar Energy Materials and Solar Cells, vol. 77, no. 1, pp. 65–82, 2003.

[50] H. Xing, H. Ma, Y. Fu, M. Xue, X. Zhang, X. Dong, X. Zhang, "Preparation of g-C3N4/ZnO composites and their enhanced photocatalytic activity," Materials Technology, vol. 30, no. 2, pp. 122–127, 2015.

[51] Q. Zhong, H. Lan, M. Zhang, H. Zhu, M. Bu, "Preparation of heterostructure g-C3N4/ZnO nanorods for high photocatalytic activity on different pollutants (MB, RhB, Cr(VI) and eosin)," Ceramics International, vol. 46, no. 8, pp. 12192–12199, 2020.

[52] X. Li, M. Li, J. Yang, X. Li, T. Hu, J. Wang, Y. Sui, X. Wu, L. Kong, "Synergistic effect of efficient adsorption g-C3N4/ZnO composite for photocatalytic property," Journal of Physics and Chemistry of Solids, vol. 75, no. 3, pp. 441–446, 2014.

SAKARYA ÜNİVERSİTESİ
FEN BİLİMLERİ ENSTİTÜSÜ DERGİSİ

Sakarya University Journal of Science
SAUJS

ISSN 1301-4048 e-ISSN 2147-835X Period Bimonthly Founded 1997 Publisher Sakarya University
http://www.saujs.sakarya.edu.tr/

Title: Some Spectral Properties of Schrödinger Operators on Semi Axis

Authors: İbrahim ERDAL

Recieved: 2023-01-20 00:00:00

Accepted: 2023-02-24 00:00:00

Article Type: Research Article

Volume: 27
Issue: 3
Month: June
Year: 2023
Pages: 542-549

How to cite
İbrahim ERDAL; (2023), Some Spectral Properties of Schrödinger Operators on Semi Axis. Sakarya University Journal of Science, 27(3), 542-549, DOI: 10.16984/saufenbilder.1240115
Access link
https://dergipark.org.tr/en/pub/saufenbilder/issue/78131/1240115

Sakarya University Journal of Science 27(3), 542-549, 2023

Some Spectral Properties of Schrödinger Operators on Semi Axis

İbrahim ERDAL *1

Abstract

The main aim of this work is to investigate some spectral properties of Schrödinger operators on semi axis. We first present the Schrödinger equation with a piecewise continuous potential function $\boldsymbol{q}$ so that the problem differs from the classical Schrödinger problems. Then, we get the Wronskian of two specific solution of the given equation which helps us to create the sets of eigenvalues and spectral singularities. The rest of the paper deals with eigenvalues and spectral singularities. By the help of the analytical properties of Jost solutions and resolvent operator of the Schrödinger operators, we provide sufficient conditions guarenteeing finiteness of eigenvalues and spectral singularities with finite multiplicities.

Keywords: Schrödinger operators, eigenvalues, spectral singularities, resolvent operator

1. INTRODUCTION

In this study, we take into consideration the following one dimensional time independent Schrödinger equation on the semi axis

$$-y'' + q(x)y = \lambda^2 y, \quad 0 \le x < \infty \qquad (1)$$

with boundary condition

$$y(0) = 0, \qquad (2)$$

where λ is a spectral parameter and q is a complex valued potential function.

Before starting to examine our problem, let us briefly give an outline about the studies in the literature on the spectral theory of differential operators without any discontinuity. The spectral analysis of Schrödinger operators or differential operators were introduced by Naimark [1]. He showed that some poles of the kernel of resolvent operator of Schrödinger operator are not the eigenvalues of the operator. Naimark proved that these poles are a mathematical obstacle for the completeness of the eigenvectors and are imbedded in the continuous spectrum as well. These poles which are called spectral singularities by Schwartz [2] are very significant in physics and mathematics especially in quantum theory and applied mathematics.

Another technique for the treatment of the spectral theory of Schrödinger operator was presented by Marchenko [3]. He exposed that equation (1) has a bounded solution fulfilling the condition

$$\lim_{x\to\infty} e(x,\lambda)e^{-i\lambda x} = 1,$$

* Corresponding author: ierdal@ankara.edu.tr (I. ERDAL)
[1] Ankara University, Faculty of Science, Department of Mathematics
ORCID: https://orcid.org/0000-0002-4445-2389

where

$\lambda \in \overline{\mathbb{C}}_+ := \{\lambda \in \mathbb{C}: Im\lambda \geq 0\}.$

$e(x,\lambda)$ is called the Jost solution of Schrödinger equation (1) and it has an image

$$e(x,\lambda) = e^{i\lambda x} + \int_x^\infty K(x,t)e^{i\lambda t}dt, \lambda \in \overline{\mathbb{C}}_+ \quad (3)$$

under the condition

$$\int_0^\infty x|q(x)|dx < \infty, \quad (4)$$

where $K(x,t)$ is identified by the potential function q [3, 4]. Also $K(x,t)$ satisfies

$$|K(x,t)| \leq c\sigma\left(\frac{x+t}{2}\right), \quad (5)$$

$$|K_x(x,t)| \leq \frac{1}{4}\left|q\left(\frac{x+t}{2}\right)\right| + c\sigma\left(\frac{x+t}{2}\right), \quad (6)$$

where $c > 0$ is a constant and

$$\sigma(x) = \int_0^\infty |q(t)|dt.$$

Up to the present, a wide range of problems connected to the spectral theory of Schrödinger and Sturm-Liouville operators with spectral singularities have been examined [5-12].

On the other hand, spectral theory of Schrödinger and Sturm-Liouville operators with discontinuities inside an interval, namely impulsive operators were studied in detail recently [13-16]. However, in all studies, the discontinuity point is not releated to the potential function or coefficient of the operator, is related to the interval in which the operator is defined.

In light of the advancements on this theory, in this work, we present a second-order one dimensional time independent Schrödinger operator on the semi axis with piecewise continuous complex valued potential function. Since the potential function q behaves as an impulsive condition, the spectral analysis of Schrödinger operator getting more diffucult. Nevertheless, by specifying the resolvent of mentioned operator, we can give some useful spectral results.

2. STATEMENT OF THE PROBLEM

Let L denote the one dimensional time independent Schrödinger operator on the semi axis in $L^2[0,\infty)$ by the equation

$$-y'' + q(x)y = \lambda^2 y, \ \ 0 \leq x < \infty \quad (7)$$

with the boundary condition

$$y(0) = 0 \quad (8)$$

and piecewise continuous potential function

$$q(x) = \begin{cases} 0, & 0 \leq x \leq 1 \\ v(x), & 1 < x < \infty \end{cases}$$

where λ is a spectral parameter and $v \neq 0$ is a complex valued function and satisfies the condition

$$\int_1^\infty x|v(x)|dx < \infty. \quad (9)$$

It can be easily seen that $cos\lambda x$ and $sin\lambda x$ are the linearly independent solutions of equation (7) for $0 \leq x \leq 1$.

On the other part, (7) accepts another solution

$$\hat{e}(x,\lambda) = e^{-i\lambda x} + \\ + \frac{1}{2i\lambda}\int_{x_0}^x e^{i(x-t)\lambda}q(t)\hat{e}(t,\lambda)dt \\ + \frac{1}{2i\lambda}\int_x^\infty e^{i(x-t)\lambda}q(t)\hat{e}(t,\lambda)dt \quad (10)$$

for $\lambda \in \overline{\mathbb{C}}_+$ in $(1,\infty)$ fulfilling the condition

$$\lim_{x\to\infty} \hat{e}(x,\lambda)e^{i\lambda x} = 1,$$

where x_0 is a positive real number. From (3) and (10), it is easy to see that

$$W[e(x,\lambda), \hat{e}(x,\lambda)] = -2i\lambda, \ \ \lambda \in \overline{\mathbb{C}}_+,$$

where $W[y_1, y_2]$ denotes the Wronskian of the solutions y_1 and y_2 of equation (7).

By means of linearly independent solutions cosλx, sinλx and e(x,λ), $\hat{e}(x,\lambda)$ of (7) in the intervals [0,1] and $(1,\infty)$ respectively, we can state two solutions of boundary value problem (7)-(8) as

$$E(x,\lambda) = \begin{cases} A(\lambda)cos\lambda x + B(\lambda)sin\lambda x, & x \in [0,1] \\ e(x,\lambda), & x \in (1,\infty) \end{cases}$$

and

$$F(x,\lambda) = \begin{cases} sin\lambda x, & x \in [0,1] \\ C(\lambda)e(x,\lambda) + D(\lambda)\hat{e}(x,\lambda), & x \in (1,\infty) \end{cases}$$

for $\lambda \in \overline{\mathbb{C}}_+$ and λ dependent arbitrary coefficients A, B, C, D. Using the continuity of the solutions $E(x,\lambda)$ and $F(x,\lambda)$ during the semi axis, we get uniquely

$$A(\lambda) = \cos\lambda\, e(1,\lambda) - \frac{sin\lambda}{\lambda} e'(1,\lambda) \qquad (11)$$

$$B(\lambda) = sin\lambda e(1,\lambda) + \frac{cos\lambda}{\lambda} e'(1,\lambda) \qquad (12)$$

$$C(\lambda) = -\frac{1}{2i\lambda}[sin\lambda\hat{e}'(1,\lambda) - \\ -\lambda cos\lambda\hat{e}(1,\lambda)] \qquad (13)$$

$$D(\lambda) = \frac{1}{2i\lambda}[sin\lambda e^{'}(1,\lambda) - \lambda cos\lambda e(1,\lambda) \qquad (14)$$

for all $\lambda \in \overline{\mathbb{C}}_+$. With the help of solutions $E(x,\lambda)$, $F(x,\lambda)$ and (11)-(14), we can introduce the following Lemma and Theorem.

Lemma 1. The following equations are valid for all $\lambda \in \overline{\mathbb{C}}_+$:

$$W[E,F](x,\lambda) = \lambda A(\lambda), \quad x \to \infty,$$

$$W[E,F](x,\lambda) = \lambda A(\lambda), \quad x \to 0.$$

Proof. Using the definition of Wronskian of two solutions E and F, for $x \in (1,\propto)$, we obtain

$$\begin{gathered} W[E,F](x,\lambda) = \\ = e(x,\lambda)[C(\lambda)e'(x,\lambda) + D(\lambda)\hat{e}'(x,\lambda)] \\ -e'(x,\lambda)[C(\lambda)e(x,\lambda) + D(\lambda)\hat{e}(x,\lambda)] \\ = D(\lambda)W[e(x,\lambda), \hat{e}(x,\lambda)] \\ = -2i\lambda D(\lambda) \\ = \lambda A(\lambda). \end{gathered}$$

Similarly, for $x \in [0,1]$, we get

$$W[E,F](x,\lambda) = \lambda A(\lambda).$$

Theorem 2. The resolvent operator of L has the representation

$$\Re_{\lambda^2}(L)\varphi(x) = \int_0^\infty G(x,t;\lambda)\varphi(t)dt,$$

for $\varphi \in L^2[0,\infty)$ where

$$G(x,t;\lambda) = \begin{cases} \frac{F(t,\lambda)E(x,\lambda)}{W[E,F](x,\lambda)}, & 0 \le t \le x \\ \frac{F(x,\lambda)E(t,\lambda)}{W[E,F](x,\lambda)}, & x < t < \infty \end{cases}$$

is the Green function for $\lambda \in \overline{\mathbb{C}}_+$.

Proof. Let us take into account the following nonhomogeneous Schrödinger equation:

$$-y'' + q(x)y - \lambda^2 y = \varphi(x), x \in [0,\infty) \qquad (15)$$

Take the advantage of two linearly independent solutions of homogeneous part of Schrödinger equation (15), the general solution of (15) can be written as

$$y(x,\lambda) = c_1(x)E(x,\lambda) + c_2(x)F(x,\lambda).$$

By means of variation of constants, we arrive at

$$c_1(x) = \alpha_1 + \int_0^x \frac{\varphi(t)F(t,\lambda)}{W[E,F](x,\lambda)}dt$$

and

$$c_2(x) = \alpha_2 + \int_x^\infty \frac{\varphi(t)E(t,\lambda)}{W[E,F](x,\lambda)}dt.$$

The rest of the proof is clear.

Theorem 3. Under the condition (9), the function $A(\lambda)$ fulfills the following asymptotic equation

$$A(\lambda) = 1 + o(1),\ \lambda \in \overline{\mathbb{C}}_+,\ |\lambda| \to \infty. \quad (16)$$

Proof. It is obtained from (11) that

$$\begin{aligned} A(\lambda) &= \left(cos\lambda e^{i\lambda}\right)\left(e(1,\lambda)e^{-i\lambda}\right) \\ &\quad - \left(sin\lambda e^{i\lambda}\right)\left(\frac{e'(1,\lambda)e^{-i\lambda}}{\lambda}\right) \\ &= e^{i\lambda}(cos\lambda - isin\lambda) + o(1) \\ &= 1 + o(1), \end{aligned}$$

for , $\lambda \in \overline{\mathbb{C}}_+,\ |\lambda| \to \infty$.

3. EIGENVALUES AND SPECTRAL SINGULARITIES

This section contains the primary results for the spectral analysis of Schrodinger operator L. Firstly, we introduce the sets of eigenvalues and spectral singularities of Schrödinger operator L as

$$\sigma_d(L) = \{\mu = \lambda^2 : Im\lambda > 0,\ A(\lambda) = 0\}$$

and

$$\sigma_{ss}(L) = \{\mu = \lambda^2 : Im\lambda = 0, \lambda \neq 0, A(\lambda) = 0\},$$

respectively.

At present, we describe the sets

$$P_1 = \{\lambda : \lambda \in \mathbb{C}_+, A(\lambda) = 0\}$$

and

$$P_2 = \{\lambda : \lambda \in \mathbb{R} \setminus \{0\}, A(\lambda) = 0\}.$$

Hence, we can write again these sets

$$\sigma_d(L) = \{\mu :\ \mu = \lambda^2, \lambda \in P_1\}$$

and

$$\sigma_{ss}(L) = \{\mu :\ \mu = \lambda^2, \lambda \in P_2\}.$$

Lemma 4. Assume (9).

(i) The set P_1 has at most countable number of elements and P_1 is bounded. If the limit points of this set exist, they are only in a bounded subinterval of the real axis.

(ii) Linear Lebesgue measure of the set P_2 is zero and P_2 is compact.

Proof. Asymptotic equation (16) shows that $A(\lambda)$ can not equal to zero for adequately large $\lambda \in \overline{\mathbb{C}}_+$. Hence, the boundedness of P_1 and P_2 comes from (16). Since $A(\lambda)$ is analytic in $\mathbb{C}_+$, the set P_1 has at most countably many elements and limit points of P_1 are only in a bounded subinterval of the real axis. Finally, by means of the uniqueness theorem of the analytic functions [17], we obtain that linear Lebesgue measure of the the set P_2 is zero and P_2 is a closed set.

The following Theorem is a straight conclusion of Lemma 4.

Theorem 5. Under condition (9),

(i) The set of eigenvalues of L has finite number of elements and it is bounded. If the limit points of this set exist, they are only in a bounded subinterval of the real axis.

(ii) The set of spectral singularities of L is compact and its linear Lebesgue measure is zero.

Proof. The proof is obtained similarly to the proof of Lemma 4.

At the moment, we continue by imposing the extra stipulation

$$\int_1^\infty \exp(\varepsilon x)\,|v(x)|dx < \infty \qquad (17)$$

on function v to ensure the finiteness of the sets of spectral singularities and eigenvalues.

Theorem 6. If the inequality (17) is satisfied for some $\varepsilon > 0$, then the Schrödinger operator L has a finite number of spectral singularities and eigenvalues, and each of them has finite multiplicity.

Proof. Using (5),(6) and (17), we obtain that

$$|K(1,t)| \le c_1 exp\left(-\varepsilon\frac{1+t}{2}\right),\ c_1 > 0$$

and

$$\left|\int_1^\infty K_x(1,t)e^{i\lambda t}dt\right| \le 2e^{Im\lambda}\int_1^\infty |v(u)|\,e^{\varepsilon u}e^{-u(\varepsilon+2Im\lambda)}du + +c_2\int_1^\infty e^{-\varepsilon/2}e^{-t(\varepsilon/2+Im\lambda)}dt,$$

where c_1, c_2 are arbitrary constants and $u = \frac{1+t}{2}$. From the last inequality and (17), we arrive at $\left|\int_1^\infty K_x(1,t)e^{i\lambda t}dt\right| < \infty$ for $Im\lambda > -\frac{\varepsilon}{2}$. Thus, $A(\lambda)$ has an analytic continuation from the real axis to the lower half plane $Im\lambda > -\frac{\varepsilon}{2}$. Hence the sets $\sigma_d(L)$ and $\sigma_{ss}(L)$ don't have any limit points on the real axis. With the help of Theorem 5, we see that this sets are bounded and have at most countable number of elements. Moreover, the uniqueness theorem of the analytic functions [17] give us, all roots of $A(\lambda)$ in $\overline{\mathbb{C}}_+$ are of finite multiplicities.

Now, let us specify the all limit points of P_1 and P_2 by P_3 and P_4, respectively. Also the set of all roots of $A(\lambda)$ with infinite multiplicity in $\overline{\mathbb{C}}_+$ is denoted by P_5.

By the help of uniqueness theorem, we can present the following Lemma.

Lemma 7. (i) $P_3 \subset P_2,\ P_4 \subset P_2,\ P_5 \subset P_2,$ $P_3 \subset P_5, P_4 \subset P_5$.

(ii) $\mu(P_3) = \mu(P_4) = \mu(P_5) = 0,$

where μ is linear Lebesgue measure.

Proof. Proof of Lemma is clear from the boundary uniqueness theorem of analytic functions in [17].

Theorem 8. If

$$\int_1^\infty e^{\varepsilon x^\delta}\,|v(x)|dx < \infty, \qquad (18)$$

for some $\varepsilon > 0$ and $\frac{1}{2} \le \delta < 1$, then $P_5 = \emptyset$.

Proof. From (11), we get

$$A(\lambda) = \left(cos\lambda e^{i\lambda}\right)\left(e(1,\lambda)e^{-i\lambda}\right) - -\left(\frac{sin\lambda}{\lambda}e^{i\lambda}\right)\left(e'(1,\lambda)e^{-i\lambda}\right) \qquad (19)$$

where $J_1(\lambda) = e(1,\lambda)e^{-i\lambda}$, $J_3(\lambda) = cos\lambda e^{i\lambda},\ J_2(\lambda) = e'(1,\lambda)e^{-i\lambda}$ and $J_4(\lambda) = \frac{sin\lambda}{\lambda}e^{i\lambda}$.
It follows from (5),(6) and (18) that

$$\left|\frac{d^m}{d\lambda^m}J_1(\lambda)\right| \le c_3\int_1^\infty t^m e^{-\varepsilon(t/2)^\delta}dt, \qquad (20)$$

$$\left|\frac{d^m}{d\lambda^m}J_2(\lambda)\right| \le c_4\int_1^\infty t^m e^{-\varepsilon(t/2)^\delta}dt, \qquad (21)$$

$$\left|\frac{d^m}{d\lambda^m}J_3(\lambda)\right| \le c_5 2^m, \qquad (22)$$

$$\left|\frac{d^m}{d\lambda^m}J_4(\lambda)\right| \le c_6 2^m, \qquad (23)$$

where c_3, c_4, c_5, c_6 are arbitrary constants. Using (19)-(23), we see that

$$\left|\frac{d^m}{d\lambda^m}A(\lambda)\right| \le \sum_{s=0}^{m}\binom{m}{s}\left|\frac{d^{m-s}}{d\lambda^{m-s}}J_1\right|\left|\frac{d^s}{d\lambda^s}J_3\right|$$

$$+\sum_{s=0}^{m}\binom{m}{s}\left|\frac{d^{m-s}}{d\lambda^{m-s}}J_2\right|\left|\frac{d^{s}}{d\lambda^{s}}J_3\right|$$

$$\leq c_7 2^m \int_1^\infty t^m e^{-\varepsilon(t/2)^\delta}dt, \quad (24)$$

for $m = 1,2,\ldots$, where c_7 is arbitrary constant.

Now, we can write

$$\left|\frac{d^m}{d\lambda^m}A(\lambda)\right| \leq A_m$$

for $m = 1,2,\ldots$ and $\lambda \in \overline{\mathbb{C}}_+$, $|\lambda| < N$, where

$$A_m = c_7 2^m \int_1^\infty t^m e^{-\varepsilon(t/2)^\delta}dt.$$

Since $A(\lambda)$ can't be zero, Pavlov's theorem [18] gives that

$$\int_0^k \ln \mathrm{Z}(s)\, d\mu(P_5, s) > -\infty, \quad (25)$$

where $\mathrm{Z}(s) = inf\left\{\frac{A_m s^m}{m!} : m = 0,1,2,\ldots\right\}$ and $\mu(P_5, s)$ is the linear Lebesgue measure of the $s-$neighbourhood of P_5. Using the definition of gamma function, we can express

$$A_m \leq K\alpha^m m^{\frac{m(1-\delta)}{\delta}} m!,$$

where K is a constant. Thus, we get

$$\mathrm{Z}(s) \leq K\alpha exp\left\{-\frac{1-\delta}{\delta}e^{-1}\alpha^{-\frac{\delta}{1-\delta}}s^{-\frac{\delta}{1-\delta}}\right\}.$$

From the last equality and (25), we obtain

$$\int_0^k s^{-\delta/(1-\delta)}\, d\mu(P_5, s) < \infty.$$

Since $\delta/(1-\delta) \geq 1$, the previous inequality gives that $P_5 = \emptyset$.

Since $P_5 = \emptyset$, it is easy to get the following Theorem.

Theorem9. Assume (18). Then the Schrödinger operator L has countably many number of spectral singularities and eigenvalues and each of them has finite multiplicity.

4. CONCLUSIONS

In this work, we discussed some primary spectral problems of one dimensional time independent Schrödinger operators on the semi axis. In particular, we presented the solutions of Schrödinger equations and found the resolvent of Schrödinger operators. In the last part, we investigated the structure and finiteness of spectral singularities and eigenvalues with the help of uniqueness theorems.

Funding
The author (s) has no received any financial support for the research, authorship or publication of this study.

Authors' Contribution
The authors contributed equally to the study.

The Declaration of Conflict of Interest/ Common Interest
No conflict of interest or common interest has been declared by the authors.

The Declaration of Ethics Committee Approval
This study does not require ethics committee permission or any special permission.

The Declaration of Research and Publication Ethics
The authors of the paper declare that they comply with the scientific, ethical and quotation rules of SAUJS in all processes of the paper and that they do not make any falsification on the data collected. In addition, they declare that Sakarya University Journal of Science and its editorial board have no responsibility for any ethical violations that may be encountered, and that this study has not been evaluated in any academic publication environment other than Sakarya University Journal of Science.

REFERENCES

[1] M. A. Naimark, "Investigation of the spectrum and the expansion in eigenfunctions of a non-selfadjoint operators of second order on a semi-axis," American Mathematical Society Translations: Series 2. vol. 2, no.16, pp. 103-193, 1960.

[2] J. T. Schwartz, "Some non-selfadjoint operators," Communications on Pure and Applied Mathematics, vol. 13, pp. 609-639, 1960.

[3] V. A. Marchenko, "Sturm-Liouville Operators and Applications Operator Theory: Advances and Applications," vol. 22, Birkhauser, Basel 1986.

[4] B. M. Levitan, I. S. Sargsjan, "Sturm-Liouville and Dirac Operators," Kluwer Academic Publishers, 1991.

[5] E. Bairamov, A. O. Celebi, "Spectral analysis of nonselfadjoint Schrödinger operators with spectral parameter in boundary conditions," Facta Universitatis, Series: Mathematics and Informatics, vol. 13, pp. 79-94, 1998.

[6] E. Bairamov, O. Cakar, A. M. Krall, "An eigenfunction expansion for a quadratic pencil of a Schrödinger operator with spectral singularities," Journal of Differential Equations, vol. 151, pp. 268-289, 1999.

[7] M. Adıvar, E. Bairamov, " Spectral singularities of the nonhomogeneous Sturm-Liouville equations," Applied Mathematics Letters, vol. 15, no.7, pp. 825-832, 2002.

[8] E. Bairamov, E. Kir, "Spectral properties of a finite system of Sturm-Liouville differential operators," Indian Journal of Pure and Applied Mathematics, vol. 35, no.2, pp. 249-256, 2004.

[9] G. Sh. Guseinov, "On the concept of spectral singularities," Pramana-Journal of Physics, vol. 73, no.3, pp. 587-603, 2009.

[10] A. M. Krall, E. Bairamov, O. Cakar, "Spectrum and spectral singularities of a quadratic pencil of a Schrödinger operator with a general boundary condition," Journal of Differential Equations, vol. 151, no.2, pp. 252-267, 1999.

[11] A. Mostafazadeh, "Optical spectral singularities as treshold resonances," Physical Review A Third Series-83:045801, 2011.

[12] E. Bairamov, S. Cebesoy, "Spectral singularities of the matrix Schrödinger equations," Hacettepe Journal of Mathematics and Statistics, vol. 45, no.4, pp. 1007-1014, 2016.

[13] S. Cebesoy, "Examination of eigenvalues and spectral singularities of a discrete Dirac operator with an interaction point," Turkish Journal of Mathematics, vol. 46, no.1, pp. 157-166, 2022.

[14] Ş. Yardımcı, İ. Erdal, "Investigation of an impulsive Sturm-Liouville operator on semi axis," Hacettepe Journal of Mathematics and Statistics, vol. 48, no.5, pp. 1409-1416, 2019.

[15] Y. Aygar, G. G. Özbey, "Scattering analysis of a quantum impulsive boundary value problem with spectral parameter," Hacettepe Journal of Mathematics and Statistics, vol. 51, no.1, pp. 142-155, 2022.

[16] T. Köprübaşi, Y. Aygar Küçükevcilioğlu, "Discrete impulsive Sturm-Liouville equation with hyperbolic eigenparameter," Turkish

Journal of Mathematics, vol. 46, no.2, pp. 387-396, 2022.

[17] E. P. Dolzhenko, “Boundary value uniqueness theorems for analytic functions,” Mathematical Notes, vol. 26, pp. 437-442, 1979.

[18] B. S. Pavlov, “The non-selfadjoint Schrödinger operators,” Mathematical Physics, vol. 1, pp. 87-114, 1967.

SAKARYA ÜNİVERSİTESİ
FEN BİLİMLERİ ENSTİTÜSÜ DERGİSİ

Sakarya University Journal of Science
SAUJS

ISSN 1301-4048 e-ISSN 2147-835X Period Bimonthly Founded 1997 Publisher Sakarya University
http://www.saujs.sakarya.edu.tr/

Title: Detection and Localization of Glioma and Meningioma Tumors in Brain MR Images using Deep Learning

Authors: Emine CENGİL, Yeşim EROĞLU,Ahmet ÇINAR, Muhammed YILDIRIM

Recieved: 2022-02-02 00:00:00

Accepted: 2023-03-02 00:00:00

Article Type: Research Article

Volume: 27
Issue: 3
Month: June
Year: 2023
Pages: 550-563

How to cite
Emine CENGİL, Yeşim EROĞLU,Ahmet ÇINAR, Muhammed YILDIRIM; (2023), Detection and Localization of Glioma and Meningioma Tumors in Brain MR Images using Deep Learning. Sakarya University Journal of Science, 27(3), 550-563, DOI: 10.16984/saufenbilder.1067061
Access link
https://dergipark.org.tr/en/pub/saufenbilder/issue/78131/1067061

Sakarya University Journal of Science 27(3), 550-563, 2023

Detection and Localization of Glioma and Meningioma Tumors in Brain MR Images using Deep Learning

Emine CENGİL*[1], Yeşim EROĞLU[2], Ahmet ÇINAR[3], Muhammed YILDIRIM[4]

Abstract

Brain tumors are common tumors arising from parenchymal cells in the brain and the membranes that surround the brain. The most common brain tumors are glioma and meningioma. They can be benign or malignant. Treatment modalities such as surgery and radiotherapy are applied in malignant tumors. Tumors may be very small in the early stages and may be missed by showing findings similar to normal brain parenchyma. The correct determination of the localization of the tumor and its neighborhood with the surrounding vital tissues contributes to the determination of the treatment algorithm. In this paper, we aim to determine the classification and localization of gliomas originating from the parenchymal cells of the brain and meningiomas originating from the membranes surrounding the brain in brain magnetic resonance images using artificial intelligence methods. At first, the two classes of meningioma and glioma tumors of interest are selected in a public dataset. Relevant tumors are then labeled with the object labeling tool. The resulting labeled data is passed through the EfficientNet for feature extraction. Then Path Aggregation Network (PANet) is examined to generate the feature pyramid. Finally, object detection is performed using the detection layer of the You Only Look Once (YOLO) algorithm. The performance of the suggested method is shown with precision, recall and mean Average Precision (mAP) performance metrics. The values obtained are 0.885, 1.0, and 0.856, respectively. In the presented study, meningioma, and glioma, are automatically detected. The results demonstrate that using the proposed method will benefit medical people.

Keywords: MRI, brain tumor detection, deep learning

* Corresponding author: ecengil@beu.edu.tr (E. CENGİL)
[1] Department of Computer Engineering, Bitlis Eren University, Bitlis, Turkey
[2] Department of Radiology, Firat University, Elazig, Turkey,
[3] Department of Computer Engineering, Firat University, Elazig, Turkey,
[4] Department of Computer Engineering, Malatya Turgut Ozal University, Malatya, Turkey,
E-mail: yeroglu@firat.edu.tr, acinar@firat.edu.tr, muhammed.yildirim@ozal.edu.tr
ORCID: https://orcid.org/0000-0003-4313-8694, https://orcid.org/ 0000-0003-3636-4810, https://orcid.org/ 0000-0001-5528-2226, https://orcid.org/ 0000-0003-1866-4721

1. INTRODUCTION

Brain tumors are tumors with high morbidity and mortality, the frequency of which increases with age. They are masses of cells that proliferate abnormally and uncontrollably in the brain. Primary brain tumors develop from the parenchymal components of the brain, or the membranes that surround the brain called the meninges. The most common primary brain tumors are gliomas originating from neuroepithelial cells and meningiomas originating from the membranes surrounding the brain. Gliomas are the most usual brain tumors that develop from neuroglial cells such as astrocytes, oligodendrocytes, and ependymal cells, and they can be benign or malignant [1, 2]. Meningiomas are mostly benign and constitute approximately 20% of brain tumors. They are extra-axial tumors because they arise from the membranes surrounding the brain [3]. Gliomas are more common in men and meningiomas in women. The main imaging modalities used in the identification of brain tumors are computed tomography (CT) and magnetic resonance imaging (MRI). The advantages of magnetic resonance imaging are its high soft-tissue resolution, noninvasiveness, and no radiation. Computed tomography is especially used in emergent pathologies such as bleeding, hydrocephalus, herniation, and for the determination of tumor calcification [4, 5]. With conventional MRI of the brain, the localization, borders and spread of the tumor are determined and treatment is planned. However, sometimes the imaging findings of tumors do not allow adequate anatomical detailing and it may be difficult to detect the tumor [6, 7].

The brain tumor is a common tumor with serious consequences. In this respect, it should be determined correctly. Routinely, radiologists and clinicians may encounter some difficulties when performing this procedure. In addition, the lack of experience of doctors may increase the rate of error. Therefore, the use of computer-assisted technology has become necessary to overcome these limitations. In this study, an expert system using artificial intelligence-based deep learning architecture, which detects the presence and localization of the tumor region on brain MR images, has been studied.

The study aims to determine the type of glioma and meningioma, which are the most common brain tumors, and in which regions they are located on MR images. A public dataset is labeled by an expert radiologist with ten years of experience [8]. Although the classification of brain tumors is widely studied, the studies determining the type and location of the tumor are not common. The knowledge of the location of the relevant region also provides convenience to the doctors.

Figure 1 shows the draft of the proposed model. Using the applied method, the two types of brain tumors are found with high accuracy. The performance of the method is evaluated according to performance metrics such as precision, recall, and mAP.

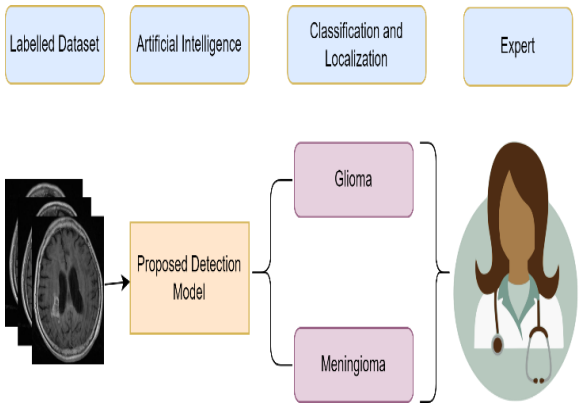

Figure 1 Draft diagram of the proposed model

The organization of the work is as follows. In section 2, artificial intelligence-based methods for the detection of brain tumors are given. In the third section, the dataset used and the proposed method are presented. The fourth section includes the experimental

results of the method. Finally, the results of the study are evaluated in section 5.

2. LITERATURE

Brain tumor classification, segmentation, and detection are the most studied topics in medical image processing. G. Garg et al. [9] intend to determine the tumor region's area and identify brain tumors as benign or malignant. For this, a hybrid ensemble method based on the Majority Voting Method is proposed, which employs Random Forest, K-Nearest Neighbor, and Decision Tree. First, Otsu's Threshold method is used to segment the data. The Stationary Wavelet Transform, Principal Component Analysis, and Gray Level Co-occurrence Matrix are used to extract thirteen features for classification. The hybrid ensemble classifier (KNN-RFDT) is used for classification, which is based on the majority voting method. In general, it is intended to improve traditional classifier performance rather than going deep learning. In the dataset of 2556 images, the proposed method had an accuracy of 97.305 percent.

V. V. Kumar and P. G. K. Prince [10] use Deep belief network and Quadratic Logit BoostClassifier (DBNQLBC) technique for brain tumor detection. The proposed technique includes differen types of layers such as input layer, hidden layers and output layer. The method yielded 70.83% Specificity on 250 MRI images The RCNN technique was proposed by N. Kesav and M.G. Jibukumar [11] for brain tumor classification and tumor-type object detection. Two publicly available datasets were used to analyze the architecture. First, Dual Channel CNN, a low-complexity architecture, is used to distinguish between glioma and meningioma tumor MRI samples. The same structure is then used as a feature extractor of an RCNN to detect tumor regions in the previously classified Glioma MRI sample. Bounding boxes are utilized to define the tumor region. The methodology yielded a confidence level of 98.83 percent on average.

M. F. Khan, et al. [12] used AdaBoost and random forest algorithms to classify brain tumors. In the related dataset, 95% accuracy was obtained for the AdaBoost algorithm, while 89% accuracy was obtained for the Random Forest algorithm.

In [13], the Whale Harris Hawks optimization (WHHO) method is proposed for detecting brain tumors using MR images. Cellular automata and rough set theory are used for segmentation. Tumor size, Local Optically Oriented Pattern, Mean, and Variance are extracted from segments. A deep convolutional neural network is utilized to detect brain tumors, with training using the recommended WHHO. The proposed WHO is created by combining the Whale optimization algorithm (WOA) and the Harris hawk optimization algorithm (HHO). The WHO-based DeepCNN has a maximum accuracy of 81.6%, a maximum specificity of 79.1%, and a maximum sensitivity of 97.4%.

The authors in [14] offer a method for identifying brain tumors that relies on a deep autoencoder and spectral data augmentation. Brain images were subjected to morphological cropping in order to downsize and decrease noise. The data space problem with feature reduction is then resolved using the discrete wavelet transform (DWT). For easier feature extraction and categorization of images of brain tumors, a dense layer is lastly proposed. The proposed algorithm gave 97% accuracy and 99.46% AUC ROC score.

Q. Chuandong, et al. [15] proposed a shared memory-based parallel optimization approach to resolve the SVM classifier for brain tumor identification. First, the wavelet transform method is utilized to compare the features of the extracted brain tumor MR image using the HOG algorithm. After, SVM was used as a classifier. Finally, the classifier solution is proposed and applied using the SMP-SGD, SMP-Momentum, SMP-Adagrad, and SMP-Adam algorithms. According to experimental

findings, the HOG algorithm extracts MRI features of brain tumors more successfully than the discrete wavelet transform technique. The SMP-SGD method that was suggested offered 96% accuracy.

S. Sangeeta and H. Nagendra [16] aimed to classify brain tumors as meningiomas, gliomas, and pituitary. For this purpose, K means and Fuzzy C-Means Clustering (FCM) algorithms were used. In the study where the two methods were compared, both reached 80% accuracy. In addition, K means performed better in terms of processing time.

M. Arif et al. [17] classify the brain glioma tumor or a meningioma tumor. In the paper, a deep learning classifier and Berkeley's wavelet transform (BWT)-based technique are suggested. Using the gray level co-occurrence matrix (GLCM) method, significant features are retrieved from each segmented tissue, and then those features are optimized using a genetic algorithm. The method achieved 98.5% accuracy on MRI brain images (normal, abnormal) from 66 patients.

G. Ramkumar et al. [18] suggested a novel method and strategy based on the Deep CNN Algorithm (DCNNA). A fuzzy-based strategy is also inserted to the suggested segmentation processing steps in brain tumor classifications, increasing the accuracy of the proposed DCNNA approach.

In [19], human brain images are classified as normal, benign, and malignant tumors. Preprocessing and Segmentation, Feature Reduction, and Feature Extraction and Classification are the four stages of the system. The Threshold function is used to process preprocessing and segmentation in the first stage. The features associated with MR images are obtained in the second step by employing the discrete wavelet transform. The third step includes of Principal component analysis, which is used to reduce the MRI features to more essential features. The final stage is the classification, in which a classifier KSVM is used to classify the site of infection in the brain tumor. The method obtained an accuracy of around 90%.

M. Jian et al. [20] proposed a tumor detection method for MRI brain images based on salience modeling. First, to overcome the skull effect, the morphological method was used to strip the skull of MRI brain images. Next, a basic local contrast-based salience detection method is introduced to enhance foreground regions that make it easier to obtain the lesion site. Eventually, noise removal, segmentation, and morphological methods are utilized to improve the results.

M. K. Islam et al. [21] proposes a brain tumor detection scheme based on the superpixel, template-based K-means algorithm, and PCA. At first, basic features are extracted using PCA. The image is then enhanced using a filter that helps enhance accuracy. Lastly, segmentation to detect brain tumors is performed via the TK-vehicle clustering algorithm. The proposed detection scheme showed 95% success for detecting brain tumors on MR images.

There are numerous papers in the literature on the detection of brain tumors. A large part of these studies focuses only on the presence of the tumor. Some classify tumors according to their types but are not concerned with the knowledge of where the tumor is. Our motivation is to suggest an artificial intelligence-based system to assist doctors. For this purpose, the type and localization of the two most common tumors are determined.

3. METHODOLOGY

In this section, information about the data set utilized and the proposed method are detailed.

3.1. Data Set

In the presented study, we use a dataset consisting of a total of 4 classes containing brain MRI images [22]. In the classes, images of the normal brain, images of glioma tumors originating from neuroepithelial cells, images of meningioma tumors originating from the membranes of the brain, and images of pituitary tumors originating from the sellar region are available, respectively.
The dataset was examined by a specialist radiologist. The class with normal brain MR images and the class with pituitary tumors in the sellar region were excluded from the study. Images of glioma and meningioma, the two most common classes of brain tumors, were also analyzed, and postoperative MR images and images with poor image quality and artifacts were excluded from the dataset. Some examples of such images are given in Figure 2. As a result, the dataset to be applied to the method consists of 602 glioma and 818 meningioma images. The images to be used are labeled with the labelImg [23]. Examples of original and labeled images of the dataset are given in Figure 3.

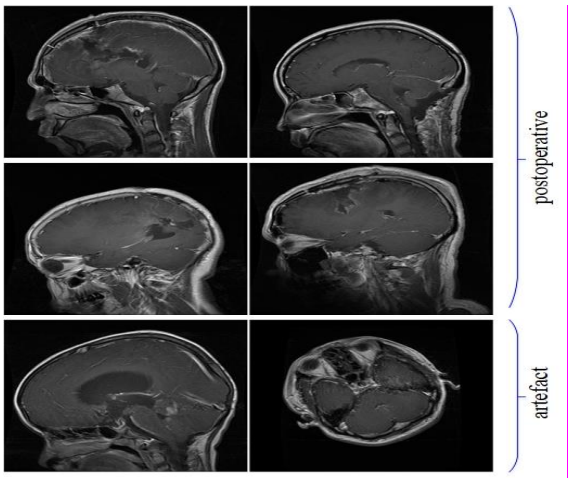

Figure 2 Samples of images extracted from the dataset

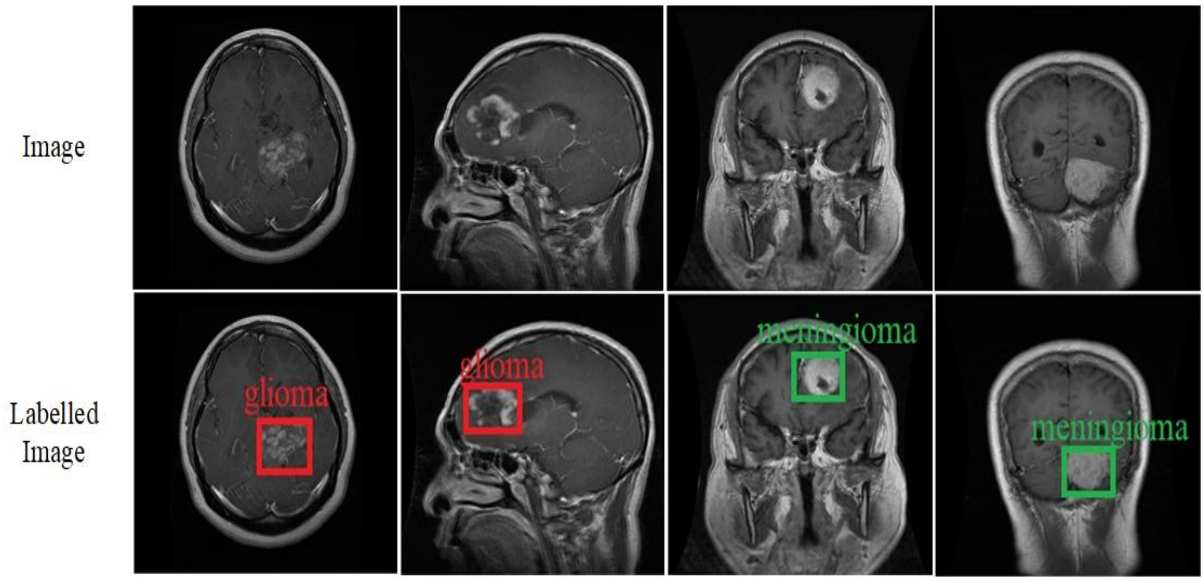

Figure 3 Samples of original and labelled images of the data set.

3.2. Convolutional Neural Network (CNN)

CNN are multi-layer architectures based on deep learning, which is a popular technique of recent times. CNN provides classification by extracting the characteristics of the labeled training data. CNN models are frequently used in image processing in academic and scientific areas. CNN architecture has convolution, pooling, and fully connected layers, etc. The convolution function is presented in equation (1) [24].

$$(a * k)(x) = \sum_{m=-\infty}^{+\infty} a(m)k(x-m) \quad (1)$$

where, a: input image, k: kernel, x: variable representing range of shifting and, m: shifting against x. The mathematical operation aids in calculating the similarity of the two signals. The depth of the network is increased by applying filters to the entered data, with the goal of producing more accurate results [25].

Activation layers are often used in CNN architectures. The most common activation functions are Tanh, Sigmoid, Relu, and Leaky ReLU [26].

The Fully Connected layer is another popular layer in CNN architectures [27]. The feature maps are fed into the fully connected layer. These feature maps are being prepared for classification. Also, multidimensional feature maps are converted to a single dimension.

The first step in object-finding problems is to extract distinctive attributes from the image. The success of the method is largely parallel to the success of this stage. Convolutional neural networks have models that have proven themselves in this field. Some of the popular ones are AlexNet [28], VGG [29], ResNet [30], and EfficientNet [31]. In the EfficientNet model, all three of the depth, width, and resolution are scaled to make the model smaller. The EfficientNet group includes of 8 models from B0 to B7, and the larger the number, the higher the number of calculated parameters and the accuracy. EfficientNet is frequently used in image processing applications in the medical field and achieves successful results [32-34]. For this reasons, the EfficientNet network is preferred in the feature extraction step.

3.3. Proposed Method

Artificial intelligence is present in many fields today. The rapid progress of technology necessitates the use of artificial intelligence in the area of medical image processing, as in most areas. The graphical depiction of the model is as in Figure 4.

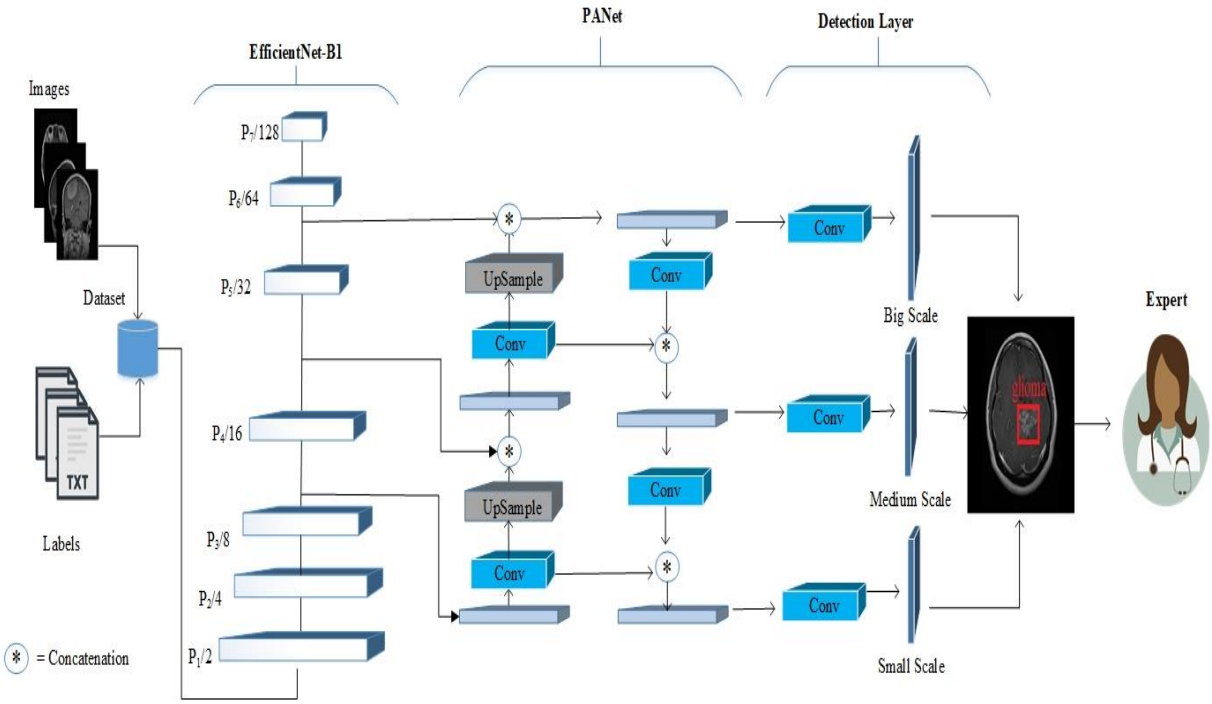

Figure 4 Graphical depiction of proposed model

In the study, a dataset containing two types of tumors labeled by the expert radiologist with the labelImg tool is used as input. In YOLOv5, CSPDarkNet is used as a backbone.

In the proposed method, features are provided with the EfficientNet model from the input images. Then PANet [35] is used to generate the feature pyramid. The utilization of accurate localization signals in the lower layers is improved by PANet, which can obviously increase the object's position accuracy. Finally, object finding is performed using the detection layer used in versions 3-4 and 5 [36, 37] of the YOLO object detection algorithm. The Yolo layer generates feature maps in 3 different sizes (18×18, 36×36, 72×72) to obtain a multi-scale prediction. In this way, it is ensured that Small, Medium, and Big Scale tumors in MR images.

4. EXPERIMENTAL RESULTS

This study was carried out with the python language. While 70% of the images in the dataset were used for training, 15% were used for validation and 15% were used for testing. The training parameters used are important for the performance of the model. In the model, the initial learning rate is 0.01 and the momentum is 0.937. Other training parameters are given in Table 1. System requirements for the experiment; Windows 10 operating system is 16GB RAM, NVIDIA GeForce 950M GPU, and Intel(R) Core(TM) i7-7500U CPU.

Table 1 Train Parameter of model

Momentum	0.937
Learning Rate	0.01
Weight Decay	0.0005
Epoch	20
Batch size	2
Opt. Alg.	SGD/Adam
Library	PyTorch

The method is run under the same conditions as SGD and Adam optimization algorithms. In terms of training time, model training is completed in 4.409 hours with SGD. On the other hand, when Adam is used, the training is completed in 4,143 hours. In terms of accuracy criteria, 0.775 mAP is provided with SGD, while 0.856 mAP is provided with Adam. Therefore, it was decided to conduct model training and testing with Adam optimization, which provided advantages in terms of both speed and accuracy criteria. The confusion matrix acquired after the training with the prepared dataset is as in Figure 5.

The training set includes 482 gliomas and 654 meningioma tumors. The validation set includes 120 gliomas and 164 meningiomas. Precision and recall curves obtained as a result of applying these images with the suggested method are as in Figure 6. Precision is obtained by dividing the number of objects found as True Positive (TP) by the sum of the number of TP and FP objects. The precision of all classes is 0.885. Recall TP is obtained by dividing the samples by the sum of the TP and FN samples [38]. The confusion matrix in Figure 5 shows that the FN value is 0. There is no object as FN in the dataset. Therefore, the recall metric was obtained as 1.

The mAP is often used to measure the performance of object detection problems. The Precision-Recall curve of the model is demonstrated in Figure 7. The AP value of the glioma class is 0.786, and the AP value of the meningioma class is 0.926. The mAP value of the two classes is provided as 0.856.

Studies done in the literature are given in section 2. Information about some of these studies is also given in Table 2 as a comparison table.

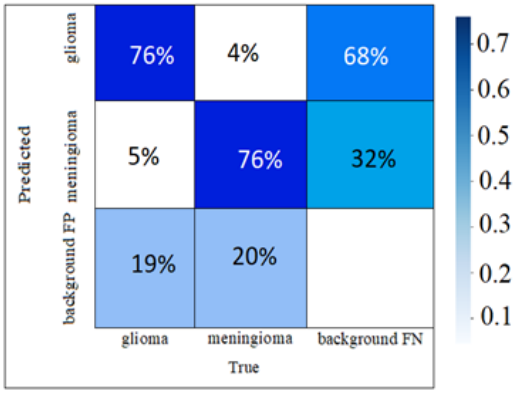

Figure 5 Confusion matrix of the model

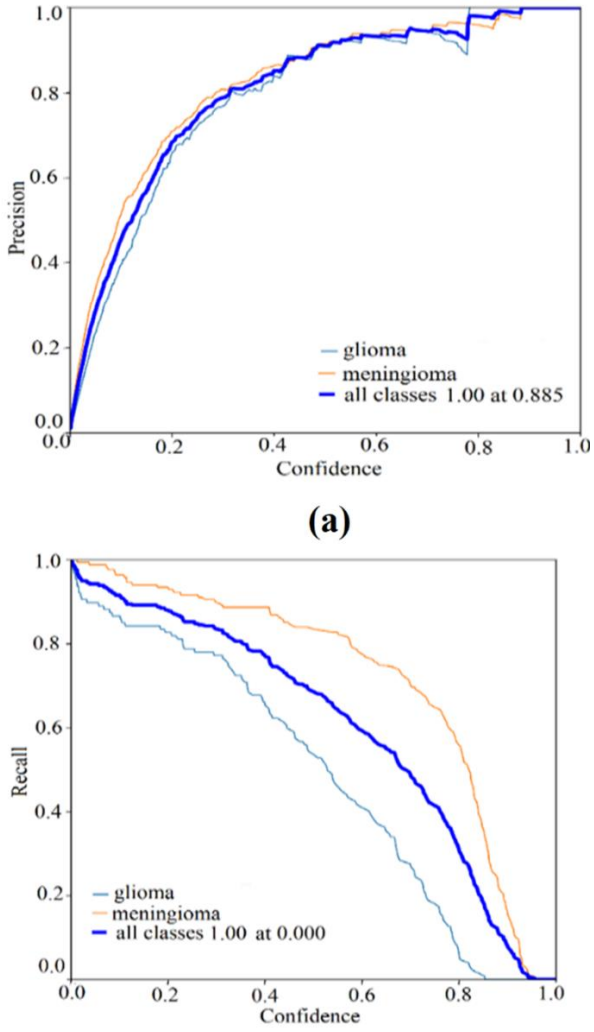

Figure 6 (a) Precision and, (b) recall curve of the model

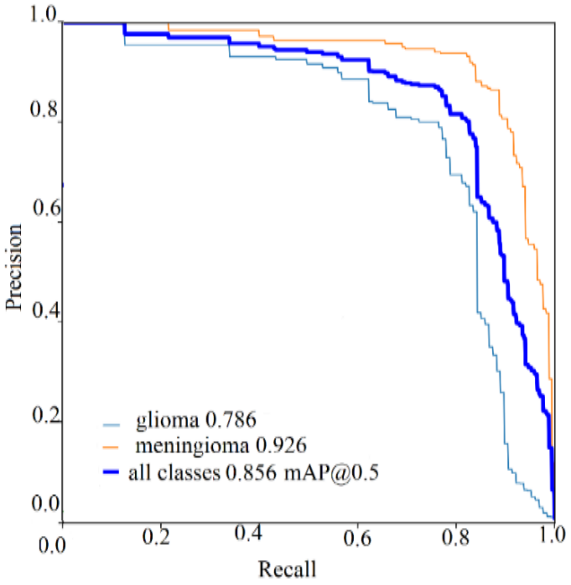

Figure 7 Precision-Recall curve of the model

The test process was carried out with the best-weighted model obtained as a result of the training. A total of 215 images are used. Some of the results obtained as a result of the test are as in Figure 8.

Table 2 Studies on classification, segmentation and detection of brain tumor

Ref No./ Year	**Dataset**	**Method**	**Performance metrics**	**Classes/Task**
[9]/2021	2556 images	Hybrid Ensemble Model	97.305 % Acc.	Benign, Malignant/ Classification
[10]/2023	250 MR images	DBNQLBC	70.83 % Specificity 94% Acc.	Normal, Abnormal/ Classification
[11[/2021	Two public datasets	RCNN & Two channel CNN	98.83 average confidence	Meningioma, Glioma, Pituitory/ Classification and detection
[12]/2021	Brain MRI Dataset	Adaboost Random Forest	95 % Acc. 89 % Sensitivity	Meningioma, Glioma, No tumor/ Classification
[14]/2022	Brain Tumor Detection MRI	Autoencoder+ DWT	97% Acc.	No, Yes/ Classification
[15]/2023	3064 MR Images	SMP-SGD	96% Acc.	Meningioma, Glioma, Pituitory/ Classification
[16]/2022	3680 MR Images	K means FCM	80% Acc. 80% Acc.	Meningioma, Glioma, Pituitory/ Classification
[17]/2022	150 MRI brain images	GLCM+BWT+CNN	98.5 % acc.	Normal, Abnormal/Classification
[18]/2021	BRATS dataset	DCNNA	95 % Acc.	Glioma tumor/ Segmentation
[19]/2021	MR Image Dataset	KPCA+ KSVM	90% Acc.	Normal, Benign, Malignant/ Segmentation
[20]/2020	100 MRI brain images	saliency computational modeling	0.8255 Precision 0.8206 Recall 0.8244 F-Measure	Brain tumor/ Segmentation
[21]/2021	40 MR images	PCA &TK-means	95% Acc.	Brain tumor/ Segmentation
Proposed model	**Brain tumor detection dataset**	**EfficientNet& PANet& YOLO**	**0.885 Precision, 1.0 Recall 0.856 mAP**	**Glioma, Meningioma/ Detection**

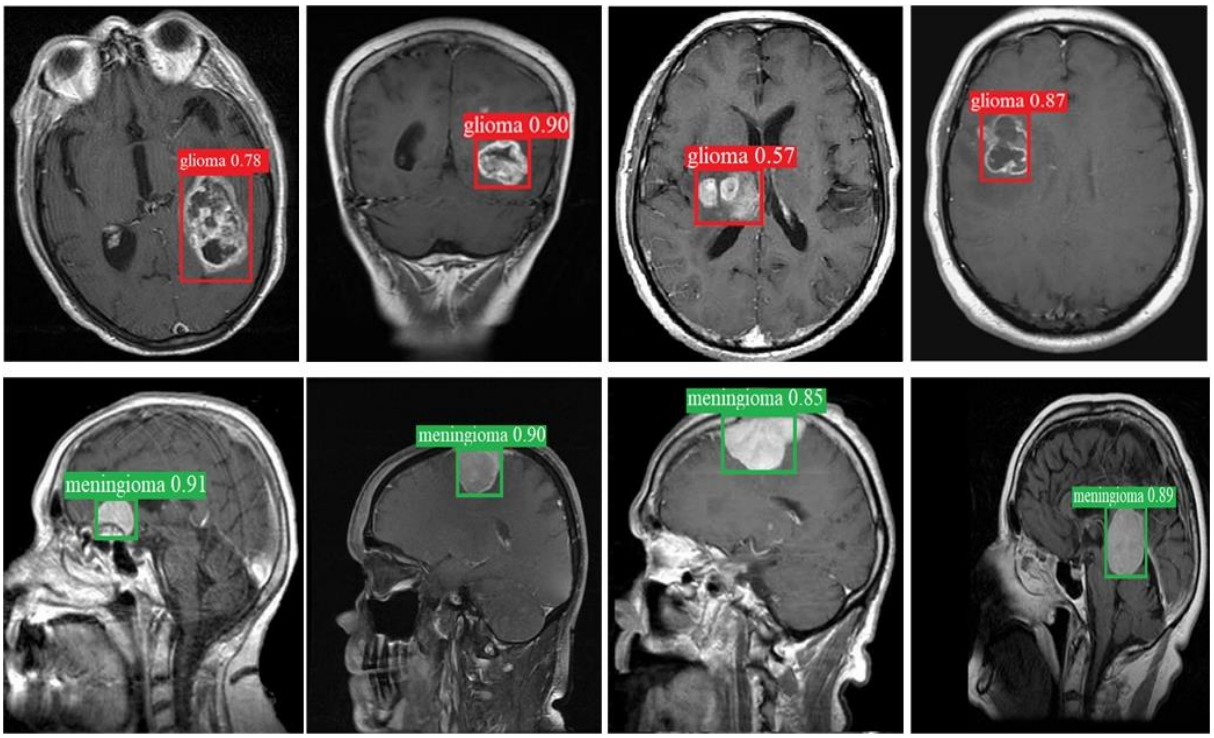

Figure 8 Samples of test results

5. DISCUSSIONS

The glioma and meningioma classes in our study can be differentiated from each other by some imaging findings in MRI. These tumors can be benign or malignant. Gliomas can be malignant more often, while meningiomas are more often benign. Gliomas are intra-axial tumors as they arise from the parenchymal cells of the brain. On MRI, especially malignant gliomas are more heterogeneous, irregularly circumscribed, and peripherally enhanced. There is edema around it [39]. Meningiomas, on the other hand, are extra-axial tumors because they arise from the membranes surrounding the brain. Therefore, they are meninges-based, more homogeneous, and well-circumscribed tumors on MRI. There is usually no edema around them [40].

However, there may be differences in imaging findings of some atypical tumors or variants. Therefore, they may not always be easily distinguished radiological and may be confused with each other.
Some images that the proposed method finds incorrect are given in Figure 9. In the axial contrast-enhanced MR image in Figure 9 (a), the localization of the glioma-class lesion in the left posterior parietal was correctly determined by our model. However, the type of the lesion was determined as meningioma and mistyped. Since the lesion is based on interhemispheric fissure, we think that our model included it in the class of meningioma, thinking that the lesion originates from the membranes surrounding the brain. In Figure 9 (b), the localization of the left frontal glioma-class lesion in the axial contrast-enhanced MR image was correctly determined by our model. However, the type of lesion was mistyped as meningioma. We think that our model included it in the class of meningioma because the lesion is located in the periphery of the cerebral hemisphere, there is no edema around it, and it is more homogeneous and well-circumscribed.

In the axial contrast-enhanced MR image in Figure 9 (c), the type of meningioma extending from the lobe to the orbit in the right temporal lobe was correctly determined by our model. However, the lesion is partially localized. We think that the inability to localize the part of the lesion extending to the orbit may be due to the complex anatomy of this region. In the coronal contrast-enhanced MR image in Figure 8(d), the localization of the glioma class lesion crossing the midline frontally from right to left was correctly determined by our model. However, the type of lesion was misclassified as meningioma. We think that since the lesion is of relatively homogeneous intensity and closer to the midline, it was misclassified as an extra-axial lesion.

6. CONCLUSIONS

Brain tumors constitute a significant portion of cancer-related deaths. Brain MRI images constitute a significant part of the daily workload of medical imaging. Knowing the location of brain tumors as well as the type is important in determining the treatment of patients. Therefore, the need to use artificial intelligence methods to determine the type and localization of brain tumors is increasing.

In our study, two common types of brain tumors were detected using the method consisting of EfficientNet architecture, PANet architecture, and YOLO algorithm. The resulting values showed that the method would be useful for detecting brain tumors.

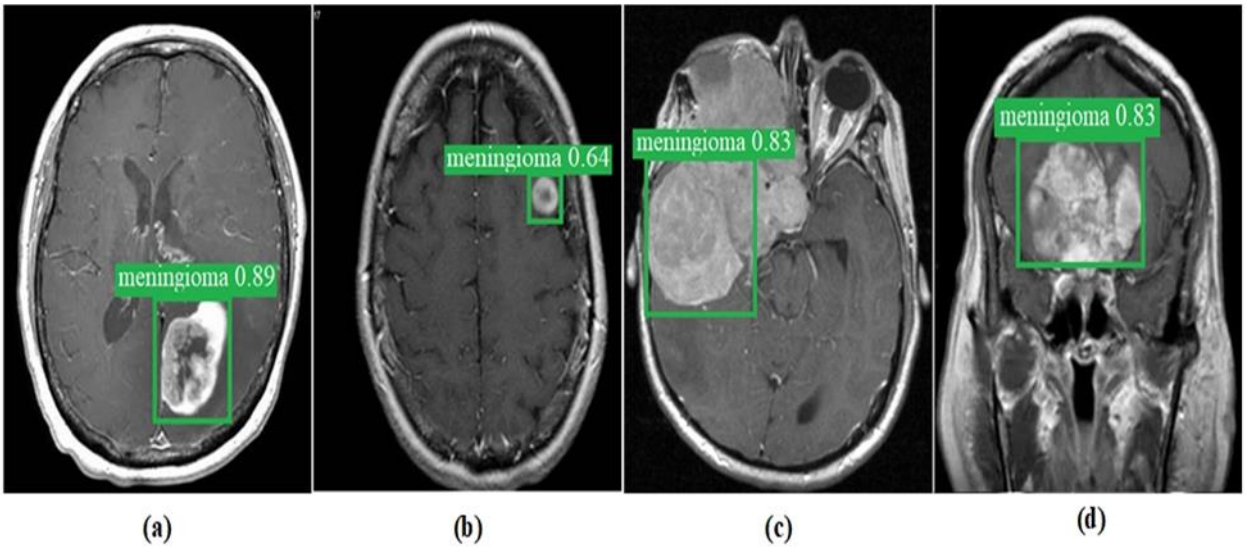

Figure 9 Some images found wrong by the proposed method

Acknowledgments
Dataset link created by authors: https://github.com/ecengil/Brain-tumor-detection-dataset.

Funding
The authors has no received any financial support for the research, authorship or publication of this study.

The Declaration of Conflict of Interest/ Common Interest
No conflict of interest or common interest has been declared by the authors.

Authors' Contribution
The first author contributed 40%, the second author 20%, the third author 20% and, the fourth author 20%."

The Declaration of Ethics Committee Approval
This study does not require ethics committee permission or any special permission

The Declaration of Research and Publication Ethics
"The authors of the paper declare that they comply with the scientific, ethical and quotation rules of SAUJS in all processes of the paper and that they do not make any falsification on the data collected. In addition, they declare that Sakarya University Journal of Science and its editorial board have no responsibility for any ethical violations that may be encountered, and that this study has not been evaluated in any academic publication environment other than Sakarya University Journal of Science."

REFERENCES

[1] J. M. Hempel, C. Brendle, B. Bender, G. Bier, M. Skardelly, I. Gepfner-Tuma, J. Schittenhelm, "Contrast enhancement predicting survival in integrated molecular subtypes of diffuse glioma: an observational cohort study," Journal of neuro-oncology, vol. 139, no.2, pp. 373-381, 2018.

[2] J. Howard, Central Nervous System Tumors. Neurology Video Textbook DVD, C., Demos and Medical.

[3] T. Ong, A. Bharatha, R. Alsufayan, S. Das, A. W. Lin, "MRI predictors for brain invasion in meningiomas," The Neuroradiology Journal, vol. 34, no.1, pp.3-7, 2021.

[4] B. Garzín, K. E. Emblem, K. Mouridsen, B. Nedregaard, P. Due-Tønnessen, T. Nome, J. K. Hald, A. Bjørnerud, A. K. Håberg, Y. Kvinnsland, "Multiparametric analysis of magnetic resonance images for glioma grading and patient survival time prediction," Acta radiologica, vol. 52 no. 9, pp. 1052-1060, 2011.

[5] C. J. Belden, P. A. Valdes, C. Ran, d. A. Pastel, B. T. Harris, C. E. Fadul, M. A. Israel, K. Paulsen, D. W. Roberts, "Genetics of glioblastoma: a window into its imaging and histopathologic variability," Radiographics, vol. 31, no. 6, pp.1717-1740, 2011.

[6] M. A. Baig, J. P. Klein, L. L. Mechtler, "Imaging of brain tumors," CONTINUUM: Lifelong Learning in Neurology, vol. 22, no. 5, pp. 1529-1552, 2016.

[7] M. C. Mabray, R. F. Barajas, S. Cha, "Modern brain tumor imaging," Brain tumor research and treatment, vol. 3, no. 1, pp. 8-23, 2015.

[8] E. Cengil, Brain tumor detection dataset [online], Available: https://github.com/ecengil/Brain-tumor-detection-dataset.

[9] G. Garg, R. Garg, "Brain Tumor Detection and Classification based on Hybrid Ensemble Classifier." arXiv preprint arXiv:2101.00216, 2021.

[10] V. V. Kumar, P. G. K. Prince, "Deep belief network Assisted quadratic logit boost classifier for brain tumor detection using MR images." Biomedical Signal Processing and Control, *81*, 104415, 2023.

[11] N. Kesav, M. Jibukumar, "Efficient and low complex architecture for detection and classification of Brain Tumor using RCNN with Two Channel CNN." Journal of King Saud University-Computer and Information Sciences, *vol.* 34, no. 8, pp. 6229-6242, 2021.

[12] M. F. Khan, P. Khatri, S. Lenka, D. Anuhya, A. Sanyal. "Detection of Brain Tumor from the MRI Images using Deep Hybrid Boosted based on Ensemble Techniques," in 2022 3rd International Conference on Smart Electronics and Communication (ICOSEC) , 2022, pp. 1464-1467.

[13] D. Rammurthy, P. Mahesh, "Whale Harris Hawks optimization based deep learning classifier for brain tumor detection using MRI images," Journal of King Saud University-Computer and Information Sciences, vol. 34, no. 6, pp. 3259-3272, 2020.

[14] D. R. Nayak, N. Padhy, P. K. Mallick, A. Singh, "A deep autoencoder approach for detection of brain tumor images," Computers and Electrical Engineering, 102, 108238, 2022.

[15] Q. Chuandong, L. Baosheng, H. Baole, "Fast brain tumor detection using adaptive stochastic gradient descent on shared-memory parallel environment," Engineering Applications of Artificial Intelligence, 120, 105816, 2023.

[16] S. Sangeeta, H. Nagendra. "Brain Tumor Detection and Classification Using Clustering and Comparison with FCM, " in 2022 International Conference on Innovative Computing, Intelligent Communication and Smart Electrical Systems (ICSES), pp. 1-6, 2022.

[17] M. Arif, F. Ajesh, S. Shamsudheen, O. Geman, D. Izdrui, D. Vicoveanu, "Brain tumor detection and classification by

MRI using biologically inspired orthogonal wavelet transform and deep learning techniques." Journal of Healthcare Engineering, 2022.

[18] G. Ramkumar, R. T. Prabu, N. P. Singh, U. Maheswaran, "WITHDRAWN: Experimental analysis of brain tumor detection system using Machine learning approach." Materials Today: Proceedings, 2021.

[19] V. Sabitha, J. Nayak, P. R. Reddy, "MRI brain tumor detection and classification using KPCA and KSVM." Materials Today: Proceedings, 2021.

[20] M. Jian, X. Zhang, L. Ma, H. Yu, "Tumor detection in MRI brain images based on saliency computational modeling." IFAC-PapersOnLine, vol. 53, no. 5, pp. 43-46, 2020.

[21] M. K. Islam, M. S. Ali, M. S. Miah, M. M. Rahman, M.S Alam, M. A. Hossain, "Brain tumor detection in MR image using superpixels, principal component analysis and template based K-means clustering algorithm." Machine Learning with Applications, 5, 100044, 2021.

[22] SartajBhuvaji, Available: https://github.com/SartajBhuvaji/Brain-Tumor-Classification-DataSet/tree/master/Training.

[23] tzutalin. labelImg. (2021). Available: https://github.com/tzutalin/labelImg.

[24] F. Keller, "Computational Foundations of Cognitive Science." Reading, 2: 2, 2010.

[25] E. Cengil, A. Çınar, "A new approach for image classification: convolutional neural network." European Journal of Technique (EJT), vol. 6, no. 2, pp. 96-103, 2016.

[26] A. D. Jagtap, K. Kawaguchi, G. E. Karniadakis, "Adaptive activation functions accelerate convergence in deep and physics-informed neural networks. "Journal of Computational Physics 404 : 109136, 2020.

[27] E. Zisselman, A. Adler, M. Elad, "Compressed learning for image classification: A deep neural network approach." In Handbook of Numerical Analysis, Elsevier. Vol. 19, pp. 3-17, 2018.

[28] A. Krizhevsky, I. Sutskever, G.E. Hinton, "Imagenet classification with deep convolutional neural networks." Communications of the ACM, vol. 60, no.6, pp. 84-90, 2017.

[29] K. Simonyan, A. Zisserman, "Very deep convolutional networks for large-scale image recognition." arXiv preprint arXiv:1409.1556, 2014.

[30] H. Kaiming, X. Zhang, S. Ren, J. Sun, "Deep residual learning for image recognition." İn Proceedings of the IEEE conference on computer vision and pattern recognition, pp. 770-778, 2016.

[31] M. Tan, Q. Le, "Efficientnet: Rethinking model scaling for convolutional neural networks." in international Conference on Machine Learning, PMLR, 2019.

[32] G. Marques, D. Agarwal, I. de la Torre Díez, "Automated medical diagnosis of COVID-19 through Efficient Net convolutional neural network." Applied soft computing, 96, 106691, 2020.

[33] J. Wang, Q. Liu, H. Xie, Z.Yang, H. Zhou, "Boosted efficientnet: Detection of lymph node metastases in breast cancer using convolutional neural networks." Cancers, vol. 13, no. 4, pp. 661, 2021.

[34] N. K. Chowdhury, M. A. Kabir, M. Rahman, N. Rezoana, "Ecovnet: An ensemble of deep convolutional neural networks based on efficientnet to detect covid-19 from chest x-rays." arXiv preprint arXiv:2009.11850, 2020.

[35] K. Wang, J. H. Liew, Y. Zou, D. Zhou, J. Feng, "Panet: Few-shot image semantic segmentation with prototype alignment." In proceedings of the IEEE/CVF international conference on computer vision, pp. 9197-9206, 2019.

[36] J. Redmon, A. Farhadi, "Yolov3: An incremental improvement." arXiv preprint arXiv:1804.02767, 2018.

[37] A. Bochkovskiy, C. Y. Wang, and H. Y. M. Liao, "Yolov4: Optimal speed and accuracy of object detection." arXiv preprint arXiv:2004.10934, 2020.

[38] E. Cengil, A. Çınar, "Poisonous Mushroom Detection using YOLOV5." Turkish Journal of Science and Technology, vol. 6, no. 1, pp. 119-127, 2021.

[39] C. H. Suh, H. S. Kim, S. C. Jung, C. G. Choi, S. J. Kim, "Clinically Relevant Imaging Features for MGMT Promoter Methylation in Multiple Glioblastoma Studies: A Systematic Review and Meta-Analysis." American Journal of Neuroradiology, vol 39, no. 8: 1439, 2018

[40] B. Tamrazi, M. S. Shiroishi, C. S. Liu, "Advanced Imaging of Intracranial Meningiomas." Neurosurgery clinics of North America, vol. 27, no. 2, pp. 137-43, 2016.

SAKARYA ÜNİVERSİTESİ
FEN BİLİMLERİ ENSTİTÜSÜ DERGİSİ

Sakarya University Journal of Science
SAUJS

ISSN 1301-4048 e-ISSN 2147-835X Period Bimonthly Founded 1997 Publisher Sakarya University
http://www.saujs.sakarya.edu.tr/

Title: Lateral Buckling of Glare for Aerospace Application

Authors: Burak ŞAHİN, Eyüp YETER

Recieved: 2022-08-10 00:00:00

Accepted: 2023-03-04 00:00:00

Article Type: Research Article

Volume: 27
Issue: 3
Month: June
Year: 2023
Pages: 564-571

How to cite
Burak ŞAHİN, Eyüp YETER; (2023), Lateral Buckling of Glare for Aerospace Application . Sakarya University Journal of Science, 27(3), 564-571, DOI: 10.16984/saufenbilder.1160160
Access link
https://dergipark.org.tr/en/pub/saufenbilder/issue/78131/1160160

Sakarya University Journal of Science 27(3), 564-571, 2023

Lateral Buckling of Glare for Aerospace Application

Burak ŞAHİN *[1], Eyüp YETER[1]

Abstract

Glare (Glass Reinforced Aluminium) which consists of fibre metal laminate composite consisting of aluminium and glass is used aerospace structures are supposed to buckling and impact loads. Lateral buckling analyses were made to determine critical buckling loads, and results were compared to Al 2024-T3 in this paper. Weight and load carrying capacity of Glare grades were taken into consideration and the importance of weight to critical load was stated. Numerical works were carried out by starting with Glass and Aluminum then continued for Glare Grades of Glare 2A, Glare 2B, Glare 3A, Glare 3B, Glare 4A, Glare 4B, Glare 5A, Glare 5B, Glare 6A and Glare 6B to estimate buckling load values. Several comparisons were presented for Glare grades based on Al 2024-T3 through paper. Glare 2A, 2B, 3A, 3B, 6A and 6B Grades have lower weight and buckling load values compared to Al 2024-T3. Lower weight is essential for aerospace applications. But optimum weight and load carrying capacity can be selected for intended applications by taking weight and load into consideration at same time. Although Glare grades of 4A 2-1, 4B 2-1, 5A 2-1 and 5B 2-1 having closer weight (17.60g, 17.60g, 19.13g and 19.13g respectively) to Al 2024-T3 (17.31g), higher buckling loads were determined for Glare grades numerically. The best choice for Glare as an alternative to Al 2024-T3 under lateral buckling loading can be decided for point of views of less weight to critical load ratio.

Keywords: Glare, lateral buckling, load carrying capacity, aerospace applications

1. INTRODUCTION

As it is well known, mechanical components fail by material failure and structural instability. The second one is also called as buckling. Machine elements and mechanical components can buckle under compressive loads.

Lateral buckling occurs because of bending on beams. Translational and rotational movement of beam section due to deformation are defined as lateral bucking.

Fibre metal laminates (FMLs) were developed as a hybrid material owing to need of light weight and high-performance structure [1]. In industries of aerospace and construction, fibre-reinforced composites have been extensively used in recent years (Figure 1).

Banat et al investigated thin-walled members of seven layers Glare which are supposed to axial compression. FML are hybrid composites consisting of alternating thin

* Corresponding author: buraksahin@gantep.edu.tr (B. SAHIN)
[1] Gaziantep University
E-mail: eyeter@gantep.edu.tr
ORCID: https://orcid.org/0000-0002-8666-4902, https://orcid.org/0000-0002-0278-588X

aluminium sheet layers and fibre-reinforced epoxy prepreg of glass fibres [2].

Glare (Glass Reinforced Aluminium) is a fibre metal laminate composite consisting of aluminium and glass (Figure 2).

Figure 1. Glare deployment in the Airbus A380 [1]

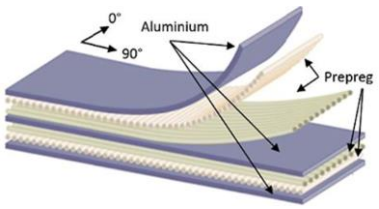

Figure 2. Lay-up Configuration of 7-layered Composite [2]

Aerospace structures are supposed to hail, bird strike, collision of service car, cargo or structure and maintenance damage owing to dropped tools so they require good impact properties [3].

Because of its superior damage tolerance properties, Glare is widely used for aerospace structures which are exposed to impact damages.

Airbus A-380 is very well-known example for Glare usage in aircrafts (Figure 1). Glare is used in the main fuselage skin and the leading edges of the horizontal and vertical tail planes of Airbus A380 [4].

Glare has superior properties of excellent impact characteristics and flame-resistant capability. So it is used for fire walls and cargo-liners. In addition, cockpit crown, forward bulkheads and leading edge are usage areas of Glare [4].

Glare provides 10% reduction in weight compared to monolithic aluminium. It has advantages over carbon fibre reinforced polymers owing to improved impact, fire and corrosion resistance, and increased damage tolerance. It takes place for application of the Airbus A380 fuselage, the Learjet 45, floor panels for the Boeing 737 and the cargo doors of the Boeing C-17 Globemaster III [5].

Glare has main advantages of low weight, longer fatigue life, low weight, high impact resistance and corrosion resistance. Glare structure has improved strength and stiffness over traditional materials on a unit weight.

Mania and York searched the thin-walled fibre metal laminates' buckling behaviour and load carrying capacity under axial load in compression analytically and experimentally [6].

Banat and Mania conducted a numerical and experimental study to determine stability of open cross section top hat and Z shaped sections under axial compression load [7].

Eglitis et al conducted numerical and experimental works on the buckling of composite cylinders under concentric and eccentric compressive loads [8].

Bikasis et al studied on the elastic buckling of Glare under different support types exposed to shear stress by finite element and eigenvalue buckling analysis [9].

Muddappa et al made an investigation for the Glare with different thickness and boundary conditions under various loading and stress distribution by applying dynamic approach to determine buckling behavior [10].

Banat et al investigated buckling behaviour of thin-walled fibre metal laminate profiles for various composite arrangements and Z-shaped and channel shaped geometries by finite element method and experimentally [11].

Wu and Yang investigated mechanical behaviour of fibre reinforced metal laminates, especially Glare for aerospace structures under tensile and compressive loadings. They stated that the importance of Glare for aerospace applications such as Airbus A380 with wings leading edge and tails [3].

The high demand on weight reduction and high level of damage tolerance necessitates fibre metal laminates. From this point of view, Glare is a unique material for applications of aerospace industry especially for fuselage skin structures for new aircrafts [12].

Erklig et al investigated the impacts of triangular, circular, square, rectangular and elliptical cutouts on the lateral buckling behaviour of composite beams experimentally [13].

Erklig and Yeter studied the effects of cutouts on buckling behaviour of polymer matrix composites numerically for different boundary conditions [14].

Yeter et al investigated the effect of hybridization on lateral buckling behavior of composite beams with different ply orientations, different cutouts and length/thickness ratio [15].

Erklig and Yeter studied the effects of circular, triangular, elliptical and square cutouts on composite plates buckling behaviour by conducting finite element analyses [16].

In consideration of literature works, there is obviously good reason to investigate the buckling behaviour of Glare grades because of superior properties and its usage in aerospace industry.

Structural elements such as ribs and spars of aircraft wings are exposed to lateral buckling loads during their service life [1].

Due to these reasons, this paper is primarily intended for lateral buckling analysis of Glare.

2. BUCKLING ANALYSIS

Finite element analyses were conducted to determine critical buckling loads for different Glare grades which have different combinations of glass fibres and thin layer sheets of Al 2024-T3 in different thickness values (Table 1). These combinations directly affect weight (Table 1) and load bearing capacity (Table 2) of Glare.

Before starting lateral buckling analysis, critical buckling load values of Al 2024-T3 under axial load were determined for fixed-free, fixed-fixed, fixed-pin and pin-pin theoretically and by finite element analyses. Results are presented in Table 3.

Boundary and loading conditions for fixed-free and fixed-pin are given in Figure 3, 4, 5 and 6 respectively. Axial buckling load values which were determined theoretically and by finite element method are very close to each other for different constraints. The smallest difference is 1.69% for pin-pin whereas the biggest one is 6.56% for fix-fix situation.

After completing axial buckling load determination, lateral buckling analysis of Glare 2A, Glare 2B, Glare 3A, Glare 3B, Glare 4A, Glare 4B, Glare 5A, Glare 5B, Glare 6A, Glare 6B and Al 2024-T3 have been carried out to determine the critical load values for buckling under specific boundary and loading conditions (Figure 7-8) for width of 50 mm and length of 100 mm (overall thickness values are presented in Table 1).

One end of beam was fixed and load was applied at the other end to make buckling analysis. Finite element analyses were conducted to determine buckling loads for Al 2024-T3, glass and Glare grades (Table 2).

Table 1. Material Thickness and Weight Values

Material	Thickness (mm)	Weight (g)
Al 2024-T3	1.250	17.31
Glare 2A	1.250	16.08
Glare 2B	1.250	16.08
Glare 3A	1.250	16.08
Glare 3B	1.250	16.08
Glare 6A	1.250	16.08
Glare 6B	1.250	16.08
Glass (0°)	1.250	15.25
Glass (0° 90°)	1.250	15.25
Glass (90° 0°)	1.250	15.25
Glass (90°)	1.250	15.25
Glare 4A 2-1	1.375	17.60
Glare 4A 3-2	2.250	28.27
Glare 4A 4-3	3.125	38.95
Glare 4B 2-1	1.375	17.60
Glare 4B 3-2	2.250	28.27
Glare 4B 4-3	3.125	38.95
Glare 5A 2-1	1.500	19.13
Glare 5A 3-2	2.500	31.33
Glare 5A 4-3	3.500	43.53
Glare 5B 2-1	1.500	19.13
Glare 5B 3-2	2.500	31.33
Glare 5B 4-3	3.500	43.53

Table 2 Lateral Buckling Load Values

Material	Buckling Load (N)
Al 2024-T3	265.59
Glare 2A	261.4
Glare 2B	260.3
Glare 3A	260.81
Glare 3B	260.81
Glare 6A	261.1
Glare 6B	261.09
Glass (0°)	68.165
Glass (0° 90°)	60.859
Glass (90° 0°)	60.861
Glass (90°)	38.704
Glare 4A 2-1	342.55
Glare 4A 3-2	1320
Glare 4A 4-3	3253.5
Glare 4B 2-1	341.02
Glare 4B 3-2	1302.6
Glare 4B 4-3	3195
Glare 5A 2-1	436.54
Glare 5A 3-2	1711
Glare 5A 4-3	4229.3
Glare 5B 2-1	434.5
Glare 5B 3-2	1707.4
Glare 5B 4-3	4224.6

Table 3. Critical Buckling Load Values of Al 2024-T3 under axial load for different boundary conditions

	Numerical (N)	Theoretical (N)	Diff. %
pin-pin	587.1	597.2	1.69
fix-free	146.8	153.1	4.14
fix-pin	1198.2	1251.9	4.29
fix-fix	2348.5	2513.3	6.56

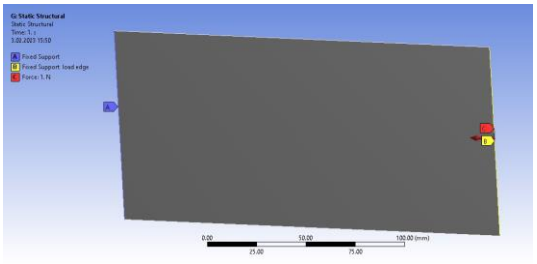

Figure 3. Boundary and Loading Conditions for Axial Buckling (fixed- fixed)

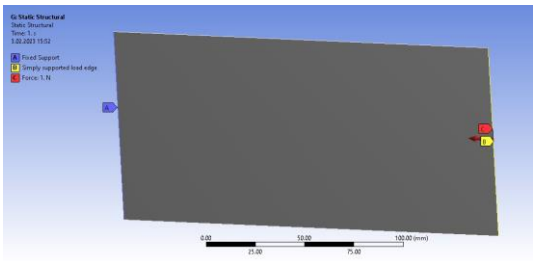

Figure 4. Boundary and Loading Conditions for Axial Buckling (fixed-pin)

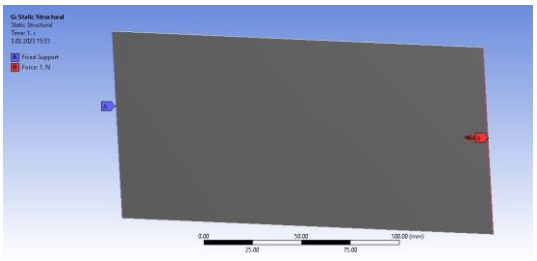

Figure 5. Boundary and Loading Conditions for Axial Buckling (fixed-free)

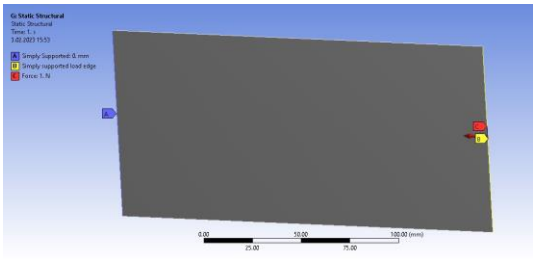

Figure 6. Boundary and Loading Conditions for Axial Buckling (pin-pin)

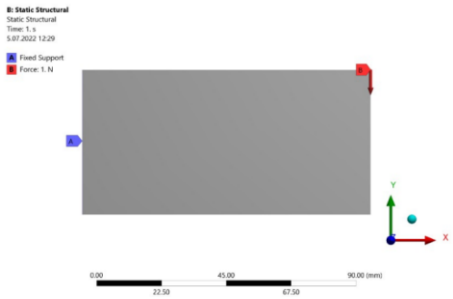

Figure 7. Boundary and Loading Conditions-1

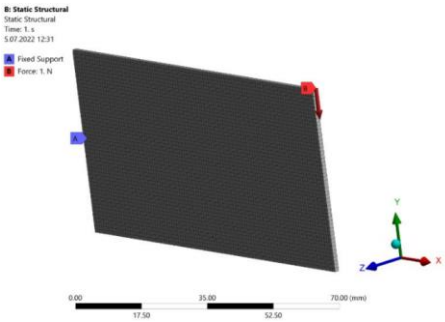

Figure 8. Boundary and Loading Conditions-2

3. RESULTS AND DISCUSSION

As expected, glass with different orientation (0°, 90°, 0°90° and 90°0°) has the lowest values of weight and critical buckling load compared to Al 2024-T3 and Glare. Glare 2A, 2B, 3A and 3B have greater weight in comparison with glass.

Weight is very significant for many applications especially for aerospace industry.
In addition, critical buckling load play a vital role for wings and fuselage. Therefore, critical buckling load must be taken into consideration. Although increase of 0.83 gram (5.44%) for selected specimen dimensions was obtained for Glare 2A, 2B, 3A and 3B compared to glass (Table 1), allowable buckling load increased four times more (Table 2).

This comparison is valuable but not enough because of rare usage of glass in mechanical systems which are subjected to different loading types such as tension, compression, shear, bending and combination of them. Comparison of change in weight and buckling load of Glare grades with Al 2024-T3 gives exact information.

Glare 2A, 2B, 3A and 3B have lower weight (7.65%) compared to Aluminum alloy for same specimen sizes (Table 1). Additionally, there is a drop in buckling load compared to Al (Table 2). Glare 2A, 2B, 3A and 3B have almost 2% lower buckling load than Al.

Weight and buckling load and values of Glare grades of 4A, 4B, 5A and 5B increase by depending on thickness increase (Table 1, 2 and Figure 9-16).

Though Glare 4A 2-1 and 4B 2-1 have almost same weight (17.60 gr) with Aluminum (17.31 gr), buckling load values of these glare grades are higher than that of Al 2024-T3.

Glare 4A/4B 3-2 and 4A/4B 4-3 have 28.27g and 38.95g weight values respectively (higher than Al) (Figure 10 and 12). Buckling loads of 4A 3-2, 4B 3-2, 4A 4-3 and 4B 4-3 are 1320, 3253.5, 1302.6, 3195N by turns (Figure 9 and 11).

Glare 4A 3-2 and 4B 3-2 have almost 39% more weight while corresponding increase in buckling load is almost 80% compared to Al (Figure 10-12). When similar comparison is made for Glare 4A 4-3, 4B 4-3 and Al 2024-T3, it is seen that weight and buckling load increase are 55% and over 90% respectively based on values of Al 2024-T3. Glare 5 grades have higher weight and buckling load values (Figure 13, 14, 15 and 16) compared to reference values (values of Al 2024-T3).

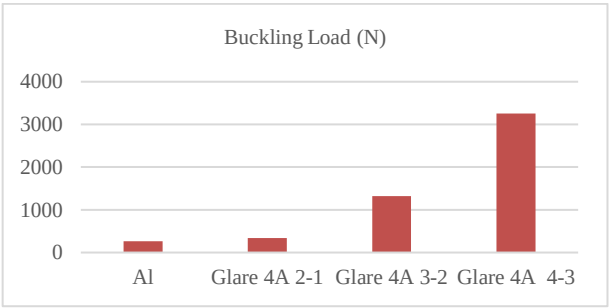

Figure 9. Buckling Load of Glare 4A Grades and Al 2024-T3

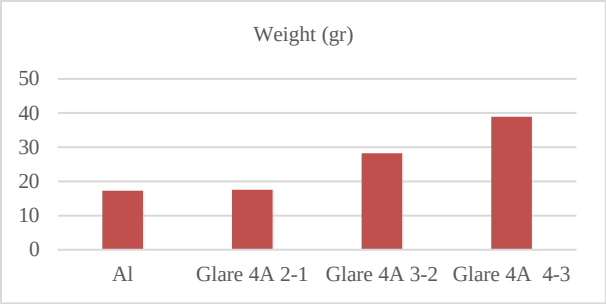

Figure 10. Weight of Glare 4A Grades and Al 2024-T3

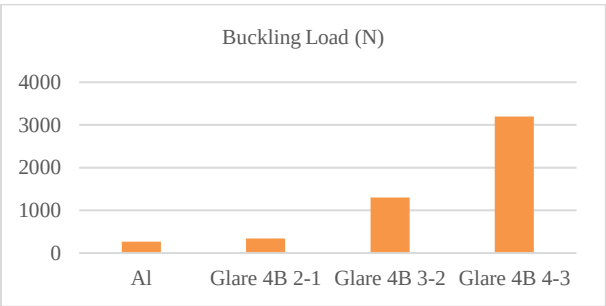

Figure 11. Buckling Load of Glare 4B Grades and Al 2024-T3

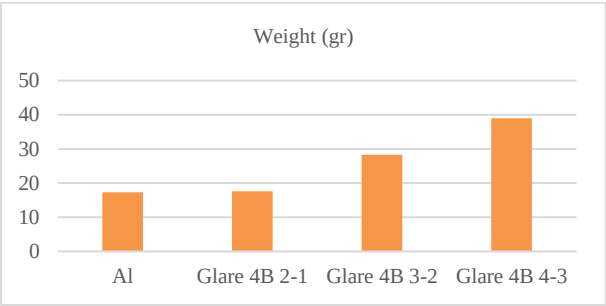

Figure 12. Weight of Glare 4B Grades and Al 2024-T3

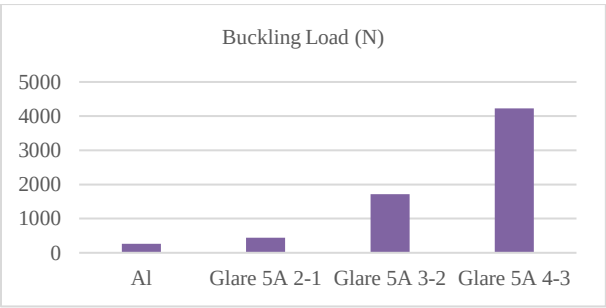

Figure 13. Buckling Load of Glare 5A Grades and Al 2024-T3

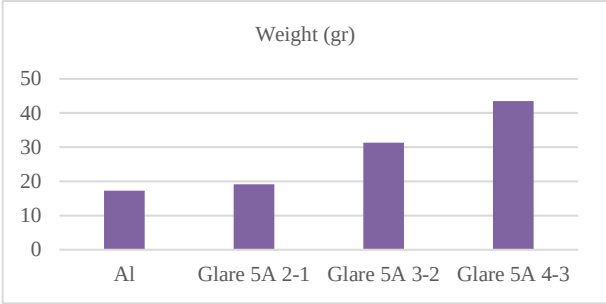

Figure 14. Weight of Glare 5A Grades and Al 2024-T3

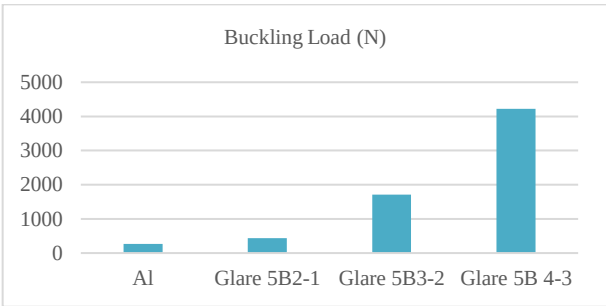

Figure 15. Buckling Load of Glare 5B Grades and Al 2024-T3

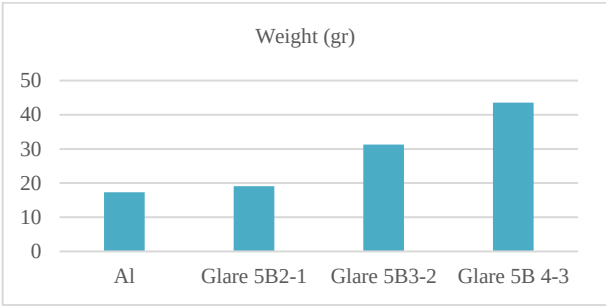

Figure 16. Weight of Glare 5B Grades and Al 2024-T3

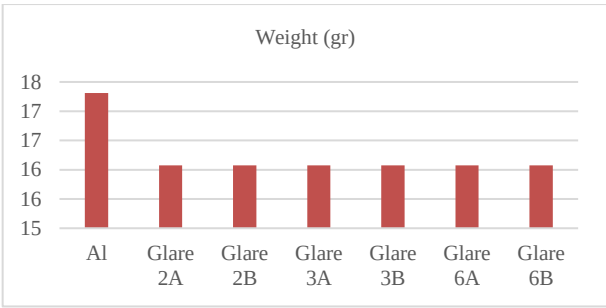

Figure 17. Weight of Glare 2A, 2B, 3A, 3B, 6A, 6B Grades and Al 2024-T3

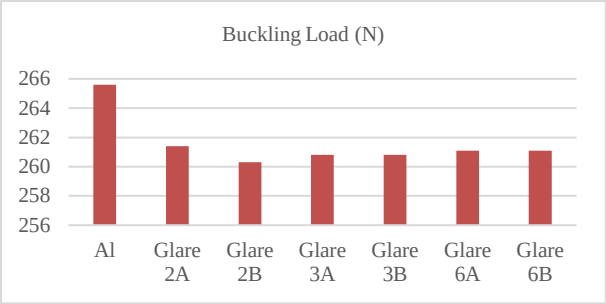

Figure 18. Buckling Load of Glare 2A, 2B, 3A, 3B, 6A, 6B Grades and Al 2024-T3

4. CONCLUSION

As it is known, increasing thickness of material yields in higher critical buckling load. This situation is intended for structures such as wings and fuselage which are exposed to lateral buckling. Conversely, weight increase is undesirable because lightness is very essential for aerospace structures.

Several comparisons were carried out for Glare grades based on Al 2024-T3 above sections of this paper. Glare 2A, 2B, 3A, 3B, 6A and 6B Grades have lower weight compared to Al 2024-T3 (Figure 17). Lower weight is essential for many applications especially aerospace ones. On the other hand, load carrying capacity must be at required level. Critical buckling load values of mentioned grades are lower than Al 2024-T3 (Figure 18). Optimum weight and load carrying capacity can be selected for intended applications by taking weight and load into consideration.

One more comparison of lateral buckling load can be performed here based on Glare grades of 4A 2-1, 4B 2-1, 5A 2-1 and 5B 2-1 having closer weight (17.60g, 17.60g, 19.13g and 19.13g respectively) to Al 2024-T3 (17.31g). Whereas these Glare grades have closer weight values to Al 2024-T3, higher buckling loads are determined for Glare grades numerically.

The best choice for Glare as an alternative to Al 2024-T3 under lateral buckling loading can be decided for point of views of less weight to critical load ratio.

Experimental works are intended for axial and lateral buckling load determination of Glare with different grades and fiber metal laminates (FMLs) as a future work.

The Declaration of Conflict of Interest/ Common Interest

No conflict of interest or common interest has been declared by the author.

The Declaration of Ethics Committee Approval

The author declares that this document does not require an ethics committee approval or any special permission.

The Declaration of Research and Publication Ethics

The author of the paper declares that he complies with the scientific, ethical, and quotation rules of SAUJS in all processes of the paper and that he does not make any falsification on the data collected. In addition, he declares that Sakarya University Journal of Science and its editorial board have no responsibility for any ethical violations that may be encountered and that this study has not been evaluated in any academic publication environment other than Sakarya University Journal of Science.

REFERENCES

[1] K. H. Rendigs, M. Knüwer, “Metal materials in Airbus 380,” 2nd Izmir Global Aerospace & Offset Conference, October 6−8, 2010, Izmir.

[2] D. Banat, R. J. Mania, R. Degenhardt, “Stress state failure analysis of thin-walled GLARE composite members subjected to axial loading in the post-buckling range,” Composite Structures, vol 289, pp. 1-11, 2022.

[3] G. Wu, J. M. Yang, “The Mechanical Behavior of GLARE Laminates for Aircraft Structures,” Failure in Structural Materials, pp. 72-79, 2005.

[4] T. Sinmazçelik, E. Avcu, M.Ö. Bora, O. Çoban, "A review: Fibre metal laminates, background, bonding types and applied test methods," Materials and Design vol 32, pp. 3671–3685, 2011.

[5] A. S. M. Al-Azzawi, J. McCrory, L. F. Kawashita, C. A. Featherston, R. Pullin, K. M. Holford, "Buckling and postbuckling behaviour of Glare laminates containing splices and doublers. Part 1: Instrumented tests," Composite Structures, vol 176 pp. 1158–1169, 2017.

[6] R. J. Mania, C. BronnYork "Buckling strength improvements for Fibre Metal Laminates using thin-ply tailoring," Composite Structures vol 159, pp. 424–432, 2017.

[7] D. Banat, R. J. Mania, "Stability and strength analysis of thin-walled GLARE composite profiles subjected to axial loading," Composite Structures, vol 212, pp. 338–345, 2019.

[8] E. Eglitis, K. Kalnins, O. Ozolinsh, "The influence of loading eccentricity on the buckling of axially compressed imperfect composite cylinders," Mechanics of Composite Materials, vol 46, no 5, pp. 83–92, 2010.

[9] G. S. E. Bikakis, C. D. Kalfountzos, E. E. Theotokoglou, "Elastic buckling response of rectangular GLARE fiber-metal laminates subjected to shearing stresses," Aerospace Science and Technology, vol 87, pp. 110–118, 2019.

[10] P. P. Y. Muddappa, G. Giridhara, T. Rajanna, "Buckling behavior of GLARE panels subjected to partial edge loads," Materials Today: Proceedings, vol 45, pp. 94–99, 2021.

[11] D. Banat, Z. Kolakowski, R. J. Mania, "Investigations of fml profile buckling and post-buckling behaviour under axial compression," Thin-Walled Structures, vol 107, pp. 335–344, 2016.

[12] L. B. Vogelesang, A. Vlot, "Development of fibre metal laminates for advanced aerospace structures," Journal of Materials Processing Technology, vol 103, pp. 1-5, 2000.

[13] A. Erklig, E. Yeter, M. Bulut, "The effects of cut-outs on lateral buckling behavior of laminated composite beams," Composite Structures, vol 104, pp. 54–59, 2013.

[14] A. Erklig, E. Yeter, "The effects of cutouts on buckling behavior of composite plates," Sci Eng Compos Mater, vol 19, pp. 323-330, 2012.

[15] E. Yeter, A. Erklig, M. Bulut, "Hybridization effects on lateral buckling behavior of laminated composite beams," Polymer Composites, vol 37 issue8, pp. 2511, 2521, 2016.

[16] A. Erklig, E. Yeter,, "Kompozit Malzemelere Açılan Dairesel, Kare, Üçgen ve Eliptik Kesitlerin Burkulmaya Etkisinin Sonlu Eleman Yöntemiyle Araştırılması", Theoretical and Applied Mechanical Turkish National Committee, 2011.

SAKARYA ÜNİVERSİTESİ
FEN BİLİMLERİ ENSTİTÜSÜ DERGİSİ

Sakarya University Journal of Science
SAUJS

ISSN 1301-4048 e-ISSN 2147-835X Period Bimonthly Founded 1997 Publisher Sakarya University
http://www.saujs.sakarya.edu.tr/

Title: Effect of Various Cross-Sections on the Flexural Behaviour of Composite Beams

Authors: Ece YİĞİT, Nurşen SAKLAKOĞLU

Recieved: 2022-10-24 00:00:00

Accepted: 2023-03-04 00:00:00

Article Type: Research Article

Volume: 27
Issue: 3
Month: June
Year: 2023
Pages: 572-579

How to cite
Ece YİĞİT, Nurşen SAKLAKOĞLU; (2023), Effect of Various Cross-Sections on the Flexural Behaviour of Composite Beams. Sakarya University Journal of Science, 27(3), 572-579, DOI: 10.16984/saufenbilder.1193796
Access link
https://dergipark.org.tr/en/pub/saufenbilder/issue/78131/1193796

Sakarya University Journal of Science 27(3), 572-579, 2023

Effect of Various Cross-Sections on the Flexural Behaviour of Composite Beams

Ece YİGİT *[1,2], Nursen SAKLAKOGLU[2]

Abstract

This study investigated the influence of various cross-sections on the flexural properties of composite beams. Within the first stage of the paper, a finite element model represented the standard three-point bending test of a composite beam was developed. The model was correlated by mesh dependency analysis and a three-point bending test. After model correlation was completed, composite beam models with 6 cross-sections were generated as CAD data and imported to the correlated finite element model. As a result of the studies, it has been determined that the F profile is the most unstable profile compared to other sections, and the D profile is the most durable profile.

Keywords: Composite materials, different cross-section, finite element analysis (FEA), three-point bending

1. INTRODUCTION

The rapid progress of technology necessitates the use of new materials with advanced properties as an alternative to classical materials. Thus, studies on composite materials have gained great importance [1, 2].

Glass fiber used in this study is a widely used reinforcing element in polymeric matrix composites. Glass fiber has high tensile strength, high corrosion resistance and very good insulation properties. The disadvantages are low modulus of elasticity, high specific gravity compared to other commercial fibers, low wear resistance, low fatigue strength and high hardness [3].

Mechanical properties define the strength of the material and changes of shape that occur in the material under force. These effects are usually in the form of either deformation or fracture. Objects first deform under increasing external impacts, then they brake by losing their strength. Geometrical change in the cross-section profile of the materials is one of the

[1]* Corresponding author: ece.yigit@olguncelik.com.tr (E. YİGİT)
Olgun Celik, R&D Center, Manisa, Turkey.
[2] Celal Bayar University, Faculty of Engineering, Department of Mechanical Engineering, Manisa, Turkey.
E-mail: nursen.saklakoglu@cbu.edu.tr
ORCID: https://orcid.org/0000-0002-1362-9444, https://orcid.org/0000-0002-6651-7542

important factors affecting the strength of the material. Esendemir et al. obtained analytical, experimental and numerical maximum deflection values for different beam lengths, widths and loads of a lattice glass-epoxy prepreg composite beam supported on both sides and subjected to a single load from its mid-point. Experimental, analytical and numerical solutions were found to correlate with each other [4]. Vanam et al. made a static analysis of an isotropic rectangular plate with various boundary conditions and various types of load applications. In this paper, finite element analysis has been carried out for an isotropic rectangular plate by considering the master element as a four-noded quadrilateral element. They confirmed the analysis results with the analytical results [5]. Salih et al., in their study, investigated the amount of deflection and bending stresses that occur in beams with different profiles that can be used in steel construction structures. Deflection and bending stress levels for the same dimensions and different cross-section profiles were obtained using ANSYS Workbench, the software. They presented by comparing with theoretical and numerical calculations [6]. Azzam and Li investigated the behavior of a composite laminate structure under a three-point bending load by subjecting two types of stacking sequences of a composite laminate structure by performing a flexural test [7]. Ansari and Cho in their study, they researched the bending and resonance frequencies of rectangular, triangular and step profile microcysts exposed to surface stress with computer -aided structural analysis program [8]. Evran investigated the bending stress in the axial functional-graded layered beams with a built-in-free limit conditions [9].

Present studies are generally emphasizing the influence of cross-section profiles on the mechanical properties of metallic materials as aforementioned. However, to the best of our knowledge, there is no study examining the effect of cross-section profiles load on the flexural properties of composite material. The aim of this study is to observe the effect of cross-sectional change on stress in composite materials. The research mainly presents the results of computational studies. As a part of the study, a glass fiber epoxy composite plate was fabricated using the prepreg compression molding method, and a three-point bending test was performed. The three-point bending test was used to model correlation. In order to reach the force and displacement values obtained as a result of the experiment, mesh dependency analysis was performed. A material correlation was provided as a result of the analysis. 6 various cross-section profiles with the same outer dimensions were designed from the Catia V5 CAD software. Generated models were divided into small parts for the simulation to be carried out in the Hypermesh software. Calculations were made separately for each design in the CAE environment [10].

2. MATERIALS AND METHODS

2.1. Material

Glass fiber-reinforced epoxy composite was used in the experimental section. 5 layers of unidirectional glass fiber reinforced epoxy prepreg were cured via compression molding process to obtain a glass fiber reinforced epoxy plate. The test plate was cut with a water-jet method according to the related test standard to obtain three-point bending test coupons. Three-point bending test coupon was illustrated in Figure 1.

Figure 1 Three-point bending test sample

2.2. Three-Point Bending Test

Three-point bending tests were carried out on the composite test coupons according to the ASTM D790 test standard in order to use in model correlation. Shimadzu universal testing machine with a 250 kN load cell was used. Test rate was determined 1 mm/min. 5 specimen was tested to avoid scattering on the test results. The three-point bending test setup is shown in Figure 2.

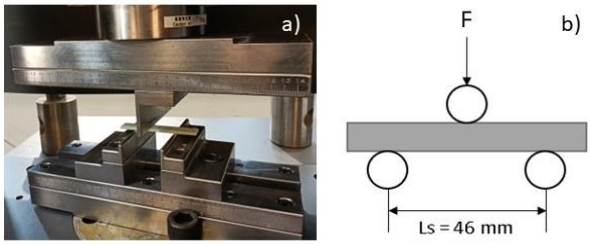

Figure 2 a) Three-point bending test set-up, b) schematical view of the test setup.

2.3. Design of Cross-Section Profiles

Three-point bending test setup and schematical view of the test setup are given in Figure 2. The sample dimensions are 14.9 x 2.84 x 90 mm.

Test sample and 6 various cross-section profiles with the same dimensions were designed from the Catia V5 solid model design program shown in Figure 3.

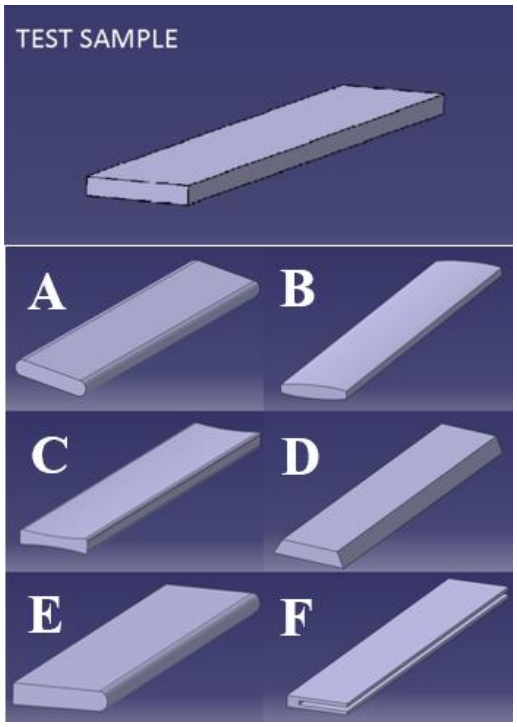

Figure 3 Design of various cross-section profiles

3. RESULT AND DISCUSSION

3.1. Model Correlation

Three-point bending test results were utilized for model correlation. The force-displacement curve of a specimen was shown in Figure 4 as a representative illustration.

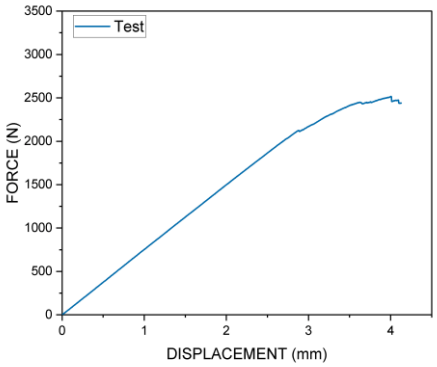

Figure 4 Force-displacement curves of three-point bending test sample

During the three-point bending test, deflection in the middle of the sample is measured as the function of force (F). Deflection values were measured at the midpoint of the sample where the highest deflection and bending moment occur for the entire sample. The image of the damaged sample as a result of the experiment is given in Figure 5. The maximum bending stress occurs at the bottom of the sample (Fig. 6).
Maximum deflection measured from the three-point bending tests was imported to the finite element model and stress distribution on the composite beam was obtained shown in Figure 7.

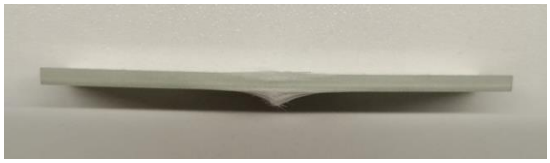

Figure 5 As a result of the bending test, the sample

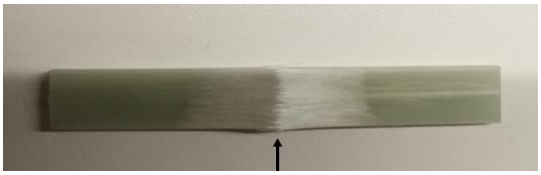

Figure 6 Maximum bending stress region of the specimen

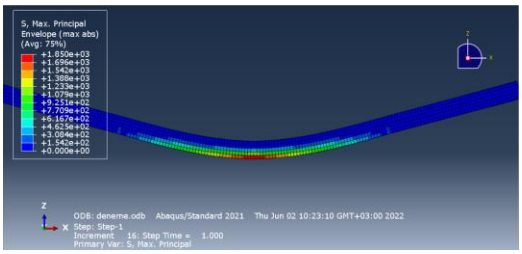

Figure 7 Maximum bending stress of the part when maximum deflection is applied

In order to converge to the force and displacement values obtained as a result of the three-point bending test with finite element model mesh dependence analysis was used. Finite element models were generated with various mesh sizes to find optimum meshing.

Figure 8 shows the 1st mesh iteration into the rectangular sample. The dimensions of the mesh are given. As a result of the analysis, it is seen in Figure 9 that the model is not correlated with the test results.

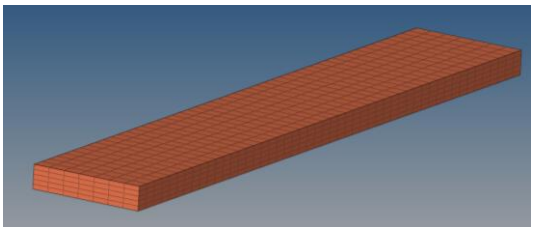

Figure 8 1st Mesh image (2.13mm-0.57mm-1.8mm)

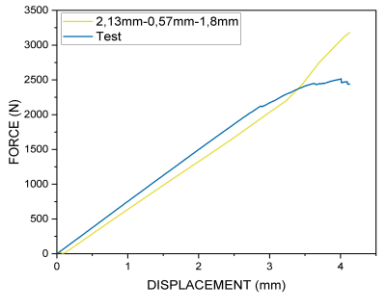

Figure 9 1st Mesh Force-displacement curves (2.13mm-0.57mm-1.8mm)

Figure 10 shows the 2nd meshing iteration. Mesh dimensions are 0.99mm-0.57mm-1mm. The results converged as the mesh size was reduced, as shown in Figure 11.

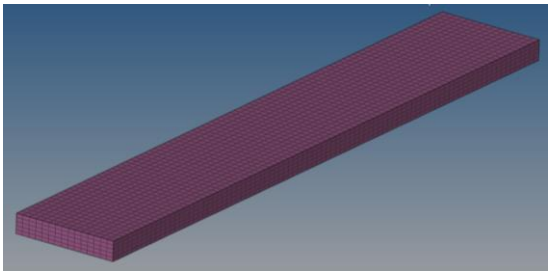

Figure 10 2nd Mesh image (0.99mm-0.57mm-1mm)

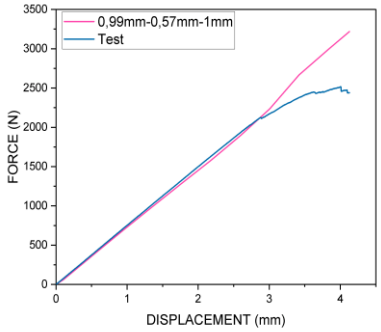

Figure 11 2nd Mesh force-displacement curves (0.99 mm-0.57mm-1mm)

The model with a mesh size of 0.99mm-0.57mm-1mm, it is aimed to improve the results by reducing the mesh sizes one step further (Figure 12). Mesh dimensions have been updated to 0.49mm-0.57mm-0.5mm. Force-displacement curves for dimensions 0.49mm-0.57mm-0.5mm are shown in Figure 13.

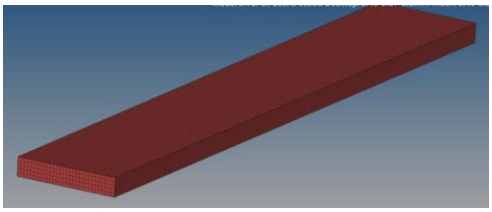

Figure 12 3rd Mesh image (0.49mm-0.57mm-0.5mm)

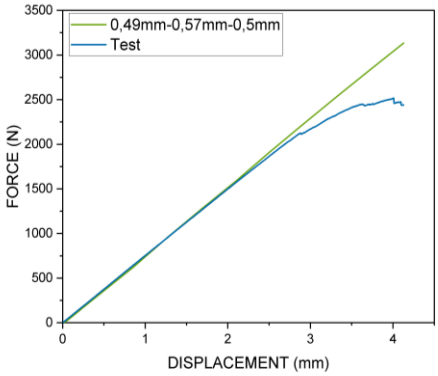

Figure 13 3rd Mesh force-displacement curves (0.49mm-0.57mm-0.5mm)

In Figure 14, while the mesh sizes are 0.99mm-0.57mm-1mm and the mesh sizes are 0.49mm-0.57mm-0.5mm, there are minor differences between them. The results are shown when the mesh size is 0.49mm-0.57mm-0.5mm was observed to converge better.

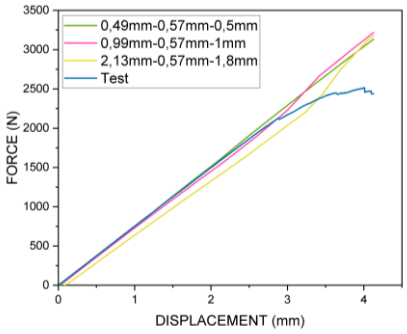

Figure 14 Force-displacement curves

As a result of the analysis, it was determined that the optimum mesh size was 0.49mm-0.57mm-0.5mm in the analysis in correlation with test results.

3.2. Analysis Results and Discussions

In this study, the stress and deflection levels that occur on different cross-section profiles were analyzed by the computer-aided structural analysis software Abaqus. For the finite element model, the mesh sizes are 0.49-0.57-0.5mm and the mesh type is Hexa Dominant. A load of 1000 N was applied to each section profile to be analyzed. The running parts are shown in Figures 15, 16, 17, 18, 19, 20, and 21.

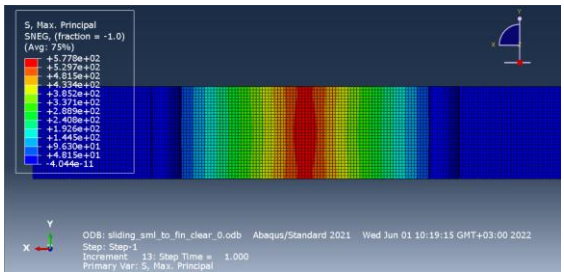

Figure 15 Bending stress resolved for rectangular profile

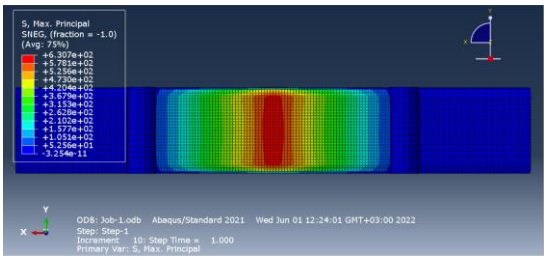

Figure 16 Bending stress resolved for A profile

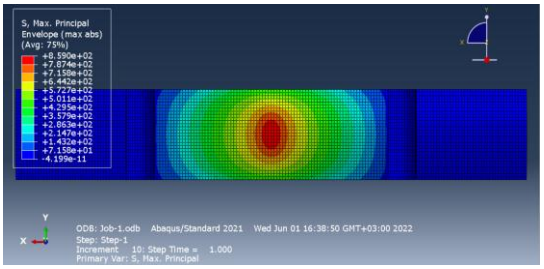

Figure 17 Bending stress resolved for B profile

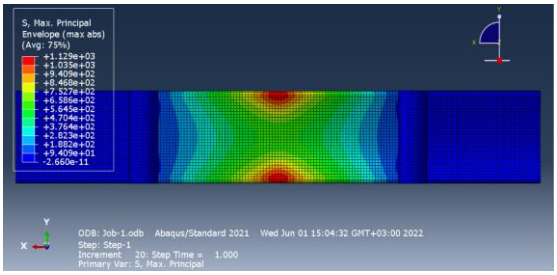

Figure 18 Bending stress resolved for C profile

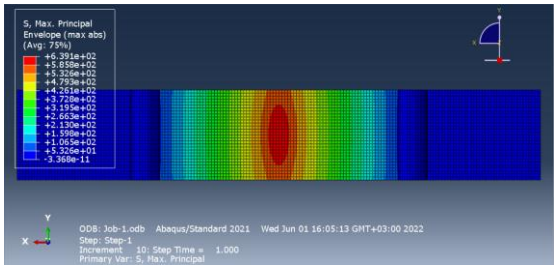

Figure 19 Bending stress resolved for D profile

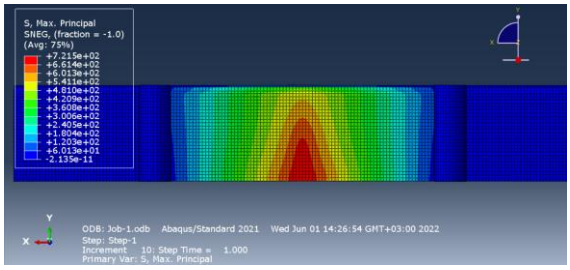

Figure 20 Bending stress resolved for E profile

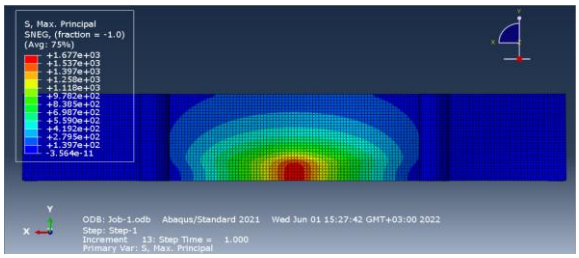

Figure 21 Bending stress resolved for F profile

The deflection and maximum bending stresses given in Table 1 have been examined section concerning the rectangular sample.

Table 1 Deflection and bending stresses determined with the help of numerical calculations of different section profiles

Section Profile	***Cross-Sectional Area***	***Maximum Bending Stress***	***Force***	***Deflection***
	(mm^2)	(σ-MPa)	(N)	(mm)
Rectangle (Test Sample)	42.32	577.8	1000	1.22444
A	40.24	630.7	1000	1.33772
B	36.33	859	1000	1.84013
C	33.98	1129	1000	2.55304
D	37.66	639.1	1000	1.39696
E	39.55	721.5	1000	1.5832
F	29.94	1677	1000	3.37653

When the rectangular section profile is excluded, Table 1 shows that the profile section with the least deflection behavior is the A profile with 1.337 mm, and the section profile with the highest deflection behavior is the F profile with 3.376 mm. When examined in terms of maximum bending stress, the minimum stress belongs to the A profile with 630.7, and the highest bending stress belongs to the F profile with 1677 MPa. Profiles showing the least deflection behavior were calculated as A profile, E profile, D profile, B profile, C profile, and F profile, respectively. The profiles with the least bending stress were found as the A profile, D profile, E profile, B profile, C profile, and F profile, respectively.

Table 2 Results of different section profiles according to rectangular section (%)

Section Profile	***Cross-Sectional Area***	***Maximum Bending Stress***
	Decreasing (%)	Increasing (%)
A	5	9
B	14	49
C	20	95
D	11	11
E	7	25
F	29	190

4. CONCLUSION

For the A-section, the cross-sectional area decreased by 5%, while the maximum bending stress increased by 9%. For the B section, the cross-sectional area decreased by 14%, while the maximum bending stress increased by 49%. For the C section, while the cross-sectional area decreased by 20%, the maximum bending stress increased by 95%. The reason for the stress of the C section to be excessive is the local stress concentrations that occur due to the loading conditions. For the D section, the cross-sectional area decreased by 11%, while the maximum bending stress increased by 11%. For the E section, while the cross-sectional area decreased by 7%, the maximum bending stress increased by 25%. For the F section, the cross-sectional area decreased by 29%, while the maximum bending stress increased by 190% (Table 2). This shows that the F profile is the weakest compared to other sections. In terms of area reduction and stress increase, it was determined that the best result was the D section profile. D section profile may be preferred for materials to be produced from composite in the future. In this way, while there is no loss in material strength, cost savings are achieved as the area is reduced.

Acknowledgments
We would like to thank Tolga Erdogus, product development manager of Olgun Celik, for allowing us to do this work. Gencay Erdur and Sinan Ali Bilmez for their support in finite element analysis. We would like to express our gratitude to Dr. Mehmet Deniz Güneş and Arzu Özüyaglı for helping us at every opportunity by sharing their experiences and valuable times.

Funding
The authors have no received any financial support for the research, authorship or publication of this study.

Authors' Contribution
The authors contributed equally to the study.

The Declaration of Conflict of Interest/ Common Interest
No conflict of interest or common interest has been declared by the authors.

The Declaration of Ethics Committee Approval
This study does not require ethics committee permission or any special permission.

The Declaration of Research and Publication Ethics
The authors of the paper declare that they comply with the scientific, ethical and quotation rules of SAUJS in all processes of the paper and that they do not make any falsification of the data collected. In addition, they declare that Sakarya University Journal of Science and its editorial board have no responsibility for any ethical violations that may be encountered, and that this study has not been evaluated in any academic publication environment other than Sakarya University Journal of Science.

REFERENCES

[1] F. C. Campbell, Structural Composite Materials, ASM International, Ohio, 2010.

[2] J. Cai, L Qiu, S. Yuan, L. Shi, P. Liu, D. Liang, "Structural Health Monitoring for Composite Materials," Composites and Their Applications, InTech Open, Ning Hu, 2012, 440.

[3] S. P. Venkatesan, L. Boobalan, S. Bennet, J. Hemanandh, S. Ganesan, "Mechanical properties and morphological study on palm Fiber/S-Glass reinforced polymer matrix composites'', Materials Today: Proceedings, vol. 47, 4373–4377, 2021.

[4] Ü. Esendemir, M. R. Usal, A. Öndürücü, M. Usal, "Orta noktasından tekil yüke maruz kompozit basit kiriş için maksimum sehim değerlerinin deneysel, nümerik ve analitik olarak bulunarak irdelenmesi'', Soma Vocational School Journal of Technical Sciences, vol. 2, no. 14, pp. 1-100, 2010.

[5] Vanam, B. C. L., Rajyalakshmi M., Inala, R., "Static analysis of an isotropic rectangular plate using finite element analysis (FEA)'', Journal of Mechanical Engineering Research, vol. 4, no. 4, pp. 148-162, 2012.

[6] S. Korucu, K. Gök, M. Tümsek, G. Soy, A. Gök, "Farklı Profillere Sahip Kirişlerde Meydana Gelen Eğilme Gerilmesi ve Sehim Miktarının Teorik ve Nümerik Yöntemler ile Analizi", Dokuz Eylul University Faculty of Engineering, Journal of Science and Engineering, vol. 21, no.62, 469-482, 2019.

[7] Azzam A., Li W., "An experimental investigation on the three-point bending behavior of composite laminate", IOP Conference Series Materials Science and Engineering, vol. 62, no. 1, IOP Publishing, 2014.

[8] M. Z. Ansari, C. Cho, "Deflection, frequency, and stress characteristics of rectangular, triangular, and step profile microcantilevers for biosensors", Sensors (Basel, Switzerland), vol. 9, no. 8, pp. 6046- 57, 2019.

[9] S. Evran, "Bending stress analysis of axially layered functionally graded beams", Omer Halisdemir University Journal of Engineering Sciences, vol. 7, no. 1, pp. 390-8, 2018.

[10] U. K. Chakravarty, "On the modeling of composite beam cross-sections", Composites Part B: Engineering, Georgia Institute of Technology, vol. 42, no. 4, pp. 982-991, 2011.

SAKARYA ÜNİVERSİTESİ
FEN BİLİMLERİ ENSTİTÜSÜ DERGİSİ

Sakarya University Journal of Science
SAUJS

ISSN 1301-4048 e-ISSN 2147-835X Period Bimonthly Founded 1997 Publisher Sakarya University
http://www.saujs.sakarya.edu.tr/

Title: Estimating the Strength and Deformation Properties of the End Milling Process Using Numerical Analysis Methods

Authors: Yasin Furkan GÖRGÜLÜ, Murat AYDIN

Recieved: 2023-02-01 00:00:00

Accepted: 2023-03-06 00:00:00

Article Type: Research Article

Volume: 27
Issue: 3
Month: June
Year: 2023
Pages: 580-589

How to cite
Yasin Furkan GÖRGÜLÜ, Murat AYDIN; (2023), Estimating the Strength and Deformation Properties of the End Milling Process Using Numerical Analysis Methods. Sakarya University Journal of Science, 27(3), 580-589, DOI: 10.16984/saufenbilder.1245764
Access link
https://dergipark.org.tr/en/pub/saufenbilder/issue/78131/1245764

Sakarya University Journal of Science 27(3), 580-589, 2023

Estimating the Strength and Deformation Properties of the End Milling Process Using Numerical Analysis Methods

Yasin Furkan GÖRGÜLÜ *[1], Murat AYDIN[1]

Abstract

In the study, the end mill made of titanium material and having a unique design with a 4-flute was simulated during the milling of the workpiece with a geometry of a rectangular prism made of aluminum material. Ansys Explicit Dynamics was used in the study. Modeling and simulation of the milling process were made with finite element analysis for the estimation of the strength properties. The end mill is chosen as a titanium alloy, while the milled workpiece is aluminum. All parameters were kept constant and only the depth of cut was examined in three scenarios 3, 6, and 9 mm. The simulations were carried out by taking the spindle speed of 4000 RPM and the feeding rate of 3350 mm/s. One of the conveniences provided by Explicit Dynamics is that it can be solved in very small time intervals, and for this reason, the time step in the analysis is solved by taking 0.001 seconds. While hexahedral mesh is applied to the tool, a tetrahedral mesh is applied to the workpiece. The generated mesh has 8,012 nodes and 17,052 mesh elements. Average deformations for both tool and workpiece are 36.92, 38.10, and 38.29 mm, respectively. Strain also shows a similar trend to the total deformation and the average values for all three scenarios were found to be 2.84 x 10^{-3}, 4.43 x 10^{-3} and 3.99 x 10^{-3} mm/mm. Also, the stress values were obtained as 78.23, 76.83, and 77.99 MPa.

Keywords: Ansys, deformation, end mill, explicit dynamics, stress and strain.

1. INTRODUCTION

In industrial applications, machining can be done in several ways such as turning, drilling, grinding, milling and so on. But, there are some challenges such as stress formation that milling (a trustable way of production of structures or parts) has to defy [1]. In milling operation, cutters are the essential elements of material processing and have different geometries or profiles. There are plenty of studies that evaluated milling experimentally and/or numerically. The following studies are focused on the finite element modeling and analysis of the end milling applications using different tools and materials.

It was verified the cutting tool forces and stresses for milling Titanium alloy Ti-6Al-4V cut by a tungsten carbide end mill [2]. It was calculated the temperature fields in the tool and workpiece [3]. It was predicted the milling forces on the processing of aluminum alloy 7050 [4]. There are studies that evaluate the influence of cryogenic cooling on the

* Corresponding author: yasingorgulu@isparta.edu.tr (Y. F. GORGULU)
[1] Isparta University of Applied Sciences, Keciborlu Vocational School, Isparta University of Applied Sciences, Isparta, Turkey.
E-mail: murataydin@isparta.edu.tr
ORCID: https://orcid.org/0000-0002-1828-2849, https://orcid.org/ 0000-0002-3015-1868

cutting temperature, forces, and chip formation on the micro-milling of Ti6Al4V [5]. Kumar and Srinivas evaluated the burr formation while small-milling of an Al6061-T6 by flat end mill with small cutters and varying geometry of the tools [6].

Praven and Elaya predicted the delamination behavior of Glass Fiber Reinforced Plastics (GFRP) while milling using a K10 end mill (carbide tool coated with Titanium nitride having four flutes each with square ends) and stated that the finite element analysis (FEA) provided close results to the experimental ones [7]. It was evaluated the cutting forces and tool tip displacement for end milling processes [8]. Prasad and Sreedhar predicted deformation and stress properties of the Tungsten Carbide tool while slow, medium, and high-speed cutting of aluminum alloy Al6061-T6 [9].

There are also studies evaluate the stress value and tool displacement in the cutting tool (TiAlN) during hard end milling of heat-treated low alloy steel (42CrMo4) [10]. It was evaluated the surface properties of thin-wall workpieces due to thermo-mechanical deflection while machining. Karidkar and Patankar [11] evaluated the machining of thin wall machining of Al8011 and stated that experimental deformation values can be well predicted (from 1.8 to 12.8% diffractions, 6.2% avg.) by FEM&A. Işık and Öztürk [12] predicted the influences of cutting speed and feed rate on the cutting forces (total deformation and von Mises stresses) while drilling holes on AISI 140 using TiAlN-coated hard carbide cutting tool. Kumar and Mall [13] evaluated the vibration behavior of high speed steel (UNST11302) single point cutting tool in turning operation. Rajpoot and Siddique [1] predicted the stress formation on the end mill cutters with varying geometry during the milling operation of AlSi 1045. It was studied the tool particle interaction and stress distribution in particles along, above, and below the cutting path under different cutting speeds and constant depth of cut while machining discontinuously reinforced aluminum composites made of 6061 aluminum alloy and 25 micron silicon carbide particles [14]. It was modeled an end mill with a damper for reducing the vibration while high-speed milling application [15].

Mustapha and Zhong analyzed the transverse vibration behavior of a micro end mill [16]. It was evaluated the depth of feed on the stress of the end mill [17]. It was evaluated the deformation of a four-flute mill [18]. Tandon and Khan [19] modeled a flat end mill (A four-fluted M42 high-speed steel with a 30° helix angle) and predicted stress distribution (von Mises stress), translational displacement, and deformation values. Yang and Zheng [20] used deform three-dimensional FEA for simulation of ball-end milling of hardened (42HRC, 52HRC, and 62HRC) workpieces (Cr12MoV) and evaluated the milling forces and stress and temperature distributions.

It was designed an end mill to optimize the structure of a variable pitch end mill for achieving better vibration and stability performances [21]. It was evaluated the influence of spindle speed and cutter length on the stress and strain values of the micro-milling cutter (2 flutes) [22]. It was predicted the cutting force while end milling of 42CrMo4 steel (40HM) [23]. When the literature was reviewed, it was seen that influence of cutting depth on the total deformation, strain, and stress of the cutter is not dynamically evaluated by explicit dynamics. Indeed, the most essential parameters that influence the stress value and tool displacement during the machining in entire machining conditions are cutting speed and depth, and machining time [10]. Therefore, this study tried to figure out this issue by numerical analysis using a unique design cutter with four-helix flutes.

2. MATERIALS AND METHODS

2.1. Tool-workpiece Design

In the study, an end mill made of titanium material [24] with 4 helical flutes was selected and designed. The total length of the end mill is 92 mm, and the diameter of the cutting edge, and the shank are 16 mm. The usable cutting length with a specified number of teeth is designed as 38 mm. It also has a helix angle of 25° for general machining purposes [25]. Tool material has a density of 4510 kg/m^3 and a specific heat value of 500 J/kg.°C. It starts the cutting process by face milling and outside the workpiece as shown in figure 1. The workpiece is Al 1100-O material with a density of 2707 kg/m^3 and a specific heat of 884 j/kg.°C [24]. The end mill was chosen as a brittle material, while the workpiece was chosen as a ductile material. The dimensions of the workpiece are designed as 28, 50, and 20 mm in width, length, and height, respectively.

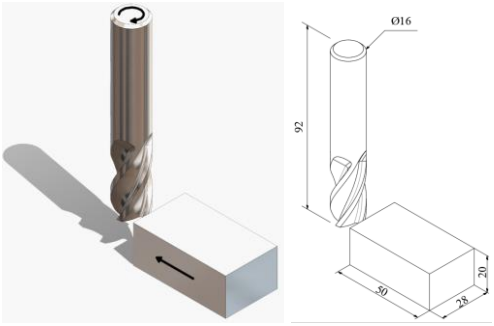

Figure 1 The three-dimensional end mill and workpiece models with dimensions.

2.2. Finite Element Analysis Using Explicit Dynamics

The mathematical description of a physical system that includes a part or assembly, material characteristics, and boundary conditions are called FEA. It is not always possible to estimate product behavior in the actual world using straightforward calculations. By precisely describing physical processes using partial differential equations, a generic methodology like FEA offers an easy way to express complex behaviors. Design engineers and professionals can utilize FEA now that it has developed and become more accessible [26]. FEA was carried out using the Explicit Dynamics tool of the Ansys software. Explicit dynamics, which is a branch of the finite element method, was used in the study. Here, the chip removal process of the end mill cutter from the workpiece was simulated.

The end mill cutter and workpiece modeling were made using a commercial computer-aided design (CAD) program called SolidWorks. Afterward, CAD designs were transferred to the Explicit Dynamics section under Ansys Workbench. One of the distinguishing differences between Explicit Dynamics and Implicit Dynamics is that they can analyze very small time intervals [27]. The time interval of the analysis made in the study was resolved as 0.001 seconds. A hexahedral mesh structure was created on the end mill and a tetrahedral mesh structure on the workpiece. The mesh has a total of 17052 mesh elements, 8012 nodes and it is demonstrated in Figure 2. Mesh quality is an important factor in terms of the accuracy of results in FEA studies. For this reason, skewness, orthogonal quality, and aspect ratio, which are 3 parameters that are important in mesh quality, were checked.

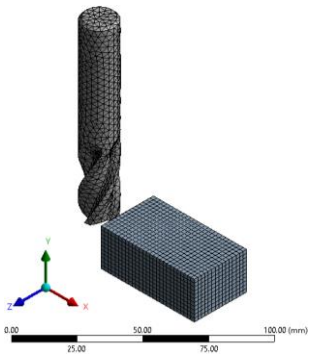

Figure 2 The mesh structure of the end mill and workpiece.

The average skewness of the generated mesh is 0.2014. Mesh quality in the range of 0 to 0.25 on the scale shared by Ansys is defined as “Excellent” [28–32]. The average orthogonal quality, which is the second quality indicator, is 0.79728. This ratio between 0.70 and 0.95 is defined as “Very

Good". The third parameter, aspect ratio, is recommended to be less than 20 and it is 1.6918 in the analysis. The aforementioned skewness and orthogonal quality ratios are given in tables 1 and 2.

Separate displacements have been defined for the tool and the workpiece. While the end mill rotates clockwise with 4000 RPM, the workpiece advances towards the end mill at 3350 mm/s (see figure 1.). After the start of the cutting process, the end mill cutter rotates to cut the workpiece along its length. The quality scale of these two parameters is given in Tables 1 and 2 [28–32].

Table 1 The skewness mesh quality metrics spectrum.

Excellent	Very good	Good	Acceptable	Bad	Inacceptable
0.00-0.25	0.25-0.50	0.50-0.80	0.80-0.94	0.95-0.97	0.98-1.00

Table 2 The orthogonal quality mesh metrics spectrum.

Inacceptable	Bad	Acceptable	Good	Very good	Excellent
0.000-0.001	0.001-0.100	0.100-0.200	0.200-0.690	0.700-0.950	0.950-1.000

The study done can be categorized as groove cutting and side cutting. Formulas used in end milling calculations are as follows [33–36]:

$$v_C = \frac{\pi \times D_C \times n}{1000}$$

Where:
v_C: cutting speed
D_C: end mill diameter
n: spindle speed

$$v_f = n \times f \quad (2)$$

Where:
v_f: feed rate
f: feed rate per tooth

3. RESULTS AND DISCUSSION

In the study, it was simulated that a 4-flute end mill cuts the workpiece from one end to another at different depths of cut. As a result of the simulation, the total deformation, strain, and stress ratios were examined and these were graphed comparatively. Graphs of these parameters are shown for end mill and workpiece (figures 3.-5.), end mill only (figures 6.-8.), and workpiece only. In figures 3.-5., the visuals have been strengthened with the simulation images of the tool and the workpiece. The 0.001-second simulation was divided into 20 equal time steps and the time steps after the end mill has completely cut the workpiece are excluded from the charts. Thus, after the 0.00055th second, it is not shown in the graphics.

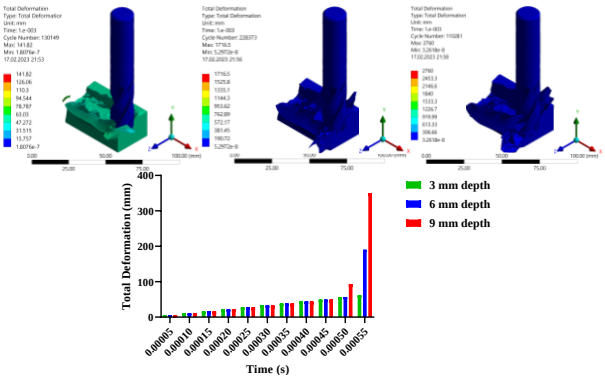

Figure 3 Total deformation amounts and scene images according to 3, 6, and 9 mm cutting depths, respectively.

A gradual increase in total deformation is observed for every 3 depths of cut up to the 0.00050th second (figure 3). In this and the next time step, there is an increase in depths of cut of 6 mm and 9 mm. As a result, it is seen that the average total deformation amount reaches 36.92 mm for 3 mm depth of cut, 38.10 mm for 6 mm depth of cut, and 38.29 mm for 9 mm depth of cut. The maximum deformation data appears to be very high and this is because some of the removed chips splash around and reach far.

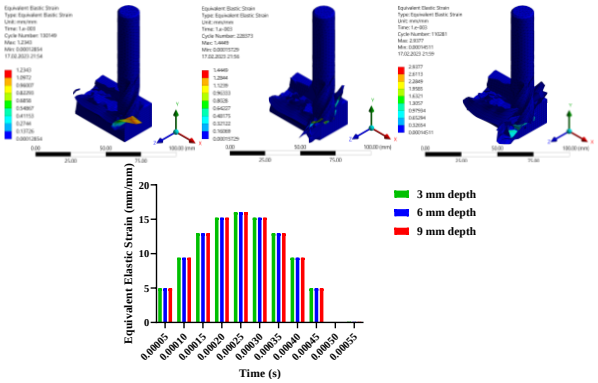

Figure 4 Strain amounts and scene images according to 3, 6, and 9 mm cutting depths, respectively.

The equivalent elastic strain graph for the tool and workpiece is illustrated in figure 4. Elastic strain rates appear relatively low but are normal since the process is geared towards plastic strain. Elastic deformation peaks in the middle of the cutting process and approaches approximately 15 mm/mm. After the peak, a regular decrease is observed. Very small strains occur in the 0.00050th and 0.00055th seconds. It is observed that all strains are very close to each other regardless of the depths of cut.

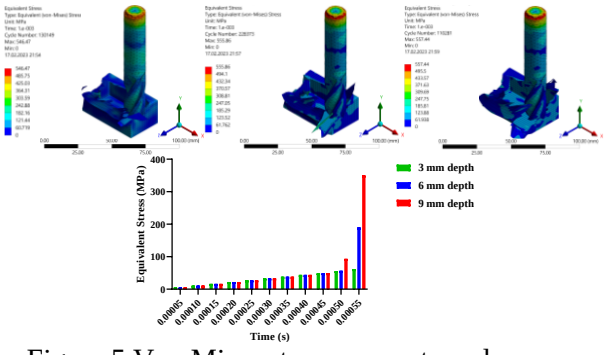

Figure 5 Von Mises stress amounts and scene images according to 3, 6, and 9 mm cutting depths, respectively.

Von Mises stresses in the tool and workpiece are depicted in figure 5 in the MPa unit. Equivalent stress follows the same trend as the graph showing the total amount of deformation for the tool and the workpiece. It shows an increase at the end of the cutting process and the amount of stress increases considerably, especially in the simulation with a cutting depth of 9 mm.

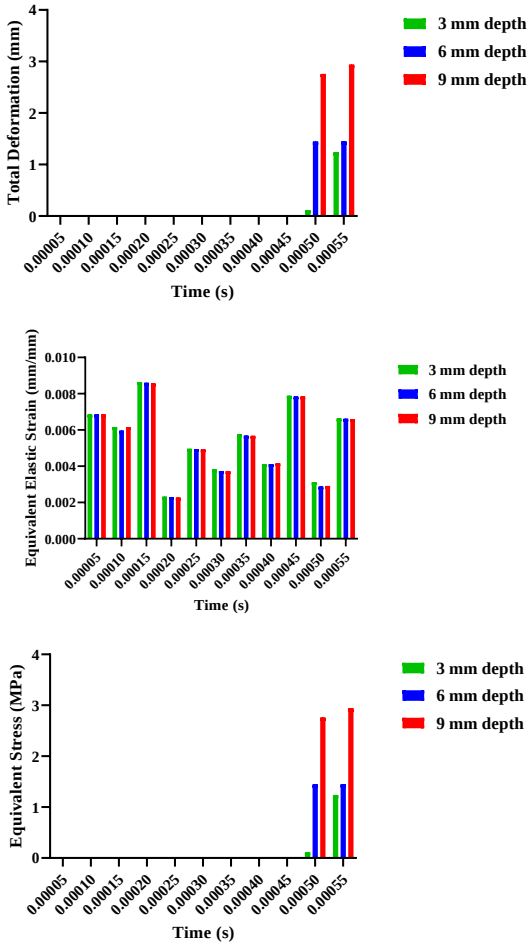

Figure 6 The total amount of deformation, strain and stress occur only in the milling cutter according to the depths of cut of 3, 6, and 9 mm.

Especially the superiority of titanium material over aluminum in the cutting process is seen in figure 6. The 4-flute end mill used in the simulation is not defined as rigid, but is defined as flexible to approach real-life applications. Even if it is small, total deformations in the cutting edge occur especially towards the end of the cutting process.

The strains that occur in the end mill according to different depths of cut are demonstrated in figure 6. Although the strain occurs at very low rates, it follows a fluctuating trend. It is noteworthy that the strain rates of all three scenarios are very close to each other. The reason for the fluctuation is thought to be related to heterogeneous cutting and serrated chip formation.

In the titanium end mill, the greatest stresses occur towards the end of the cut. In the previous time steps, the stress ratios are not visible on the chart because they are much smaller than 1. The greatest stresses occur at the end mill with a depth of cut of 9 mm (see figure 6).

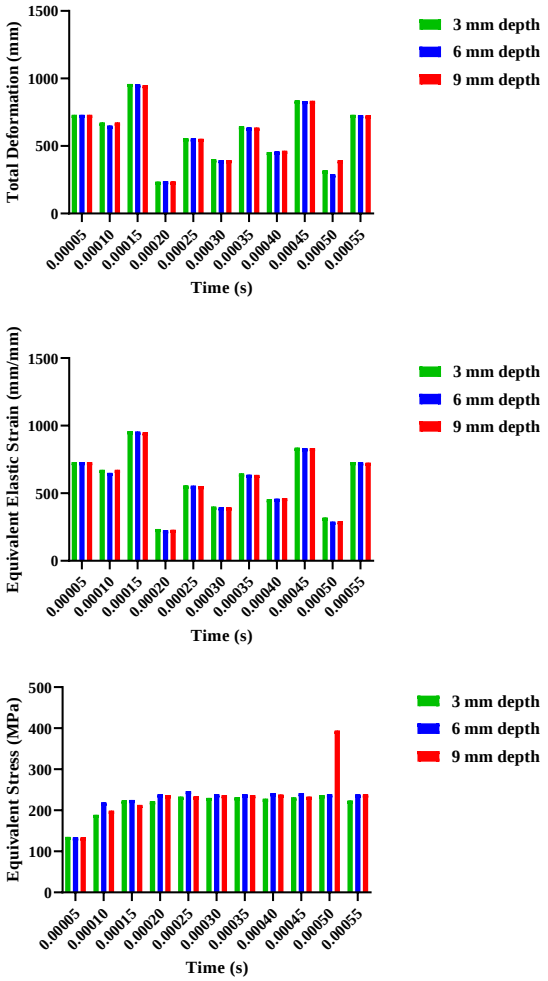

Figure 7 The total amount of deformation, strain and stress occurs only in the workpiece according to the depths of the cut of 3, 6, and 9 mm.

The total deformation of the workpiece is given in figure 7. When the total deformation rates of the workpiece are examined, fluctuating and close to each other rates are observed. Except for the 0.00010^{th} and 0.00050^{th} seconds, the deformation data appear to be almost very close according to the cutting depths.

Figure 7 also shows the strain of the workpiece, but is similar to the general image of figure 6. Minor changes are observed at the 0.00010^{th}, $0.00020^{th,}$ and 0.00050^{th}-time steps compared to the other time steps.

A constant transition is observed in the von Mises stresses of the workpiece, except for two time steps. While the stresses are around 100 MPa in the 0.00005^{th} second, the stress levels approximately double after the end mill is fully inserted into the part and continue to be constant. In the scenario with a depth of cut of 9 mm at 0.00050 seconds, an extreme increase appears. The reason for this is thought to be due to the formation of serrated chips and the inability of the end mill to cut the workpiece properly.

It should be taken into consideration that almost all performed milling trials will adopt dry cutting to prevent the effects of cutting fluid or coolant, which are hard to bear in mind while simulating by FEA [4]. In this study, neither fluid nor a coolant was applied but contrary to this expression, they performed FEA using cryogenic cooling and stated that tool life, dimensional accuracy, and roughness values can be advanced by cryogenic utilization [5].

Cutting depth is one of the most influencing parameters in milling applications. According to FEA results, it was reported that a decrease in cutting depth causes an increase in stress value due to a decrease in the contact zone between the tool and chip [10]. The authors also approved that FEA can be well enough to forecast the stress value and displacement of the cutting tool. As can be seen in the figures 5, 6, and 7, the total amount of deformation and von Mises Stress values were increased with the increase in cutting depth which is opposed to the conclusion of a study [10].

Işık and Öztürk [12] stated that cutting forces increase with the increase in cutting speed and feed rate while removing chips. According to the authors, not only there is a direct interaction between the cutting forces and

total deformation of the tool, but also the von Mises stresses. In this study, speed and feed rate were constant, but should be considered by a future study for comparison.

4. CONCLUSIONS

The simulation of a 16 mm diameter end mill made of titanium material with 4 flutes, which is the cutting tool, cutting the workpiece made of aluminum material was performed using Ansys Explicit Dynamics. As a result of the simulation, the total deformation, strain, and stress values were created according to different depths of cut for all three scenarios. In all three scenarios:

- Serrated chips on the workpiece are noticeable after the milling process. Even if the type and size of the end mill, material kind, and processing parameters such as feed rate and spindle speed were not the evaluated factors, it is thought that these variables have to be optimized for proper milling.
- The average deformations occurring in both the tool and the workpiece were found to be 36.92 mm for 3 mm cutting depth, 38.10 mm for 6 mm, and 38.29 mm for 9 mm.
- Considering the average total elastic strains, values are 2.84 x 10^{-3} mm/mm, 4.43 x 10^{-3} mm/mm, and 3.99 x 10^{-3} mm/mm respectively.
- When the average von Mises stresses are evaluated, it reaches 78.23 MPa for the 3 mm depth of cut scenario, 76.83 for 6 mm, and 77.99 MPa for 9 mm.
- Considering the resulting stresses, the cutting depth of 6 mm, which is the second of the three scenarios, can be stated as the most successful scenario since it has the lowest stress values.

Funding
The authors have not received any financial support for the research, authorship or publication of this study.

Authors' Contribution
The authors contributed equally to the study.

The Declaration of Conflict of Interest/ Common Interest
No conflict of interest or common interest has been declared by the authors.

The Declaration of Ethics Committee Approval
This study does not require ethics committee permission or any special permission.

The Declaration of Research and Publication Ethics
The authors of the paper declare that they comply with the scientific, ethical and quotation rules of SAUJS in all processes of the paper and that they do not make any falsification on the data collected. In addition, they declare that Sakarya University Journal of Science and its editorial board have no responsibility for any ethical violations that may be encountered, and that this study has not been evaluated in any academic publication environment other than Sakarya University Journal of Science.

REFERENCES

[1] I. Rajpoot, S. N. Siddique, "Investigation and numerical analysis of milling cutter," International Research Journal of Engineering and Technology (IRJET), vol. 05, no. 06, pp. 1508–1513, 2018.

[2] V. Kumar, A. Eakambaram, A. Arivazhagan, "FEM analysis to optimally design end mill cutters for milling of Ti-6Al-4V," Procedia Engineering, vol. 97, pp. 1237–1246, 2014.

[3] D. V. Evdokimov, D. G. Fedorov, D. L. Skuratov, "Thermal stress resarch of processing and formation of residual stress when end milling of a workpiece," World Applied Sciences Journal, vol. 31, no. 1, pp. 51–55, 2014.

[4] W. Ma, R. Wang, X. Zhou, X. Xie, "The finite element analysis–based

simulation and artificial neural network–based prediction for milling processes of aluminum alloy 7050," Proceedings of the Institution of Mechanical Engineers, Part B: Journal of Engineering Manufacture, vol. 235, no. 1–2, pp. 265–277, 2021.

[5] M. A. Oymak, E. Bahçe, İ. Gezer, "Investigation Of Cryogenic Cooling Effect With Finite Element Method In Micro Milling Of Ti6al4v Material," International Journal of Innovative Engineering Applications, 2021.

[6] K. K. Kumar, N. Srinivas, "Optimization and Process Control in Small Diameter End Mill," International Journal of Engineering Science and Computing, vol. 6, no. 8, pp. 2581–2585, 2016.

[7] P. Praveen Raj, A. Elaya Perumal, "Prediction of Delamination in End Milling of GFRP Using ANSYS," Asian International Journal of Science and Technology in Production and Manufacturing Engineering, vol. 6, no. 2, pp. 39–46, 2013.

[8] A. C. Araujo, A. M. Savi, P. M. L. C. Pacheco, "Experimental and Numerical Analysis of End Milling," in VI National Congress of Mechanical Engineering, 2010.

[9] S. S. Prassad, C. Sreedhar, "Finate Element Analysis of Multi Point Cutting Tool," ANVESHANA's International Journal of Research in Engineering and Applied Sciences, vol. 1, no. 11, pp. 123–135, 2016.

[10] M. Dragicevic, S. Jozic, D. Bajic, "Finite element simulation of stresses distribution and tool displacement in the cutting tool during hard nd-milling in different machining conditions," in Mechanical Technology and Structural Materials, 2017, vol. 2017, no. 55, pp. 29–36.

[11] S. S. Karidkar, V. A. Patankar, "Finite Element Modeling and Simulation of Thin Wall Machining of Al 8011," International Journal of Engineering Research and Technology, vol. 10, no. 1, pp. 654–658, 2017.

[12] Y. Işık, E. Öztürk, "Experimental Analysis of Cutting Forces and Finite Element Simulation in Milling Operations," International Journal of Mechanical Engineering, vol. 8, no. 11, pp. 1–7, 2021.

[13] V. Kumar, R. N. Mall, "Analysis and Modelling of Single Point Cutting Tool with help of ANSYS for Optimization of Vibration Parameter," International Journal for Scientific Research & Development, vol. 3, no. 9, pp. 175–177, 2015.

[14] R. Shetty, K. Laxmikant, R. Pai, S. S. Rao, "Finite element modeling of stress distribution in the cutting path in machining of discontinuously reinforced aluminium composites," ARPN Journal of Engineering and Applied Sciences, vol. 3, no. 4, pp. 25–31, 2008.

[15] N. H. Kim, D. Won, J. C. Ziegert, "Numerical analysis and parameter study of a mechanical damper for use in long slender endmills," International Journal of Machine Tools and Manufacture, vol. 46, no. 5, pp. 500–507, 2006.

[16] K. B. Mustapha, Z. W. Zhong, "A new modeling approach for the dynamics of a micro end mill in high-speed micro-cutting," JVC/Journal of Vibration and Control, vol. 19, no. 6, pp. 901–923, 2013.

[17] D. R. Pradica, Andoko, D. Z. Lubis, "Simulation on the spindle of a five-

axis multifunctional CNC machine using finite element method," IOP Conference Series: Materials Science and Engineering, vol. 1034, no. 1, p. 012017, 2021.

[18] Q. Liu, H. Xu, J. Wang, "Analysis of four-edge mill modality and stress deformation based on ANSYS," Journal of Physics: Conference Series, vol. 1939, no. 1, 2021.

[19] P. Tandon, M. Rajik Khan, "Three dimensional modeling and finite element simulation of a generic end mill," CAD Computer Aided Design, vol. 41, no. 2, pp. 106–114, 2009.

[20] L. Yang, M. L. Zheng, "Simulation and analysis of ball-end milling of panel moulds based on deform 3D," International Journal of Simulation Modelling, vol. 16, no. 2, pp. 343–356, 2017.

[21] W. Nie, M. Zheng, S. Xu, Y. Liu, H. Yu, "Design and Optimization of Variable Pitch End Mills Based on Dynamic Balance Accuracy," 2021.

[22] X. X. Wang, X. H. Lu, G. H. Xu, F. C. Wang, "The finite element analysis of the stress and deformation of the micro-milling cutter based on ANSYS," Applied Mechanics and Materials, vol. 494–495, pp. 345–348, 2014.

[23] M. Madajewski, S. Wojciechowski, N. Znojkiewicz, P. Twardowski, "Hybrid numerical-analytical model for force prediction in end milling," Mechanik, vol. 91, no. 8–9, pp. 757–759, 2018.

[24] D. Steinberg, Equation of state and strength properties of selected materials. Lawrence Livermore National Laboratory, 1996.

[25] Conical Cutting Tools, "Choosing the Correct Angle End Mill For Your Job," 2023. https://conicalendmills.com/ordering/selection-guide/helical-angle-selection/ (accessed Feb. 16, 2023).

[26] M. Melchiorre, T. Duncan, "The Fundamentals of FEA Meshing for Structural Analysis," 2021. https://www.ansys.com/blog/fundamentals-of-fea-meshing-for-structural-analysis (accessed Jul. 04, 2022).

[27] A. A. Carvalho, "Tips and Tricks for Explicit Simulations," 2019.

[28] Ansys Inc., "Introduction to Ansys Meshing." Ansys Inc., pp. L5-16, 2011.

[29] Ansys Inc., "Mesh Quality And Advanced Topics Ansys Workbench 16.0," 2015.

[30] A. Cambaz, Y. F. Gorgulu, H. Arat, "Analysing fluid-structure interaction with CFD and FEA on a marine double-wall LNG piping system," Multidisciplinary Scientific Journal of Maritime Research, vol. 36, no. 1, pp. 51–60, 2022.

[31] A. Cambaz, Y. F. Görgülü, H. Arat, "Two-Phase Numerical Modelling of a Wet Exhaust System in a Catamaran Motor Yacht Diesel Engine," European Journal of Science and Technology, vol. 31, no. Supp. 1, pp. 165–170, 2021.

[32] Y. F. Görgülü, M. A. Özgür, R. Köse, "NACA 0009 Profilli Bir Kanadin Düşük Bir Reynolds Sayisinda Had Analizi," Journal of Polytechnic, vol. 0900, no. 3, pp. 1237–1242, 2021.

[33] A.L.M.T Corp., "Formula to calculate cutting process," 2022. https://www.allied-material.co.jp/en/products/diamond/knowledge/cutting_formula.html (accessed Jul. 04, 2022).

[34] Helical Solutions, Machining Guidebook. 2016.

[35] J. R. Walker, B. Dixon, Machining Fundamentals, 10th ed. The Goodheart-Willcox Company, Inc., 2019.

[36] E. Oberg, F. D. Jones, H. L. Horton, H. H. Ryffel, C. J. McCauley, Machinery's Handbook, 31st ed. Industrial Press, Inc., 2020.

SAKARYA ÜNİVERSİTESİ
FEN BİLİMLERİ ENSTİTÜSÜ DERGİSİ

Sakarya University Journal of Science
SAUJS

ISSN 1301-4048 e-ISSN 2147-835X Period Bimonthly Founded 1997 Publisher Sakarya University
http://www.saujs.sakarya.edu.tr/

Title: Machine Learning Supported Nano-Router Localization in WNSNs

Authors: Ömer GÜLEÇ

Recieved: 2023-02-02 00:00:00

Accepted: 2023-03-06 00:00:00

Article Type: Research Article

Volume: 27
Issue: 3
Month: June
Year: 2023
Pages: 590-602

How to cite
Ömer GÜLEÇ; (2023), Machine Learning Supported Nano-Router Localization in WNSNs. Sakarya University Journal of Science, 27(3), 590-602, DOI: 10.16984/saufenbilder.1246617
Access link
https://dergipark.org.tr/en/pub/saufenbilder/issue/78131/1246617

Sakarya University Journal of Science 27(3), 590-602, 2023

Machine Learning Supported Nano-Router Localization in WNSNs

Omer GULEC *[1]

Abstract

Sensing data from the environment is a basic process for the nano-sensors on the network. This sensitive data need to be transmitted to the base station for data processing. In Wireless Nano-Sensor Networks (WNSNs), nano-routers undertake the task of gathering data from the nano-sensors and transmitting it to the nano-gateways. When the number of nano-routers is not enough on the network, the data need to be transmitted by multi-hop routing. Therefore, there should be more nano-routers placed on the network for efficient direct data transmission to avoid multi-hop routing problems such as high energy consumption and network traffic. In this paper, a machine learning-supported nano-router localization algorithm for WNSNs is proposed. The algorithm aims to predict the number of required nano-routers depending on the network size for the maximum node coverage in order to ensure direct data transmission by estimating the best virtual coordinates of these nano-routers. According to the results, the proposed algorithm successfully places required nano-routers to the best virtual coordinates on the network which increases the node coverage by up to 98.03% on average and provides high accuracy for efficient direct data transmission.

Keywords: Wireless nano-sensor networks, IoNT, machine learning, nano-router localization

1. INTRODUCTION

Wireless Nano-Sensor Networks (WNSNs) consist of a large group of energy-limited nano-machines running in the Terahertz (THz) band which are distributedly placed on the nano-domain used in smart healthcare, environmental monitoring, robotics, food industry, security, medicine, military and agriculture applications [1-3].

In WNSN architecture, the network is formed by the nano-devices. These devices are tiny machines that are running on WNSNs for Internet of Nano-Things (IoNT) applications [4]. To be more specific, they are divided into sub-categories according to their types. These devices are called nano-sensors, nano-routers, nano-interfaces and nano-gateways [5].

The basic nano-device on the network is the nano-sensor that is responsible for sensing the data from the environment at the molecular level such as temperature, pressure, glucose concentration, chemicals, oxygen levels, heartbeats and such values [3].

In a WNSN, the data sensed from the nano-sensors need to be transmitted eventually to the base station for data processing. In

* Corresponding author: omer@pau.edu.tr (O. GULEC)
[1]Pamukkale University
ORCID: https://orcid.org/0000-0002-7657-3230

WNSNs, this task is undertaken by the nano-routers. A nano-router transmits the data from nano-nodes to the nano-interfaces. The nano-interface also transmits data from nano-routers to nano-gateways.

A nano-gateway is a nano-device that gathers data from nano-routers on a WNSN and sends it to the base station for data processing over the Internet. The nano-gateways are typical devices such as wristbands, wound bands, smartwatches and smartphones.

The illustration of hierarchical WNSN architecture running on IoNT applications is given in Figure 1. In an example WNSN shown in the figure, there are 2 nano-routers placed on the network that gather data from the nano-sensors which are represented by green nodes. These nano-routers transmit data to the nano-interface and then it transmits to the nano-gateway. Finally, the data is transmitted to the base station for data processing. The transmission processes are executed over nano-links.

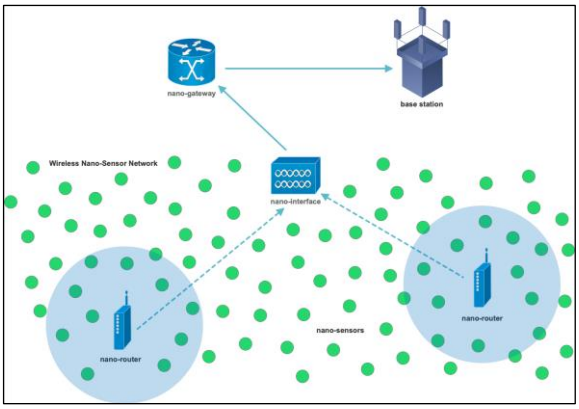

Figure 1 An illustration of a WNSN architecture

The communication range of nano-devices in a WNSN is very limited therefore, multi-hop routing protocols are used in order to provide data transmission from nano-sensors to nano-routers [6]. Although multi-hop routing is a basic routing scheme for WNSNs, the packet transmission process consumes more energy than direct transmission. On the other hand, network traffic is a critical problem to be solved in multi-hop routing. While the packets are transmitting to a nano-router over hops, the network load should be balanced for lossless communication.

According to the study of Gulec (2022) [2], a nano-sensor node consumes 0.88 nJ while receiving a packet having 22 kB size, and 8.8 nJ while transmitting a packet in a WNSN. Therefore, in multi-hop routing, it takes 9.68 nJ in total for transmitting a packet. Assuming the nano-router is 5 hops further from a nano-sensor node on average, it takes 48.4 nJ in total. This means more energy consumption on a multi-hop routing scheme despite sending a packet to a nano-router directly.

Hence, in this paper, a localization algorithm is proposed for WNSNs that finds the required nano-routers and estimates their virtual coordinates ensuring direct data transmission from a nano-sensor to these nano-routers and avoiding higher energy consumption and packet loss by using multi-hop routing.

Due to the nano-sensor nodes not having a GPS module, they can not determine their real coordinates on the network as in traditional sensor networks. According to the work of Zhou et al. (2017) [7], the nano-sensor node distances can be calculated using electromagnetic pulse durations. Pierobon et al. (2014) [8] proposed an energy harvesting routing framework for WNSNs in THz band by using the distances and the coordinates of the nano-nodes. Therefore, the location information mentioned in this study is the relative positions of the nodes to each other on the network which is specified as their virtual coordinates.

In order to estimate the numbers and their virtual coordinates of these required nano-routers, a machine learning technique – the *k*-means clustering method is used. According to the network size, the *k* parameter is predicted and the cluster heads are chosen as nano-routers. For measuring the efficiency and the accuracy of the proposed algorithm, the results are compared with the hierarchical clustering method which is another

unsupervised machine learning approach. To the best of our knowledge, there exists no machine learning-supported nano-router localization algorithm for WNSNs of IoNT applications in the literature.

The main contribution of this paper is summarized as follows.

- The proposed algorithm estimates the number of required nano-routers on a WNSN and the best coordinates to locate them by machine learning method that can connect with many nano-sensors. Therefore, the nano-sensors can easily transmit the data they sense from the environment to these nano-routers directly despite transmitting it to the uttermost nano-router by multi-hop routing.
- The proposed algorithm increases the node coverage by the estimated nano-routers therefore, any nano-node can easily find the nearest nano-router.
- The proposed algorithm saves the energy of the nodes on the network which prolongs the network lifetime.
- The proposed model prevents the nano-network from problems caused by multi-hop routing.

The rest of the paper is organized as follows. Related works on node localization, machine learning models on sensor networks and WNSN applications are summarized in Section 2. The methodology and the proposed algorithm of the current study are given in Section 3. The simulation and the results are given in Section 4. Finally, Section 5 concludes the study.

2. RELATED WORKS

Node localization is one of the critical issues that should be taken into account in Wireless Sensor Networks (WSNs) related to network design and topology which causes faults, low performance, scalability, latency and coverage problems [9].

To this end, Nain et al. (2022) [10] proposed a range-based model for underwater WSNs using both particle swarm optimization and crow search optimization which reduces localization latency and provides accuracy. Yu et al. (2023) [11] proposed a quantum annealing bat algorithm to improve localization accuracy and applicability for WSNs.

Similarly, a node localization model is developed using the salp swarm algorithm for WSNs in Kanoosh et al. (2019) [12] which outperforms the other localization algorithms in terms of computing time, the number of nodes and localization error. Sekhar et al. (2021) [13] proposed a metaheuristics-based node localization technique for WSNs that aims to find the coordinates of unknown nodes by the anchor nodes with minimum error and maximum accuracy. Javed et al. (2022) [14] proposed a mobile node localization algorithm for WSNs that improves positioning accuracy. Aroba et al. (2023) [15] proposed an algorithm to address the problem of determining sensor node localization with the minimum error when the data is transmitted over the wireless channel.

In the literature, machine learning-based methods also have been developed for WSNs in several areas. Thereby, Galal and Hesselbach (2020) [4] analyzed and classified nano-network traffic using five supervised machine learning models. Dampage et al. (2022) [16] proposed a system to detect forest fires at the initial stage using WSNs and a machine learning regression model. Bacanin et al. (2022) [17] proposed a deep learning-based model to predict air quality using Dragonfly optimization for node localization in WSNs. Esmaeili et al. (2022) [18] designed a combined model for WSNs using metaheuristics and machine learning methods for clustering-based network routing.

A *k*-means clustering-based node localization algorithm for WSNs is proposed by Khediri et al. (2020) [19] where single-hop communication is used in intra-clusters and

multi-hop communication is used in inter-clusters. Mahmood et al. (2022) [20] designed a fault detection and energy-efficient routing system for WSNs using routing-based reinforcement learning. Li et al. (2022) [21] proposed a model using *k*-means clustering for routing in underwater wireless sensor networks (UWSNs). Sathyamoorthy et al. (2022) [22] proposed a Q-learning-based clustering and load-balancing technique using *k*-means for WSNs that maximizes throughput, packet delivery ratio and minimizes end-to-end delay and energy consumption.

Recently, several methods have been developed for WNSNs problems in many fields. Xu et al. (2021) [23] developed a multi-hop routing protocol for intra-body WNSNs which estimates link states. Gulec and Sahin (2023) [24] proposed a Red Deer Algorithm based nano-sensor node clustering method for WNSNs. Garcia-Sanchez et al. (2023) [25] proposed a multi-hop routing scheme using reinforcement learning in body WNSNs.

3. METHODOLOGY

3.1. The Machine Learning Method

Node localization is one of the most difficult challenges for sensor networks to achieve due to the harsh or dangerous environment in which the nodes are deployed. To find the accurate location of the nodes, machine learning approaches can be helpful [26].

For this purpose, in the proposed model the prediction of the number of required nano-routers depending on WNSN size and their best coordinates is predicted with the *k*-means clustering method which is one of the most known unsupervised machine learning models that gives the center points (centroids) of the clusters [27, 28].

The *k*-means clustering model divides the points into *k* clusters therefore, it is important to find the optimal *k* number. The model finds centroids that cover the points close to them and include the points in the proper clusters. These points are located in these clusters by using Euclidean distance. This machine learning model iteratively computes the mean of the clusters until the minimum number of optimal centroids is found [26].

In this paper, *k*-means clustering as a machine learning model is used for clustering the nano-nodes in order to find optimal centroids as the nano-routers that should be placed on the network for ensuring efficient direct data transmission on WNSNs.

3.2. The Proposed Algorithm

In the proposed model, first of all, the initial nano-router (R_0) is placed in the coordinate [0, 0] on the network. In a 0.0015 meters transmission range, many of the nano-sensor nodes on the network can not communicate to this nano-router directly. Therefore, new nano-routers need to be placed at suitable coordinates on the network to ensure direct data transmission.

When the proposed algorithm is initialized, it is assumed that the nano-sensor nodes know their IDs and virtual coordinates. The nano-sensor nodes first broadcast *NEIGHBOUR* messages to know their neighbour nodes. When a nano-sensor node receives this message, adds the sender node to its neighbourhood list (Γ_m). This operation is repeated several times until all nano-sensor nodes know their neighbours. Finally, the nano-sensors send *NEIGHBOUR_DONE* message to the initial nano-router.

Then the initial nano-router (R_0) broadcasts *CALCULATE* message including its coordinates to collect the distances of the nano-sensor nodes. When a nano-sensor node receives this message, calculates its distance by the Euclidean distance given in Equation 1 where x_m is its x-coordinate, y_m is its y-coordinate, x_r is the nano-router's x-coordinate and y_r is the nano-router's y-

coordinate. After calculating this value, it sends back to R_0.

$$d = \sqrt{(x_m - x_r)^2 + (y_m - y_r)^2} \quad (1)$$

The initial nano-router receives all the distance values from all nano-sensor nodes on the network and then sends these values to the nano-gateway (*NG*). The nano-gateway calculates the *k* value for the *k*-means clustering method. In this step, *NG* finds the *k* value by the elbow technique of the *k*-means clustering method. Then it sends the cluster information to R_0 by *CLUSTER* message.

As an example, the graph of an elbow technique on a sample WNSN having 500 nodes for finding the optimal cluster number on the network is given in Figure 2. According to the figure, the optimal cluster number is calculated as 4.

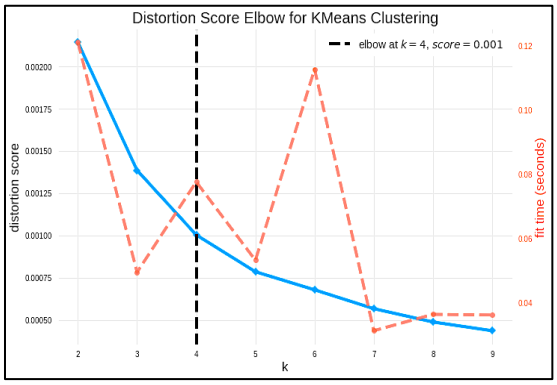

Figure 2 The elbow technique for calculating optimal cluster number on a sample WNSN

In the first iteration of placing new nano-routers on the network, the proposed algorithm finds the optimal coordinates on each cluster and directs new nano-routers to these coordinates. Unfortunately, the nano-routers have a 0.002 meters transmission range. Therefore, in this step, the node coverage may not be ensured yet. In other words, these new nano-routers may not cover all of the nano-sensor nodes.

Hence, the proposed algorithm checks if there exists any nano-sensor node that has no direct connection to any nano-router. Thus, the nano-routers broadcast *COVERAGE* messages including their information on the medium. A nano-sensor node that receives this message, adds this nano-router to its router list (Γ_{mr}) and sends *COVERED* message including its information to the sender nano-router (R_i). If a nano-node is covered by several clusters, it adds all nano-routers having a direct connection to its router list (Γ_{mr}).

If there exists any nano-sensor node that is not covered yet by *checkCoverage()* function, the nano-gateway executes another *k*-means clustering method for a cluster by calculating the distances between the nano-sensor nodes and the relevant cluster heads to place more nano-routers instead of the previous ones and finds their best coordinates to ensure more node coverage.
In the last step of the algorithm, all of the new nano-routers are placed on the network that they cover almost all nano-sensor nodes. If the node coverage conditions are satisfied, then the algorithm terminates. The first part of the proposed algorithm which is executed by nano-sensors is given in Algorithm 1, the second part which is executed by nano-routers is given in Algorithm 2 and the last part of the proposed algorithm executed by the nano-gateway is given in Algorithm 3, respectively.

Algorithm 1 Nano-sensor part

1. **data:**
2. $\Gamma_m \leftarrow$ neighbour list of nano-sensor node m
3. $\Gamma_{mr} \leftarrow$ nano-router list of node m
4: $R_0 \leftarrow$ initial nano-router placed at [0, 0]
5: $d_m \leftarrow$ the distance between node m and R_0
6: **initially:**
7. $\Gamma_m \leftarrow \emptyset$, $\Gamma_{mr} \leftarrow \emptyset$
8. **upon the algorithm started:**
9. broadcast *NEIGHBOUR* msg to Γ_m
10. **upon receiving *NEIGHBOUR* msg from node *n*:**
11: add node *n* to Γ_m
12: send *NEIGHBOUR_DONE* msg to R_0
13: **upon receiving *CALCULATE* msg from R_0 or node *n*:**
14: calculate d_m
15: send d_m to R_0
16: **upon receiving *COVERAGE* msg from R_i:**
17: add R_i to Γ_{mr}
18: send *COVERED* msg to R_i

Algorithm 2 Nano-router part

1. **data:**
2: $NG \leftarrow$ nano-gateway
3: **upon the algorithm started:**
4: wait until nano-sensors finish the first process
5: **upon receiving *NEIGHBOUR_DONE* msg from node *n*:**
6: broadcast *CALCULATE* msg
7: **upon receiving d_n values from $\forall n$:**
8: send $\forall d_n$ values to NG
9: **upon receiving *CLUSTER* msg from NG:**
10: send $[x_i, y_i] \in R_i$ to n_i by *COVERAGE* msg

Algorithm 3 Nano-gateway part

1. **data:**
2: $finished \leftarrow true$ if the algorithm terminates
3: **initially:**
4: $finished \leftarrow false$
5. **upon receiving d_n values from R_0:**
6: estimate the number of required R_i
7: cluster nodes by d_n using *k*-means
8: send $[x_i, y_i] \in R_i$ to R_0 by *CLUSTER* msg
9: **if checkCoverage() == FALSE:**
10: repeat clustering nodes by d_u using *k*-means
11: send $[x_j, y_j] \in R_j$ to R_0 by *CLUSTER* msg
12: **else:**
13: $finished \leftarrow true$

4. SIMULATIONS AND RESULTS

In order to estimate the number of required nano-routers and their virtual coordinates on the network, NS-3 [29] simulation tool and Nano-Sim [30] framework are both used for the simulations. In NS-3 simulator, basically, a nano-network is formed by the nano-nodes, the nano-routers, nano-interfaces and the nano-gateway. To illustrate all of the nano-devices and the network, Python packages, Networkx [31] and Matplotlib [32] are also used in the simulations.

Besides, different network topologies have been generated in different network sizes for the simulations. Therefore, the proposed algorithm was conducted 100 times on these topologies having 500, 750, 1000 and 2000 nano-nodes. The size of the network area is 0.01×0.01 meters, the transmission range of nano-sensors is 0.0015 meters and the transmission range of nano-routers is 0.002 meters. All of the simulation parameters are given in Table 1.

Table 1 Simulation parameters

Simulator	NS-3, Nano-Sim
Python Package	Networkx, Matplotlib
Network Area	0.01 x 0.01 m^2
Transmission Range of Nano-Nodes	0.0015 m

Table 1 Simulation parameters (continue)

Transmission Range of Nano-Routers	0.002 m
Packet Size	22 kB
Topologies	100 on each simulation
Number of Nano-Sensor Nodes	500, 750, 1000, 2000

A sample nano-network having 250 nodes is illustrated in Figure 3. According to the figure, the rest of the nano-sensor nodes are given that are not in the transmission range of the initial nano-router which is placed in [0, 0]. These nano-sensor nodes are clustered according to the distances to the initial nano-router by the *k*-means clustering method. In the figure, for this sample network, there are 3 clusters having nano-sensor nodes that are colored red, green and blue.

After clustering these nano-sensor nodes, the optimal centroids/cluster heads are placed in each cluster as nano-routers which are colored orange. These nano-routers have 0.002 meters transmission range, hence, they do not cover all of the nano-sensor nodes in their own clusters. According to Figure 3, it is clearly seen that placing a nano-router in each cluster is not enough to ensure node coverage. Therefore, the *k*-means clustering method is executed once more on each cluster for placing new nano-routers instead of the centroid cluster heads due to the transmission range of nano-routers.

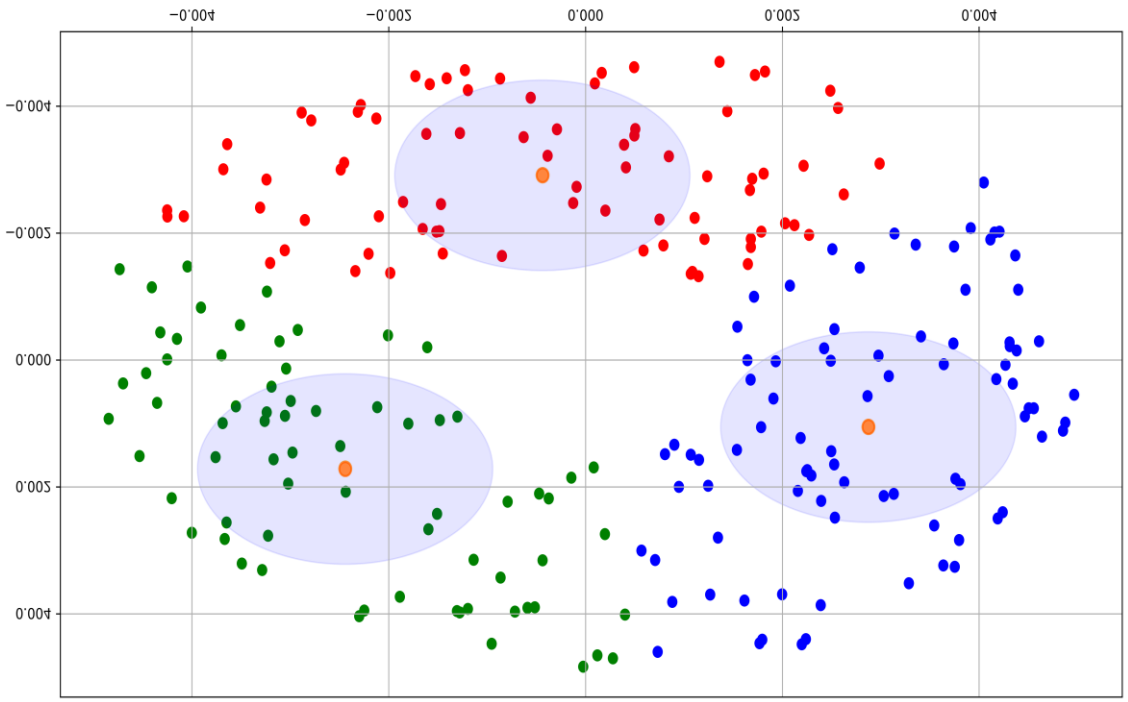

Figure 3 The first iteration of nano-router localization by the proposed algorithm on a sample WNSN

In Figure 4 and Figure 5, it is shown that there are more nano-routers that are placed on the network for each cluster. In Figure 6, the final network topology of a sample WNSN having 250 nano-nodes and 7 nano-routers is illustrated. Similarly, another WNSN having 2000 nano-nodes and 17 nano-routers that are placed by the proposed algorithm is given in Figure 7.

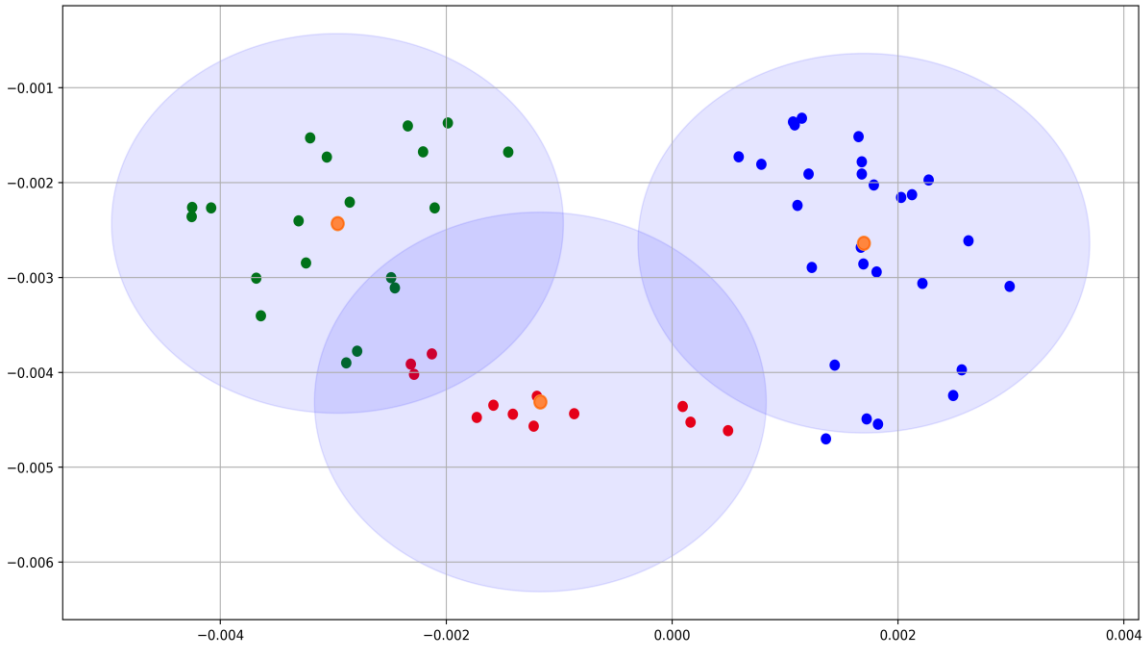

Figure 4 The second iteration of nano-router localization algorithm for red-colored clusters

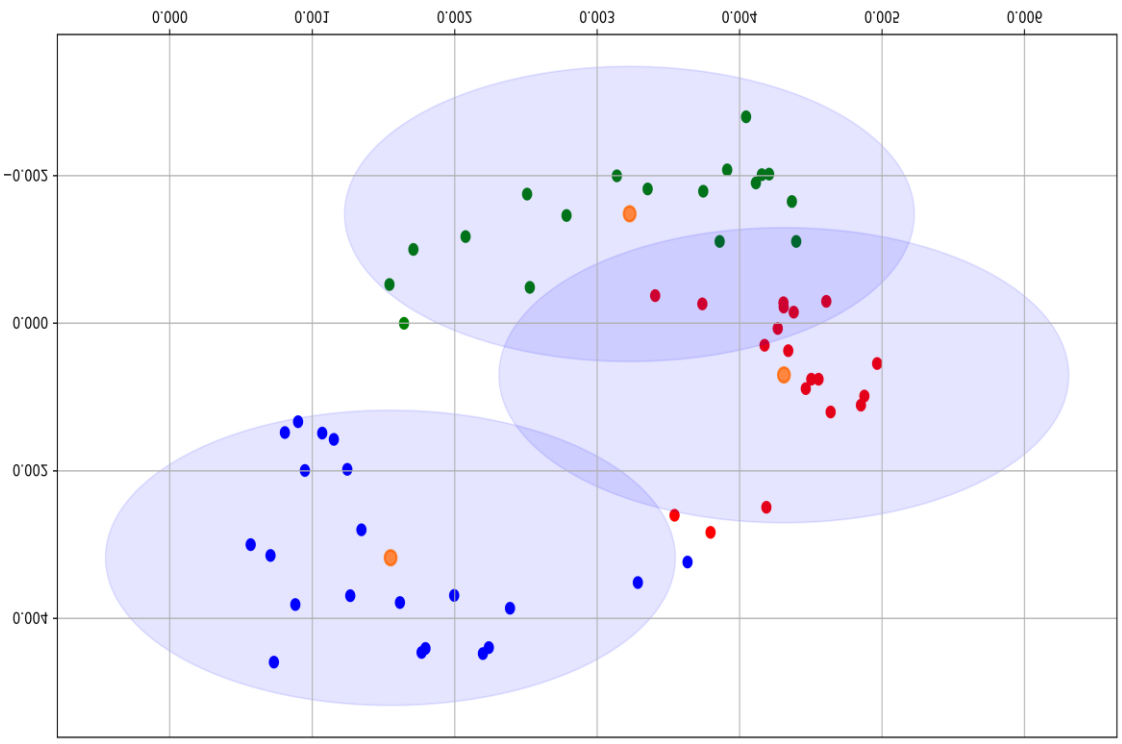

Figure 5 The second iteration of nano-router localization algorithm for blue-colored clusters

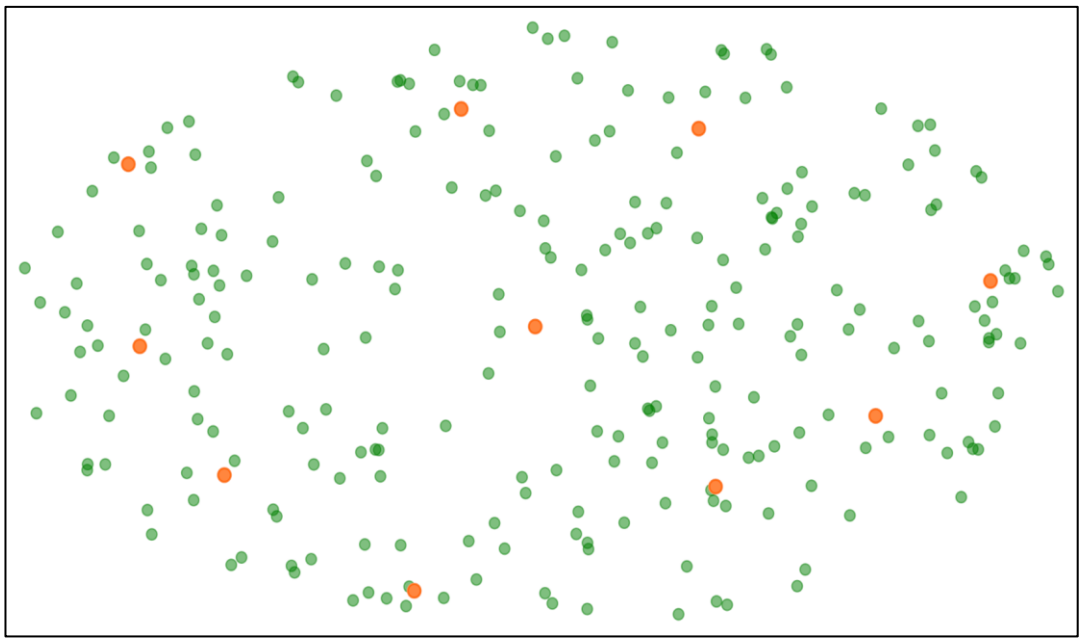

Figure 6 The final nano-router localization using the proposed algorithm on a sample WNSN

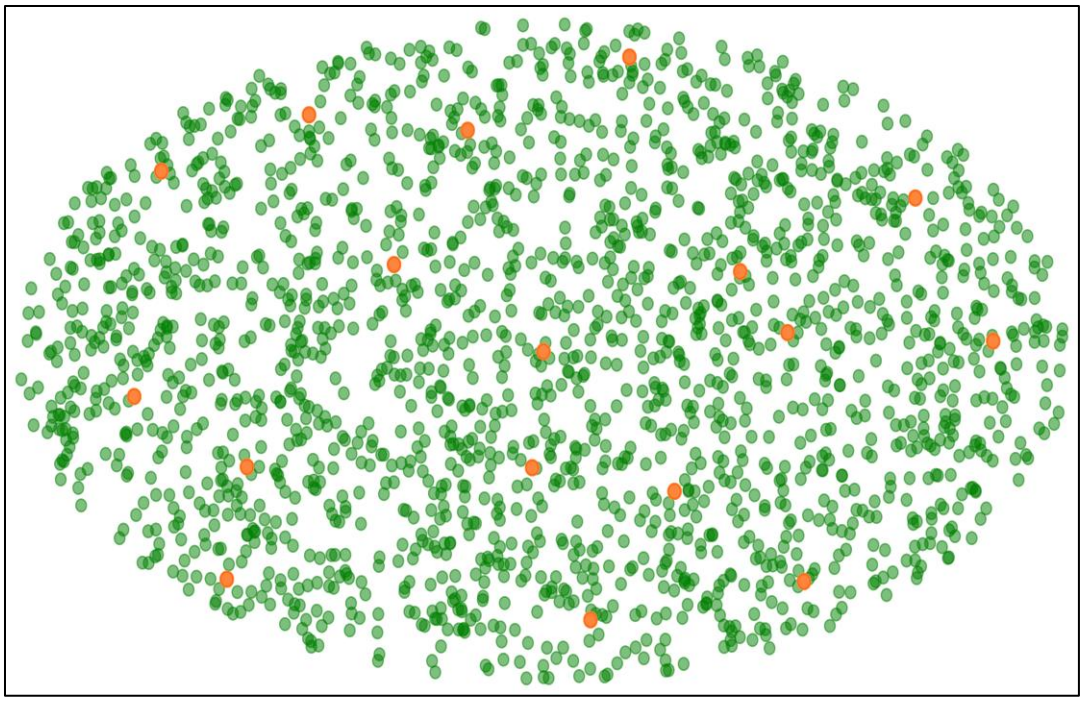

Figure 7 The nano-routers placed by the proposed algorithm on another WNSN

According to the average simulation results of the proposed algorithm given in Table 2, when a nano-network has 500 nodes, the nano-router localization takes 0.096 seconds while 461.43 nano-nodes are covered having 92.28% coverage percentage on average. When a nano-network has 750 nano-sensor nodes, the nano-router localization process takes 0.103 seconds while 695.2 nodes are covered having 92.66% percentage of coverage on average. If the WNSN has 1000 nano-nodes, the time spent for nano-router localization is 0.13 seconds, 980.31 nodes are covered while the node coverage is 98.03% on average. If a WNSN consists of 2000 nano-nodes, it takes 0.175 seconds to find new nano-routers while 1953.41 nodes are covered as 97.67% percentage on average.

According to the average simulation results of the hierarchical clustering method given in Table 3, when a nano-network has 500 nodes, the nano-router localization takes 0.113 seconds while 394.29 nano-nodes are covered having 78.85% coverage percentage on average. When a nano-network has 750 nano-sensor nodes, the nano-router localization process takes 0.124 seconds while 587.08 nodes are covered having 78.27% percentage of coverage on average. If the WNSN has 1000 nano-nodes, the time spent for nano-router localization is 0.157 seconds, 818.84 nodes are covered while the node coverage is 81.88% on average. If a WNSN consists of 2000 nano-nodes, it takes 0.224 seconds to find new nano-routers while 1640.29 nodes are covered as 82.01% percentage on average.

Table 2 Average simulation results

Node Count	Total Time (s)	Covered Node Count	Coverage (%)
500	0.096	461.43	92.28
750	0.103	695.2	92.66
1000	0.13	980.31	98.03
2000	0.175	1953.41	97.67

Table 3 Average hierarchical clustering results

Node Count	Total Time (s)	Covered Node Count	Coverage (%)
500	0.113	394.29	78.85
750	0.124	587.08	78.27
1000	0.157	818.84	81.88
2000	0.224	1640.29	82.01

In brief, the proposed algorithm achieves 13.43% more coverage over 500 nodes, 14.39% more coverage over 750 nodes, 16.15% more coverage over 1000 nodes and 15.66% more coverage over 2000 nodes on average by placing the proper nano-routers on WNSNs according to the comparison results given in Figure 8.

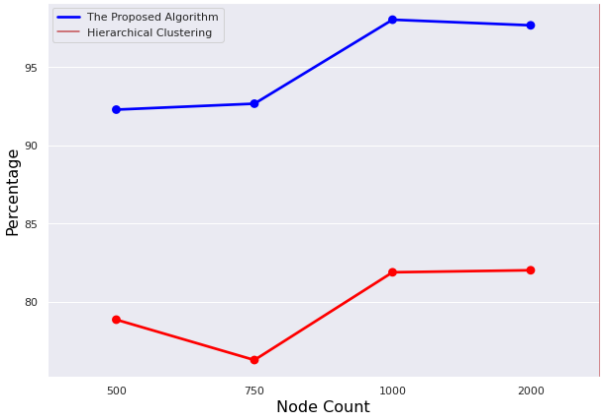

Figure 8 The coverage percentage results of the proposed algorithm and hierarchical clustering

5. CONCLUSION

In this paper, a machine learning-supported nano-router localization algorithm is proposed for providing direct communication between nano-sensor nodes and nano-routers on WNSNs running on IoNT applications. For finding the optimal nano-routers, *k*-means clustering is used as a machine learning method iteratively for providing maximum node coverage.

The proposed algorithm has been developed and tested in NS-3 simulator and Nano-Sim framework under different network topologies having different network sizes. Each simulation is conducted 100 times with different simulation setups for obtaining average results. For the illustration of the networks, Python packages, Networkx and Matplotlib are also used. The obtained simulation results of the proposed algorithm have been compared with the hierarchical clustering method which is another unsupervised machine learning approach.

According to the simulation results, the proposed algorithm successfully predicts the required number of nano-routers and estimates their optimal virtual coordinates that ensure higher node coverage on a WNSN for providing direct communication between nano-sensor nodes and the nano-routers. The proposed algorithm increases node coverage up to 98.03% by placing new nano-routers on the network. Besides, the proposed algorithm avoids higher energy consumption of the nano-sensor nodes for transmitting the data packets on multi-hop routing to the available nano-router.

Node localization is a critical problem to be considered in all types of sensor networks. For a better solution to the localization problem in WNSNs, mobile nano-routers may be used for redirecting the estimated coordinates by the nano-gateways for future studies.

Energy-efficient multi-hop routing algorithms may be used on WNSNs in cases where there are not enough nano-routers can be placed on the network. Therefore, both nano-router localization and multi-hop routing hybrid algorithms will be developed for future studies.

Funding
The author has no received any financial support for the research, authorship or publication of this study.

Authors' Contribution
O.G: Conceptualization, literature review, methodology/study design, software development, simulation, analysis, validation, writing – original draft, writing – review and editing, visualization, supervision.

The Declaration of Conflict of Interest/ Common Interest
No conflict of interest or common interest has been declared by the authors.

The Declaration of Ethics Committee Approval

This study does not require ethics committee permission or any special permission.

The Declaration of Research and Publication Ethics

The authors of the paper declare that they comply with the scientific, ethical and quotation rules of SAUJS in all processes of the paper and that they do not make any falsification on the data collected. In addition, they declare that Sakarya University Journal of Science and its editorial board have no responsibility for any ethical violations that may be encountered, and that this study has not been evaluated in any academic publication environment other than Sakarya University Journal of Science.

REFERENCES

[1] A. O. Balghusoon, M. Saoucene, "Routing protocols for wireless nanosensor networks and internet of nano things: A comprehensive survey",IEEE Access, 8, 200724-200748, 2020.

[2] O. Gulec, "Extending lifetime of Wireless Nano-Sensor Networks: An energy efficient distributed routing algorithm for Internet of Nano-Things", Future Generation Computer Systems, 135, 382-393, 2022.

[3] A. Rizwan, A. Zoha, R. Zhang, W. Ahmad, K. Arshad, N. A. Ali, Q. H. Abbasi, "A review on the role of nano-communication in future healthcare systems: A big data analytics perspective", IEEE Access, 6, 41903-41920, 2018.

[4] A. Galal, X. Hesselbach, "Machine Learning Models for Traffic Classification in Electromagnetic Nano-Networks", IEEE Access, 10, 38089-38103, 2022.

[5] M. A. Akkaş, R. Sokullu, "Wireless Communications Beyond 5 g: Teraherzwaves, Nano-Communications and the Internet of Bio-Nano-Things", Wireless Personal Communications, 126, 3543–3568, 2022.

[6] A. Galal, X. Hesselbach, "Probability-based path discovery protocol for electromagnetic nano-networks", Computer Networks, 174, 107246, 2020.

[7] L. Zhou, G. Han, L. Liu, "Pulse-based distance accumulation localization algorithm for wireless nanosensor networks", IEEE Access, 5, 14380-14390, 2017.

[8] M. Pierobon, J. M. Jornet, N. Akkari, S. Almasri, I. F. Akyildiz, "A routing framework for energy harvesting wireless nanosensor networks in the Terahertz Band", Wireless Networks, 20, 1169-1183, 2014.

[9] P. Yadav, S. C. Sharma, "A Systematic Review of Localization in WSN: Machine Learning and Optimization-Based approaches", International Journal of Communication Systems, e5397, 2022.

[10] M. Nain, N. Goyal, L. K. Awasthi, A. Malik, "A range based node localization scheme with hybrid optimization for underwater wireless sensor network", International Journal of Communication Systems, 35(10), e5147, 2022.

[11] S. Yu, J. Zhu, C. Lv, "A Quantum Annealing Bat Algorithm for Node Localization in Wireless Sensor Networks", Sensors, 23 (2), 782, 2023.

[12] H. M. Kanoosh, E. H. Houssein, M. M. Selim, "Salp Swarm Algorithm for Node Localization in Wireless Sensor Networks", Journal of Computer

Networks and Communications, vol. 2019, 1028723, 2019.

[13] P. Sekhar, E. L. Lydia, M. Elhoseny, M. Al-Akaidi, M. M. Selim, K. Shankar, "An effective metaheuristic based node localization technique for wireless sensor networks enabled indoor communication", Physical Communication, 48, 101411, 2021.

[14] I. Javed, X. Tang, M. A. Saleem, M. U. Sarwar, M. Tariq, C. S. Shivachi, "3D localization for mobile node in wireless sensor network", Wireless Communications and Mobile Computing, 2022)

[15] O. J. Aroba, N. Naicker, T. T. Adeliyi, "Node Localization in Wireless Sensor Networks using a Hyper-Heuristic DEEC-Gaussian Gradient Distance Algorithm", Scientific African, e01560, 2023.

[16] U. Dampage, L. Bandaranayake, R. Wanasinghe, K. Kottahachchi, B. Jayasanka, "Forest fire detection system using wireless sensor networks and machine learning", Scientific Reports, 12 (1), 46, 2022.

[17] N. Bacanin, M. Sarac, N. Budimirovic, M. Zivkovic, A. A. Al Zubi, A. K. Bashir, "Smart wireless health care system using graph LSTM pollution prediction and dragonfly node localization", Sustainable Computing: Informatics and Systems, 35, 100711, 2022.

[18] H. Esmaeili, B. M. Bidgoli, V. Hakami, "CMML: Combined metaheuristic-machine learning for adaptable routing in clustered wireless sensor networks", Applied Soft Computing, 118, 108477, 2022.

[19] S. El Khediri, W. Fakhet, T. Moulahi, R. Khan, A. Thaljaoui, A. Kachouri, "Improved node localization using K-means clustering for Wireless Sensor Networks", Computer Science Review, 37, 100284, 2020.

[20] T. Mahmood, J. Li, Y. Pei, F. Akhtar, S. A. Butt, A. Ditta, S. Qureshi, "An intelligent fault detection approach based on reinforcement learning system in wireless sensor network", The Journal of Supercomputing, 78(3), 3646-3675, 2022.

[21] L. Li, Y. Qiu, J. Xu, "A K-means clustered routing algorithm with location and energy awareness for underwater wireless sensor networks", Photonics, Vol. 9, No. 5, p. 282, MDPI, 2022.

[22] M. Sathyamoorthy, S. Kuppusamy, R. K. Dhanaraj, V. Ravi, "Improved K-means based q learning algorithm for optimal clustering and node balancing in WSN", Wireless Personal Communications, 122(3), 2745-2766, 2022.

[23] J. Xu, Y. Zhang, J. Jiang, J. Kan, "A multi-hop routing protocol based on link state prediction for intra-body Wireless Nanosensor Networks", Ad Hoc Networks, 116, 102470, 2021.

[24] O. Gulec, E. Sahin, " Red Deer Algorithm based nano-sensor node clustering for IoNT", Journal of Network and Computer Applications, 103591, 2023.

[25] A. J. Garcia-Sanchez, R. Asorey-Cacheda, J. Garcia-Haro, J. L. Gomez-Tornero, "Dynamic Multihop Routing in Terahertz Flow-Guided Nanosensor Networks: A Reinforcement Learning Approach", IEEE Sensors Journal, vol. 23, no. 4, pp. 3408-3422, 2023.

[26] P. Nayak, K. G. Swetha, S. Gupta, K. Madhavi, "Routing in wireless sensor

networks using machine learning techniques: Challenges and opportunities", Measurement, 178, 2021.

[27] D. Stiawan, M. E. Suryani, M. Y. Idris, M. N. Aldalaien, N. Alsharif, R. Budiarto, "Ping flood attack pattern recognition using a K-means algorithm in an Internet of Things (IoT) network", IEEE Access, 9, 2021.

[28] H. Mahboubi, B. Stéphane, A. G. Aghdam, "A machine learning assisted method for coverage optimization in a network of mobile sensors", IEEE Transactions on Industrial Informatics, 2022.

[29] NS-3. Discrete-event network simulator for Internet systems [Online] Available: https://www.nsnam.org

[30] Nano-Sim. [Online] Available: https://telematics.poliba.it

[31] Networkx. Network analysis in Python [Online] Available: https://networkx.org

[32] Matplotlib. Visualization with Python [Online] Available: https://matplotlib.org

SAKARYA ÜNİVERSİTESİ
FEN BİLİMLERİ ENSTİTÜSÜ DERGİSİ

Sakarya University Journal of Science
SAUJS

ISSN 1301-4048 e-ISSN 2147-835X Period Bimonthly Founded 1997 Publisher Sakarya University
http://www.saujs.sakarya.edu.tr/

Title: Analyses of Chemical and Physical Egg Quality Parameters of Laying Hens Housed in Different Conditions in Turkey

Authors: Reyhan Selin UYSAL AFACAN

Recieved: 2022-07-26 00:00:00

Accepted: 2023-03-07 00:00:00

Article Type: Research Article

Volume: 27
Issue: 3
Month: June
Year: 2023
Pages: 603-613

How to cite
Reyhan Selin UYSAL AFACAN; (2023), Analyses of Chemical and Physical Egg Quality Parameters of Laying Hens Housed in Different Conditions in Turkey . Sakarya University Journal of Science, 27(3), 603-613, DOI: 10.16984/saufenbilder.1148878
Access link
https://dergipark.org.tr/en/pub/saufenbilder/issue/78131/1148878

Sakarya University Journal of Science 27(3), 603-613, 2023

Analyses of Chemical and Physical Egg Quality Parameters of Laying Hens Housed in Different Conditions in Turkey

Reyhan Selin UYSAL AFACAN*[1]

Abstract

The aim of the present study is to determine the content of chemical and physical quality parameters of hen eggs (liquid whole egg (LWE), liquid egg yolk (LEY), and liquid egg white (LEW)) produced for different housing and feeding conditions in Turkey. Chemical quality parameters (protein, lipid, and moisture) and physical quality parameters (total soluble solid (°Brix), pH, conductivity, and yolk:white ratio) were analyzed using different egg samples. Kjeldahl, wet ashing, and oven-drying official methods were used for the protein, total lipid, and moisture analyses of egg samples. The highest protein content in the LEY and LEW samples were found to be 19.0% and 15.13%, respectively for the tenth sample having fortified feeding (selenium+DHA) parameters. For LWE samples, it was also obtained 15.65% with the second sample having a not fortified feeding parameter. The highest total lipid content for LWE samples was determined as 10.43% for the seventh sample which housed under cage free conditions and fed with organic (omega3+EPA+DHA) fortifiers, while it was found with a value 25.7% for the second and third LEY samples possessing a not fortified feeding parameters. The highest moisture content was determined as 78.37%, 54.64%, and 89.11 for thirty-first LWE sample (with not fortified feeding), third LEY sample (with not fortified feeding) and sixth LEW sample (having cage free and organic parameters), respectively. As a result, the minimum, average, and maximum contents of the chemical and physical quality parameters were determined for laying hen eggs raised in several housing and feeding conditions in Turkey.

Keywords: Liquid egg, egg quality, egg component, egg analysis, laying hen

1. INTRODUCTION

Egg is one of the essential food in human diet due to its high nutrient (protein, essential lipids, vitamins and minerals) content [1]. Besides of its high nutritional values, it is one of the fundamental ingredients used in the products because of its multifunctional properties including emulsifying, foaming, gelling, thickening, and flavoring all of which provide the texture and sensory qualifications of food products [2].

In food industry, liquid egg products (whole egg, egg yolk, and egg white) usually are preferred by manufacturers instead of shell eggs because of its ease of use and microbial reliability [3]. In this point, it is crucial for the

* Corresponding author: selinuysal@beykoz.edu.tr (R. S. UYSAL)
[1] Department of Gastronomy and Culinary Arts, Faculty of Art and Design, Beykoz University, Beykoz, 34810, Istanbul, Turkey
ORCID: https://orcid.org/0000-0003-0028-7286

manufacturers to know that the quality parameters of the liquid egg products are within the expected values. The quality of egg has been determined by analyzing some interior physical (egg weight, albumen height, Haugh units, and yolk color, etc.) and chemical (contents of protein, lipid, and total solid, etc.) quality parameters [4, 5].

On the other hand, breeding conditions and age of hens could affect the level of egg components and the quality parameters of egg [6]. Therefore, it is critical for the manufacturers to know that the change in the level of the egg quality parameters according to the breeding conditions (such as feeding and housing) of hen. Hens have been breeding in different housing conditions such as conventional cage, free range, and barn [7]. In addition to this housing system, they have been feeding supplemented with several nutrients (such as chia, fish oil, and flaxseed) to improve the nutrition level (such as omega 3 fatty acids) of the egg [8]. While the housing and feeding conditions are the major factors affecting the chemical composition of egg, hen age and egg size are also one of the minor factors affecting the quality parameters of egg [9].

In these concepts, many studies have been performed in the literature results. Total fat and fatty acid contents were analyzed for different brands and housed in different systems of hen egg [10]. Effects of special dietary feeding of hen on mineral, vitamin, and albumen protein contents were investigated [11]. In another study with a special feeding, the effects of dietary Turkish propolis and vitamin C supplementation in diets were investigated on feed intake, body weight, body weight gain, feed conversion rate, digestibility, and on egg production and qualities in laying hens [12].

Fatty acid compositions were analyzed for hen egg housed in cage and cage free conditions [13]. Cholesterol, vitamins, and fatty acid compositions in egg were compared between the hen housed in conventional cage and range [14]. Chemical composition (protein and fat) and quality traits were tested for eggs yolk and from different production systems in Serbian [15]. In another study, laying performance, egg quality parameters, and yolk fatty acid profile of two Turkish layer genotypes were evaluated and their suitability for organic poultry production was investigated [16]. According to the above-mentioned research, the effect of different housing and feeding systems of hen on some chemical and quality parameters of eggs have been studied. However, in Turkey, the effect of several housing and feeding conditions of laying hen both on physical and chemical quality parameters of liquid whole egg (LWE), liquid egg yolk (LEY), and liquid egg white (LEW) has not been studied comprehensively in the literature.

The objective of the present study was to determine the content (the level of maximum, minimum, and average points) of chemical (protein, lipid, and moisture) and physical (yolk:white ratio, °Brix, pH, and conductivity) quality parameters of eggs (LWE, LEY, and LEW samples) produced in Turkey in different feeding and housing conditions such as cage, cage free, organic, fed with enriched dietary (omega 3, eicosapentaenoic acid (EPA), and docosahexaenoic acid (DHA), and selenium).

2. MATERIAL AND METHOD

2.1. Materials

A set of fresh shell egg samples (n=34) were purchased from the local markets in Turkey, housed and fed under a variety of parameters, including caged, cage free, and organic and enriched with omega 3, EPA, DHA, and selenium. In terms of the freshness of the egg samples, attention was paid to purchase only those whose production date was within the first week. Only medium-sized eggs were used in the analysis. In addition, egg samples were also classified according to whether the hen was young or not. Housing, feeding, and hen age parameters of LWE, LEY, and LEW

samples are listed in Table 1. As can be seen in the table; these parameters can be categorized as cage (n=19), cage-free (n=15), and organic (n=11) housing systems; various feeding systems fortified with omega 3, (omega3 + EPA + DHA), and (selenium + DHA) or not and hen ages young or not.

Table 1 Housing and feeding parameters of liquid egg samples

No	Cage	Cage free	Organic	Fortified (Omega3)	Fortified (Omega3+EPA+DHA)	Fortified (Selenium+DHA)	Hen age (Young)
1¶	X						
2¶	X						
3¶	X						X
4¶	X						X
5¶		X	X				X
6¶		X	X				
7¶		X	X		X		
8¶	X						
9¶	X			X			
10¶	X					X	
11¶		X	X				
12¶		X					
13¶		X	X				
14		X					
15		X					
16		X					
17	X						
18		X	X				
19	X						X
20		X	X				
21		X	X				
22	X						
23	X						
24	X						X
25	X						X
26		X	X				
27	X						
28	X						
29	X						X
30		X	X				
31	X						
32	X						
33		X	X				
34	X						

¶ The bold numbers indicate shell egg samples whose liquid whole egg, liquid egg yolk, and liquid egg white were analysed.

All samples of LWE (n=34), LEY (n=13) and LEW (n=13) were prepared using shell eggs at laboratory scale. LEY and LEW samples were prepared manually, shell egg was broken and separated as white and yolk. Then the white and yolk samples were homogenized (IKA T-18 Ultra Turrax Digital Homogenizer, IKA Company, Deutschland, Germany) separately at 615×g for 3 minutes. The LWE egg samples were also manually broken as a whole egg and homogenized at 615×g for 3 minutes. Yolk:white ratio of LWE samples were determined by weighing their weight (yolk and white) separately and then calculated the ratio of yolk:white as percentage. The quality of liquid egg samples

was evaluated by analyzing chemical parameters such as the content of protein, total lipid, and moisture and by measuring of physical parameters that are °Brix, pH, and conductivity.

2.2. Chemical analyses of liquid egg samples

LWE, LEY, LEW samples were prepared for the protein, total lipid, and moisture analyses. Kjeldahl analysis was performed to measure the protein content in accordance with the method proposed by AOAC. Moisture content of the egg samples was also determined by AOAC method [17]. The percentage of nitrogen is multiplied by a conversion factor of 6.25 to calculate the percentage of protein in the egg samples. Total lipid content of the egg samples was detected as defined in the Official Methods of Analysis of AOAC [18].

2.3. Physical measurements of liquid egg samples

Total soluble solid (TSS, °Brix), pH, and electrical conductivity values of liquid egg samples were measured. The pH values of LWE, LEY, and LEW samples were measured by using pH meter (Mettler-Toledo, Columbus, USA) at the ambition temperature. TSS contents of LWE, LEY and LEW samples were measured with an optical refractometer (RFM 330, Bellinghma + Stanley Ltd, UK). 1 mL was poured into the refractometer glass prism, and the measurements were taken at 25°C. Then, the measured data were recorded as °Brix value of the sample. Conductivity measurements of LWE samples were also taken using a handheld conductivity meter (HI8734, Hanna Instruments, Melbourne, Australia). Then, the reading was recorded as conductivity value of the sample.

3. CONCLUSIONS AND DISCUSSION

For liquid whole egg (LWE) samples, the chemical parameter values with protein, lipid, moisture, and physical parameter values, TSS (°Brix), pH, conductivity, and yolk:white ratio are presented in Table 2. As can be seen from the table, yolk:white ratios of egg are observed between 25.7:74.3 and 36.1:63.9. The average yolk:white ratio of LWE was calculated as 31:69 that value seems to be compatible with the literature results [19, 20]. As can be given in Table 2, protein values of the LWE samples were observed in the range from 11.59% to 15.65%. The average protein value of these samples is obtained as 12.84%. When detected values were compared to with the findings in the literature, proteins of LWE was found consistent with the reported results [21].

The average total lipid values of LWE samples were obtained 7.71%. The total lipid values were observed between in the range of 5.47–10.43%. The range of the lipid values were consistent with the literature results [22]. It can be seen in Table 2 that feeding with (omega3 + EPA + DHA) fortifiers affected to increase in lipid value of egg such as seventh sample (10.43%) which is the highest lipid value among the samples. Then, usage of fortifiers (omega 3) and (selenium + DHA) also led to increment in lipid values as 9.93% (ninth) and 9.01% (tenth sample). Huang, et al. [23] reported that feeding with dietary fish oil affected on omega-3 fatty acid levels (EPA and DHA) in hen egg.

Table 2 Values of chemical and physical parameters of liquid whole egg samples

No	Protein (%)	Lipid (%)	Moisture (%)	°Brix	pH	Conductivity (m/S)	Yolk:White Ratio (w:w, %)
1	14.08±0.57	7.98±0.69	78.06±0.03	22.5	7.59	5.92	30.5:69.5
2	15.65±0.66	8.39±0.58	77.91±0.01	22.2	7.20	6.48	28.7:71.3
3	15.18±0.17	7.07±0.26	76.88±0.03	22.5	7.41	6.22	34.5:65.5
4	15.15±0.16	9.36±0.40	76.16±0.01	25.4	7.45	6.36	29.7:70.3
5	13.20±0.05	6.99±0.40	76.23±0.03	25.1	7.40	6.22	32.3:67.7
6	13.61±0.31	8.55±0.90	76.38±0.02	24.6	7.38	5.11	33.2:66.8
7	14.87±0.35	10.43±0.45	76.62±0.03	22.2	7.41	5.13	36.1:63.9
8	14.62±0.27	7.87±0.88	77.64±0.05	22.5	7.56	6.42	32.6:67.4
9	13.64±0.30	9.93±0.50	75.11±0.02	26.3	7.60	6.37	31.1:68.9
10	13.98±0.03	9.01±0.30	77.12±0.07	23.6	7.59	6.37	32.6:67.4
11	15.21±0.74	7.78±0.28	76.31±0.19	25.5	7.55	6.50	29.8:70.2
12	13.98±0.65	7.67±0.91	76.83±0.27	24.4	7.59	6.21	33.4:66.6
13	13.80±0.29	6.29±0.34	78.58±0.09	23.0	7.70	6.22	27.0:73.0
14	13.96±0.25	6.75±0.21	76.18±0.02	26.9	7.12	6.50	28.0:72.0
15	13.13±0.21	6.32±0.25	76.43±0.01	25.6	7.34	6.55	30.0:70.0
16	14.58±0.27	7.03±0.32	75.82±0.01	27.6	7.25	6.10	29.5:70.5
17	14.12±0.10	6.95±0.52	77.94±0.02	24.8	7.61	6.52	25.7:74.3
18	13.84±0.35	7.80±0.30	77.48±0.00	26.3	7.54	6.49	29.6:70.4
19	14.04±0.44	5.50±0.21	76.54±0.01	25.9	7.43	6.34	30.1:69.9
20	13.49±0.17	8.15±0.65	75.77±0.01	28.0	7.39	6.21	32.9:67.1
21	14.73±0.15	7.35±0.47	75.87±0.01	24.9	7.67	6.36	29.3:70.7
22	15.22±0.19	6.90±0.80	75.68±0.01	28.0	7.55	6.40	29.0:71.0
23	13.72±0.07	7.02±0.55	74.94±0.01	27.3	7.17	6.50	35.5:64.5
24	13.72±0.29	7.05±0.22	76.17±0.02	27.0	7.39	6.20	31.4:68.6
25	12.08±0.07	8.10±0.32	76.59±0.01	26.2	7.53	5.70	33.2:66.8
26	12.31±0.30	8.14±0.78	75.89±0.02	27.2	7.38	5.10	30.5:69.5
27	12.22±0.18	6.77±0.57	76.89±0.01	25.9	7.63	6.10	28.5:71.5
28	12.50±0.03	6.81±0.86	76.88±0.03	26.2	7.58	5.60	34.6:65.4
29	12.35±0.36	5.47±0.19	77.30±0.02	25.7	7.60	5.90	29.9:70.1
30	13.73±0.34	7.21±0.09	76.67±0.01	26.8	7.81	6.20	27.2:72.8
31	11.59±0.59	6.82±0.15	78.37±0.00	24.5	7.68	6.50	31.3:68.7
32	12.06±0.04	7.31±0.86	76.82±0.01	26.6	7.58	6.20	33.2:66.8
33	12.92±0.06	8.70±0.26	76.08±0.00	26.5	7.69	6.10	30.7:69.3
34	12.46±0.11	7.39±0.05	76.01±0.00	27.5	7.55	6.40	30.4:69.6

Enrichment of eggs with omega 3 sources is an applied method to increase and improve the fatty acid profiles in hen eggs [24]. The moisture level of LWE samples were obtained in the range from 74.94% to 78.58%. The average level of moisture was calculated as 76.64%. The moisture range was found compatible with another studies. Besides chemical parameters of egg, value, TSS content (°Brix) was also measured for LWE samples. TSS content of LWE samples were obtained within the range of 22.2–28.0 °Brix. The average TSS content of LWE samples were calculated as 25.57 °Brix. Average value of TSS content with 26.03 °Brix was found in consistent with the literature results.

Another physical parameter of egg, pH value was also controlled. The pH value of LWE egg was observed between these values of

7.12–7.81. the average value of pH measurements of LWE samples was obtained as 7.5. In another study, pH value of LWE was measured as 7.67 that is consistent with the result of present study [25]. pH measurement has an important role to indicate the fresh of shell egg. Storage can affect some characteristics of egg such as loss of carbon dioxide that causes to increase in the pH of the albumen albumen [26]. The last analysis from physical measurements was electrical conductivity of LWE samples. Electrical conductivity of egg is one of the main characteristics of egg that changes according to storage time. Measurement of electrical conductivity uses to check the physical change during storage period of egg [27]. In the present study, results of conductivity measurements of LWE were obtained in the range from 5.10–6.55 m/S. The average value of electrical conductivity of egg was calculated as 6.16 m/S.

For liquid egg yolk (LEY) and white (LEW) samples, physical and chemical analyses were also performed. Using a set of 13 egg samples, values of protein, lipid, moisture, TSS (°Brix), and pH were analyzed. The housing and feeding properties of the egg samples are also presented in Table 1. As can be seen in the table, the differences between the samples include several housing and feeding systems, organic egg, and hen ages. Protein values of LEY and LEW samples are shown in Figure 1.

As can be seen in Figure 1, protein values were in the range of 16.74–19.0% and 10.69–15.13% for LEY and LEW samples, respectively. The average protein values of LEY and LEW samples were 17.89% and 12.57%. Obtained values were found consistent with the literature results. Among yolk components, proteins are the main molecules, which compose 64% of yolk granules on a moisture-free basis. Most yolk protein structure exists in lipoprotein structure such as low-density lipoprotein (LDL) and high-density lipoprotein (HDL). The other proteins are available as apoproteins (phosvitin and livetin) [28].

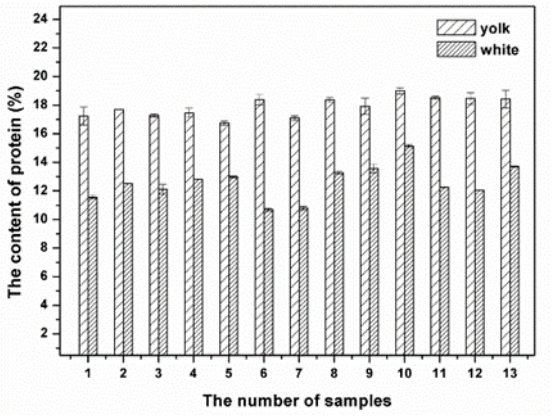

Figure 1 The protein contents (%) of liquid egg yolk (LEY) and liquid egg white (LEW) samples

Egg white (albumen) is approximately 10% aqueous solution of various proteins that mainly comprises of ovalbumin (54%), conalbumin (12%), ovomucoid (11%), ovomucin (3.5%) [29]. Lipid values of LEY and LEW samples are presented in Figure 2.

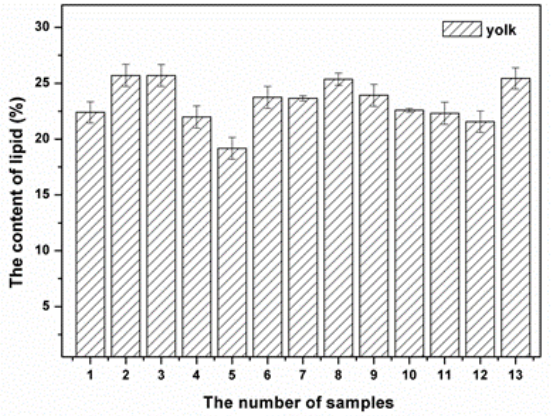

Figure 2 The total lipid contents (%) of liquid egg yolk (LEY) samples

As expected, for LEY samples, high lipid values were obtained between 19.17–25.7%. The average lipid value was calculated as 23.35%. On the other hand, the lipid content of LEW was relatively low and obtained as <0.1%. Thus, this value can be neglected in the LEW samples. Consequently, the measured values were compared with the findings in another studies, lipid values of LEY and LEW were found consistent with the reported results.

Moisture contents of LEY and LEW samples are demonstrated in Figure 3. Moisture contents were found between 49.26–54.64% and 86.54–89.11% for LEY and LEW samples, respectively. The average moisture values of LEY and LEW samples were 51.85% and 87.51%. As lipid and protein contents are high in LEY, dry matter content in LEY is lower compared to the LEW samples. Moisture results of the LEY and LEW samples were found consistent with the literature results [30].

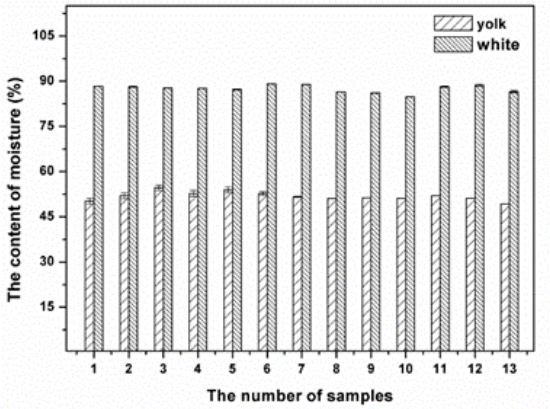

Figure 3 The moisture contents (%) of liquid egg yolk (LEY) and liquid egg white (LEW) samples

°Brix measurement, one of the physical analyses of egg samples, was performed to determine TSS content of the LEY and LEW samples. The TSS contents of LEY and LEW samples are shown in Figure 4. The TSS contents of the LEY and LEW samples were obtained in the range of 45.6–48.4 °Brix and 13.5–19.2 °Brix, respectively. Average TSS contents of the LEY and LEW samples were calculated as 46.6 and 16.2 °Brix, respectively. °Brix measurement can be used in the quality control analysis of eggs. As can be seen in Figures 3 and 4, moisture and TSS values of the LEY and LEW samples seem compatible when these values are compared to each other.

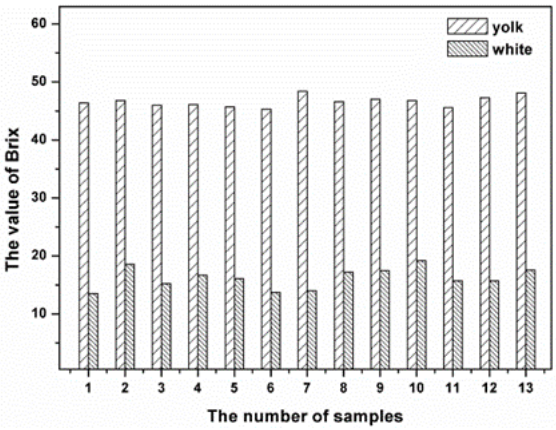

Figure 4 The total soluble solid contents (°Brix) of liquid egg yolk (LEY) and liquid egg white (LEW) samples

The last measurements of LEY and LEW samples were pH analysis. pH values of these samples are demonstrated in Figure 5. While pH values of the LEY samples were observed between 6.08–6.37, the LEW samples were between 8.84–9.04. The average pH values of the LEY and LEW samples were calculated as 6.2 and 8.9.

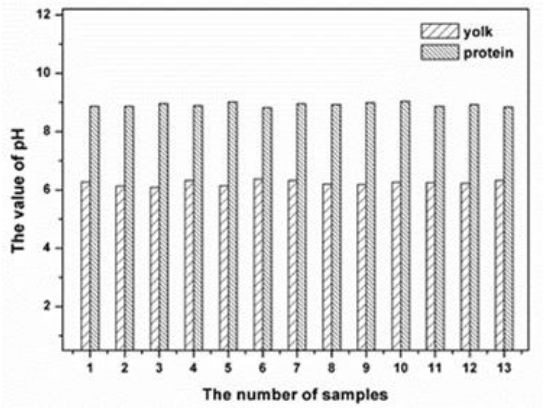

Figure 5 The values of pH measurements of liquid egg yolk (LEY) and liquid egg white (LEW) samples

In a study, the mean pH value of egg albumen was detected as 8.8 [31]. pH measurements are associated with the freshness and storage of egg albumen. As can be mentioned in the above, storage can affect the pH value of egg albumen due to loss of carbon dioxide that causes to increase in the pH of the albumen [32]. In another study, pH values of fresh egg albumen (the first day) were measured as about 7.9 then, it increased to the value of 8.9 during the egg storage (within about five

days). In another work, pH value of albumen increased from 7.4 to 8.6 in daily storage. Then, in the second day of storage, it raised up to 9.0 [33].

These results show that pH of albumen is very sensitive to the storage of egg. In the experiments, it was tried to use fresh eggs (within the first week of production date). However, the egg samples were purchased from the market, getting a daily egg has been difficult. Thus, used eggs in the experiments might be a few days old. Consequently, the maximum, minimum, and average values of protein, lipid, moisture, TSS (°Brix), conductivity, and pH analyses of liquid egg samples, which were produced under several housing and breeding parameters of hen egg in Turkey, were presented and evaluated with the literature results. In conclusion, these results will provide important contributions to the the literature and the food industry regarding egg quality parameters.

4. CONCLUSION

The present study provides measurements of chemical and physical parameters of eggs with a wide range of samples. Analyses were performed for the LWE, LEY, and LEW samples. The average yolk:white ratio of the egg samples was obtained as 31:69. The protein values of LWE, LEY, and LEW samples were found in the range of 11.59–15.65%, 16.74–19.00%, and 10.69–15.13%, respectively. The highest lipid value was analyzed for the LEY samples. These values of the egg samples, LWE, LEY, and LEW, were obtained between 5.47–10.43%, 19.17–25.7%, and <0.1%, respectively. The least moisture level was also found for the LEY samples due to the high value of lipid and protein. The moisture levels of the samples were observed in the range from 74.94 to 78.58%, 49.26 to 54.64%, and 86.54 to 89.11%. On the other hand, TSS values were measured proportional to the total solid contents of the samples (LWE, LEY, and LEW) such as, 22.2–28.0 °Brix, 45.6–48.4 °Brix, and 13.5–19.2 °Brix. The average pH level of the LEW, LEY, and LEW samples were measured as 7.67, 6.2 and 8.9. At last, conductivity measurements of the LWE samples were resulted as the average value of 6.16 m/S.

Funding
The author (s) has no received any financial support for the research, authorship or publication of this study.

Authors' Contribution
The authors contributed equally to the study.

The Declaration of Conflict of Interest/ Common Interest
No conflict of interest or common interest has been declared by the authors.

The Declaration of Ethics Committee Approval
This study does not require ethics permission or any special permission.

The Declaration of Research and Publication Ethics
The authors of the paper declare that they comply with the scientific, ethical and quotation rules of SAUJS in all processes of the paper and that they do not make any falsification on the data collected. In addition, they declare that Sakarya University Journal of Science and its editorial board have no responsibility for any ethical violations that may be encountered, and that this study has not been evaluated in any academic publication environment other than Sakarya University Journal of Science.

REFERENCES

[1] B. A. Watkins, "The Nutritive Value of the Egg," in Egg Science and Technology, J. S. William and O. J. Cotterill, Eds. New York: Haworth Press, 1995, pp. 177-194.

[2] M. Rossi, E. Casiraghi, L. Primavesi, C. Pompei, A. Hidalgo, "Functional properties of pasteurised liquid whole

egg products as affected by the hygienic quality of the raw eggs," LWT - Food Science and Technology, vol. 43, no. 3, pp. 436-441, 2010.

[3] Y. C. Wong, T. J. Herald, K. A. Hachmeister, "Comparison Between Irradiated and Thermally Pasteurized Liquid Egg White on Functional, Physical, and Microbiological Properties," Poultry Science, vol. 75, no. 6, pp. 803-808, June 1, 1996 1996.

[4] D. Jones M. Musgrove, "Effects of extended storage on egg quality factors," Poultry Science, vol. 84, no. 11, pp. 1774-1777, 2005.

[5] J. R. Roberts, "Factors affecting egg internal quality and egg shell quality in laying hens," The Journal of Poultry Science, vol. 41, no. 3, pp. 161-177, 2004.

[6] Y. Suk C. Park, "Effect of breed and age of hens on the yolk to albumen ratio in two different genetic stocks," Poultry Science, vol. 80, no. 7, pp. 855-858, 2001.

[7] C. Sherwin, G. Richards, C. Nicol, "Comparison of the welfare of layer hens in 4 housing systems in the UK," British Poultry Science, vol. 51, no. 4, pp. 488-499, 2010.

[8] R. Coorey, A. Novinda, H. Williams, V. Jayasena, "Omega-3 fatty acid profile of eggs from laying hens fed diets supplemented with chia, fish oil, and flaxseed," Journal of Food Science, vol. 80, no. 1, pp. 180-187, 2015.

[9] F. Silversides, D. Korver, K. Budgell, "Effect of strain of layer and age at photostimulation on egg production, egg quality, and bone strength," Poultry Science, vol. 85, no. 7, pp. 1136-1144, 2006.

[10] G. Cherian, T. Holsonbake, M. Goeger, "Fatty acid composition and egg components of specialty eggs," Poultry Science, vol. 81, no. 1, pp. 30-33, 2002.

[11] C. Novak, H. Yakout, S. Scheideler, "The combined effects of dietary lysine and total sulfur amino acid level on egg production parameters and egg components in Dekalb Delta laying hens," Poultry Science, vol. 83, no. 6, pp. 977-984, 2004.

[12] P. T. Seven, "The effects of dietary Turkish propolis and vitamin C on performance, digestibility, egg production and egg quality in laying hens under different environmental temperatures," Asian-Australasian Journal of Animal Sciences, vol. 21, no. 8, pp. 1164-1170, 2008.

[13] R. G. Torde, A. J. Therrien, M. R. Shortreed, L. M. Smith, S. M. Lamos, "Multiplexed analysis of cage and cage free chicken egg fatty acids using stable isotope labeling and mass spectrometry," Molecules, vol. 18, no. 12, pp. 14977-14988, 2013.

[14] K. E. Anderson, "Comparison of fatty acid, cholesterol, and vitamin A and E composition in eggs from hens housed in conventional cage and range production facilities," Poultry Science, vol. 90, no. 7, pp. 1600-1608, 2011.

[15] L. Perić, M. Đ. Stojčić, S. Bjedov, "Effect of production systems on quality and chemical composition of table eggs," Contemporary Agriculture, vol. 65, no. 3-4, pp. 27-31, 2016.

[16] A. Sözcü, A. İpek, Z. Oguz, S. Gunnarsson, A. B. Riber, "Comparison of performance, egg quality, and yolk fatty acid profile in two Turkish genotypes (Atak-S and Atabey) in a free-range system," Animals, vol. 11, no. 5, p. 1458, 2021.

[17] W. Horwitz, Official Methods of Analysis of the AOAC. Arlington, VA: Washington DC, 1980.

[18] S. Willians, Official methods of Analysis of the Association of Official Analytical Chemists, 14th ed. Arlington, VA: Association of Official Analytical Chemists, 1984.

[19] M. Warren, D. Larick, H. Ball Jr, "Volatiles and sensory characteristics of cooked egg yolk, white and their combinations," Journal of Food Science, vol. 60, no. 1, pp. 79-84, 1995.

[20] M. Warren H. Ball Jr, "Effect of concentration of egg yolk and white on fresh scrambled egg flavor," Poultry Science, vol. 70, no. 10, pp. 2186-2190, 1991.

[21] J. Wu, "Eggs and Egg Products Processing," in Food Processing: John Wiley & Sons, Ltd, 2014, pp. 437-455.

[22] H.-D. Belitz, W. Grosch, P. Schieberle, "Eggs," in Food Chemistry, W. Grosch and P. Schieberle, Eds. Leipzig, Germany: Springer, 2009, pp. 546-562.

[23] Z. Huang, H. Leibovitz, C. M. Lee, R. Millar, "Effect of dietary fish oil on .omega.-3 fatty acid levels in chicken eggs and thigh flesh," Journal of Agricultural and Food Chemistry, vol. 38, no. 3, pp. 743-747, 1990.

[24] I. Fraeye, C. Bruneel, C. Lemahieu, J. Buyse, K. Muylaert, I. Foubert, "Dietary enrichment of eggs with omega-3 fatty acids: A review," Food Research International, vol. 48, no. 2, pp. 961-969, 2012.

[25] N. Hermawan, G. A. Evrendilek, W. Dantzer, Q. Zhang, E. Richter, "Pulsed electric field treatment of liquid whole egg inoculated with Salmonella enteritidis," Journal of Food Safety, vol. 24, no. 1, pp. 71-85, 2004.

[26] H. Akyurek A. A. Okur, "Effect of storage time, temperature and hen age on egg quality in free-range layer hens," Journal of Animal Veterinary Advances, vol. 8, no. 10, pp. 1953-1958, 2009.

[27] L. Ragni, A. Al-Shami, G. Mikhaylenko, J. Tang, "Dielectric characterization of hen eggs during storage," Journal of Food Engineering, vol. 82, no. 4, pp. 450-459, 2007.

[28] M. Anton, V. Beaumal, G. Gandemer, "Adsorption at the oil–water interface and emulsifying properties of native granules from egg yolk: effect of aggregated state," Food Hydrocolloids, vol. 14, no. 4, pp. 327-335, 2000.

[29] R. S. Uysal, İ. H. Boyacı, E. A. Soykut, N. Ertaş, "Effects of heat treatment parameters on liquid whole egg proteins," Food Chemistry, vol. 216, pp. 201-208, 2017.

[30] D. Ahn, S. Kim, H. Shu, "Effect of egg size and strain and age of hens on the solids content of chicken eggs," Poultry Science, vol. 76, no. 6, pp. 914-919, June 1, 1997 1997.

[31] E. Shenga, R. Singh, A. Yadav, "Effect of pasteurization of shell egg on its quality characteristics under ambient storage," Journal of Food Science and Technology, vol. 47, no. 4, pp. 420-425, 2010.

[32] N. Abdel-Nour, M. Ngadi, S. Prasher, Y. Karimi, "Prediction of egg freshness and albumen quality using visible/near infrared spectroscopy," Food Bioprocess Technology, vol. 4, no. 5, pp. 731-736, 2011.

[33] J. Goodrum, W. Britton, J. Davis, "Effect of storage conditions on albumen pH and subsequent hard-cooked egg peelability and albumen shear strength," Poultry Science, vol. 68, no. 9, pp. 1226-1231, 1989.

SAKARYA ÜNİVERSİTESİ
FEN BİLİMLERİ ENSTİTÜSÜ DERGİSİ

Sakarya University Journal of Science
SAUJS

ISSN 1301-4048 e-ISSN 2147-835X Period Bimonthly Founded 1997 Publisher Sakarya University
http://www.saujs.sakarya.edu.tr/

Title: Comparing the Shielding Features of Graphene and Impregnated Activated Carbon with Selected Traditional Shielding Materials For Gamma-Rays

Authors: Dilara İCKECAN, Nureddin TURKAN, Doğan ERBAHAR, Hasan GÜLBİÇİM

Recieved: 2022-08-02 00:00:00

Accepted: 2023-03-07 00:00:00

Article Type: Research Article

Volume: 27
Issue: 3
Month: June
Year: 2023
Pages: 614-620

How to cite
Dilara İCKECAN, Nureddin TURKAN, Doğan ERBAHAR, Hasan GÜLBİÇİM; (2023), Comparing the Shielding Features of Graphene and Impregnated Activated Carbon with Selected Traditional Shielding Materials For Gamma-Rays . Sakarya University Journal of Science, 27(3), 614-620, DOI: 10.16984/saufenbilder.1152986
Access link
https://dergipark.org.tr/en/pub/saufenbilder/issue/78131/1152986

Sakarya University Journal of Science 27(3), 614-620, 2023

Comparing the Shielding Features of Graphene and Impregnated Activated Carbon with Selected Traditional Shielding Materials For Gamma-Rays

Dilara ICKECAN [*1], Nureddin TURKAN[2], Dogan ERBAHAR[3], Hasan GULBICIM[4]

Abstract

Graphene and carbon-based materials are widely used in daily life applications. The richness of optical and electronic properties has made them rapidly rising materials on the horizon of material science and condensed matter physics. Having the sheets of atoms stacked in disorganized manner makes activated carbon different from other forms of graphitic structures. The research about the shielding properties of reduced graphene oxide (RGO) and activated carbon for gamma-rays are very rare and active domain of study. Since the use of radioactive sources in different fields (nuclear industry, shielding materials, radiation biophysics and space research application, etc.) has been increasing expeditiously, the photon interactions with matter have gained importance in the world of material science technology. In this work, we review the basics of the impregnated activated carbon (AC) and RGO, as well as the relationship between the structures and the gamma shielding properties in terms of both quality and efficiency. XCom software and EGSnrc simulation code were used to obtain the theoretical values of various shielding parameters which are significantly important to be able to understand the shielding properties of AC and RGO for gamma-rays. We report the mass attenuation coefficients (μ_m), the half value layer (HVL), the tenth value layer (TVL), and the mean free path (MFP) values and compare them with other commonly used shielding materials like lead, borosilicate, concrete, and vermiculite. The calculated data showed that AC is very appropriate and consistent to be one of the candidates for shielding materials of gamma-rays even though the graphene is seen as inconsistent for such purpose.

Keywords: Activated carbon, graphene, absorption, shielding materials, gamma-rays

1. INTRODUCTION

The use of radiation sources has been increasing in various technological and industrial domains. Considering the potential health risks of ionizing radiation, shielding becomes an important issue in all these applications. For this reason, research on

* Corresponding author: dilaraickecan@marun.edu.tr (D. ICKECAN)
[1] Marmara University, Department of Physics, 34724, Istanbul, Turkey
[2] Istanbul Medeniyet University, Department of Physics Engineering,Istanbul, Turkey
[3] Dogus University, Department of Mechanical Engineering, Istanbul, Turkey
[4] Ondokuz Mayıs University, Department of Nuclear Medicine,Samsun, Turkey
E-mail: nureddin.turkan@medeniyet.edu.tr; derbahar@dogus.edu.tr; hasanglbcm@gmail.com
ORCID: https://orcid.org/0000-0002-6957-9095, https://orcid.org/0000-0002-0452-9484, https://orcid.org/0000-0002-8633-4284, https://orcid.org/0000-0003-4518-2509

radiation shielding material for protection radiation have become important [1]. In the field of radiation shielding, studies are continuing to develop light, durable, economical, and non-toxic [2, 3] materials. In this context Carbon-based materials constitute an important candidate [4-9].

Carbon is a strange special material having s[low dimensional structures such as activated carbon (AC), graphite, graphene, and carbon nanotubes. The graphene has excellent mechanical, thermal, electrical and optical properties coming from its two-dimensional structure [10] for various applications [11, 12] (supercapacitors, batteries, solar cells, biosensors etc.).The activated carbon structures are similar to graphite, but it is an amorphous carbon structure primarily containing six-membered rings with sp2 hybridized carbons and is one the first materials applied as absorbent [13] for filtering purposes. AC has been widely used for water treatment, chemical industry, food industry, etc .[14] Recently it has been demonstrated that AC impregnated with various metal atoms (copper, silver, chromium, etc.) which usually exists in the form of an oxide crystallite can be effective for gamma ray shielding [9]. This form of carbon is called impregnated activated carbon (AC).

The purpose of this work is to search the shielding features of graphene along with AC for gamma-ray absorption. The important shielding parameters like the the half-value layer (HVL), mean free path (MFP), mass attenuation coefficients (μ_m), and the tenth value layer (TVL) were calculated for reduced graphene oxide (RGO) and AC. These values were compared with the data from vermiculite, borosilicate glass, lead, and concrete samples. The obtained results show that AC can be thought to be one of the candidates for shielding materials of gamma-rays, but graphene can not be.

2. EXPERIMENTAL AND THEORETICAL DETAILS

2.1. Materials

The reduced graphene oxide (RGO) which is also called as graphene was used in the present work and was essentially carried out by the process having two steps. So, in the first step, the graphene oxide (GO) is obtained by oxidation of graphene and then it was reduced via the agents to form RGO as a second step. The experimental details related to the study was presented in our previous work [15, 16]. The AC (obtained by the shell of coconut having the particle size about 8~16 mesh) was supplied by Norit Company, in which such materials composing of 5 % wt of triethylenediamine TEDA [17, 18].

2.2. Methods

2.2.1 SEM/EDS analysis

The physical morphology of the surface was analyzed, and the elemental analysis of RGO and AC samples was conducted by scanning electron microscopy (*JEOL 6510-LV JSM SEM* by TUBITAK). The sample properties of AC and RGO on EDS are summarized in Table 1. EDS results show that, RGO sample contains 78.99 %C, 16.04 %O, 2.98 %S, 0.98 %H, 1.01 %N whereas AC has 3.84 % Mo, 79.88 %C, 0.55% K, 1.95 % Zn, 6% Cu, 7.65 %O and 0.13% Si.

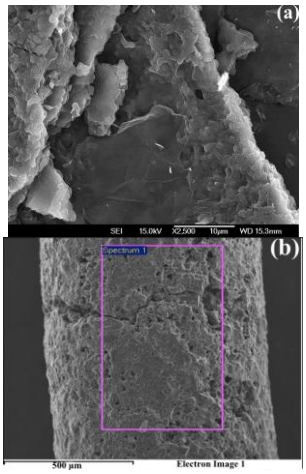

Figure 1 Comparing of (a) SEM image of RGO and (b) SEM image of AC [9].

It can be seen from Table 1 that graphene (RGO) gives the higher density 1.91 g/cm^3 when compared to AC (0.54 g/cm^3).

Table 1 The weight percentages of different elements forming the surfaces (%) of RGO, and AC samples based on EDS.

Elements	Weight percentages of surface elements	
	Graphene (RGO)	AC
C	78.99	79.88
O	16.04	7.65
S	2.98	-
H	0.98	-
N	1.01	-
Zn	-	1.95
Cu	-	6.0
Mo	-	3.84
Si	-	0.13
K	-	0.55
Density g/cm^3	1.91	0.54

SEM images of RGO and AC are given in Figure 1. (a-b). Figure 1. (a) shows SEM image of RGO with little wrinkles on the surface and some folds at the edges. It can be shown from Figure 1. (b) that AC has grains and cracks of various sizes hosting micro holes in its structure. EDS analysis is performed with the current images coming from SEM. So, such images enable assessment of the surface of a sample as well as individual components and targeted analysis of the sample.

2.1.1. Calculation Methods of Shielding Parameters

Linear attenuation coefficients (μ) is an important parameter to explain the gamma and X-rays radiation protection properties of a material. The linear attenuation coefficients (μ) is computed according to Beer-Lambert Law [19],

$$I=I_0e^{-\mu x} \quad (1)$$

where I and I_0 indicates the attenuated and incident radiation intensity and x is the thickness of the absorber. The definition of mass attenuation coefficient is the ratio of linear attenuation coefficient to the material density. It is possible to compare materials in terms of their mass attenuation coefficient. The μ_m is defined as μ/ρ. The HVL, TVL and MFP are important parameters used to compare samples for each other to understand their gamma shielding features. The HVL is defined as the absorber thickness required to halve the radiation intensity. To calculate HVL, ln 2 is divided by linear attenuation coefficient (ln $2/\mu$). TVL, is the absorber thickness required to absorb 90 % of the radiation intensity. TVL is calculated as ln $10/\mu$. The values of HVL and TVL depend on the linear attenuation coefficient. The mean free path (MFP) of photons in matter is defined as the thickness of the sample at which 36.8 % of the initial radiation intensity can be absorbed [20]. The mean free path is equal to inverse of linear attenuation coefficient.

2.2.3 Monte Carlo calculation

The Monte Carlo (MC) is a method which is widely used in shielding simulation. In this study, The Electron Gamma Shower (EGSnrc) simulation code and XCom software are chosen to calculate the radiation shielding parameters. For the MC calculations, the material content was first created in EGSnrc using the PEGS4 user code which is used as software of general-purpose device. So, such a simulation of coupled electron-photons are set in a random 3D geometry with a wide energy range from a few keV up to hundreds of GeV [21]. The simulation setup is then modeled as having a narrow-beam geometry. In this geometry, the sample is modeled with infinite dimensions in the x-y plane and with appropriate thickness in the z plane. The simulated photons were directed perpendicular towards the center of x-y plane and the photons having the same incident energy and direction parallel to +z-axis were counted. Afterwards, the linear attenuation coefficients were calculated for different photon energies using Eq. 1. Figure 2 gives the schematic diagram of geometry of the set up used in Monte Carlo simulations.

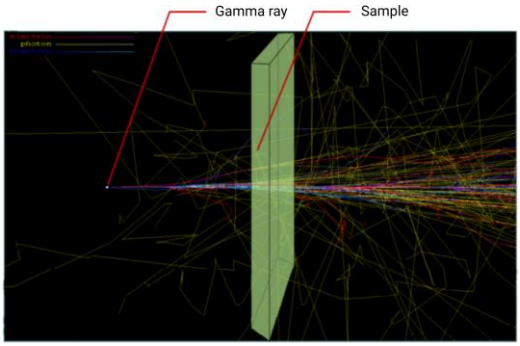

Figure 2 Schematic diagram of geometry of the set up used in Monte Carlo simulations.

The important parameters interested in the photon energies, geometry and materials definitions were provided and the simulations were performed by using 2 x 10^8 photon history to reduce the uncertainty to a value less than 1 %. The calculated μ_m of graphene for gamma-rays at photon energies of 1.0 kev-10.0 MeV were compared with the results of AC, vermiculite, borosilicate glass, lead, and concrete materials [9, 22].

3. RESULT AND DISCUSSION

The radiation shielding properties of RGO are examined to be able to understand the gamma-ray absorption characteristics along with those of AC, vermiculite, borosilicate glass, lead, and vermiculite. The XCom code and EGSnrc software are used for the theoretical calculations of the μ_m values for the RGO. The calculated results were compared to the previous theoretical [9] and experimental [21] results of some known shielding materials as AC, vermiculite, borosilicate glass, lead, and concrete. Such comparisons are clearly seen in the following figures in which the μm, the HVL, the TVL and MFP are shown as figures 3,4,5 and 6.

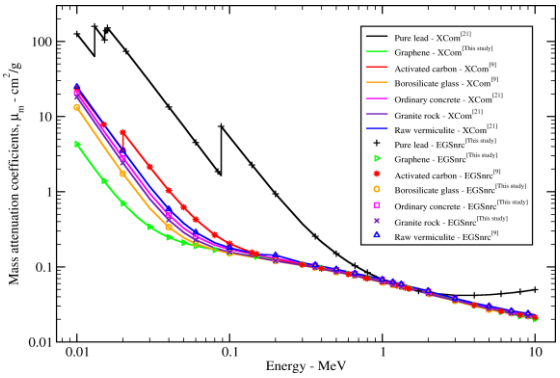

Figure 3 The comparing of the calculated μm for graphene (RGO) is supplied with some previous calculated results [9, 22] for AC, vermiculite, borosilicate glass, lead, and concrete.

As it is seen from the Figure 3, the μm are exponentially decreasing with the increase of the photon energy. The mass attenuation coefficient of RGO is at the lowest values of that of the others, which is showing that it isthe weakest candidate of shielding materials for gamma radiation when compared to the standard materials. In addition, as it is seen from the figure, the μ_m values decreases rapidly at the photon energies less than 0.1 MeV for all materials, since the interaction process between the photon and matter is more dominant in this energy region. From Figure 3, it can easily be seen that there are some jumps which are discontinuous for AC and lead in the same energy region. The reason can be defined by the absorption edges in K, L, M... shells of atoms of such elements. The μ_m values reduce slowly in the range of energy changing from 0.1 to 2.0 MeV, in which the Compton scattering is dominant. At photon energies below 0.1 MeV, photon absorption properties of materials are more prominent, and the photon absorption abilities of materials vary strongly with atomic number. However, above this energy, since the dependence on the atomic number decreases, the photon absorption ability of the materials begin to converge and decrease slowly as the energy increases. For this reason, as can be seen from the Figure 3, the results obtained at low photon energies for low-density materials are more distinctive.

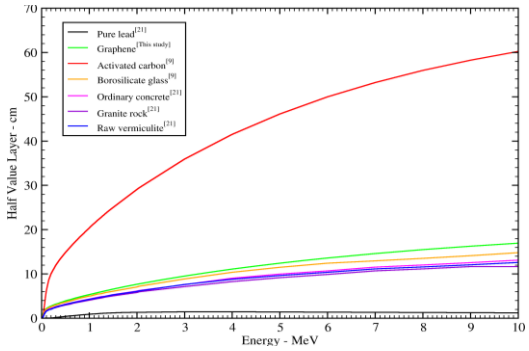

Figure 4 The comparing of the HVL values for graphene (RGO) is supplied with some previously calculated results [9, 22] for AC, vermiculite, borosilicate glass, lead, and concrete.

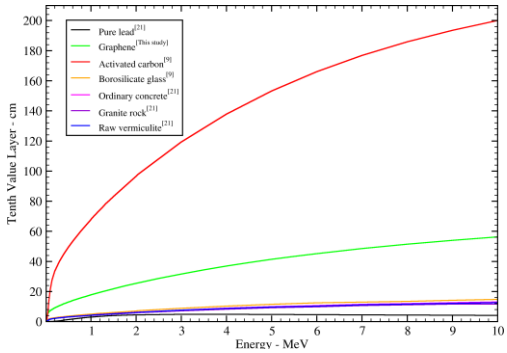

Figure 5 The comparing of the TVL values for graphene (RGO) is supplied with some previously calculated results [9, 22] for AC, vermiculite, borosilicate glass, lead, and concrete.

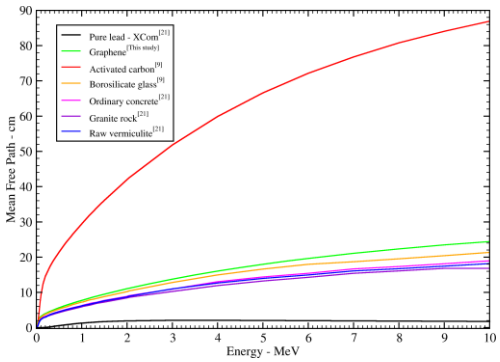

Figure 6 The comparing of the MFP values for graphene (RGO) is supplied with some previously calculated results [9, 22] for AC, vermiculite, borosilicate glass, lead, and concrete.

The calculated HVL, TVL and MFP values of graphene (1.91 g/cm^3) are given in the figures 4, 5 and 6 along with the properties of some known materials as AC (0.54 g/cm^3), vermiculite (2.5 g/cm^3), borosilicate glass (2.2 g/cm^3), lead (11.3 g/cm^3), concrete (2.4 g/cm^3) and granite (2.7 g/cm^3). Those values which are produced from the linear attenuation coefficient are also directly related to their own density. For this reason, they may take different values for the different densities of such materials.

The AC which is investigated before by the authors has better radiation absorption property than graphene in low photon energy region (<150 keV). This interpretation is based on the mass attenuation coefficients (μ_m) given in Figure 3. The μ_m parameter is one of the most studied parameter in radiation shielding, because it provides characteristic data for materials, regardless of their density. For this reason, the mass attenuation coefficients are commonly used in comparison of radiation shielding materials. However, when looking at the HVL, TVL and MFP graphs, it is understood AC should be higher than graphene because of its lower density.

4. CONCLUSIONS

In this study, the gamma-ray absorption properties are theoretically analyzed for graphene and then they were compared with AC, vermiculite, borosilicate glass, lead, and concrete. The important shielding parameters such as Mean free path (MFP), the mass attenuation coefficients (μm), the Tenth value layer (TVL), and the Half-value layer (HVL), were calculated for graphene and then compared with other materials' values that have been previously studied. The calculated results show that AC can be thought as one of the candidates of gamma shielding materials when compared to other known materials. The same conclusion about graphene is however suspicious due to its weak shielding properties. Here, it was also concluded that AC gives satisfactory results -however due to its low density requires a slightlly higher thickness especially in lower energy regime. Graphene is a weak radiation absorber due to the low atomic number value of Carbon, whereas AC is a good radiation absorber due

to the absorbent atoms it contains. So as a conclusion, the calculated data of such investigated samples significantly give advantageous ideas about absorbing properties of gamma rays, besides they have good features as having low density, being cheaper and harmless effect on health, also being easy and abundant quantities to produce.

Funding
The author (s) has no received any financial support for the research, authorship or publication of this study.

The Declaration of Conflict of Interest/ Common Interest
No conflict of interest or common interest has been declared by the authors.

The Declaration of Research and Publication Ethics
The authors of the paper declare that they comply with the scientific, ethical and quotation rules of SAUJS in all processes of the paper and that they do not make any falsification on the data collected. In addition, they declare that Sakarya University Journal of Science and its editorial board have no responsibility for any ethical violations that may be encountered, and that this study has not been evaluated in any academic publication environment other than Sakarya University Journal of Science.

REFERENCES

[1] M. Büyükyıldız, M. Kurudirek, M. Ekici, O. İçelli, Y. Karabul, "Determination of radiation shielding parameters of 304L stainless steel specimens from welding area for photons of various gamma ray sources", Progress in Nuclear Energy, vol. 100, pp 245-254,2017.

[2] H.C. Schniepp, J.-L. Li, M. J. McAllister, H. Sai, M. Herrera-Alonso, D. H. Adamson, R. K. Prud'homme, R. Car, D. A. Saville, I. A. Aksay, "Functionalized single graphene sheets derived from splitting graphite oxide", The Journal of Physical Chemistry B ,vol. 110, pp 8535-8539, 2006.

[3] M. Zdrojek, J. Bomba, A. Łapińska, A. Dużyńska, K. Żerańska-Chudek, J. Suszek, L. Stobiński, A. Taube, M. Sypek, J. Judek, Graphene-based plastic absorber for total sub-terahertz radiation shielding, Nanoscale 10 (2018) 13426-13431.

[4] J. Viegas, L. A. Silva, A. M. Batista, C. A. Furtado, J. P. Nascimento, L. O. Faria, "Increased X-ray attenuation efficiency of graphene-based nanocomposite", Industrial & Engineering Chemistry Research, vol. 56 pp 11782-11790,2017.

[5] S. A. Hashemi, S. M. Mousavi, R. Faghihi, M. Arjmand, S. Sina, A. M. Amani, "Lead oxide-decorated graphene oxide/epoxy composite towards X-Ray radiation shielding", Radiation Physics and Chemistry, vol.146 , pp 77-85, 2018.

[6] A. K. Singh, A.N. Yadav, A. Srivastava, K. K. Haldar, M. Tomar, A.V. Alaferdov, S. A. Moshkalev, V. Gupta, K. Singh, "CdSe/V2O5 core/shell quantum dots decorated reduced graphene oxide nanocomposite for high-performance electromagnetic interference shielding application", Nanotechnology, vol 30, pp 505-704,2019.

[7] A. Ansón-Casaos, J. Puértolas, F. J. Pascual, J. Hernández-Ferrer, P. Castell, A. M. Benito, W. K. Maser, M. Martínez, "The effect of gamma-irradiation on few-layered graphene materials", Applied Surface Science, vol 301, pp. 264-272,2014.

[8] K. W. Fornalski, "Theoretical considerations on charged graphene as

active gamma radiation shields", The European Physical Journal Applied Physics, vol 81, pp 30401,2018.

[9] D. Ickecan, M. N. Turkan, H. Gulbicim, "Investigation of shielding properties of impregnated activated carbon for gamma-rays", Applied Radiation and Isotopes, vol 172,pp 109687, 2021.

[10] A. K. Geim, "Graphene: status and prospects", science, vol 324, pp 1530-1534,2009.

[11] Y. Zhu, S. Murali, W. Cai, X. Li, J. W. Suk, J. R. Potts, R. S. Ruoff, "Graphene and graphene oxide: synthesis, properties, and applications", Advanced materials,vol 22 pp 3906-3924, 2010.

[12] R. S. Edwards, K. S. Coleman, "Graphene synthesis: relationship to applications", Nanoscale ,vol 5, pp 38-51, 2013.

[13] M. J. Sweetman, S. May, N. Mebberson, P. Pendleton, K. Vasilev, S. E. Plush, J. D. Hayball, "Activated carbon, carbon nanotubes and graphene: materials and composites for advanced water purification", Carbon, vol 3, pp 18, 2017.

[14] E. Pérez-Mayoral, I. Matos, M. Bernardo, I. M. Fonseca, "New and advanced porous carbon materials in fine chemical synthesis. Emerging precursors of porous carbons", Catalysts, vol 9, pp 133,2019.

[15] D. Ickecan, R. Zan, S. Nezir, "Eco-friendly synthesis and characterization of reduced graphene oxide", Journal of Physics: Conference Series, IOP Publishing, pp. 012027, 2017.

[16] D. Ickecan, N. Turkan, A. Ozcan, An Eco-friendly Material: Graphene, LAP LAMBERT Academic Publishing, Germany, 2021.

[17] S. S. Kiani, Y. Faiz, A. Farooq, M. Ahmad, N. Irfan, M. Nawaz, S. Bibi, "Synthesis and adsorption behavior of activated carbon impregnated with ASZM-TEDA for purification of contaminated air", Diamond and Related Materials, pp 107916,2020.

[18] D. T. Doughty, J. E. Groose, "Chromium-free impregnated activated carbon for adsorption of toxic gases and/or vapors", U.S. Patent 0405404A1, June 25 1991.

[19] M. Medhat, "Application of gamma-ray transmission method for study the properties of cultivated soil", Annals of Nuclear Energy ,vol 40 , pp 53-59,2012.

[20] Y. K. Vermani, T. Singh, "Numerical investigation on photon energy absorption parameters for some Bi–Sn–Zn alloys in wide energy region", Pramana, vol 95, pp 1-14, 2021.

[21] I. Kawrakow, D. Rogers, "The EGSnrc code system", NRC Report PIRS-701, NRC, Ottawa , 2000.

[22] H. Gülbiçim, M. Ç. Tufan, M. N. Türkan, "The investigation of vermiculite as an alternating shielding material for gamma rays", Radiation Physics and Chemistry,vol 130, pp 112-117, 2017.

SAKARYA ÜNİVERSİTESİ
FEN BİLİMLERİ ENSTİTÜSÜ DERGİSİ

Sakarya University Journal of Science
SAUJS

ISSN 1301-4048 e-ISSN 2147-835X Period Bimonthly Founded 1997 Publisher Sakarya University
http://www.saujs.sakarya.edu.tr/

Title: The Effect of Mg Content on the Physical Properties of ZnO Films Deposited by Ultrasonic Spray Pyrolysis

Authors: Emrah SARICA

Recieved: 2022-10-17 00:00:00

Accepted: 2023-03-12 00:00:00

Article Type: Research Article

Volume: 27
Issue: 3
Month: June
Year: 2023
Pages: 621-633

How to cite
Emrah SARICA; (2023), The Effect of Mg Content on the Physical Properties of ZnO Films Deposited by Ultrasonic Spray Pyrolysis. Sakarya University Journal of Science, 27(3), 621-633, DOI: 10.16984/saufenbilder.1190168
Access link
https://dergipark.org.tr/en/pub/saufenbilder/issue/78131/1190168

Sakarya University Journal of Science 27(3), 621-633, 2023

The Effect of Mg Content on the Physical Properties of ZnO Films Deposited by Ultrasonic Spray Pyrolysis

Emrah SARICA *1

Abstract

ZnO is a versatile material and tailoring its physical properties to the field of application is technologically crucial. Intentionally doping with a foreign element is the most common and useful method for that. In this presented work, ZnO films doped at different Mg concentrations (0%, 5%, 10%, and 15%) were deposited onto glass substrates by ultrasonic spray pyrolysis in order to investigate the effect of Mg doping. AFM and SEM images captured for the morphological investigations revealed that Mg doping deteriorated the surface of the films. The structural analysis showed that the Mg doping at 5% enhanced the structural properties, but the crystallization level was adversely affected at higher Mg concentrations. Optical band gap and Urbach energies increased from 3.30 eV to 3.45 eV and from 79.5 meV to 119.8 meV, respectively. The lowest electrical resistivity was noted as 8.72×10^{1} Ωcm for Mg-doped ZnO films at 5%.

Keywords: Ultrasonic spray pyrolysis, Mg doping, ZnO thin films, optical properties

1. INTRODUCTION

One of the most studied metal oxide semiconductors, ZnO has unique physical properties such as consisting of abundant and non-toxic elements, having n-type electrical conductivity in its nature due to native defects (i.e., oxygen vacancies-V_O, zinc interstitials-Zn_I), large band gap (~3.3 eV) and high exitonic binding energy (~60 meV) etc., [1]. In particular, the high exciton binding energy along with the wide band gap makes ZnO well-suited for opto-electronic devices such as LEDs [2]. Its high transparency which is another feature of ZnO allows transmitting light with very low losses and this makes ZnO a favorable material in solar cells as a buffer layer or transparent conductive layer in which the light penetrates through and reaches the active region [3–5]. High carrier mobility along with a wide band gap and high optical transmittance also makes ZnO an important material for thin film transistors to be used in future display technologies such as invisible electronic devices [6–8].

However, these superior properties of ZnO may still be insufficient to achieve more efficient optoelectronic or electronic devices. At this point, the effort to tailor the physical

* Corresponding author: emrahsarica@baskent.edu.tr (E. SARICA)
[1] Faculty of Engineering, Department of Electrical and Electronics Engineering, Baskent University, 06790, Ankara, Turkey
ORCID: https://orcid.org/0000-0002-9339-5114

properties of ZnO by external doping with various elements takes the stage. Substitution of Group III (Al, In, Ga etc.) and Group VII (F, Cl etc.) elements with Zn and O, respectively, increases the free electron concentration and hence n-type conductivity whereas p-type conductivity can be achieved with the substitution of Group II (Li, Na, and K) and Group V (N, P, As, and Sb) elements. However, it should be noted that obtaining p-type ZnO requires quite a laborious effort due to the compensation of acceptors by donor defects such as Zn_i, V_O [9].

Bandgap engineering is another endeavor to get efficient devices. For instance, widening in bandgap of ZnO allows transmittance of light in the short wavelength region and it makes ZnO a preferred material for solar blind UV photodetectors, UV-LEDs etc., [10]. At this point, Mg doping reveals remarkable results due to the fact that the bandgap of MgO (7.8 eV) is quite larger than that of ZnO [11]. Liu et al. reported that doping of Mg into ZnO in nanorod form provides a high potential application in UV photodetectors due to its high UV/visible detection ratio as well as fast rise/fall time [12]. Besides, non-toxic ZnO is considered as novel buffer layer in thin film solar cells, and Mg doping is proposed as an effective way to altering conduction band offset at the buffer/absorber interface [13]. Törndahl et al. experimentally investigated the impact of ALD deposited $Zn_{1-x}Mg_xO$ buffer layer in Cu(In,Ga)Se2 solar cells and reported that the increasing Mg content till a certain concentration lead to enhancement in open circuit voltage in CIGS solar cells. They also showed that the conduction band offset at buffer/absorber interface can be tailored for $x<0.2$, effectively [14]. Similarly, Li et al. inserted a $Zn_{1-x}Mg_xO$ layer between ZnO/Sb_2Se_3 interface and reported that $Zn_{1-x}Mg_xO$ layer enables to enhance the efficiency by passivating interfacial defects and reducing recombination loss at the ZnO/Sb_2Se_3 interface [15]. On the other hand, Mg doping into ZnO is not only useful for adjusting energy band levels, but can also provide functionality to the ZnO. Islam and Azam experimentally showed that Mg doping into ZnO lattice improves the photocatalytic activity by creating localized electronic states within the band gap. It was explained that the probability of electron-hole recombination diminishes due to these localized states that behave as traps for the electrons in the conduction band and hereby photocatalytic activity is enhanced [16]. Okeke et al., on the other hand, proved that Mg doping into ZnO also allows enhancement in antibacterial properties as well as photocatalytic activity [17].

All these studies reveal that Mg doping gives superior properties to ZnO films. Therefore, this study aims to examine the variation in physical properties of ZnO thin films due to the Mg doping, by ultrasonic spray pyrolysis technique.

2. MATERIALS AND METHODS

2.1. Deposition of Thin Films

In the first step of thin film deposition, microscope slides used as substrate were ultrasonically cleaned in soapy water, acetone, methanol and deionized (DI) water for 15 min, respectively. Substrates were rinsed under running DI water between two consecutive steps. At the second stage, spray solutions were prepared by mixing of (0.05 M) $Zn(CH_3COO)_2{\cdot}2H_2O$ and (0.05 M) $MgCl_2{\cdot}6H_2O$ aqueous solution at certain concentrations of 0, 5, 10 and 15 %v/v. Finally, the prepared spray solution was sprayed by passing through the ultrasonic atomizer which operates at 100 kHz onto pre-heated glass substrates for 25 min by keeping the solution flow rate at 4 ml/min. Temperature of glass substrates was kept at 425±5°C during the deposition and controlled by using an PID controller equipped with iron-constantan thermocouple. Distance between ultrasonic nozzle and substrate was maintained at 30 cm. Compressed air at 0.7 bar pressure was used as carrier gas.

2.2. Characterization of Thin Films

Surface morphologies of undoped and Mg-doped ZnO thin films were evaluated by means of atomic force microscope (AFM) and scanning electron microscope (SEM) images. AFM images were captured by Park Systems XE-100 and surface roughness values were determined via XEI version 1.7.1 software. HITACHI SU5000 Field Emission Scanning Electron Microscope was used to get both top surface images and cross-sectional view to determine the film thickness. In addition to that, elemental compositions of all films were confirmed by means of energy-dispersive X-ray spectroscopy (EDS) spectra taken by the Oxford X-MaxN 80 detector which is an attachment of SEM system. Structural investigations of all deposited thin films were carried out by means of X-ray diffraction pattern taken by x-ray diffractometer (PANalytical Empyrean), having CuKα radiation (λ= 1.5406 Å) operating at 40 mA and 45 kV. A continuous scan mode was used to collect 2θ data from 25° to 65° with a step of Δ(2θ) = 0.013°. Optical transmittance and absorbance spectra belonging to deposited films were recorded by Rigol Ultra-3660 double beam UV-Visible spectrophotometer.

3. RESULTS AND DISCUSSIONS

3.1. Morphological and Elemental Investigations

Figure 1 shows the 3D-AFM images of undoped and Mg-doped ZnO thin films. Bright and dark regions throughout the surfaces are related to the hill and valley formations, respectively. It indicates the presence of randomly distributed particle formations with different sizes on the surface. Although the ultrasonic nozzle used to spray the prepared solution in fine droplets enables to get droplets of most frequently 20 μm in diameter, the size of the droplets obtained varies in the range of 10-60 μm. This leads to formation of hill and valley along the surface of thin films and inhibits to get perfectly smooth surfaces. Average (R_a) and root mean square (R_q) values of surface roughness of all films were found to be in the range of 2.02-4.39 nm and 2.69-5.68 nm, respectively, and listed in Table 1.

As seen from the Table 1, lowest surface roughness was obtained for undoped ZnO films and roughness increased due to Mg doping. This deterioration in the surface morphologies is also clearly seen in the SEM images given in Figure 2. As seen from Figure 2, undoped ZnO films consisted of grains with a certain geometry but the grain-like appearance disappeared for the Mg-doped films, gradually. This may also be correlated with the deterioration of the crystal structure, as will be discussed later.

Meanwhile, the cross-sectional SEM images were inserted in Figure 2. Film thicknesses were determined as the average of measurements taken from ten different regions along these images via ImageJ software. Thickness of the films were also listed in Table 1.

Figure 3 represents the EDS spectra taken for the compositional analysis of ZnO:Mg thin films. As seen from these spectra strong signals were detected belonging to Zn and O atoms for all films and whereas Mg signal existed for only Mg-doped ZnO films as expected. Besides the Zn, O and Mg signal, a C peak observed for all films it may have come out as surface contamination or environmental impurity. Detected atomic percentage of Mg is noted as 2.4%, 3.6% and 5.7% for Mg doped ZnO at 5%, 10% and 15% v/v, respectively. Although the Mg ratio in EDS spectra was not exactly the same as the ratio in the spray solution, the detected Mg atomic percent in EDS spectra increased as the manganese ratio in the solution increased.

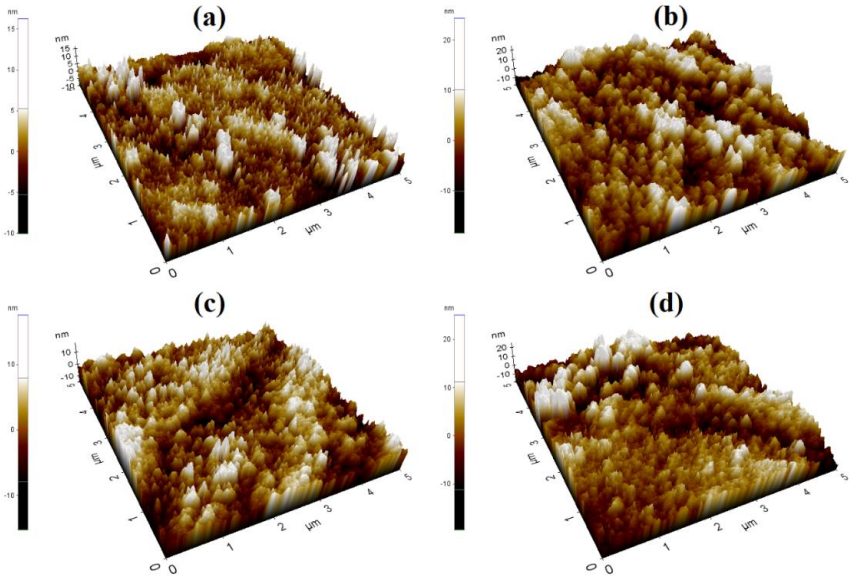

Figure 1 AFM images of (a) undoped and (b) Mg doped at 5% (c) Mg doped at 10% and (d) Mg doped at 15% ZnO thin films

Table 1 Thickness and surface roughness (R_a and R_q are the average and root mean square values of roughness) values of all deposited thin films

Material	**Thickness (nm)**	**R_a (nm)**	**R_q (nm)**
ZnO	300	2.02	2.69
ZnO:Mg(5%)	305	4.04	5.16
ZnO:Mg(10%)	205	3.24	4.05
ZnO:Mg(15%)	340	4.39	5.68

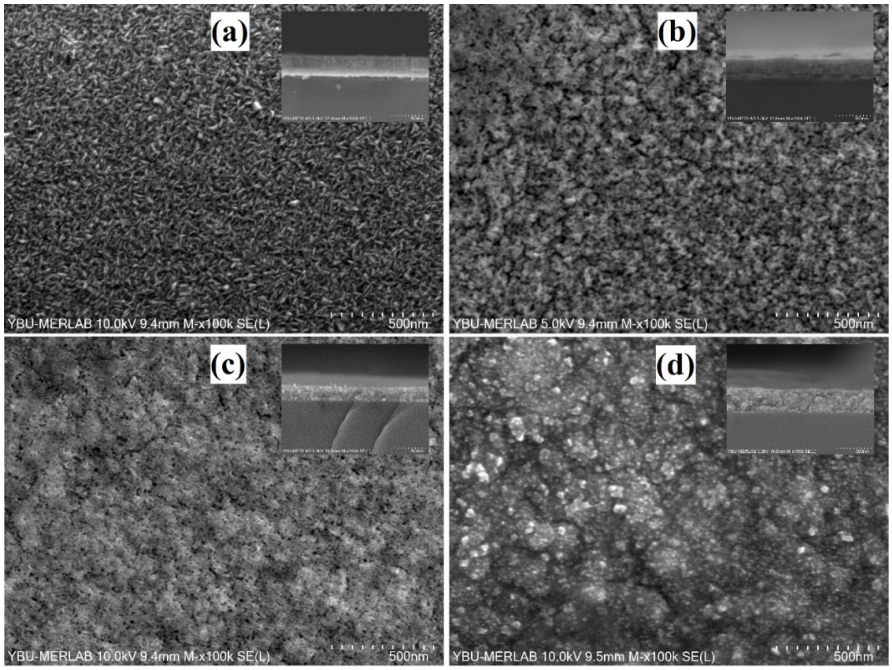

Figure 2 100K magnified surface and cross-sectional (inserted) SEM images of (a) undoped and (b) Mg doped at 5% (c) Mg doped at 10% and (d) Mg doped at 15% ZnO thin films

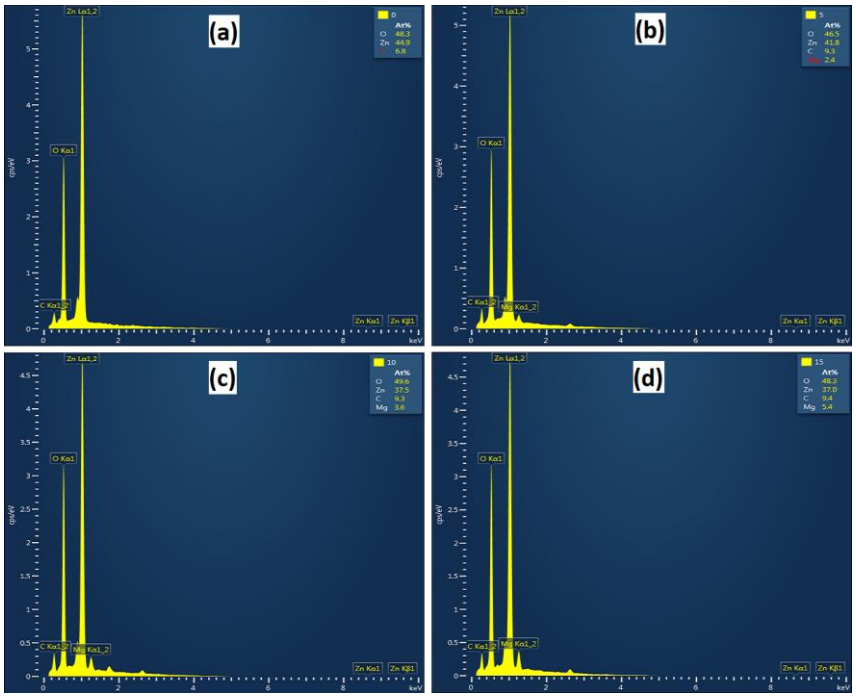

Figure 3 EDS spectra of (a) undoped and (b) Mg doped at 5% (c) Mg doped at 10% and (d) Mg doped at 15% ZnO thin films

3.2. Structural Investigations

Structural analysis of ZnO:Mg films were performed by using XRD patterns given in Figure 4. Three diffraction peaks on these patterns located at 2θ ≈32.1°, 34.8° and 36.6° were observed and indexed to (100), (002) and (101) planes of hexagonal ZnO by comparing with PDF 00-036-1451 reference card. However, Mg-related peaks did not exist and it implies that there was no any secondary phase of Mg_xO_y or ZnMgO. Some structural parameters extracted from the peaks on XRD patterns were listed in Table 2. The intensity of (100) plane peak was found to be higher than peaks of other planes for undoped ZnO films, but it decreased gradually with Mg content. Moreover, full width half maximum (FWHM) values of all peaks exist on XRD patterns increased, except for (200) plane of Mg doped ZnO at 5%. All these indicate that the crystallinity of ZnO films deteriorated by Mg doping.

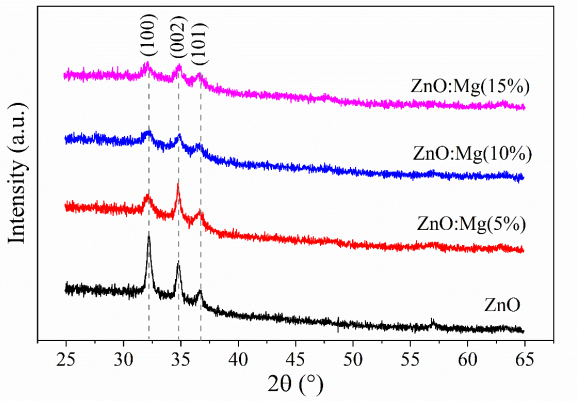

Figure 4 XRD patterns of undoped and Mg doped ZnO thin films

Diffraction angle (2θ) and FWHM (β) are determinative on the structural parameters of films. Therefore, by using these extracted parameters, lattice constants (*a* and *c*), unit volume cell (V), mean crystallite size (D), and micro-strains were calculated by using the following relations and listed in Table 2.

Lattice constants (*a* and *c*) were calculated by following equation [18]

$$\frac{1}{d^2_{(hkl)}} = \frac{4}{3}\left(\frac{h^2+hk+k^2}{a^2}\right)+\frac{l^2}{c^2} \qquad (1)$$

where (*hkl*) and *d* are the miller indices and interplanar distance $\left(d = \lambda/2\sin\theta\right)$, respectively. Unit cell for hexagonal crystal structure [18];

$$V = \frac{\sqrt{3}}{2}a^2c \qquad \rho = 1/\left(qn\mu\right) \tag{2}$$

Mean crystallite size was calculated by using well-known Scherrer's equation [18]

$$D = \frac{K\lambda}{\beta_{hkl}\cos\theta} \tag{3}$$

where K is shape factor (0.94), λ is the wavelength of x-ray ($\lambda_{CuK\alpha}$=0.154 nm), θ is the Bragg angle. Micro-strain (ε) values were calculated by using following equation [18]

$$\varepsilon = \beta/4\tan\theta \tag{4}$$

Based on these calculations it can be concluded that Mg doping adversely affected the crystalline level of ZnO thin films. This may be due to slight differences between ionic radii of Zn^{2+} (~0.74 Å) and Mg^{2+} (~0.71 Å) which are also known as crystal radii described as the physical size of ions in a solid by Shannon R.D [19]. Moreover, Mg may have also prevented the formation of ZnO as reported by others [20–22].

Table 2 Peaks position (2θ) FWHM (β), interplanar spacing (d), miller indices (*hkl*), *a*-lattice and *c*-lattice, c/a ratio, unit cell volume (V), crystallite size (D) and micro-strain values (ε)

2θ (°)	**β (°)**	**d (Å)**	**(*hkl*)**	**D (Å)**	**ε×10^{-3}**	***a* (Å)**	***c* (Å)**	***c*/*a***	**V (Å^3)**
32.22	0.4131	2.7764	100	209	6.24				
34.78	0.4515	2.5776	002	193	6.29	3.2059	5.1553	1.608	45.89
36.70	0.4312	2.4471	101	203	5.67				
32.14	0.7632	2.7825	100	113	11.6				
34.77	0.3643	2.5779	002	239	5.08	3.2130	5.1557	1.605	46.09
36.61	0.6891	2.4524	101	127	9.09				
32.14	0.7566	2.7824	100	114	11.5				
34.84	0.5696	2.5727	002	153	7.92	3.2128	5.1454	1.602	45.99
36.58	0.6769	2.4547	101	129	8.94				
32.05	0.8284	2.7901	100	104	12.6				
34.83	0.6251	2.5740	002	139	8.70	3.2218	5.1480	1.598	46.28
36.57	0.7838	2.4554	101	111	10.4				

3.3. Optical Investigations

Optical properties were evaluated by means of transmittance and absorbance spectra given in Figure 5(a) and (b), respectively. Figure 5(a) shows that all films exhibit high transparency (>90%) in the visible range of the electromagnetic spectrum and no considerable variation was observed along with the Mg doping. On the other hand, the absorption edge emerged in the range of 325-390 nm as seen from Figure 5(b) and shifted towards shorter wavelength with the Mg doping as clearly seen from the plot given as inset in Figure 5(b). In addition to that, the absorption edge began to become more oblique with the addition of Mg. These indicate that band gap of deposited films enlarged and band tail fluctuation increased with Mg doping.

In order to determine the band gap of all deposited thin films, extrapolation of the linear portion of the plots of $(\alpha h\nu)^2$ *vs.* $h\nu$ at $(\alpha h\nu)^2 = 0$ was used according to Tauc's method given by Eq (5), and listed in Table 3.

$$\left(\alpha h\nu\right)^n = A\left(h\nu - E_g\right) \tag{5}$$

where h is the Planck's constant, ν is frequency, n is equal to 2 for allowed direct transition, A is a constant and E_g is the optical band gap. As seen from Table 3, band gap increased from 3.30 eV to 3.45 eV along with the Mg doping. These values are consistent with the previously reported studies and increment in band gap with increasing amount of doped Mg also reported by others [23–27]. In fact, in some reported studies [16, 28–31], the increase in the band gap is higher than this work. Mostly, the enlargement in band gap is attributed to Burstein-Moss effect [16, 25, 26, 30, 32, 33]. Besides, Etacheri et al. state that another important factor affecting the band gap of the semiconductors is the lattice parameter, and an increase in the band gap values is observed along with the decrease of the c/a ratio [33]. Also, the electronegativity between Zn and Mg has also been suggested as the reason for the band gap widening [24, 28]. In addition to these, a wider band gap of MgO (~7.8 eV) has compared to ZnO may also be the reason for the increase in the band gap in the Mg doped ZnO films [20, 34, 35]. In this study, as will be discussed in the electrical analysis section, there were no findings that shows a remarkable improvement in electrical properties that could indicate an increase in carrier concentration with the incorporation of Mg. For this reason, it is very hard to explain the enlargement in the band gap seen in this study by the Burstein-Moss effect. So, the enlargement in the band gap might be related to the fact that MgO has a wider bandgap than ZnO. In order to investigate band tail fluctuations, $ln\alpha$ vs. $h\nu$ plots given in Figure 5(d) were constructed and Urbach energy (E_u) values for all films extracted from the slope of linear portion according to Eq. (6) and listed in Table 3.

$$\alpha = \alpha_0 \exp\left(\frac{h\nu}{E_U}\right) \tag{6}$$

where α_0 is a constant. As seen from Table 3, Mg doping into ZnO led to increase in E_u from 79.5 meV to 119.8 meV. This implies that the degree of electronic disorder increases by Mg doping, in another words, the width of the localized states within the forbidden gap increases. Structural disorders such as crystal defects contributes to band tail states and increases the Urbach energy [16, 36].

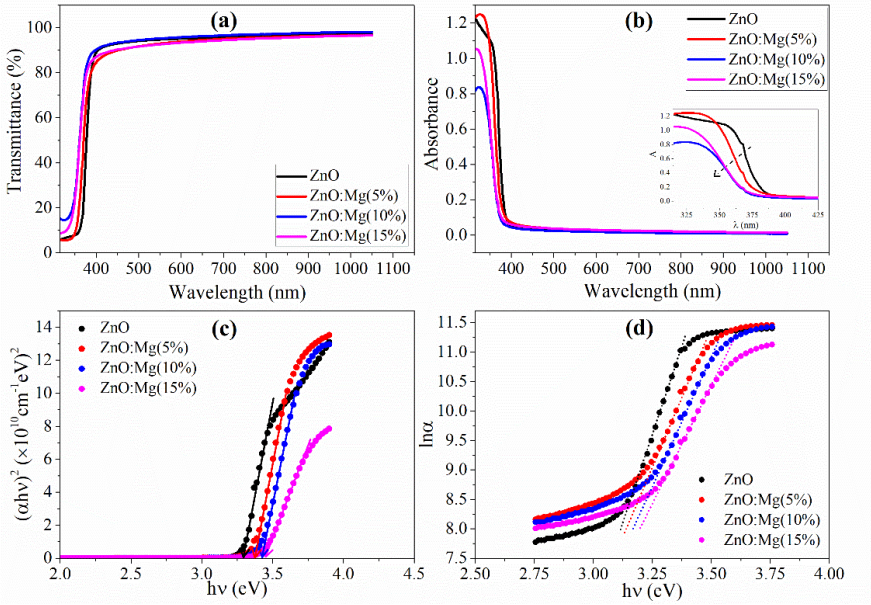

Figure 5 (a) Transmittance (b) absorbance, (c) $\alpha h\nu$~$h\nu$ plots, (d) $ln\alpha$~$h\nu$ plots of undoped and Mg doped ZnO thin films

Table 3 Band gap (E_g), Urbach energy (E_u) and resistivity (ρ) values of ZnO:Mg thin films

Material	E_g (eV)	E_u (meV)	ρ (Ωcm)
ZnO	3.30	79.5	1.57×10^{2}
ZnO:Mg(5%)	3.38	102.8	8.72×10^{1}
ZnO:Mg(10%)	3.42	106.9	4.33×10^{2}
ZnO:Mg(15%)	3.45	119.8	3.05×10^{4}

The increase in Urbach energies is also correlated with the deterioration in the crystallization levels of the ZnO:Mg thin films deposited in this work. Similar deviation in the Urbach energies of ZnO with the Mg doping were also reported by Islam and Azam [16]. On the other hand, it is known that band tails tend to reduce the energy band gap of thin films [37, 38]. Therefore, in this work, observed increase in the width of band tails may have suppressed the enlargement in bandgap with Mg doping and inhibited getting larger band gaps.

3.4. Electrical Investigations

Electrical investigations were carried out in two steps. In the first step electrical conductivity type was determined by hot point probe techniques and it was noted that all films have n-type conductivity. It is very well known that point defects (i.e., donor defects such as O vacancies and Zn interstitials) are the reason for the n-type conductivity nature in ZnO films.

In the second step electrical resistivity values were measured by means of four-point probe technique at room temperature listed in Table 3. As seen from Table 3, electrical resistivity of Mg doped ZnO at 5% is found to be less than that of the undoped film. However, Mg doping at 10% and 15% led to increasing the electrical resistivity, and it was even found to be higher than the undoped ZnO films. As known, electrical resistivity is related to carrier mobility and carrier concentration according to $\rho = 1/(qn\mu)$. It is reported that carrier concentration increases by formation of oxygen vacancies through the Mg doping due to the difference of electronegativity between Mg and Zn [33, 39]. Meanwhile, increased oxygen vacancy concentration also means a decrease in mobility [40]. Besides, Caglar et. al have stated that the substitution of Mg^{2+} and Zn^{2+} does not yield extra free electrons because of their equivalent valence state while the interstitial Mg ions donate extra electrons [41]. On the other hand, carrier mobility is directly dependent on the scattering of free carriers, and these scatterings implicitly depend on retardation by hopping transport, phonon scattering, impurity scattering, and grain boundary scattering [42, 43]. High carrier concentration can be achieved with externally doping, but this restricts carrier mobility because it will result in a high amount of ionized impurity and hence impurity scattering [43–45]. Grain boundary scattering, one of the primary carrier scattering mechanisms, is directly linked with the crystallite size as crystallites with small size results in a higher amount of grain boundaries, namely, a higher possibility of grain boundary scattering. Beyond that, segregation of excess Mg ions at the grain boundaries gives rise to an electrical barrier and thus enhances the effectiveness scattering of the carriers [39]. Vinoth et al. also reported that the electrical resistance increased with the decrease of mobility in Mg-doped ZnO films [46].

In fact, the trend in electrical resistivity variations in this work is in harmony with the variation of crystallite size of the films, which can be associated with grain boundary scattering. It can be argued that less electrical resistivity for 5% Mg-doped films compared to that of the undoped film may have been due to the enhancement in crystallite size along with the increase in carrier concentration resulting from the Mg incorporation. However, the relatively high Mg concentration (10% and 15 % v/v) in the spray

solution may have caused Mg segregation at the grain boundaries which may have resulted in grain boundary scattering more effective. Therefore, increase in the resistivity of 10% and 15% Mg-doped films may have been predominantly related to carrier mobility suffering grain boundary scattering. Additionally, as given in the optical analysis section, the increase in Urbach energies indicates the increase in localized states that act as traps for charge carriers [16]. This may be another reason for the rise in electrical resistivity.

4. CONCLUSION

In this work, Mg-doped ZnO thin films were successfully deposited onto glass substrates without any crack or void along the surface. However, the increase in surface roughness with Mg doping indicates that the morphology deteriorated. In addition to that, high amount of Mg doping led to not only a decrease in x-ray diffraction peak intensity but also a broadening of them which indicates shrinkage in crystallite size. Therefore, it can be concluded that Mg doping at these ratios has adversely affected both the crystallization and morphology of ZnO thin films.

In terms of optical properties, it was found that Mg doping is convenient to get a ZnO film with a larger bandgap, whereas it causes an increase in localized defects within the band gap and band fluctuations considering the increase in Urbach energies. In addition to these, it was determined that electrical conductivity can be enhanced by Mg doping at 5%, but further doping concentrations caused a decrease in conductivity, due to the possibility of increased scattering mechanisms.

In order to enhance the crystallization level of Mg doped ZnO films post-annealing treatment can be applied. This may also allow for an increase in the electrical conductivity by reducing free carrier scattering with the enhancement in crystallization level. On the other hand, enhancement in crystallization level (i.e., reduction in point defects) may also make it possible to obtain a wider band gap by reducing the tailing of the band edges.

Authors' Contribution

The author confirms sole responsibility for all section of the manuscript.

The Declaration of Conflict of Interest/ Common Interest

No conflict of interest or common interest has been declared by the author.

The Declaration of Ethics Committee Approval

This study does not require ethics committee permission or any special permission.

The Declaration of Research and Publication Ethics

The author of the paper declare that he complies with the scientific, ethical and quotation rules of SAUJS in all processes of the paper and that he does not make any falsification on the data collected. In addition, he declares that Sakarya University Journal of Science and its editorial board have no responsibility for any ethical violations that may be encountered, and that this study has not been evaluated in any academic publication environment other than Sakarya University Journal of Science.

REFERENCES

[1] H. Morkoç, Ü. Özgür, Zinc Oxide: Fundamentals, Materials and Device Technology, Weinheim: Wiley-VCH, 2008.

[2] J. C. Fan, S. L. Chang, Z. Xie, “ZnO-Based Light-Emitting Diodes,” in Optoelectronics - Advanced Materials and Devices, London: IntechOpen, 2013.

[3] M. A. Martínez, J. Herrero, M. T. Gutiérrez, “Deposition of transparent and conductive Al-doped ZnO thin

films for photovoltaic solar cells," Solar Energy Materials and Solar Cells, vol. 45, no. 1, pp. 75–86, 1997.

[4] Y. Lare, A. Godoy, L. Cattin, K. Jondo, T. Abachi, F. R. Diaz, M. Morsli, K. Napo, M. A. del Valle, J. C. Bernède., "ZnO thin films fabricated by chemical bath deposition, used as buffer layer in organic solar cells," Applied Surface Science, vol. 255, no. 13–14, pp. 6615–6619,2009.

[5] X. Wen, Y. He, C. Chen, X. Liu, L. Wang, B. Yang M. Leng, H. Song, K. Zeng, D. Li, K. Li, L. Gao, J. Tang, "Magnetron sputtered ZnO buffer layer for Sb2Se3 thin film solar cells," Solar Energy Materials and Solar Cells, vol. 172, pp. 74–81, 2017.

[6] J. H. Lee, C. H. Ahn, S. Hwang, C. H. Woo, J. S. Park, H. K. Cho, J. Y. Lee, "Role of the crystallinity of ZnO films in the electrical properties of bottom-gate thin film transistors," Thin Solid Films, vol. 519, no. 20, pp. 6801–6805, 2011.

[7] M. Kumar, H. Jeong, A. Kumar, B. P. Singh, D. Lee, "Magnetron-sputtered high performance Y-doped ZnO thin film transistors fabricated at room temperature," Materials Science in Semiconductor Processing, vol. 71, pp. 204–208, 2017.

[8] Z. Xiaming, W. Huizhen, W. Shuangjiang, Z. Yingying, C. Chunfeng, S. Jianxiao, Y. Zijian, D. Xiaoyang, D. Shurong, "Optical and electrical properties of N-doped ZnO and fabrication of thin-film transistors," Journal of Semiconductors, vol. 30, no. 3, pp. 033001, 2009.

[9] Y. S. Choi, J. W. Kang, D. K. Hwang, S. J. Park, "Recent Advances in ZnO-Based Light-Emitting Diodes," Ieee Transactıons On Electron Devıces, vol. 57, no. 1, pp. 26–41, 2010.

[10] M. N. H. Mia, M. F. Pervez, M. K. Hossain, M. R. Rahman. M. J. Uddin, M. A. Al Mashud, H.K. Ghosh, M. Hoq, "Influence of Mg content on tailoring optical bandgap of Mg-doped ZnO thin film prepared by sol-gel method," Results in Physics, vol. 7, pp. 2683–2691, 2017.

[11] P. Giri, P. Chakrabarti, "Effect of Mg doping in ZnO buffer layer on ZnO thin film devices for electronic applications," Superlattices and Microstructures, vol. 93, pp. 248–260, 2016.

[12] Y. H. Liu, S. J. Young, C. H. Hsiao, L. W. Ji, T. H. Meen, W. Water, S. J. Chang, "Visible-Blind Photodetectors With Mg-Doped ZnO Nanorods," IEEE Photonics Technology Letters, vol. 26, no. 7, pp. 645–648, 2014.

[13] X. He, L. Wu, X. Hao, J. Zhang, C. Li, W. Wang, L. Feng, Z. Du, "The Band Structures of $Zn_{1-x}Mg_xO$(In) and the Simulation of CdTe Solar Cells with a $Zn_{1-x}Mg_xO$(In) Window Layer by SCAPS," Energies, vol. 12, no. 2, pp. 291, 2019.

[14] T. Törndahl, C. Platzer-Björkman, J. Kessler, M. Edoff, "Atomic layer deposition of $Zn_{1-x}Mg_xO$ buffer layers for Cu(In,Ga)Se_2 solar cells," Progress in Photovoltaics: Research and Applications, vol. 15, no. 3, pp. 225–235, 2007.

[15] K. Li, K. Li, R. Kondrotas, C. Chen, S. Lu, X. Wen, D. Li, J. Luo, Y. Zhao, J. Tang, "Improved efficiency by insertion of $Zn_{1-x}Mg_xO$ through sol-gel method in ZnO/Sb_2Se_3 solar cell," Solar Energy, vol. 167, pp. 10–17, 2018.

[16] M. R. Islam, M. G. Azam, "Enhanced photocatalytic activity of Mg-doped

ZnO thin films prepared by sol–gel method," Surface Engineering, vol. 37, no. 6, pp. 775–783, 2021.

[17] I. S. Okeke, K. K. Agwu, A. A. Ubachukw, I. G. Madiba, M. Maaza, G. M. Whyte, F. I. Ezema, "Impact of particle size and surface defects on antibacterial and photocatalytic activities of undoped and Mg-doped ZnO nanoparticles, biosynthesized using one-step simple process," Vacuum, vol. 187, pp. 110110, 2021.

[18] B. D. Cullity, Elements of X-ray Diffraction, Massachusetts: Addison-Wesley Publishing Company, Inc, 1956.

[19] R. D. Shannon, "Revised effective ionic radii and systematic studies of interatomic distances in halides and chalcogenides," Acta Crystallographica Section A, vol. 32, no. 5, pp. 751–767, 1976.

[20] A. Mahroug, B. Mari, M. Mollar, I. Boudjadar, L. Guerbous, A. Henni, N. Selmi, "Studies On Structural, Surface Morphological, Optical, Luminescence and Uv Photodetection Properties Of Sol–Gel Mg-Doped ZnO Thin Films," Surface Review and Letters, vol. 26, no. 03, pp. 1850167, 2019.

[21] Ş. Ţălu, S. Boudour, I. Bouchama, B. Astinchap, H. Ghanbaripour, M. S. Akhtar, S. Zahra, "Multifractal analysis of Mg-doped ZnO thin films deposited by sol–gel spin coating method," Microscopy Research and Technique, vol. 85, no. 4, pp. 1213-1223, 2021.

[22] M. Arshad, M. M. Ansari, A. S. Ahmed, P. Tripathi, S. S. Z. Ashraf, A. H. Naqvi, A. Azam, "Band gap engineering and enhanced photoluminescence of Mg doped ZnO nanoparticles synthesized by wet chemical route," Journal of Luminescence, vol. 161, pp. 275–280, 2015.

[23] Y. Bouachiba, A. Mammeri, A. Bouabellou, O. Rabia, S. Saidi, A. Taabouche, B. Rahal, L. Benharrat, H. Serrar, M. Boudissa, "Optoelectronic and birefringence properties of weakly Mg-doped ZnO thin films prepared by spray pyrolysis," Journal of Materials Science: Materials in Electronics, vol. 33, no. 9, pp. 6689–6699, 2022.

[24] M. Rouchdi, E. Salmani, B. Fares, N. Hassanain, A. Mzerd, "Synthesis and characteristics of Mg doped ZnO thin films: Experimental and ab-initio study," Results in Physics, vol. 7, pp. 620–627, 2017.

[25] J. Varghese, S. K. Saji, N. R. Aswathy, R. Vinodkumar, "Influence of Mg doping on structural, optical and dielectric properties of sol–gel spin coated ZnO thin films," The European Physical Journal Plus, vol. 136, no. 12, pp. 1206, 2021.

[26] K. Upadhya U. G. Deekshitha, A. Antony, A. Ani, I. V. Kityk, J. Jedryka, A. Wojciechowski, K. Ozga, P. Poornesh, S. D. Kulkarni, N. Andrushchak, "Second and third harmonic nonlinear optical process in spray pyrolysed Mg:ZnO thin films," Optical Materials, vol. 102, pp. 109814, 2020.

[27] R. Kara, L. Mentar, A. Azizi, "Synthesis and characterization of Mg-doped ZnO thin-films electrochemically grown on FTO substrates for optoelectronic applications," RSC Advances, vol. 10, no. 66, pp. 40467-40479, 2020.

[28] F. Hussain, M. Imran, R. M. A. Khalil N. A. Niaz, A. M. Rana, M. A. Sattar, M. Ismail, A. Majid, S. Kim, F. Iqbal, M. A. Javid, S. Saeed, A. Sattar, "An

insight of Mg doped ZnO thin films: A comparative experimental and first-principle investigations," Physica E: Low-dimensional Systems and Nanostructures, vol. 115, pp. 113658, 2020.

[29] A. Goktas, A. Tumbul, Z. Aba, M. Durgun, "Mg doping levels and annealing temperature induced structural, optical and electrical properties of highly c-axis oriented ZnO:Mg thin films and Al/ZnO:Mg/p-Si/Al heterojunction diode," Thin Solid Films, vol. 680, pp. 20–30, 2019.

[30] J. Singh, P. Kumar, K. S. Hui, K. N. Hui, K. Ramam, R. S. Tiwaria, O. N. Srivastavaa, "Synthesis, band-gap tuning, structural and optical investigations of Mg doped ZnO nanowires," CrystEngComm, vol. 14, no. 18, pp. 5898, 2012.

[31] D. İskenderoğlu, A. E. Kasapoğlu, E. Gür, "Valance band properties of MgZnO thin films with increasing Mg content; phase separation effects," Materials Research Express, vol. 6, no. 3, pp. 036402, 2018.

[32] P. Sahoo, A. Sharma, S. Padhan, R. Thangavel, "Visible light driven photosplitting of water using one dimensional Mg doped ZnO nanorod arrays," International Journal of Hydrogen Energy, vol. 45, no. 43, pp. 22576–22588, 2020.

[33] V. Etacheri, R. Roshan, V. Kumar, "Mg-Doped ZnO Nanoparticles for Efficient Sunlight-Driven Photocatalysis," ACS Applied Materials and Interfaces, vol. 4, no. 5, pp. 2717–2725, 2012.

[34] H. Zhuang, J. Wang, H. Liu, J. Li, P. Xu, "Structural and Optical Properties of ZnO Nanowires Doped with Magnesium," Acta Physica Polonica A, vol. 119, no. 6, pp. 819–823, 2011.

[35] S. H. Jeong, J. H. Park, B. T. Lee, "Effects of Mg doping rate on physical properties of Mg and Al co-doped $Zn_{1-0.02}Mg\ Al_{0.02}O$ transparent conducting oxide films prepared by rf magnetron sputtering," Journal of Alloys Compounds, vol. 617, pp. 180–184, 2014.

[36] H. S. So, S. Bin Hwang, D. H. Jung, H. Lee, "Optical and electrical properties of Sn-doped ZnO thin films studied via spectroscopic ellipsometry and hall effect measurements," Journal of the Korean Physical Society, vol. 70, no. 7, pp. 706–713, 2017.

[37] S. K. O'Leary, S. Zukotynski, J. M. Perz, "Disorder and optical absorption in amorphous silicon and amorphous germanium," Journal of Non-Crystalline Solids, vol. 210, no. 2–3, pp. 249–253, 1997.

[38] F. Z. Bedia, A. Bedia, M. Aillerie, N. Maloufi, B. Benyoucef, "Structural, Optical and Electrical Properties of Sn-doped Zinc Oxide Transparent Films Interesting for Organic Solar Cells (OSCs)," Energy Procedia, vol. 74, pp. 539–546, 2015.

[39] K. Huang Z. Tang, L. Zhang, J. Yu, J. Lv, X. Liu, F. Liu, "Preparation and characterization of Mg-doped ZnO thin films by sol–gel method," Applied Surface Science, vol. 258, no. 8, pp. 3710–3713, 2012.

[40] B. Kim, D. Lee, B. Hwang, D.-J. Kim, C. K. Kim, "Effects of Mg doping and annealing temperature on the performance of Mg-doped ZnO nanoparticle thin-film transistors," Molecular Crystals and Liquid Crystals, vol. 235, no.1, pp. 61–74, 2021.

[41] M. Caglar, Y. Caglar, S. Ilican,

"Investigation of the effect of Mg doping for improvements of optical and electrical properties," Physica B: Condensed Matter, vol. 485, pp. 6–13, 2016.

[42] B. H. Kim, C. M. Staller, S. H. Cho, S. Heo, C. E. Garrison, J. Kim, D. J. Milliron, "High Mobility in Nanocrystal-Based Transparent Conducting Oxide Thin Films," ACS Nano, vol. 12, no. 4, pp. 3200–3208, 2018.

[43] L. T. C. Tuyen, S.-R. Jian, N. T. Tien, P. H. Le, "Nanomechanical and Material Properties of Fluorine-Doped Tin Oxide Thin Films Prepared by Ultrasonic Spray Pyrolysis: Effects of F-Doping," Materials (Basel), vol. 12, no. 10, pp. 1665, 2019.

[44] P. Senthilkumar, S. Raja, R. Ramesh Babu, G. Vasuki, "Enhanced electrical and optoelectronic properties of W doped SnO2 thin films," Optical Materials, vol. 126, pp. 112234, 2022.

[45] G. Turgut, E. F. Keskenler, S. Aydın, D. Tatar, E. Sonmez, S. Dogan, B. Duzgun, "Characteristic evaluation on spray-deposited WFTO thin films as a function of W doping ratio," Rare Metals, vol. 33, no. 4, pp. 433–441, 2014.

[46] E. Vinoth, S. Gowrishankar, N. Gopalakrishnan, "Effect of Mg doping in the gas-sensing performance of RF-sputtered ZnO thin films," Applied Physics A, vol. 124, no. 6, p. 433, 2018.

SAKARYA ÜNİVERSİTESİ
FEN BİLİMLERİ ENSTİTÜSÜ DERGİSİ

Sakarya University Journal of Science
SAUJS

ISSN 1301-4048 e-ISSN 2147-835X Period Bimonthly Founded 1997 Publisher Sakarya University
http://www.saujs.sakarya.edu.tr/

Title: The Support Vector Regression with L1 Norm: Application to Weather Radar Data in Adjusting Rainfall Errors

Authors: Arzu OZKAYA, Asım Egemen YILMAZ

Recieved: 2022-03-19 00:00:00

Accepted: 2023-03-22 00:00:00

Article Type: Research Article

Volume: 27
Issue: 3
Month: June
Year: 2023
Pages: 634-642

How to cite
Arzu OZKAYA, Asım Egemen YILMAZ; (2023), The Support Vector Regression with L1 Norm: Application to Weather Radar Data in Adjusting Rainfall Errors. Sakarya University Journal of Science, 27(3), 634-642, DOI: 10.16984/saufenbilder.1090178
Access link
https://dergipark.org.tr/en/pub/saufenbilder/issue/78131/1090178

Sakarya University Journal of Science 27(3), 634-642, 2023

The Support Vector Regression with L_1 Norm: Application to Weather Radar Data in Adjusting Rainfall Errors

Arzu ÖZKAYA [*1], Asım Egemen YILMAZ[2]

Abstract

This paper presents the results of the research on radar rainfall estimate errors with the support vector regression (SVR) method using the observed rain gauge data. The paper depicts the methodological base of the algorithm that covers additive and multiplicative corrections and the practical implementations considering the locations of gauge measurements. The preliminary results show that the SVR has a location-oriented performance. The multiplicative and additive correction factors show decreasing and unstable trends respectively, as the distance from the radar location increase. Another particular outcome is that the SVR shows better results for almost all stations in decreasing the error in maximum rainfall amounts measured with weather radar.

Keywords: Support vector regression, weather radar data, flood, error minimization

1. INTRODUCTION

With the increasing world population, climate change, and rapid urbanization, extreme weather events are expected to occur with growing frequencies. According to World Meteorological Organization (WMO), 44% of disasters have been associated with floods all over the world [1]. This outcome makes studies in forecasting floods extremely important. Moreover, success in flood estimation primarily depends on accurate rainfall data [2]. Rain gauge stations, treated as ground-truth measurements, are the basic source in flood forecasting studies. However, rainfall has a dynamic spatio-temporal pattern and rain gauge stations, pointwise measurements, are generally too sparse to capture this variability [3]. Representation of rainfall distribution in ungauged or poorly-gauged areas, remote sensing products can be used because of their wide coverage and fine resolutions. In the field of hydrology, weather radar products have been used for decades with some inaccuracy [4]. The quality of radar products can be improved with the implementation of methods using ground reference data [5]. Although there is a wide range of studies to assess and increase the performance of radar rainfall data, the generalization of the methods for a broader area causes a limitation in error reduction [6]. And this points out that future analysis should focus on working with more radar products.

* Corresponding author: a.ozkaya@aybu.edu.tr (A. OZKAYA)
[1] Ankara Yıldırım Beyazıt University
[2] Ankara University
E-mail: aeyilmaz@eng.ankara.edu.tr
ORCID: https://orcid.org/0000-0003-3983-8831, https://orcid.org/0000-0002-4156-4238

Since rainfall depth is indirectly measured by the weather radar systems, uncertainties in the products are inevitable. And, errors that come from these uncertainties can be alleviated by various kinds of methods in the pre-or post-processing stages of data production. Although uncertainties coming from the error sources like signal attenuation, ground clutter, anomalous propagation, beam blockage, miscalibration, vertical air motion, and precipitation drift [7] can be reduced by pre-processing techniques, our knowledge about these errors is limited. As for post-processing techniques, geostatistical methodologies, statistical objective analysis, and deep learning models are generally used. In statistical analysis, vector norms with correction factors like multiplicative and additive can also be useful in error minimization. And, the recent application with Taxicab Norm showed that error reduction performed well in the multiplicative model but, correction values were dominated by location [8]. Since there is a nonlinear systematic error in the radar data, error generalization with norm methods may not fit completely, and obviously, it is not the unique way for the solution.

In learning algorithms, the support vector regression (SVR) is a famous one based on Vapnik's concept [9]. And, SVR indicates powerful results in time series analysis in most of the studies [10–13]. Moreover, since SVR is based on computational learning theory, optimum weights and thresholds for the trained network can be found conveniently. In searching parameters, although SVR has a lack of knowledge memory, problems related to inefficiency or time consumption do not appear especially for the processes that are nonlinear and nonstationary [14]. Since atmospheric processes have complex interactions, especially over complex terrain, hydrologic elements exhibit high nonlinearity. Rainfall, the driving force in flood studies, is one of the important nonlinear variables among hydrologic elements. However, an error that is the difference between the amount of rainfall recorded from the gauge and that estimated from the weather radar, can be reduced with SVR.The study in this paper is motivated by a desire to apply the SVR method in error minimization of radar rainfall estimates recorded in flood events in Mugla, Turkey for 16 flood events. To the best of our knowledge, the SVR application using weather radar data is the first in Turkey.

The paper is organized as follows. In Section II, the study area and datasets are described. Section III gives the methodology. In Section IV, results are given and the paper ends with conclusions in Section V.

2. STUDY AREA AND DATASETS

The study area covers the city of Muğla in Turkey (Figure 1). According to the Köppen-Geiger climate classification, cold-rainy winters and Mediterranean hot summer climates prevail over the region. Due to its climate characteristics, heavy rainfalls and floods are observed in late autumn and early winter, and this causes loss of lives and damage to infrastructures [15]. In the time between 2015 and 2019, 16 flood events were observed within Muğla province (Table 1). For the southwest part of Turkey, the spatiotemporal distributed rainfall data can be acquired by Muğla weather radar. It is a C-band Doppler weather radar and has a 120-km range with 333.33-m spatial resolution.

Table 1 Information about the flood events

No	Date (dd/mm /yyyy)	Location	Max. Cum. Rainfall (Gauge/ Radar)	Max. Rainfall (Gauge/ Radar)	Stand. Dev. (Gauge/ Radar)	data (hrs)
1	11/5/2015	Muğla	60.5/14.9	27.8/3.9	3.9/0.6	71
2	21/09/2015	Bodrum	211.4/24.1	36.8/5.8	7.9/1.0	71
3	21/10/2015	Bodrum	109.4/31.5	29.9/6.2	4.6/1.1	71
4	16/01/2017	Muğla	85.6/82.6	10.2/13.4	2.1/2.9	71
5	7/2/2017	Bodrum	58.4/26.3	17.6/9.5	3.0/1.5	71
6	7/3/2017	Marmaris	173.8/69.2	23.2/8.2	3.9/1.5	71
7	10/3/2017	Ortaca	41.3/43.6	5.3/5.0	1.1/1.1	71
8	23/10/2017	Muğla	63.0/24.1	14.8/3.7	2.5/0.8	71
9	13/11/2017	Datça	42.1/28.5	9.8/9.1	1.9/1.6	71
10	28/12/2017	Fethiye	127.8/69.1	36.2/10.3	4.9/1.8	71
11	16/11/2018	Bodrum	149.5/71.0	41.0/15.9	7.2/3.0	71
12	16/07/2019	Muğla	44.4/22.9	16.8/8.8	2.8/1.5	71
13	23/09/2019	Dalaman	45.7/22.0	21.5/10.2	3.4/1.6	71
14	4/10/2019	Köyceğiz	101.6/23.3	58.5/12.7	12.3/2.8	31
15	3/11/2019	Marmaris	185.8/49.0	47.8/11.8	8.7/2.0	71
16	24/11/2019	Ortaca	126.5/60.4	46.2/13.6	6.0/1.9	71
Av.	-	-	101.7/41.4	27.7/9.3	4.8/1.4	

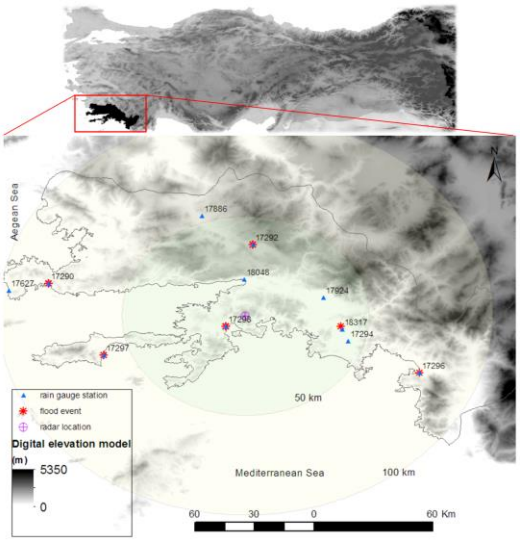

Figure 1 Study area, locations of rain gauge stations, flood events, and weather radar station with radar ranges (50 km and 100 km) over digital elevation model

For application, the flood data from the observational stations and Muğla weather radar were provided by the Turkish State Meteorological Service (TSMS). The locations of flood events and stations over the digital elevation model can be seen in Figure 1. The information about the flood events that cover maximum accumulated rainfall amounts both gauge and radar datasets for each event and corresponding maximum hourly rainfall values and standard deviations are given in Table 2. Given datasets, the length of the data is 71 hrs except for event number 14, lasting 31 hours.

Table 2 Station information

Station No	longitude	latitude	Elevation (m)
17290	27.440	37.033	26
17292	28.367	37.210	646
17294	28.799	36.772	12
17296	29.124	36.627	3
17297	27.692	36.708	28
17298	28.245	36.840	16
17886	28.137	37.340	365
17924	28.687	36.970	24
18317	28.772	36.826	13
18048	28.327	37.051	1
17627	27.260	37.000	6

3. METHOD

The SVR algorithm is a nonlinear Generalized Portrait algorithm proposed by Vapnik, used for solving classification and regression problems. It is based on the principle of structural risk minimization (SRM). A visualization of the problem is depicted in Figure 2. The primary goal of this study is to correct radar data with gauge measurements by giving tolerated errors, ε.

As the increase of ε, the number of adjusted radar data in the ε-intensive tube increases, therefore evaluation is performed with regression parameters variation instead of ε.

A simple linear regression problem trained using the dataset with k vector size can be given as

$$[(x_{n-k+1}, y_{n-k+1}), (x_{n-k+2}, y_{n-k+2}), \dots, (x_{n-1}, y_{n-1}), (x_n, y_n)], \quad (1)$$

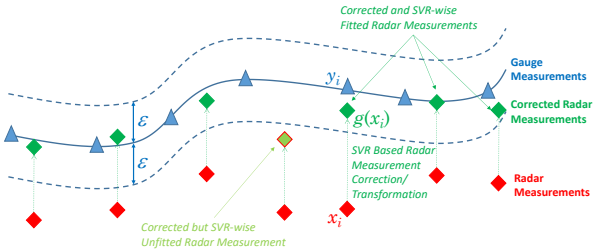

Figure 2 Illustration of an SVR regression function

where $x_i$is the input data, rainfall value obtained from radar measurement, and y_i is the corresponding output data, rainfall value gathered from gauge observation. By a nonlinear function $\emptyset(x)$, the regression function can be defined as

$$f = g(x) = w^T.\emptyset(x) + b, \quad (2)$$

where w and b are the regression function parameters. The coefficients (w and b) are estimated by minimizing the following general function;

$$r(f) = C\frac{1}{n}\sum_{i=1}^{n} L_\varepsilon(y_i) + \frac{1}{2}||w||^2, \quad (3)$$

where C and ε are predefined parameters. $L_\varepsilon(y_i)$ is the ε-insensitive loss function. When the adjusted value is within the ε-tube, the loss becomes zero. The tolerated errors can be stated with penalized loss as

$$L_\varepsilon(y_i) = \begin{cases} 0, & for\ |y_i - [g(x)]| < \varepsilon, \\ |y_i - [g(x)]| - \varepsilon, & for\ |y_i - [g(x)]| \geq \varepsilon. \end{cases} \quad (4)$$

The regression problem can be expressed with the following optimization problem,

$$\min_{w^T,b} \sum_{i=1}^{k} \|g(x_i) - y_i\|, \quad (5)$$

where ||…|| is the L_1 norm. By these definitions x_i (the rainfall value gathered from radar measurement) is corrected as $g(x_i)$ by means of the support vector regression.

For the selection of ε value, the input noise value should be known [16]. However, such noise is not generally known nor is this study. In the determination of the ε value, the maximum rainfall amount which is significant in flood studies due to being of the main driving force for the maximum streamflow amount is analyzed for all flood events (Table 1). The average value of maximum observed rainfall is calculated as 27.7 mm/hr. Since epsilon has a direct effect on the results of the SVR, the value selection is constrained as 2 mm. C is the other parameter that controls the penalty on observations. In this study, C is taken as unity, 1.

4. RESULTS AND DISCUSSIONS

Using the SVR algorithm with L_1 norm, regression function parameters are determined for each station. And, variation of averaged regression function parameters for each station is evaluated considering the radar distance (Figure 3). From the results, it is noticed that the multiplicative factors have a decreasing trend as radar distance increases (Figure 3 (a)), whereas the additive factors show an unstable trend in which stations located in mid-distance (40 km - 60 km) have the highest value (Figure 3 (b)).

In order to determine SVR power, four criteria are used in the evaluation. These are the difference between gauge and radar data that is given as error (e), standard deviation (std), the relative error in maximum rainfall (re), and root mean square percentage error (RMSPE). The equations that represent the four criteria are given below,

$$e = \frac{1}{k}\sum_{i=1}^{k}|g(x_i)-y_i|, \quad (6)$$

$$std = \sqrt{\frac{1}{k-1}\sum_{i=1}^{k}(e_i-\bar{e})^2}\,, \quad (7)$$

$$re = \left(\frac{1}{k}\sum_{i=1}^{k}\left|g(x_{i,max})-y_{i,max}\right|/y_{i,\max}\right)100\,, \quad (8)$$

$$RMSPE = \sqrt{\frac{\sum_{i=1}^{k}((g(x_i)-y_i)/y_i)^2}{k}}\,, \quad (9)$$

where $\overline{g(x)}$, $\overline{y}$ and $\overline{e}$ are averages of corrected radar values, gauge rainfall values and mean absolute error values, respectively. $g(x_{i,max})$ and $y_{i,max}$ are the maximum corrected radar rainfall data and the maximum gauge rainfall data for the i[th] event. k is the number of data pairs used for each flood event.

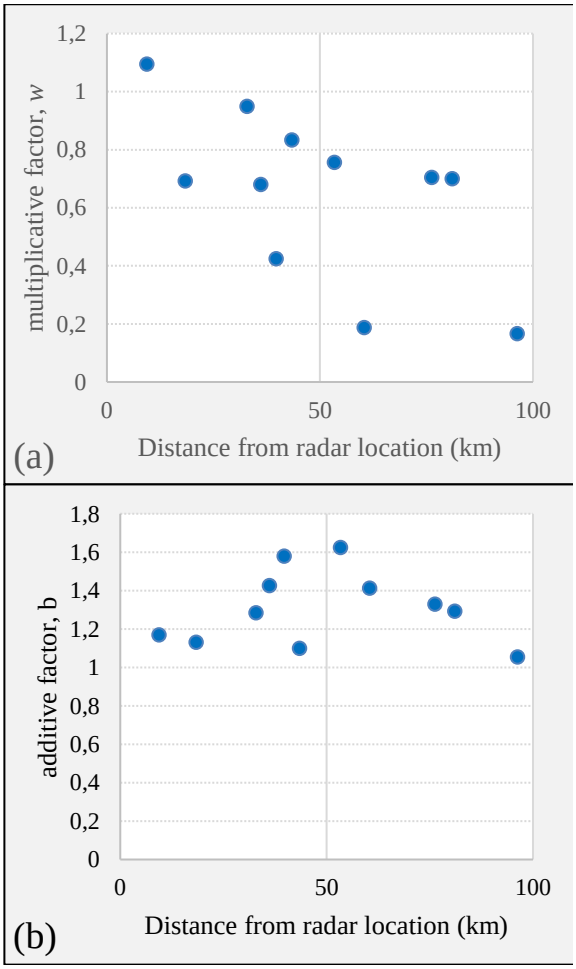

Figure 3 Variation of regression parameters to distance between stations and radar location

The averages of the difference between gauge observations and radar measurements considering the order of stations from closely located stations to further ones are given in Figure 4 (a) and (b). Although there is an increase in the rainfall differences at all stations regardless of proximity to radar location, a decrease in the interquartile range of the box plots belongs to the stations located in mid and long-distance to the radar point (17292, 17886, 17297, 17296, 17290, and 17627) is observed.This outcome is related to error increase and can be explained by the fact that constraining the radar data in the ε-intensive tube makes an increase in the differences.

When the results of standard deviations are analyzed it is seen that all median values show an improvement with the SVR method (Figure 4 (c) and (d)). Moreover, the lengths of the whiskers and quartiles decrease (Figure 4 (d)).

The results for the maximum rainfall amounts show that the error in these data decreases with the SVR application except for the station located in the outermost (Figure 5(a)). With RMSPE calculations, it is seen that the original dataset (depicted with blue color) shows an erorr increase as distance increases in general. With SVR, the stations that show high RMSPE values achieve a decrease but, stations that show low RMSPE values get small improvements or increases in the error. Furthermore, the number of data pairs that fall into the ε-intensive tube does not give apparent relation between the station closeness. The highest three values are noticed in the mid-located stations (in the range of 40-60 km) (Figure 5 (c)).

5. SUMMARY AND CONCLUSION

To save human lives and properties, accurate rainfall forecasting is significant for the areas that are prone to flash floods. The rainfall data of stations that are located under the umbrella of Muğla weather radar show that extreme events are likely to be seen in cold seasons. This study introduces an SVR technique for adjusting weather radar rainfall data belonging to 16 flood events. The results

reveal that the SVR model with the L_1 norm is a promising alternative in correcting amounts of rainfall data. In the error-adjusting process, additive and multiplicative correction factors are used simultaneously.

The main conclusions of this study are the following:

- Since the data from weather radar is based on the scaling law formulation that is obtained from raindrop size distribution and each event has different atmospheric characteristics, the error improvement is not the same for all stations and shows a location-oriented performance.

- The values for the correction factor show that as the distance between the radar and the station increases, the values of the multiplicative factor show a decreasing trend and the majority of the values are less than one. Meanwhile, the values of additive factors indicate a variable trend in which stations that are located in the mid-range have the greatest ones, almost 1.6. Furthermore, all stations have additive factors greater than the value of 1. These results point out that although weather radars generally underestimate the rainfall amounts, the SVR algorithm with defined tolerated error makes a variation in additive factor instead of a multiplicative one.

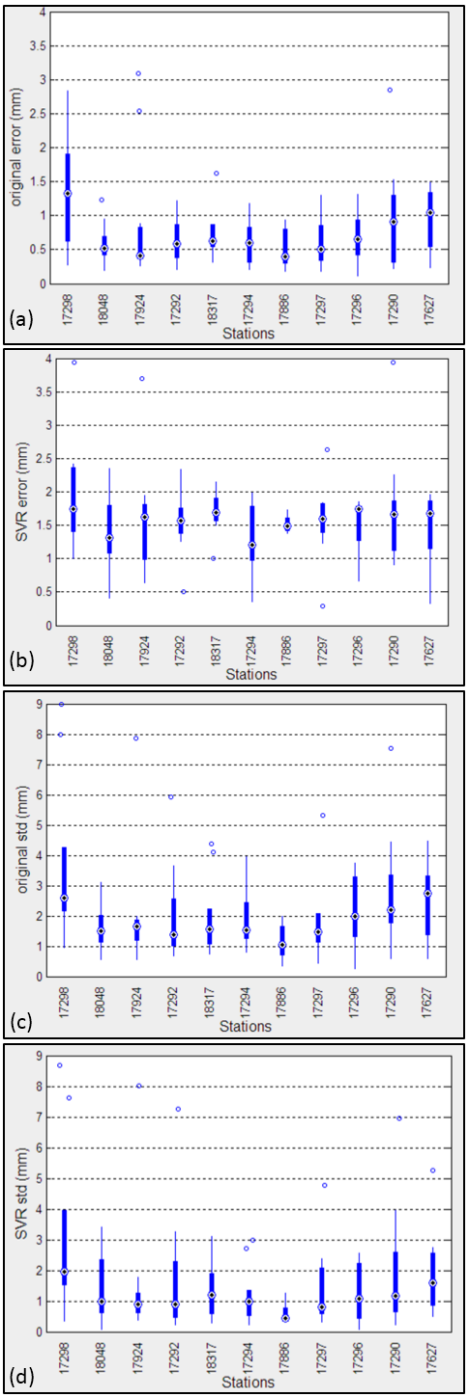

Figure 4 Error and standard deviation results for original and SVR applied datasets ((a) and (c) show the statistics related to original data, (b) and (d) show the SVR applied data, the order of stations in the x-axis is the same as the order of radar closeness given in the map)

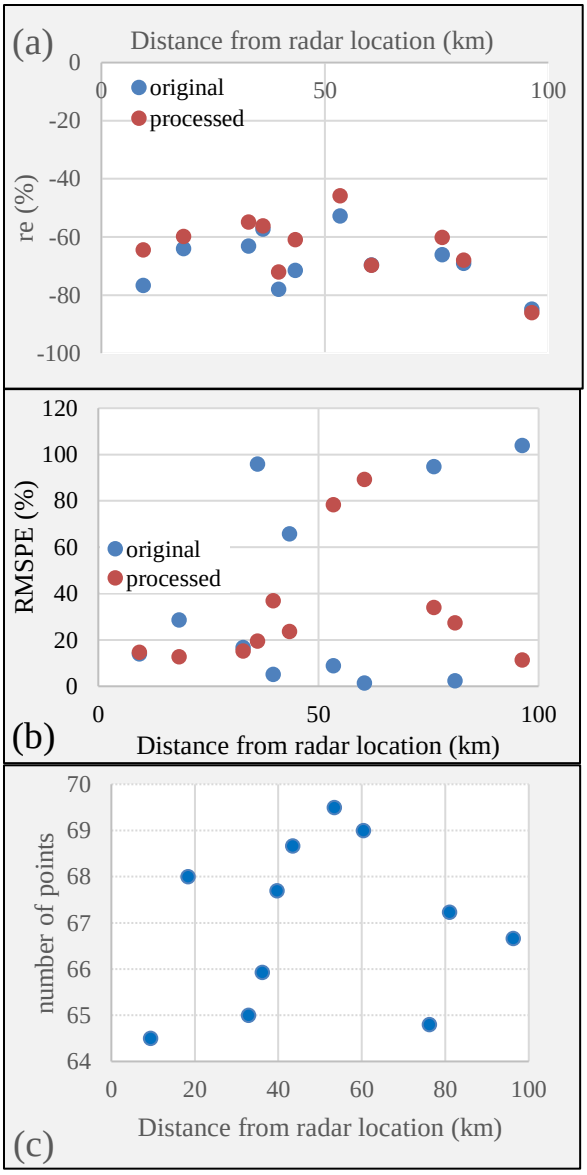

Figure 4 Statistical resultts for original and SVR applied (processed) datasets

- In the point of error reduction, it is discerned that the SVR has poor results independent of location. Contrary to this, the standard deviation of the error decreases for all stations.

- Since other norms, L_2 and L_∞ norms are not working well most probably owing to the non-Gaussian distribution of datasets, detailed investigations considering the physical properties of the topology and time will probably present a clearer conclusion. Moreover, some other optimization techniques, like ant search algorithms, particle swarm optimization algorithms, and genetic algorithms can be used for tuning the SVR parameters. For future studies, revealing the performance in determining SVR parameters by using different optimization techniques will be a challenging issue.

Acknowledgments
The radar and gauge rainfall data were provided by the Turkish State Meteorological Service (TSMS).

Funding
The authors have not received any financial support for the research, authorship, or publication of this study.

The Declaration of Conflict of Interest/ Common Interest
No conflict of interest or common interest has been declared by the authors

Authors' Contribution
The authors contributed equally to the study.

The Declaration of Ethics Committee Approval
This study does not require ethics committee permission or any special permission.

The Declaration of Research and Publication Ethics
The authors of the paper declare that they comply with the scientific, ethical, and quotation rules of SAUJS in all processes of the paper and that they do not make any falsification on the data collected. In addition, they declare that Sakarya University Journal of Science and its editorial board have no responsibility for any ethical violations that may be encountered and that this study has not been evaluated in any academic publication environment other than Sakarya University Journal of Science.

REFERENCES

[1] WMO, "WMO atlas of Mortality and Economic Losses from Weather, Climate and Water Extremes (1970–

2019)", 2021. [Online]. Available: https://library.wmo.int/doc_num.php?explnum_id=10989

[2] X. Sun, R. G. Mein, T. D. Keenan, J. F. Elliott, "Flood estimation using radar and raingauge data," Journal of Hydrology, vol. 239, no. 1, pp. 4–18, 2000.

[3] C. Chwala, H. Kunstmann, "Commercial microwave link networks for rainfall observation: Assessment of the current status and future challenges," WIREs Water, vol. 6, no. 2, pp. 1337, 2019.

[4] L. J. Battan, "Vertical Air Motions and the Z-R Relation," Journal of Applied Meteorology, vol. 15, no. 10, pp. 1120–1121, 1976.

[5] I. Emmanuel, H. Andrieu, P. Tabary, "Evaluation of the new French operational weather radar product for the field of urban hydrology," Atmospheric Research, vol. 103, pp. 20–32, 2012.

[6] I. V. Sideris, M. Gabella, R. Erdin, U. Germann, "Real-time radar–rain-gauge merging using spatio-temporal co-kriging with external drift in the alpine terrain of Switzerland," Quarterly Journal of the Royal Meteorological Society, vol. 140, no. 680, pp. 1097–1111, 2014.

[7] G. Villarini, W. F. Krajewski, "Review of the Different Sources of Uncertainty in Single Polarization Radar-Based Estimates of Rainfall," Surveys in Geophysics, vol. 31, no. 1, pp. 107–129. 2010.

[8] A. Ozkaya, A. E. Yılmaz, "Muğla Radarı Yağış Tahmin Hatalarının L2 ve L∞ Normlarıyla Analizi," in International Symposium on Remote Sensing in Meteorology, İstanbul, Dec. 2021. [Online]. Available: https://meteouzal.itu.edu.tr/#/en/home

[9] V. Vapnik, The Nature of Statistical Learning Theory. Springer Science and Business Media, 1999.

[10] P.-F. Pai, W.-C. Hong, "A recurrent support vector regression model in rainfall forecasting," Hydrological Processes, vol. 21, no. 6, pp. 819–827, 2007.

[11] W.-C. Hong, P.-F. Pai, "Potential assessment of the support vector regression technique in rainfall forecasting," Water Resources Management, vol. 21, no. 2, pp. 495–513, 2007.

[12] Z. Zeng, W. W. Hsieh, A. Shabbar, W. R. Burrows, "Seasonal prediction of winter extreme precipitation over Canada by support vector regression," Hydrology and Earth System Sciences, vol. 15, no. 1, pp. 65–74, 2011.

[13] A. Danandeh Mehr, V. Nourani, V. Karimi Khosrowshahi, M. A. Ghorbani, "A hybrid support vector regression–firefly model for monthly rainfall forecasting", International journal of Environmental Science and Technology, vol. 16, no. 1, pp. 335–346, 2019.

[14] Y. Xiang, L. Gou, L. He, S. Xia, W. Wang, "A SVR–ANN combined model based on ensemble EMD for rainfall prediction," Applied Soft Computing, vol. 73, pp. 874–883, 2018.

[15] A. G. Yilmaz, "The effects of climate change on historical and future extreme rainfall in Antalya, Turkey," Hydrological Sciences Journal, vol. 60, no. 12, pp. 2148–2162, 2015.

[16] C.-C. Chuang, C.-C. Hsu, and C. W. Tao, "Embedded support vector

regression on Cerebellar Model Articulation Controller with Gaussian noise," Applied Soft Computing, vol. 11, no. 1, pp. 1126–1134, 2011.

SAKARYA ÜNİVERSİTESİ
FEN BİLİMLERİ ENSTİTÜSÜ DERGİSİ

Sakarya University Journal of Science
SAUJS

ISSN 1301-4048 e-ISSN 2147-835X Period Bimonthly Founded 1997 Publisher Sakarya University
http://www.saujs.sakarya.edu.tr/

Title: Application of Soft Computing Techniques in River Flow Modeling

Authors: Sefa Nur YESİLYURT, Hüseyin Yildirim DALKILIÇ, Pijush SAMUI

Recieved: 2022-08-10 00:00:00

Accepted: 2023-03-22 00:00:00

Article Type: Research Article

Volume: 27
Issue: 3
Month: June
Year: 2023
Pages: 643-659

How to cite
Sefa Nur YESİLYURT, Hüseyin Yildirim DALKILIÇ, Pijush SAMUI; (2023), Application of Soft Computing Techniques in River Flow Modeling. Sakarya University Journal of Science, 27(3), 643-659, DOI: 10.16984/saufenbilder.1152982
Access link
https://dergipark.org.tr/en/pub/saufenbilder/issue/78131/1152982

Sakarya University Journal of Science 27(3), 643-659, 2023

Application of Soft Computing Techniques in River Flow Modeling

Sefa Nur YESILYURT *[1], Huseyin Yildirim DALKILIC[1], Pijush SAMUI[2]

Abstract

Modeling of data is critical in the analysis and evaluation of hydrological behavior. River flow data is one of the most important data in explaining hydrology. Management of water resources; It takes place in the literature as an area that needs to be investigated in order to provide early warning for undesirable situations such as floods and drought. For this reason, it is of important to develop different techniques for the estimation and modeling of river flow or to make comparisons between techniques. In this study, the flow data of fourteen stations located in the Euphrates-Tigris basin between 1981 and 2010 were used. Adaptive Network Based Fuzzy Inference Systems (ANFIS), Support Vector Machine (SVM) techniques that are frequently used in the literature, and newly introduced Gaussian Process Regression (GPR), Extreme Learning Machine (ELM) and Emotional Neural Network (ENN) artificial intelligence techniques are compared. In addition, considering all performance indices, it was determined which technique gave better results with rank analysis. Although all models worked well, it was seen that the methods were ranked as ELM, GPR, ENN, SVM and ANFIS starting from the best. This has shown that ELM, GPR and ENN methods, which have been used recently in flow modeling, give better results than traditional methods with complex structures. In addition, flow values were used in the whole study and these values were examined in 3 different combinations. It was seen that the model structure that gave the best performance was the model structure that used the flow data from one, two and three days ago as an estimator. The results were analyzed with a Taylor diagram and time series graphs.

Keywords: ANFIS, ELM, ENN, GPR, SVM

1. INTRODUCTION

Water, the main component of life, is an indispensable resource used to provide the energy required for living things to survive. In cases such as efficient use of existing water resources and development of water structures, basin modeling and estimation are required. At the same time, the fact that there are many unknown factors in the occurrence of

* Corresponding author: sefa.yesilyurt@erzincan.edu.tr (S.N. YESİLYURT)
[1] Erzincan Binali Yildirim University
[2] National Institute of Technology Patna
E-mail: hydalkilic@erzincan.edu.tr, pijush@nitp.ac.in
ORCID: https://orcid.org/ 0000-0001-6173-3038, https://orcid.org/ 0000-0002-4405-9341, https://orcid.org/ 0000-0003-2906-6479

hydrological events, instabilities in the work field, irregularities in river systems and flow data have made it necessary for researchers to create models and make estimations for the future. These estimations, which can be made through some mathematical methods, provide more successful results through artificial intelligence techniques and fuzzy logic methods, and thus, can be modeled within a shorter time. When the studies on this subject are examined, it is seen that Zhou et al. used Genetic Algorithm (GA)- Least Square Estimator (GL) and adaptively developed Adaptive Network Based Fuzzy Inference Systems (ANFIS); R (ANFIS) and R-ANFIS (GL) for river flow modeling [1].

It has been observed that the R-ANFIS (GL) model gives better results when time series are used by Zhou et al. [1]. In another study by He et al., Artificial Neural Network (ANN), ANFIS and Support Vector Machine (SVM) based on three different data were used for river flow estimation. It was seen that the SVM method gave better results and it was stated that these methods could be used in regions with complex topography [2]. In their study Yaseen et al. improved the Extreme Learning Machine (ELM) model (improved ELM) as EELM, compared it with SVM, and found that the improved ELM model gives much better results [3]. According to Yasin et al. Emotional Neural Network (ENN), Multivariate Adaptive Regression Splines (MARS), Minimax Probability Regression (MPMR) and Fitness Vector Machine (RVM) methods were used for hourly river flow modeling. He also proposed the ENN algorithm for the first time for river flow modeling. It was also stated that the ELM model was found to be far superior to other models [4].

Wang et al. analyzed the deterministic and stochastic components of the modeling at the same time and examined four different station data between 1971–2010. They conducted a performance comparison between hybrid models and found that SETAR (Self-Exciting Threshold Autoregressive) model gave better results [5]. Sun et al. made river flow estimations using Gaussian Process Regression (GPR) for MOPEX basins. They observed that the GPR model worked well for long-term flow data [6]. Yaseen et al. analyzed the artificial intelligence models for flow estimations and determined the advantages and disadvantages of the models. They examined the possible applications of artificial intelligence and conducted comprehensive literature research [7]. Khadangi et al. applied ANFIS and Radial Base Function (RBF) methods for daily river flow modeling in their study and found that ANFIS provided much better performance [8].

The ELM construct created to eliminate the need for iterative tuning of hidden neuron parameters in traditional models was proposed by Huang et al. The model was first used by Siqueira et al. for river flow modeling. They observed that the model is suitable for hydraulic power plants in Brazil and for river flow studies. At the same time, the ELM structure was developed within time and different ELM structures were created for different studies [9, 10]. Yaseen et al. used ELM and ANFIS to estimate river flows in their studies and observed that the improved ELM gave better results when compared to these techniques. In addition, in a study conducted in Iran, a semi-arid region, Generalized Regression Neural Network (GNRR), SVM, and ELM were compared and it was concluded that ELM gave better results [11].

In another study Adnan et al., in which ELM was used as Optimally Pruned ELM (OP-ELM), ANFIS-PSO (Particle Swarm Optimization), MARS, and M5 model tree (M5Tree) techniques were compared by cross-validation and it was concluded that OP-ELM method could be used successfully in daily stream flow estimation [12]. The ENN structure, which takes emotional parameters into account in addition to other models that

simulate the brain structure in modeling studies, was developed by Rumelhart, and was used in river flow modeling for the first time by Yaseen et al., ENN was used in the study to create an hourly river flow model, it was compared with other well-structured machine learning methods, and it was found that ENN performed better. In a study in which SVM, developed by Rumelhart, was used for river flow modeling, ELM was compared with Artificial Intelligence (AI),

Genetic Programming (GP) and SVM and it was observed that ELM method gave faster and better results in river flow forecasting than the other methods [4, 13, 14]. Sun et al. studied the monthly estimation of GPR, compared GPR with Autoregressive Moving Average with Exogenous variables (ARMAX) and multilayer perceptron (MLP), used for more than four hundred stations in the USA, and concluded that GPR performed better [6].

In this study, conducted for river flow forecasting and modeling, which is of great importance for water resources engineering, it is aimed to find the best results in the shortest time in river flow modeling by comparing widely used methods such as ANFIS and SVM with the rarely used ones such as ELM, GPR and ENN methods, to find the membership functions in traditional methods by trial and error, and to eliminate undesirable conditions.

2. MATERIALS AND METHODS

There are many methods for flow modeling which have various advantages and disadvantages. In the current study, ANFIS and SVM methods, which are known to give good results and are frequently used in flow modeling, have been compared to more recent methods. The advantages and disadvantages of these methods have been taken into account. Data from fourteen flow observation stations located in the Euphrates-Tigris Basin were used in the study. ELM, which has good learning capacity and generalization performance and is much faster than traditional algorithms, ENN, which has high application convenience and efficiency, and GPR, which can seamlessly integrate various machine learning tasks such as hyperparameter estimation, model training and uncertainty estimation, have been preferred.

2.1. Adaptive Neuro-Fuzzy Inference System (ANFIS)

ANFIS, based on Takagi-SugenoKang inference system, was developed by Jang to model nonlinear functions, determine nonlinear components in the control system, and predict the chaotic time series [15-16]. The fuzzy logic inference system evaluated in ANFIS is transformed into adaptive networks and the most suitable condition is created through a learning algorithm. Neural adaptive learning techniques develop a model that "learns" the related system by using the data set selected for the fuzzy modeling.

In other words, ANFIS uses the input/output data set and the backpropagation algorithm used in artificial neural networks alone or together with the least-squares method, and thus, by regulating the membership functions parameters, creates a Fuzzy İnference System (FIS). This regulation allows the fuzzy system to learn the relevant system with the help of the data that it has modeled. Namely, it customizes/adapts itself to the data that will be modeled. Thanks to this structure, ANFIS has both used the environmental information about the system and gained the ability to update itself using the input and output data related to the system [17] (Figure 1).

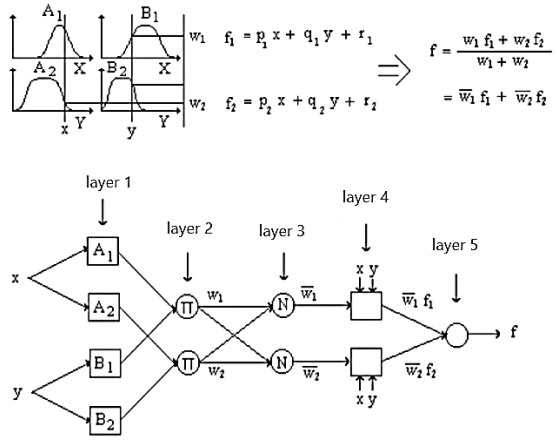

Figure 1 ANFIS Structure [18]

While the biggest advantages of the ANFIS model can be regarded as its efficiency in mathematical analysis, success in adaptation and successful conclusion in numerical data, too much human intervention can be supposed as a disadvantage since the training of ANFIS parameters takes quite a long time and the model has a structure with many rules [18].

2.2. Extreme Learning Machine (ELM)

ELM is a fully connected artificial neural network model developed by Huang et al. and consists of an input layer, a hidden layer and an output layer [9]. Unlike the commonly used gradient-based network structures, ELM, whose input weights and threshold values are randomly generated but output weights are analytically generated, creates an analytical equation of the model beyond finding the model weights, and thus, it prevents error clogging at a local point and removes the problem of learning process that takes a long time as in the other methods. In this way, it provides better performance compared to other methods and speeds up the model production process.

At the same time, other learning algorithms sometimes have to apply procedures such as stopping the training process of the model earlier, adding regulation parameters, breaking weights or using validity sets as they may encounter undesirable situations such as improper learning rate, excessive learning and memorization, and stuck in local minimums, whereas ELM reaches the solution directly without any intermediate processing. In addition to all these advantages, the structure of the ELM method, which offers the possibility to use many activation functions which can be derivative, underivative or discrete, consists of the input layer where the data is read, the output layer where the classes are determined and the hidden layer where the intermediate operations are conducted, as shown in Figure 2.

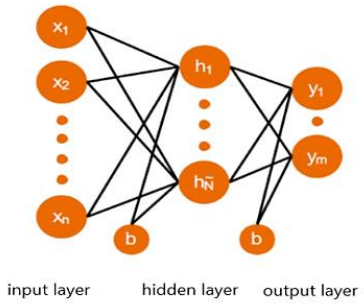

Figure 2 Algorithm of Extreme Learning Machine [19]

The ELM structure can calculate the output weight with the Moore-Penrose generalized inverse latent matrix without any need for iterative optimization. If L stands for the hidden node, β_j symbolizes the output neurons, and jth is symbolized as the weight value connecting the hidden neurons, then the ELM structure can be expressed as;

$$\sum_{j=1}^{L} \beta_j h_j(x_i) = y_i, \qquad i = 1, \ldots, N, \tag{1}$$

Mapping the properties for J_{th} hidden node output $h_j(x_i)$; is

$$h_j(x_i) = \frac{1}{1+exp\left(-\left(w_j^T x_i + b_j\right)\right)} \tag{2}$$

w_j refers to the weight vector connecting input neurons used in this equation,

$W_j = [W_{j1}, \ldots, W_{jD}]^T \epsilon \mathbb{R}^D$ and J_{ht} hidden neuron, and b_j is expressed as trend (deviation) term.

$$H\beta = y, \beta = [\beta_1, \ldots, \beta_L]^T \in \mathbb{R}^L, \; y = [y_1, \ldots, y_N]^T \in \mathbb{R}^N \quad (3)$$

$$H(w_1, \ldots, w_L, b_1, \ldots, b_L, x_1, \ldots, x_N) = \begin{bmatrix} h_1(x_1) & \ldots & h_L(x_1) \\ \vdots & \ddots & \vdots \\ h_1(x_N) & \ldots & h_L(x_N) \end{bmatrix} \in \mathbb{R}^{N*L} \quad (4)$$

H used in these equations denotes the hidden layer output matrix. ELM chooses the case with the minimum error and the lowest output weight among different traditional learning algorithms. Randomly initialized w_j hidden node parameters and bj is (j = 1; . . .; L) and the least squares solution of equation 1 is as follows;

$$\beta = H^{\dagger} \quad (5)$$

Here † Moore-Penrose denotes the generalized opposite. Decision function to be created to write $\hat{x}$, which is the new test example of ELM structure, can be expressed as [19];

$$\hat{y} = sign\,(h(\hat{x})\beta) \quad (6)$$

2.3.Emotional Neural Network Algorithm (EmNN-ENN)

This section describes the emotional neural network algorithm (EmNN). EmNN is based on the emotional back-propagation algorithm (EmBP- emotional backpropagation), which is a modified version of the traditional back-propagation algorithm (BP-back propagation). As stated by David and James, the BP method is often preferred because of its simplicity of application and its rapid operation, especially when it has a sufficient database. EmBP is described according to the information flow layers of the three-layer EmNN algorithm [20]. Layers of the EmNN algorithm are called as follows:

i: input layer with neurons

h: hidden layer with neurons

j: output layer with neurons

(Figure 3) shows the process for EmNN feed-forward calculation [21–22];

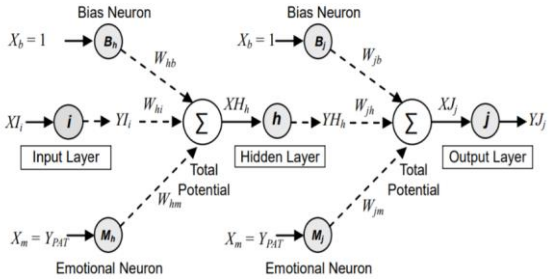

Figure 3 Process for EmNN feed-forward calculation [21-22]

Emotional parameters are used in conjunction with the current learning coefficient (η) and α momentum ratio. (μ) is defined as the anxiety coefficient and k is defined as the confidence coefficient, and it is observed how these two parameters act when learning each new task. Anxiety level decreases as confidence level increases. Both coefficients have normalized values between 0 and 1. The level of anxiety depends on the mean value of the input pattern and the error indicator for each period. The average input value used here must always be positive because the pixel values are normalized to values between 0-1. At the same time, the error indication may provide negative feedback if an unstable condition exists there. In this case, the heuristic network will be unreliable and unstable, similar to traditional networks. Therefore, three parameters are arranged until stable learning is found. These three parameters stand for the learning rate, momentum ratio and the count of hidden neurons. Therefore, as learning progresses, the

anxiety rate decreases and the value of the confidence coefficient increases [12].

The anxiety coefficient can be defined as follows:

$$\mu = Y_{AvPAT} + E \quad (7)$$

Y_{AvPAT} is defined as the mean value of the patterns presented in the EmNN algorithm.
If p represents the pattern index, N is the total number of patterns presented in a period, and E is the feedback error, then;

$$Y_{AvPAT=} \frac{\sum_{p=1}^{N_P} Y_{PAT}}{N} \quad (8)$$

$$E = \frac{\sum_{j=1}^{N_j} (T_{j-Y} J_j)^2}{N_p . N_j} \quad (9)$$

k confidence coefficient;

$$k = \mu_0 - \mu_i \quad (10)$$

μ_0: the value of anxiety coefficient at the end of the first iteration

μ_i : coefficient of anxiety at the end of subsequent iterations

2.4.Support Vector Machine (SVM)

SVM, an algorithm based on optimization, was designed by Vapnik as a classification algorithm that minimizes the error [23]. Later, the algorithm started to be used for regression purposes with the name SVR. Since SVM depends on core functions, it is considered a nonparametric technique. SVM, created by including the maximum value in the structure, has become more efficient than other regression models. When the weight vector in the structure is expressed as w and the error value as ε, the minimization process is expressed based on the following equations;
$\min 1/2\|w\|^2$

$$y_i - (w, x_i + b) \leq \varepsilon \ , \ (w, x_i + b) - y_i \leq \varepsilon \quad (11)$$

When x is a point on the hyperplane and b is called a bias, then the constraint equation is as follows;

$$f(x) = y_i (w, x_i + b) \quad (12)$$

If the model margin value is wanted to be calculated to keep all data in it, minimization is used. However, it is not possible to use all values in this way. In this case, slack variables are used (ξi, ξi*).

$$\min 1/2\|w\|^2 + C \sum_{i=1}^{N} (\xi i + \xi i^*) \quad (13)$$

Equation is formed depending on the $y_i - (w, x_i + b) \leq \varepsilon + \xi i$ ve $(w, x_i + b) - y_i \leq \varepsilon + \xi i$ equations. C>0 constant is used and values where equation f is greater than ± ε are tolerated as shown in Figure 4 [24-28].

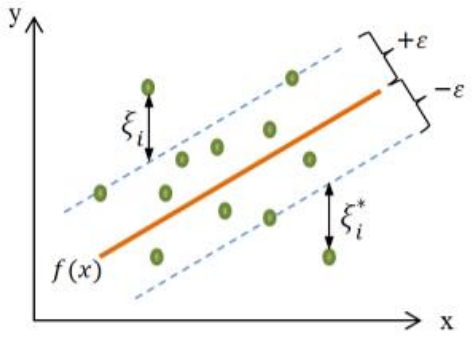

Figure 4 An example for SVM model structure [29]

SVM, which is widely preferred due to its ease of application and compatibility with both linear and nonlinear data, also has disadvantages such as difficulties in interpreting model parameters and long duration of model training [30-31].

2.5. Gauss Process Regression (GPR)

GPR, a non-parametric model suitable for use in solving nonlinear regression problems, is based on the conversion of prior functions to

posterior functions in Gaussian distribution GP describes the probability distribution on functions and when M (x) refers to mean, K(x,x') refers to covariance function, then the

$$f(x) \sim GP(m(x), K(x, x')) \quad (14)$$

equation is formed. In this equation m(x) and K(x,x') are expressed as follows;

$$m(x) = \mathbb{E}[f(x)] \quad (15)$$

$$K(x, x') = \mathbb{E}[(f(x) - m(x))((f(x') - m(x'))^T] \quad (16)$$

If θ_f indicates x- scaling (amplitude) and θ_t indicates y- scaling (length), then the covariance function is expressed with the equation below [17-26-32-33];

$$K =. \theta_f^2 \exp\left(-\frac{1}{\theta_t^2}\|x - x'\|^2\right) \quad (17)$$

The covariance matrix is as follows;

$$K = Ƕ\big((x_1, \dots, x_n), (x_1, \dots, x_n)\big) = \begin{bmatrix} Ƕ(x_1, x_1) & Ƕ(x_1, x_2) & \dots & Ƕ(x_1, x_n) \\ Ƕ(x_2, x_1) & Ƕ(x_2, x_2) & \dots & Ƕ(x_2, x_n) \\ \vdots & \vdots & \ddots & \vdots \\ Ƕ(x_n, x_1) & Ƕ(x_n, x_2) & \dots & Ƕ(x_n, x_n) \end{bmatrix} \quad (18)$$

2.6.Model development-evaluation criteria and rank analysis

Four different performance indices were used to evaluate the performance of the developed models. These indices, called correlation coefficient (R), Root Mean Squared Error (RMSE), Mean Squared Error (MSE), Mean Absolute Error (MAE), can be obtained with the help of the following equations;

$$R = \sqrt{1 - \frac{\sum_i (y_i - f_i)^2}{\sum_i (y_i - \bar{y})^2}} \quad (19)$$

$$RMSE = \sqrt{\frac{1}{N}\sum_{i=1}^{N}(y_i - \bar{y})^2} \quad (20)$$

$$MSE = RMSE^2 = \frac{1}{N}\sum_{i=1}^{N}(y_i - \bar{y})^2 \quad (21)$$

$$MAE = \frac{1}{N}\sum_{j=1}^{N}|y_i - y_j| \quad (22)$$

y refers to the measured value, $\bar{y}$ refers to the average of measured values, and N refers to the total number of data. R-value may have the best value of 1 and RMSE, MAE and MSE may have the best value of 0 [30, 34-36]. The performance criteria have been chosen in a way that best suits the model structure and data. It has been aimed that the results could be easily interpreted and the data could be fully handled. The failures in the model which may be caused by the outlier structure of the data have been ignored by the MAE, and the case that the loss functions create has been taken into account calculating the RMSE and MSE. Considering that the data are not linear, rank analysis has been applied to evaluate both cases.

Although there are many statistical methods, rank analysis has been preferred because of its suitability, easy application and interpretation. All model evaluation criteria have affected the final result and the models have been fully evaluated thanks to rank analysis. Rank analysis is a method applied to determine the best-performing model among the models by considering all evaluation criteria. This method, aiming to determine the performance evaluation score of the models and to find the model that gives the best result, is performed by assigning a rank to the models according to their proximity to the best value for each data set, and collecting and comparing the scores for all data sets. If R_i is represented as the rank value in the selected model of each data set and n is the number of models, the total rank value is determined by the equation that follows [37].

$$Modal\ Total\ Ranke = \sum_{i=1}^{n} R_i \quad (23)$$

3. STUDY AREA AND DATA

The Euphrates-Tigris basin, consisting of the Euphrates and Tigris Rivers in eastern Turkey, has a total river basin area of 184,914 km^2, of which 127,300 km^2 of the Euphrates Basin and 57,614 km^2 of the Tigris Basin (Figure 5). Examination of this basin, which is the largest drainage area in Turkey and consisting of the Euphrates River, the longest river in Western Asia, and the Tigris River, the second largest river in Western Asia, is of great importance since its average annual flow value is 52.94 km^3, its average annual output is 21.4l sec / km^2 and its annual average energy generation potential is 54.7 GWh. At the same time, the Euphrates-Tigris basin is also very important for the riparian countries.

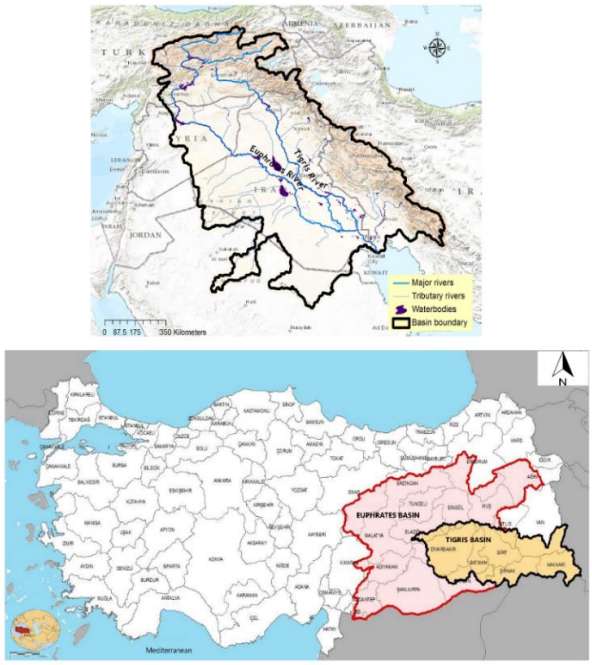

Figure 5 Euphrates-Tigris River Basin bordering on Turkey and riparian countries and the part of the basin in Turkey (examined in this study) [38]

Euphrates-Tigris Basin, in addition to these important features, has the most complete daily stream data of all the basins in Turkey. This is crucial for getting better and more reliable results with more data. Among the many stations, 14 were selected to standardize global assessment and climate monitoring studies, and the stream data averages, standard deviation values, minimum and maximum values of those stations between 1981–2010 are shown in a Table (Directorate General for S Hydraulic Works (dsi) (Turkey) (Table 1) (Figure 6) [39]. Intergovernmental Panel on Climate Change–IPCC projection reference interval has been determined to be between 1981–2010. As the data after 2010 have been thought to provide similar results, the data between the years 1981–2010 have been selected. The data have been arranged as 70% training, 30% testing, taking into account the rates at which the best result was achieved in the experiments.

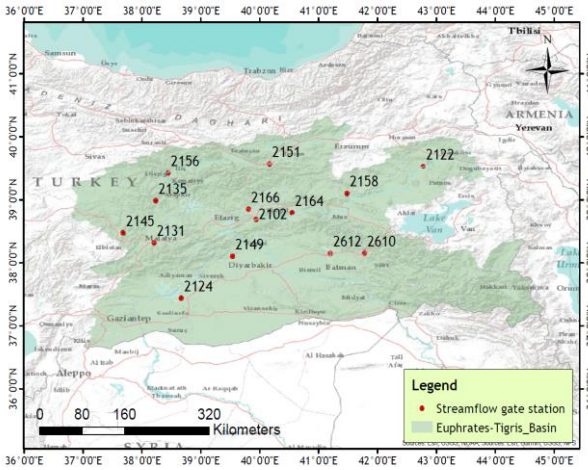

Figure 6 Selected stream observation stations in the Euphrates-Tigris Basin

Table 1 Selected stream stations in the Euphrates-Tigris Basin

Station number	Name	Longitude-latitude	Mean (flow) (m^3/sn)	Max (flow) (m^3/s)	Min (flow) (m^3/s)	Standard deviation (flow)
2102	Murat Rıver - Palu	(39° 56' 22" E - 38° 41' 49" N)	179,23	997	12,1	207,606
2122	Murat Rıver- Tutak	(42° 46' 49" E - 39° 32' 19" N)	47,48	821	1,97	73,041
2124	Tohma Bourn - Yazıkoy	(37° 26' 33" E - 38° 40' 21" N)	6,605	59,8	0,425	3,855
2131	Bey Stream - Kılayık	(38° 12' 36" E - 38° 19' 21" N)	1,343	38,8	0,11	1,894
2135	Bulam Stream - Fatopasa	(38° 14' 13" E - 37° 59' 38" N)	3,624	27,3	0,844	2,438
2145	Tohma Bourn - Hısarcık	(37° 41' 08" E - 38° 28' 32" N)	20,019	251	5,53	13,285
2149	Munzur Bourn - Mıskısag	(39° 32' 35" E - 39° 06' 29" N)	24,714	274	5,53	23,045
2151	Fırat Rıver - Demirkapı (Sansa)	(40° 10' 05" E - 39° 34' 41" N)	58,863	712	4,07	74,378
2156	Karasu - Asagıkagdarıc	(38° 26' 55" E - 39° 25' 57" N)	150,9272	980	54,8	116,844
2158	Bingöl Stream - Abdurrahman paşa Brıdge	(41° 29' 14" E - 39° 06' 30" N)	18,4965	338	1,3	29,181
2164	Goynuk Stream - Çayagzı	(40° 33' 17" E - 38° 48' 06" N)	32,497	630	0,45	56,143
2166	Perı Bourn - Logmar	(39° 48' 50" E - 38° 51' 31" N)	76,742	967	0,55	96,458
2610	Bıtlıs Stream - Baykan	(41° 46' 57" E - 38° 09' 41" N)	17,969	420	1,95	24,602
2612	Batman stream - Malabadı Brıdge	(41° 12' 16" E - 38° 09' 16" N)	112,848	990	0,015	150,300

4. RESULTS

For flow data, it was obtained from the Flow Observation Yearbooks published as open access by the Turkish State Hydraulic Works. In this study conducted with the data of 14 stations in the Euphrates-Tigris Basin, daily stream data were divided into two as 70% training and 30% testing. While choosing the training/testing ratio, the tests conducted with limited data had been taken into consideration and the most successful ratio has been used. In addition, the studies that used a low number of variables with a large amount of data were examined and it was found that 70% training and 30% testing rates were successful [40–43].

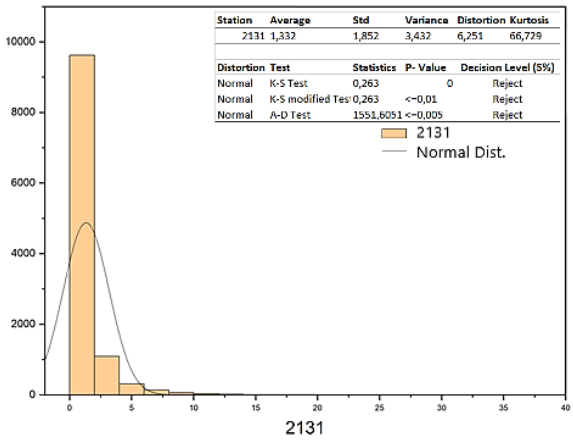

Figure 7 Normal distribution graph of station 2131

In addition, in order to examine the correlation status of the flow data, firstly, the compatibility

of the data with the normal distribution was examined. It was seen that the data did not fit the normal distribution and as an example, the distribution graph of station 2151 is given in Figure 7.

Since it was seen that the data did not fit the normal distribution, input selection was made by Spearman's correlation analysis. As an example, the correlation matrix of station 2131 is given in Figure 8.

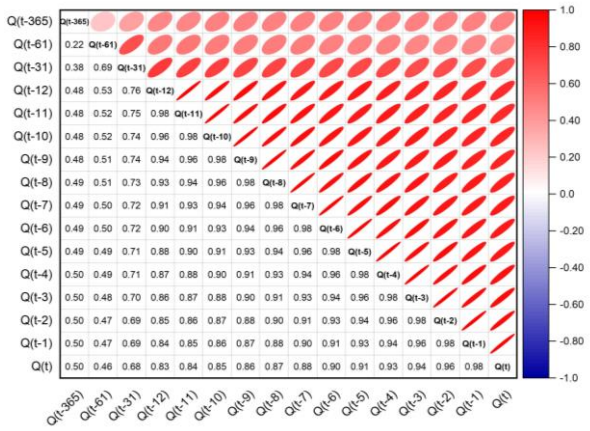

Figure 8 Correlation matrix of station 2131

Table 2 Model Results of Murat River- Palu (2131) station.

		TRAIN								TEST								
	M	**RMSE**	*Rn*	**MSE**	*Rn*	**R**	*Rn*	**MAE**	*Rn*	**RMSE**	*Rn*	**MSE**	*Rn*	**R**	*Rn*	**MAE**	*Rn*	**TP**	**TP**
ELM	M1	0,627	4	0,393	4	0,953	4	0,000	5	0,662	1	0,438	1	0,844	1	0,016	5	25	
	M2	0,620	4	0,384	4	0,957	4	0,000	5	0,640	2	0,410	2	0,856	2	0,020	3	26	81
	M3	0,631	3	0,398	4	0,951	3	0,000	5	0,639	4	0,408	4	0,861	3	0,019	4	30	
ANFIS	M1	0,635	3	0,404	3	0,952	3	0,006	4	0,622	5	0,386	5	0,867	4	0,020	3	30	
	M2	0,683	1	0,466	1	0,942	1	0,013	4	0,613	5	0,375	5	0,873	4	0,035	2	23	68
	M3	0,767	1	0,589	1	0,931	1	0,011	4	0,658	2	0,433	2	0,850	2	0,042	2	15	
SVM	M1	0,645	1	0,416	1	0,949	2	0,160	2	0,633	3	0,401	3	0,863	3	0,024	2	17	
	M2	0,646	2	0,418	2	0,949	3	0,160	2	0,639	3	0,409	3	0,864	3	0,018	4	22	60
	M3	0,640	2	0,410	2	0,949	2	0,157	2	0,642	3	0,412	3	0,862	4	0,023	3	21	
GPR	M1	0,528	5	0,279	5	0,964	5	0,140	3	0,657	2	0,432	2	0,858	2	0,019	4	28	
	M2	0,249	5	0,062	5	0,990	5	0,068	3	0,678	1	0,460	1	0,842	1	0,011	5	26	80
	M3	0,177	5	0,031	5	0,995	5	0,042	3	0,683	1	0,466	1	0,846	1	0,012	5	26	
ENN	M1	0,644	2	0,415	2	0,948	1	0,173	1	0,632	4	0,400	4	0,886	5	0,170	1	20	
	M2	0,633	3	0,401	3	0,950	2	0,167	1	0,625	4	0,390	4	0,888	5	0,167	1	23	71
	M3	0,624	4	0,390	3	0,951	4	0,165	1	0,634	5	0,402	5	0,884	5	0,167	1	28	

The first of these input combinations uses the stream data from a month ago (Q(t-1)) as input, and includes the current stream data as output (Q(t)), the second combination comprises Q(t-2)+Q(t-1) input data and Q(t) output data, and the third combination contains Q(t-3),Q(t-2),Q(t-1) input data and Q(t) output data. Modeling results of station 2131 made through these combinations are given in Table 2. As can be seen in the Table, according to the results of R, RMSE, MSE and MAE, rank analysis was performed both between models and between data set combinations, and it was observed that the ELM model gave the best results for station 2131, while the best result among data set combinations was found to be input Q(t-2)+Q(t-1)/ output Q(t) combination (Q (t-*i*): flow data *i* days ago). Owing to the large number of data used in the study, limited data sets have been tried first. Experimental models have been created with the previous period data used annually, monthly and daily. Since daily data and combinations used in the study have given better results in the experiments, the

models have been created with these data. Due to different structures of performance evaluation criteria and no superiority among them, the final decision had been taken by considering all performance evaluation indexes (Table 2, Table 3).

Table 3 Rank value table for the 14 stations.

TOTAL RANK (Evaluation According To The Method)															
Station	**Q(t−1)_−Q(t)**					**Q(t−1)+Q(t−1)_−Q(t)**					**Q(t−1)+Q(t−2)+Q(t−1)_−Q(t)**				
	ELM	**ANFIS**	**SVM**	**GPR**	**ENN**	**ELM**	**ANFIS**	**SVM**	**GPR**	**ENN**	**ELM**	**ANFIS**	**SVM**	**GPR**	**ENN**
2102	31	28	19	25	17	32	11	27	29	21	26	12	26	30	26
2122	27	31	16	25	21	34	14	20	27	25	34	14	20	28	24
2124	19	31	23	26	21	33	16	26	22	23	26	16	25	23	30
2131	25	30	17	28	20	26	23	22	26	23	30	15	21	26	28
2135	24	24	21	30	21	30	21	20	27	22	25	15	27	23	30
2145	28	26	18	25	23	29	12	26	28	25	27	12	26	28	27
2149	30	24	18	29	19	33	12	21	28	26	31	12	21	31	25
2151	24	31	18	25	22	34	12	22	27	25	35	13	19	30	23
2156	30	21	18	25	26	32	14	22	27	25	33	11	23	28	25
2158	26	29	20	26	19	35	20	17	26	22	34	11	21	28	26
2164	31	29	16	26	18	35	22	14	26	23	33	11	21	31	24
2166	25	29	24	26	16	36	24	18	25	17	34	15	24	26	21
2610	32	28	17	25	18	34	24	14	26	22	33	13	19	29	26
2612	24	26	23	25	22	27	24	23	24	22	26	26	22	24	22
Total	376	387	268	366	283	450	249	292	368	321	427	196	315	385	357
Comb. Total	**Total ELM**		1253	**Total ANFIS**		832	**Total SVM**		875	**Total GPR**		1119	**Total ENN**		961

TOTAL RANK (Evaluation by Data Combination)			
Station	**Q(t−1)_−Q(t)**	**Q(t−1)+Q(t−1)_−Q(t)**	**Q(t−1)+Q(t−2)+Q(t−1)_−Q(t)**
2102	73	95	72
2122	66	83	91
2124	64	86	90
2131	75	87	78
2135	72	79	89
2145	68	87	85
2149	63	89	88
2151	61	75	104
2156	66	81	93
2158	67	82	91
2164	72	72	96
2166	83	73	84
2610	67	75	98
2612	69	81	90
Total	**966**	**1145**	**1249**

In addition, rank values of all stations are given in Table 3, out of five points for five methods and out of three points for three data combinations.

Taking the 14 stations selected for the Euphrates-Tigris basin into consideration, it is seen that the model performance ranking appears to be ELM, GPR, ENN, SVM, ANFIS, which proves the eligibility of ELM, GPR and ENN techniques, which are rarely used for river flow. At the same time, this result shows that the problems and uncertainties in commonly used ANFIS and SVM models are solved in ELM, GPR and ENN models. Moreover, it is seen that the best data set combination is the one that takes the stream data from 1, 2 and/or 3 days ago as input and the current stream data as output. In order to better understand the results, the Taylor diagram of station 2131, which is taken as an example, is presented in Figure 9.

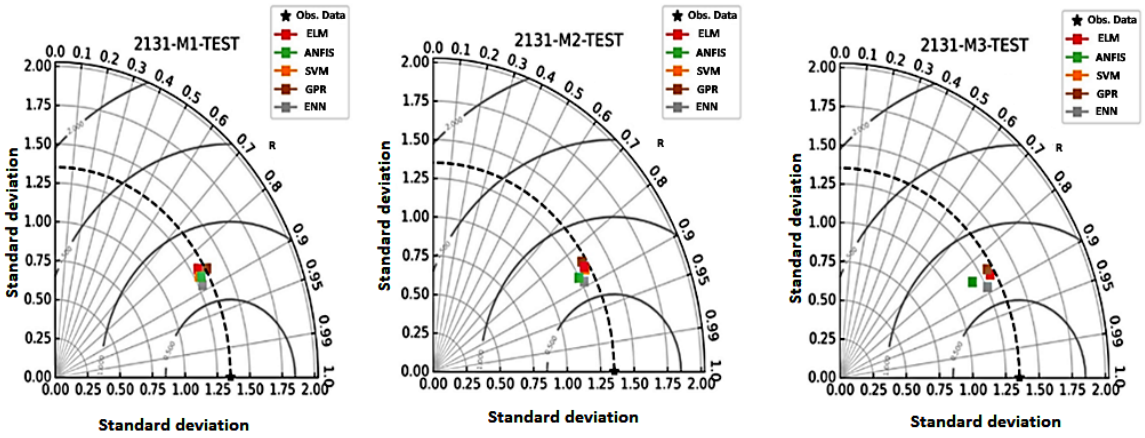

Figure 9 Taylor diagram of station 2131

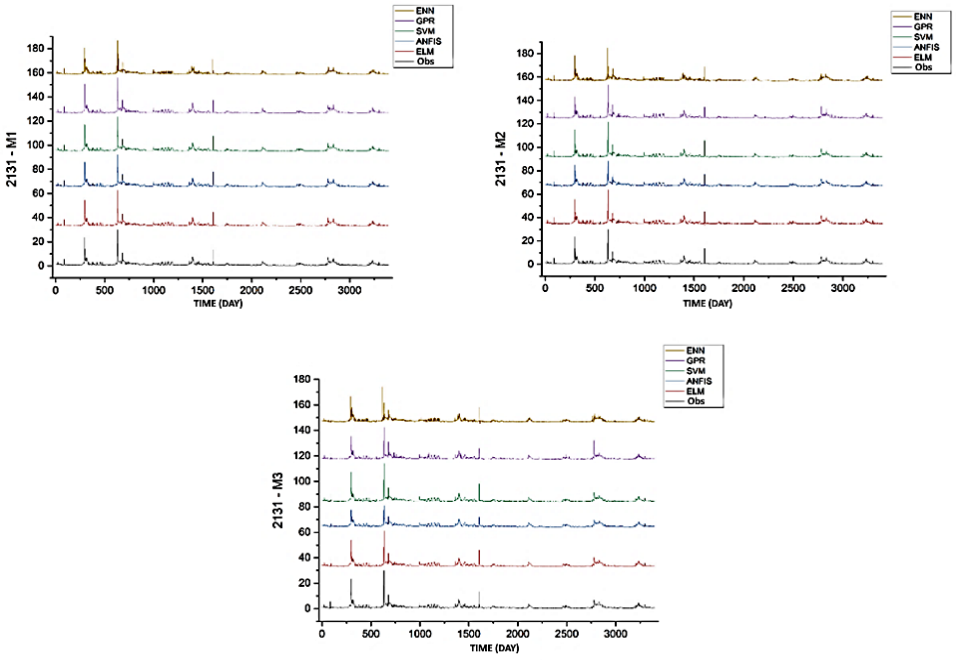

Figure 10 Time series graph of station 213

When the Taylor diagrams are examined, it is seen that the performance values are very close, but the ENN, ELM and GPR models give better results. When the time series given in Figure 10 are examined, it is seen that the model outputs produce outputs close to the observed data. It is also seen that the extreme situations experienced in the data can be represented in the models. This shows that the models can model the flow data with high performance.

5. CONCLUSION

In this study, five different artificial intelligence techniques were used for daily river stream estimation and it was aimed to find the best technique. As the first step of the study; The data were analyzed and the distributions and correlations of the data were determined. Considering the correlation conditions, the second stage, the modeling stage, was started. In this context, river stream estimations were made using ANFIS, ELM, ENN, SVM, GPR techniques and daily stream data from the climate reference periods between 1981-2010. Rank analysis was applied to decide the best model and it was observed that the method with the highest rank value was ELM. In addition, the performance ranking was observed to be ELM, GPR, ENN, SVM, and ANFIS respectively. These results show that ELM, GPR and ENN give much better results when compared with traditional artificial intelligence techniques such as ANFIS and SVM. This shows that these techniques are also reliable models for river stream modeling, and the problems seen in traditional methods can be solved, and these models can be applied more quickly. When the evaluation was made on the basis of the data combination, it was observed that the best combination was the one created with Q(t–3), Q(t–2), Q(T–1) inputs and Q(t) output. In this way, more than one data set type was examined and it was found that the results given by the models for different input numbers were consistent. This means that these methods are reliable for flow modeling. They are thought to be influential in solving the problems such as the complex structures in traditional methods, a large number of membership functions, the increase in the number of rules when the number of entries increases, too much human intervention, and issues in interpreting model parameters. It is also thought that these models can be applied faster when compared with the models used commonly. The study is expected to encourage the use of these uncommon methods in river flow modeling. In addition, it is hoped that ELM, ENN and GPR methods, which are rarely used in hydrology, will lead up to hyperparameter optimization or hybrid model use in future studies.

Acknowledgments
T.R. We thank the General Directorate of State Hydraulic Works (DSI) for the data provided. https://www.dsi.gov.tr/Sayfa/Detay/744

Funding
The author (s) has no received any financial support for the research, authorship or publication of this study.

Authors' Contribution
The authors contributed equally to the study.

The Declaration of Conflict of Interest/ Common Interest
No conflict of interest or common interest has been declared by the authors.

The Declaration of Ethics Committee Approval
This study does not require ethics committee permission or any special permission.

The Declaration of Research and Publication Ethics
The authors of the paper declare that they comply with the scientific, ethical and quotation rules of SAUJS in all processes of the paper and that they do not make any

falsification on the data collected. In addition, they declare that Sakarya University Journal of Science and its editorial board have no responsibility for any ethical violations that may be encountered and that this study has not been evaluated in any academic publication environment other than Sakarya University Journal of Science.

REFERENCES

[1] Y. Zhou, S. Guo, F. Chang, "Explore an Evolutionary Recurrent ANFIS for Modelling Multi-Step-Ahead Flood Forecasts", Journal of Hydrology, vol. 570, pp. 343-355, 2019.

[2] Z. He, X. Wen, H. Liu, J. Du, "A Comparative Study Of Artificial Neural Network, Adaptive Neuro Fuzzy İnference System And Support Vector Machine For Forecasting River Flow İn The Semiarid Mountain Region", Journal of Hydrology, vol. 509, pp. 379-386, 2014.

[3] Z. Yaseen, S. Sulaiman, R. Deo, K. Chau, "An Enhanced Extreme Learning Machine Model For River Flow Forecasting: State-Of-The-Art, Practical Applications İn Water Resource Engineering Area And Future Research Direction", Journal of Hydrology, vol. 569, pp. 387-408, 2019.

[4] Z. Yaseen, S. R. Naganna, Z. Sa'adi, P. Samui, M.A. Ghorbani, S. Shahid, "Hourly River Flow Forecasting: Application Of Emotional Neural Network Versus Multiple Machine Learning Paradigms", Water Resources Management, vol. 34, no. 3, pp. 1075-1091, 2020.

[5] Z. Wang, N. F. Attar, K. Khalili, J. Behmanes, S. S. Band, A. Mosavi, K. K. Chau, "Monthly Streamflow Prediction Using A Hybrid Stochastic-Deterministic Approach For Parsimonious Non-Linear Time Series Modeling", Engineering Applications of Computational Fluid Mechanics, vol. 14, no. 1, pp. 1351-1372, 2020.

[6] A. Sun, D. Wang, X. Xu, "Monthly Streamflow Forecasting Using Gaussian Process Regression", Journal of Hydrology, vol. 511, pp. 72-81, 2014.

[7] Z. Yaseen, A. El-shafie, O. Jaafar, H. Afan, K. Sayl, "Artificial İntelligence Based Models For Stream-Flow Forecasting: 2000–2015", Journal of Hydrology, vol. 530, pp. 829-844, 2015.

[8] E. Khadangi, H. R. Madvar, M. M. Ebadzadeh "Comparison Of ANFIS And RBF Models İn Daily Stream Flow Forecasting". In 2009 2nd International Conference on Computer, control and Communication (pp. 1-6). IEEE.

[9] G. Huang, Q. Zhu, C. Siew, "Extreme Learning Machine: Theory And Applications", Neurocomputing, vol. 70, no. 1-3, pp. 489-501, 2006.

[10] H. Sıqueıra, L. Boccato, R. Attux, C. Lyra, "Unorganızed Machınes For Seasonal Streamflow Serıes Forecastıng", International Journal of Neural Systems, vol. 24, no. 03, p. 1430009, 2014.

[11] Z. Yaseen, O. Jaafar, R. C. Deo, O. Kisi, J. Adamowski, J. Qulity, A. El-Shafie, "Stream-Flow Forecasting Using Extreme Learning Machines: A Case Study İn A Semi-Arid Region in Iraq", Journal of Hydrology, vol. 542, pp. 603-614, 2016.

[12] R. Adnan, Z. Liang, S. Trajkovic, M. Zounemat-Kermani, B. Li, O. Kisi,

"Daily Streamflow Prediction Using Optimally Pruned Extreme Learning Machine", Journal of Hydrology, vol. 577, p. 123981, 2019.

[13] D. E. Rumelhart, G.E. Hinton, R. J. Williams "Learning Internal Representations By Error Propagation", Parallel Distributed Processing.

[14] M. Atiquzzaman, J. Kandasamy, "Robustness of Extreme Learning Machine İn The Prediction of Hydrological Flow Series", Computers & Geosciences, vol. 120, pp. 105-114, 2018.

[15] D. Kukolj, "Design of Adaptive Takagi–Sugeno–Kang Fuzzy Models", Applied Soft Computing, vol. 2, no. 2, pp. 89-103, 2002.

[16] Jang, "ANFIS: Adaptive-Network-Based Fuzzy Inference System", IEEE Transactions on Systems, Man, and Cybernetics, vol. 23, no. 3, pp. 665-685, 1993.

[17] A. Mosavi, P. Ozturk, K. Chau, "Flood Prediction Using Machine Learning Models: Literature Review", Water, vol. 10, no. 11, p. 1536, 2018.

[18] H. B. Demuth, "Fuzzy Logic Toolbox for Use With MATLAB", User's Guide Version 4. MA, 2000.

[19] Z. Jin, G. Zhou, D. Gao, Y. Zhang, "EEG Classification Using Sparse Bayesian Extreme Learning Machine For Brain–Computer Interface", Neural Computing and Applications, vol. 32, no. 11, pp. 6601-6609, 2018.

[20] E. R. David, L. M. James, "Learning Internal Representations By Error Propagation. In Parallel Distributed Processing: Explorations in The Microstructure Of Cognition: Foundations", MITP, pp. 318-362,1987.

[21] A. Khashman, "Application of An Emotional Neural Network to Facial Recognition", Neural Computing and Applications, vol. 18, no. 4, pp. 309-320, 2008.

[22] A. Khashman, "Blood Cell Identification Using Emotional Neural Networks", Journal of Information Science & Engineering, 2009, vol. 25,6.

[23] V. N. Vapnik, "Statistical Learning Theory", New York: Wiley, 1998, ISBN: 978-0-471-03003-4

[24] C. J. Burges, "A Tutorial on Support Vector Machines for Pattern Recognition". Data mining and knowledge discovery, 1998, Vol. 2(2), pp. 121-167.

[25] F. Fotovatikhah, M. Herrera, S. Shamshirband, K. Chau, S. Faizollahzadeh Ardabili, M. Piran, "Survey of Computational İntelligence As Basis to Big Flood Management: Challenges, Research Directions And Future Work", Engineering Applications of Computational Fluid Mechanics, vol. 12, no. 1, pp. 411-437, 2018.

[26] A. Mehr, A. Gandomi, "MSGP-LASSO: An Improved Multi-Stage Genetic Programming Model for Streamflow Prediction", Information Sciences, vol. 561, pp. 181-195, 2021.

[27] U. Okkan, Z. Serbes, "Rainfall-Runoff Modeling Using Least Squares Support Vector Machines", Environmetrics, vol. 23, no. 6, pp. 549-564, 2012.

[28] N. Ceryan, U. Okkan, P. Samui, S. Ceryan, "Modeling of Tensile Strength of Rocks Materials Based on Support Vector Machines Approaches", International Journal for Numerical and Analytical Methods in Geomechanics, vol. 37, no. 16, pp. 2655-2670, 2012.

[29] R. Chanklan, N. Kaoungku, K. Suksut, K. Kerdprasop, N. Kerdprasop, "Runoff Prediction With a Combined Artificial Neural Network and Support Vector Regression", International Journal of Machine Learning and Computing, vol. 8, no. 1, pp. 39-43, 2018.

[30] S. Shamshirband, S. Hashemi, H. Salimi, S. Samadianfard, E. Asadi, S. Shadkani, K. Kargar, A. Mosavi, N. Nabipour, k. W. Chau, "Predicting Standardized Streamflow Index For Hydrological Drought Using Machine Learning Models", Engineering Applications of Computational Fluid Mechanics, vol. 14, no. 1, pp. 339-350, 2020.

[31] C. Wu, K. Chau, "Prediction of Rainfall Time Series Using Modular Soft Computing Methods", Engineering Applications of Artificial Intelligence, vol. 26, no. 3, pp. 997-1007, 2013.

[32] K. P. Murphy, “Machine Learning: A Probabilistic Perspective”. MIT press, 2012.

[33] R. Richardson, M. Osborne, D. Howey, "Gaussian Process Regression for Forecasting Battery State of Health", Journal of Power Sources, vol. 357, pp. 209-219, 2017.

[34] Z. Zhang, Q. Zhang, V. Singh, "Univariate Streamflow Forecasting Using Commonly Used Data-Driven Models: Literature Review and Case Study", Hydrological Sciences Journal, vol. 63, no. 7, pp. 1091-1111, 2018.

[35] A. Danandeh Mehr, V. Nourani, E. Kahya, B. Hrnjica, A. Sattar, Z. Yaseen, "Genetic Programming in Water Resources Engineering: A State-Of-The-Art Review", Journal of Hydrology, vol. 566, pp. 643-667, 2018.

[36] R. Taormina, K. Chau, "ANN-Based İnterval Forecasting of Streamflow Discharges Using The LUBE Method and MOFIPS", Engineering Applications of Artificial Intelligence, vol. 45, pp. 429-440, 2015.

[37] Y. Zhang, H. Yang, H. Cui, Q. Chen, "Comparison of The Ability of ARIMA, WNN and SVM Models for Drought Forecasting in The Sanjiang Plain, China", Natural Resources Research, vol. 29, no. 2, pp. 1447-1464, 2019.

[38] Z. Chen, M. Kavvas, N. Ohara, M. Anderson, J. Yoon, "Coupled Regional Hydroclimate Model and Its Application to the Tigris-Euphrates Basin", Journal of Hydrologic Engineering, vol. 16, no. 12, pp. 1059-1070, 2011.

[39] DSI:https://web.archive.org/web/20050813023730/http://www.dsi.gov.tr/topraksu.htm ((2020, 07 16).

[40] C. C. Aggarwal, “Data Mining: The Textbook”, Springer, New York, 2015.

[41] G. B. Guacho, S. Abdali, N. Shah, E. E. Papalexakis, “Semi-Supervised Content-Based Detection of Misinformation Via Tensor Embeddings”, In 2018 IEEE/ACM international conference on advances in social networks analysis and

mining (ASONAM), 2018, pp. 322-325. IEEE.

[42] Y. Khan, S. S Chai, “Ensemble of ANN and ANFIS for Water Quality Prediction And Analysis-A Data Driven Approach”, Journal of Telecommunication, Electronic and Computer Engineering (JTEC), 2017, Vol. 9(2-9), pp. 117-122.

[43] S. Samantaray, P. Dash, "Decision Tree Based Discrimination Between Inrush Currents And Internal Faults İn Power Transformer", International Journal of Electrical Power & Energy Systems, vol. 33, no. 4, pp. 1043-1048, 2011.

SAKARYA ÜNİVERSİTESİ
FEN BİLİMLERİ ENSTİTÜSÜ DERGİSİ

Sakarya University Journal of Science
SAUJS

ISSN 1301-4048 e-ISSN 2147-835X Period Bimonthly Founded 1997 Publisher Sakarya University
http://www.saujs.sakarya.edu.tr/

Title: Investigation of the Effect of Hot Fluid on Deformation in T-Shaped Pipes by FSI Method Using Different Material

Authors: Haydar KEPEKÇİ, Erman ASLAN

Recieved: 2023-02-24 00:00:00

Accepted: 2023-03-29 00:00:00

Article Type: Research Article

Volume: 27
Issue: 3
Month: June
Year: 2023
Pages: 660-669

How to cite
Haydar KEPEKÇİ, Erman ASLAN; (2023), Investigation of the Effect of Hot Fluid on Deformation in T-Shaped Pipes by FSI Method Using Different Material . Sakarya University Journal of Science, 27(3), 660-669, DOI: 10.16984/saufenbilder.1255815
Access link
https://dergipark.org.tr/en/pub/saufenbilder/issue/78131/1255815

Sakarya University Journal of Science 27(3), 660-669, 2023

Investigation of the Effect of Hot Fluid on Deformation in T-Shaped Pipes by FSI Method Using Different Material

Haydar KEPEKCİ*[1], Erman ASLAN[2]

Abstract

In this study, the high-temperature liquid water flow through the cross-section of a T pipe and the effect of the temperature of the liquid on the pipe material has been investigated. Pipe deformation caused by fluid temperature has been analyzed by the Fluid-structure interaction method. The effect of temperature distribution inside the pipe has been considered as thermal load in the structural analysis of the pipe body. The finite volume method has been used in the study with numerical methods. While $\boldsymbol{k-\varepsilon}$ is preferred as the turbulence model, the mesh file created to be used in the analysis contains 200,000 grid cells. For all calculations, the Reynolds number has been set to 3900 and kept constant. The geometry of the T pipe, the fluid passing through the pipe and used the boundary have been constant for the numerical analysis made in the study. The pipe material has been determined as the only parameter that changed. As different pipe materials magnesium, aluminum, copper, steel, concrete, cast iron, and titanium have been used. As a result of the study, thermal strain, total deformation, and directional deformation values have been determined. As a result, it has been determined that the greatest deformation under thermal load is in magnesium pipes, and the smallest deformation is in titanium pipes. It has been observed that the total amount of deformation of the pipe made of magnesium is three times higher than that of the titanium pipe.

Keywords: Fluid-structure interaction, computational fluid dynamics, flow and heat transfer, T-shaped pipes.

1. INTRODUCTION

With the spread of industrialization, the usage area of hydraulic and pneumatic systems has also expanded. These systems are used in petrochemical plants to energy production areas, from thermal heating systems to car engines. Energy transmission in hydraulic and pneumatic systems is done through pipes. The pipe surface is required to be smooth so that the uniformity of the flow in the pipe is not disturbed, there is no noise caused by vibration and it does not cause undesired turbulence during the flow. The unpredictability of turbulence during any flow means not knowing the characteristics of the flow. This means that the wrong components are selected in the system design, thus

* Corresponding author: hikepekci@gelisim.edu.tr (H. Kepekci)
[1] İstanbul Gelişim University
[2] Kocaeli University
E-mail: erman.aslan@kocaeli.edu.tr
ORCID: https://orcid.org/0000-0001-8595-6092, https://orcid.org/0000-0002-0037-8332

disrupting the energy transmission. In all pneumatic and hydraulic systems used, the amount and speed of the in-pipe flow are of great importance. In order to calculate these parameters correctly, it is necessary to know the deformity of the pipe surface. However, the idea is that the pipes are not deformed. Because pipes with increased deformation become unusable and need to be replaced. There are two main reasons for the deformation of pipes. These are the mechanical loads caused by the pressure of the fluid passing through it and the thermal loads caused by the temperature difference between the fluid and the pipe surface. Detection of deformations occurring during flow and heat transfer is important in terms of ensuring continuity in production and power transfer [1].

Fluid-Structure Interaction (FSI) is a scientific subject that examines the relationship between a moving fluid and a solid surface that has deformations in its structure. During flow fluctuations, such as increasing the flow rate or switching a pump on and off, the effect of the fluid on the solid surface may increase. FSI serves to calculate this incremental effect and to examine its consequences [2]. Accurate calculations cannot be made without knowing the roughness and amount of deformation of the solid surface that any flow contacts. For this reason, the FSI method should be considered to calculate the amount of power and energy transmitted by continuous flows. The interaction of the fluid with the solid surface is one of the topics that has attracted attention both academically and in the sector recently. There are many studies on this subject in the literature.

Xu et al. created a pipe system model operating under various boundary conditions and examined the effect of fluid motion on the solid surface using the fluid-structure interaction model. They integrated straight, curved, and T-shaped pipe models into a more complex system and worked on the overall solution of the multi-branch pipe system. They carried out their studies both numerically and experimentally. As a result, they found that the data they obtained were compatible with each other [3]. Hös et al. have derived mathematical equations for a straight pipe connected to the discharge valve of the pressure tank, taking into account the fluid velocity. They found that the results of the simulations they made using the new model they obtained and the FSI model were compatible with each other [4].

Dongwei et al. investigated the response of fluids in hydraulic systems affected by external loading. While doing this study, they proposed alternative models to the fluid-structure interaction method that can predict pressure values along the pipeline. FSI analyses were performed using the CFD program to validate the proposed models. As a result, they found that the models they proposed were successful in pressure estimation [5]. Evrim and Lauiren investigated the thermal fatigue failure of the turbulent mixture inside the T-type pipes used in nuclear power plants. They used the Large Eddy Simulation method as the turbulence method in their work using OpenFoam. As a result of their analysis, they determined that there are significant temperature fluctuations near the mixing zone of the hot and cold fluid inside the T-pipe. They obtained similar results in their experiments to validate the simulations [6]. Yao et al. used CFD-DEM-FEM and FSI methods to analyze pipe vibration when the solid-liquid two-phase flow is carried in oil pipes. As a result of their research, they found that when the velocity of the two-phase flow and the sand ratio increase, the accumulation of particles is more important where the pipe diameter changes. They said that their study will guide the design process of the pipes to be used during high-concentration solid-liquid two-phase flow [7].

Tijsseling has derived a one-dimensional mathematical model to study the acoustic behavior of thick-walled liquid-filled pipes. The basis of this model is the fluid-structure interaction (FSI) [8]. Li and He conducted investigations using the FSI model to detect

the mechanical failure of buried gas pipelines. They found relations to calculate pipeline deformations and pipeline reliability [9]. Zhang and Lu performed analyses using the ANSYS program to calculate the thermal stress and thermal fatigue of a T-pipe under turbulent flow mixing. They used the FSI model in their work. They also conducted experiments to confirm the results they obtained from their analysis. As a result, they found that thermal fatigue occurred mostly at the T-junction [10]. Espinosa and Garcia studied vibrations arising from fluid-structure interaction at the junctions of the T-junction during flow. As a result of their work with the CFD method, they determined that the vibrations occurred due to the unstable structure of the flow [11].

Jaing et al. carried out studies to examine the vibrations caused by the fluid-structure interaction in the centrifugal pump. During the calculations of their work with the CFD method, they neglected the vibrations at the blade transition frequencies. During their studies, they said that the pipe-valve system increased the flow instability of the fittings [12]. Zhou et al. carried out experiments to investigate the effects of thermal fatigue in the regions of T-section pipes close to the weld joint during turbulent flow. While the hot fluid used during the experiments had a temperature of 280 degrees and the cold fluid had a temperature of 20 degrees, the pressure inside the pipe was chosen as 75 bar. As a result of their experiments, they determined that the temperature difference change has a significant effect on the stability of the thermal stratification [13].

In this study, the effect of the hot fluid passing through the T-shaped pipe, which is frequently used in hydraulic systems, on the pipe deformation has been investigated by the FSI method using the CFD program. Numerical and visual data obtained as a result of numerical analyzes by selecting seven different materials have been compared with each other and the material most resistant to thermal load has been determined.

2. NUMERICAL METHODS

This study, which examines the deformation created by the hot fluid on the pipes through which it passes, has been carried out numerically using computational fluid dynamics software. The reason why CFD method studies replace experimental studies in both academic and sectoral studies is to save cost and time. Because while experimental studies correspond to large sums, calculations made using computer software can be made much cheaper. This causes them to be preferred [14]. The first thing to consider when performing a study using CFD software is to correctly determine the boundary conditions. The geometry to be worked on is created. The geometry of the T pipe drawn to be used in the analysis is shown in Figure 1 as measured and the boundary conditions used in the analysis are shown in Figure 2.

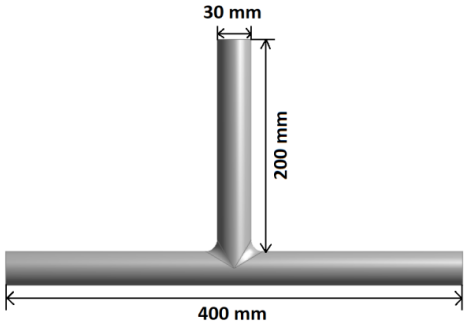

Figure 1 Dimensioning of the T-shaped pipe

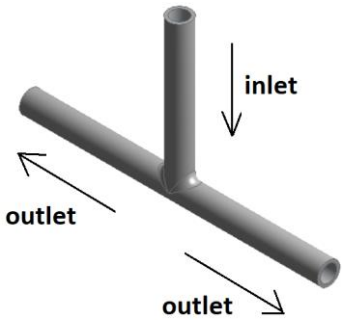

Figure 2 Boundary conditions of the T-shaped pipe

After the geometry is created, it is divided into small regions called grids with a process called mesh. The higher the mesh number, the

higher the accuracy of the analysis. However, as the number of meshes increases, the solution times of numerical analyzes also increase. For this reason, the number of meshes should not be kept too high [15]. Then, analyses are made using the created mesh file. The mesh file used in this study consists of 200,000 grid cells. The mesh structure consists of hexahedral cells. The piece of pipe being worked on is designed with minimum dimensions. A large-diameter geometry has been not preferred as the analysis would take longer as the pipe size grew. Since the purpose of this study is to compare T pipe materials, geometry size and analysis time do not matter in analyzes without changing boundary conditions. Mesh independence has not been done in this study. Instead, a value close to the number of grids in the mesh files used for analysis in similar studies has been determined. Thus, time is saved by not repeating the same process. In the mesh file creation process, the y+ value has been taken into account in order to keep the mesh quality high. The expression y+ means the mesh fineness in the area close to the wall and indicates the sensitivity of the mesh file to be used in the analysis. As the sensitivity of the y+ value increases, the accuracy of the data obtained from the CFD calculations also increases. In this study, the y+ value has been determined as 0.8. The view of the created mesh geometry is given in Figure 3.

Figure 3 General view of the mesh structure

In this study, it is necessary to determine the turbulence method for the solution. Among the turbulence models, the best option to solve this problem has been determined as k–ε as a result of the research made in the literature [15]. The k-epsilon model is one of the most widely used turbulence models, but that doesn't well perform in cases of large adverse pressure gradients [16]. It is a two-equation model, which includes two extra transport equations to represent the turbulent properties of the flow. This allows a two-equation model to account for historical effects like convection and diffusion of turbulent energy. The first transported variable is turbulent kinetic energy, k.

The second transported variable, in this case, is the turbulent dissipation, epsilon. It is the variable that determines the scale of the turbulence, whereas the first variable, k, determine the energy in the turbulence [16]. Turbulence kinetic energy and dissipation equations are given in Eq. 1 and Eq. 2.

For turbulent kinetic Energy, k;

$$\frac{\partial(\rho k)}{\partial t}+\frac{\partial(\rho k u_i)}{\partial x_i}=\frac{\partial}{\partial x_j}\left[\frac{\mu_t}{\sigma_k}\frac{\partial k}{\partial x_j}\right]+2\mu_t E_{ij}E_{ij}-\rho\varepsilon \quad \text{.....} \quad (1)$$

For dissipation, ε;

$$\frac{\partial(\rho\varepsilon)}{\partial t}+\frac{\partial(\rho\varepsilon u_i)}{\partial x_i}=\frac{\partial}{\partial x_j}\left[\frac{\mu_t}{\sigma_\varepsilon}\frac{\partial\varepsilon}{\partial x_j}\right]+C_{1\varepsilon}\frac{\varepsilon}{k}2\mu_t E_{ij}E_{ij}-C_{2\varepsilon}\rho\frac{\varepsilon^2}{k}\ldots \quad \text{.....} \quad (2)$$

In Eq. 1 and Eq. 2 u_i is represents the velocity component in the corresponding direction, E_{ij} is represents a component of the rate of deformation, and μ_t is represents eddy viscosity [16]. At the inlet section velocity inlet boundary condition is applied as 0.5m/s, and constant temperature is given as 370K. The drichlet boundary condition is applied at the wall, and constaant temperature is 300K. Pressure outlet is given at outlet sections (P_{gauge} =0). The FSI method has been preferred to examine the effect of the material change of the T pipe on the solid surface. In recent studies, it has been determined that there is an interaction between the fluid and solid surface due to contact, and this situation causes deformation. The amount of

deformation is estimated using CFD programs. Related programs use Eq. 3 and Eq. 4 to detect deformation on a solid surface;

$$[M_s]\{\ddot{U}\} + [K_s]\{U\} = [F_s] + [R]\{P\} \quad (3)$$

$$\begin{bmatrix} M_s & 0 \\ \rho R^T & M_f \end{bmatrix} . \{\ddot{U}/\ddot{P}\} + \begin{bmatrix} K_s & R \\ 0 & K_f \end{bmatrix} . \{U/P\} = F_s/F_f \ \ldots\ldots\ldots\ldots\ldots \quad (4)$$

M_s represents the structural mass matrix, M_f liquid mass matrix, F_s structural force matrix, F_f fluid force matrix, R represents the effective surface area matrix where the fluid and solid surface are in contact, ρ represents fluid density, R static pressure given in Eq. 3 and 4 [17]. In this study, the deformation of the hot fluid passing through the T pipe according to the material type has been investigated by choosing seven different materials. The selected materials are magnesium, aluminum, copper, stainless steel, concrete, gray cast iron, and titanium. The physical properties of these materials are given in Table 1.

Table 1 Physical properties of materials used in the analysis

Material	**Density** $[kg/m^3]$	**Coefficient of Thermal Expansion** $[K^{-1}]$	**Specific Heat** $[J/kg.K]$
Magnesium	1800	2.6E-05	1024
Aluminum	2770	2.3E-05	875
Copper	8300	1.8E-05	385
Stainless Steel	7750	1.7E-05	480
Concrete	2300	1.4E-05	780
Gray Cast Iron	7200	1.1E-05	447
Titanium	4620	9.4E-06	522

In analyses of solid models, there are different parameters used in deformation calculations. These parameters are Young's modulus, Poisson's ratio, and density. Young's modulus is a term that expresses a material's elastic properties. It is usually represented by the symbol "E" and determines how much a material can return to its original shape after being stretched or bent. Young's modulus is equal to the ratio of stress to strain. Young's modulus is particularly important for material behavior under tensile and compressive forces and determines the material's deformation capacity. Each material has a unique Young's modulus value, and it can be used to compare the elastic properties of different materials [18].

Poisson's ratio is a material property that expresses the transverse deformation ratio that occurs with longitudinal stress. It is used to determine how deformation occurs in other directions when a material is stressed in one direction. Poisson's ratio is also known as the Poisson coefficient and has a negative value. This means that when a material is stressed in one direction, it tends to compress in the other direction. Poisson's ratio is important for understanding a material's elastic behavior and is used in structural engineering, material science, and many other industries [18].
Density is a physical property defined as the mass of a substance per unit volume. This property is used to determine how dense a substance is and how much matter it contains in a unit volüme [19]. Table 2 provides the values for Young's modulus, Poisson's ratio, and density for the materials used in this study.

Table 2 The other physical properties of materials used in the analysis

Material	**Young's modulus [GPa]**	**Poisson Oranı**	**Mass density** $[kg/m^3]$
Magnesium	45	0.29	1738
Aluminum	70	0.33	2700
Copper	120	0.34	8960
Stainless Steel	200	0.30	7930
Concrete	30	0.15	2300
Gray Cast Iron	170	0.26	6800
Titanium	110	0.34	4500

The fluid used in the study was water, and its properties at a temperature of 370 K are given in Table 3.

Table 3 Properties of water at 370 K

Density	940.8 [kg/m³]
Viscosity	0.000366 Pa.s]
Thermal conductivity	0.625 [W/(m.K)]
Heat capacity	4182 [J/(kg K)]
Coefficient of thermal expansion	0.00021 [K^{-1}]
Surface tension	0.0589 [N/m]

The physical properties of the selected materials are completely different from each other. As a result of the study, it has been desired to determine which physical properties of the materials have been more effective on the deformation caused by thermal effects. "AMD Ryzen 9-5900HX CPU@4.6 GHz, 8 cores" gaming notebook has been used in the analysis. Calculations have been solved in a steady-state manner independent of time and numerical analysis is stop when converge is done.

3. RESULTS

The temperature and velocity distributions of the flow in the pipe with the results of the analysis whose solution has been completed are given in Figures 4 and 5, respectively.

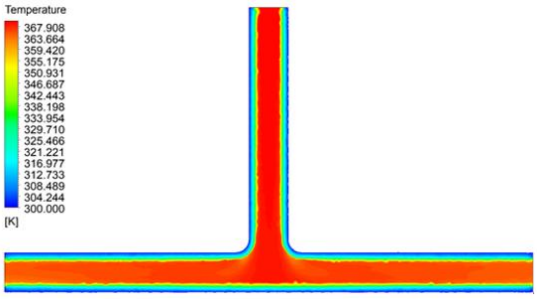

Figure 4 Temperature distribution in the T-shaped pipe

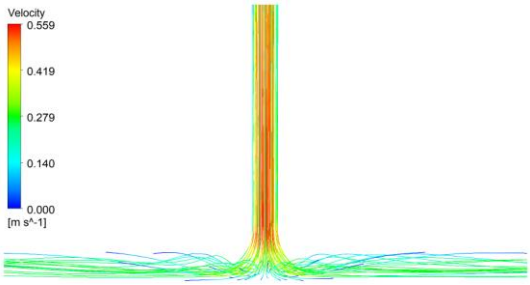

Figure 5 Velocity distribution in the T-shaped pipe

Since only the pipe material has been determined as the variable parameter in the analysis, it has been observed that the flow velocity and temperature distribution within the pipe have been the nearly same in every calculation. In Figure 4, it is seen that the fluid temperature cools down when it approaches the pipe surface.

The reason for this is thought to be heat transfer by conduction arising from contact with the cold surface. In Figure 5, it is seen that the fluid velocity at the outlet of the T pipe is lower than the velocity at the inlet. This situation is thought to be caused by the pressure drop caused by the pipe geometry. Visuals of the thermal strain results obtained from the analyzes using seven different materials for the T pipe are given in Figures 6.

When Figures 6 is examined, it is seen that the highest thermal strain amount is in magnesium pipe with 0.0010335 mm, and the lowest thermal strain amount is in titanium pipe with 0.00037363 mm. It has been understood that there is a thermal strain difference of about three times between these materials. Among the materials used in the analysis, it has been determined that the most heat-resistant material after the magnesium pipe is aluminum and its thermal strain is 0.00091421 mm, close to the strain amount of the magnesium pipe. This value is 0.00071547 mm for copper, 0.00067667 for steel, and 0.00055648 mm for concrete.

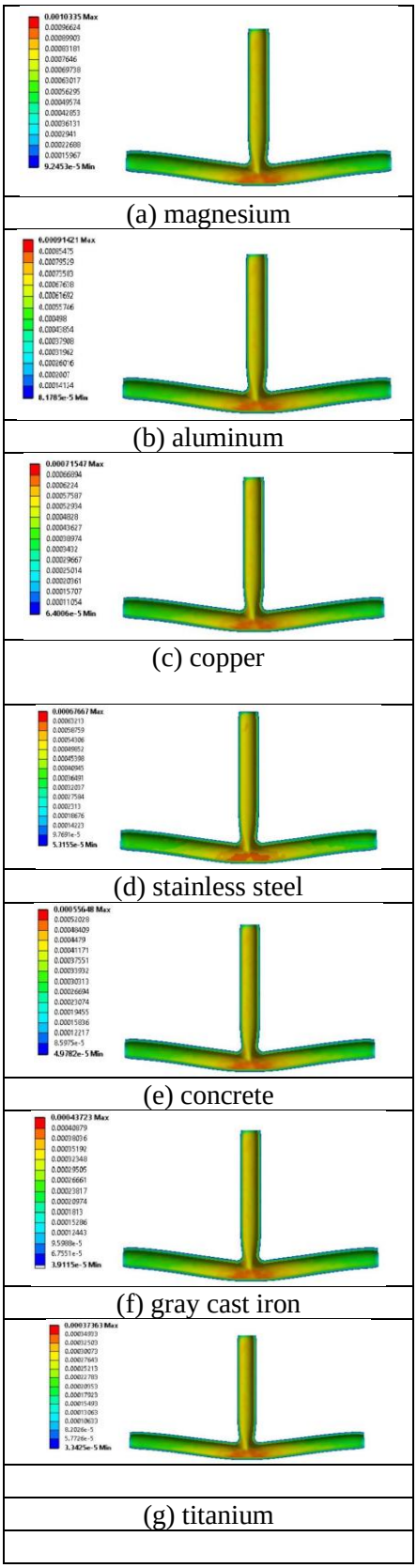

(a) magnesium

(b) aluminum

(c) copper

(d) stainless steel

(e) concrete

(f) gray cast iron

(g) titanium

Figure 6. Thermal strain in the pipe made of (a)magnesium, (b) aluminum, (c) copper, (d) stainless steel, (e) concrete, (f) gray cast iron, (g) titanium

It has been determined that the most heat-resistant pipe material after titanium is gray cast iron. The elongation amount of this material due to thermal effects is 0.00043727 mm from the results obtained from the analysis. Thermal strain is not the only reason why materials deform. Materials can be deformed due to different reasons during flow. From the analyzes made, the total deformation amounts of the materials used for the T pipe design have been also calculated. The visuals of the total deformation results obtained from the analyzes using seven different materials for the T pipe are given in Figures 7.

When Figures 7 is examined, it is seen that the highest total deformation amount is in the magnesium pipe with 0.096304 mm, and the lowest total deformation amount is in the titanium pipe with 0.034882 mm. Looking at the results of the analyzes made using these materials, it has been understood that the total deformation amount differences have been approximately three times. It has been determined that aluminum is the most unstable material after magnesium in case of hot fluid passing through the materials used in the analysis. The highest total amount of deformation of the aluminum pipe has been calculated as 0.08498 mm. This value is very close to the total deformation amount of the magnesium pipe. In this case, it can be said that there is not much difference between them. This value is 0.06615 mm for copper, 0.062661 for stainless steel, and 0.050873 mm for concrete. It has been determined that the most resistant pipe material to thermal deformation after titanium is gray cast iron. It is among the results obtained from the analyses that the amount of deformation of this material due to thermal effects is 0.040424 mm. The total deformation and thermal strain amounts of the materials obtained from the analysis are given in Table 4.

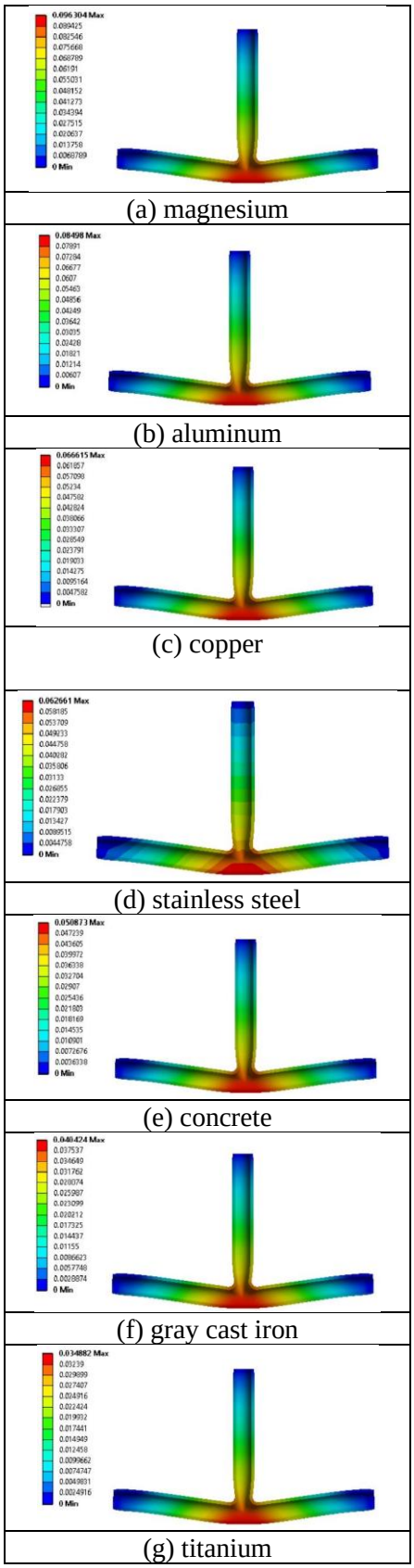

(a) magnesium

(b) aluminum

(c) copper

(d) stainless steel

(e) concrete

(f) gray cast iron

(g) titanium

Figure 7 Total deformation in the pipe made of (a)magnesium, (b) aluminum, (c) copper, (d) stainless steel, (e) concrete, (f) gray cast iron, (g) titanium

Table 4 Thermal strain and deformation values of different materials obtained from the results of the analyzes

Material	**Thermal Strain** [mm]	**Total Deformation** [mm]
Magnesium	0.0010335	0.096304
Aluminum	0.00091421	0.08498
Copper	0.00071547	0.066615
Stainless Steel	0.00067667	0.062661
Concrete	0.00055648	0.050873
Gray Cast Iron	0.00043723	0.040424
Titanium	0.00037363	0.034882

When Table 4 is examined, it is seen that there is a directly proportional relationship between thermal strain and total deformation. Materials with high thermal strain values also have high total deformation values.

4. CONCLUSIONS AND DISCUSSION

In this study, the deformation of the T pipe, through which the hot fluid passes, due to thermal effects have been investigated. In this examination, which has been carried out with numerical methods, seven different pipe materials have been selected and CFD analyzes have been carried out using the FSI method. Numerical data and images obtained as a result of the analyzes have been compared with each other and some inferences have been made. The temperature distributions inside the pipe have been examined and it has been determined that the flow cooled down where it approached the pipe walls. This situation, which is caused by the heat transfer between the hot fluid and the cold surface, has been seen in all analyses.

In addition, when the velocity distribution inside the pipe is examined, it is seen that the velocity at the inlet is greater than the velocity at the outlet. This is due to the pipe geometry and the axis difference between the inlet and outlet directions of the fluid. Since the temperature and velocity distribution have been obtained in the same way in all analyses, it has been understood that the pipe material

change did not affect these results. According to the data obtained from the FSI solutions, it has been determined that the magnesium pipes with the highest thermal strain are not suitable for systems with the hot fluid transmission. The tube with the lowest thermal strain has been determined to be made of titanium. However, since titanium is a very expensive material and it is known that it is generally used in the aviation industry, it can be said that gray cast iron material, which gives close values to it in FSI analyses, is more suitable for hydraulic systems with hot fluids. In addition, it has been clearly seen from the analysis that the region with the highest deformation risk in the T pipe is the junction point. For this reason, the junction point of the T pipes through which hot fluid passes should be supported with materials with low thermal strain value. Otherwise, the micro-cracks in the pipes will grow over time and cause the pipes to lose their function. This is of great importance for the continuation of the systems and the deterioration of the flow characteristics.

Funding
The author (s) has no received any financial support for the research, authorship or publication of this study.

Authors' Contribution
The authors contributed equally to the study.

The Declaration of Conflict of Interest/ Common Interest
No conflict of interest or common interest has been declared by the authors.

The Declaration of Ethics Committee Approval
This study does not require ethics committee permission or any special permission.

The Declaration of Research and Publication Ethics
The authors of the paper declare that they comply with the scientific, ethical and quotation rules of SAUJS in all processes of the paper and that they do not make any falsification on the data collected. In addition, they declare that Sakarya University Journal of Science and its editorial board have no responsibility for any ethical violations that may be encountered, and that this study has not been evaluated in any academic publication environment other than Sakarya University Journal of Science.

REFERENCES

[1] D. Andrade, F. Rachid, A. Tjsseling, "A new model for fluid transients in piping systems taking into account the fluid-structure interaction", Journal of Fluids and Structures, vol. 114, pp. 103720, 2022.

[2] M. Li, J. Pan, M. Ni, N. Zhang, "Heat transfer and thermal stress analysis in fluid-structure coupled field", Applied Thermal Engineering, vol. 88, pp. 473-479, 2015.

[3] Y. Xu, D. Johnston, Z. Jiao, A. Plummer, "Frequency modeling and solution of fluid-structure interaction in complex pipelines", Journal of Sound and Vibration, vol. 333 (2014), pp. 2800-2822, 2014.

[4] C. Hös, A. Champneys, K. Paul, M. McNeely, "Dynamic behaviour of direct spring loaded pressure relief valves: III valves in liquid service", Journal of Loss Prevention in the Process Industries, vol. 43, pp. 1-9, 2016.

[5] S. Dongwei, D. Jianbo, Z. Yong, "Investigation of pressure in pipe subjected to axial-symmetric pulse loading", International Journal of Impact Engineering, vol. 25, pp. 523-536, 2001.

[6] C. Evrim, E. Laurien, "Large-Eddy Simulation of turbulent thermal flow mixing in a vertical T-Junction configuration", International Journal of Thermal Sciences, vol.150, pp. 106231, 2020.

[7] L. Yao, Z. Xiao, J. Liu, Q. Zhang, "A new multi-field coupled dynamic analysis method for fracturing pipes", Journal of Petroleum Science and Engineering, vol. 196, pp. 108023, 2021.

[8] A. Tijsseling, "Water hammer with fluid-structure interaction in thick-walled pipes", Computers and Structures, vol. 85, pp. 844-851, 2007.

[9] Q. C. Li, S. He, "Research on effect factors of mechanical response of cross-fault buried gas pipeline based on fluid-structure interaction", Journal Pressure Vessel Technology, vol. 143, no. 6, pp. 061402, 2021.

[10] Y. Zhang, T. Lu, "Study of the quantitative assessment method for high-cycle thermal fatigue of a T-pipe under turbulent fluid mixing based on the coupled CFD-FEM method and the rainflow counting method", Nuclear Engineering and Design, vol. 309, pp. 175-196, 2016.

[11] F. Espinosa, J. Garcia, "Vibration failure in admission pipe of a steam turbine due to flow instability", Engineering Failure Analysis, vol. 27, pp. 30-40, 2013.

[12] Y. Jiang, S. Yoshimura, R. Imai, H. Katsura, T. Yoshida, C. Kato, "Quantitative evaluation of flow-induced structural vibration and noise in turbomachinery by full-scale weakly coupled simulation", Journal of Fluids and Structures, vol. 23, no. 4, pp. 531-544, 2007.

[13] M. Zhou, R. Kulenovic, E. Laurien, "Experimental investigation on the thermal mixing characteristics at a 90^{o} T-Junction with varied temperature differences", Applied Thermal Engineering, vol. 128, pp. 1359-1371, 2018.

[14] H. Kepekci, B. Zafer, H. Guven, B. Korbahti, "Aeroacoustics Investigation of a Wind Turbine for Different Blade Tip Shapes Using Computational Fluid Dynamics Software", Fresenius Environmental Bulletin, vol. 30, no. 11, pp. 12037-12047, 2021.

[15] H. Kepekci, E. Aslan, "CFD Analysis of Convection Heat Transfer in Corrugated Channels for Different Inclination Angle", Sakarya University Journal of Science, vol. 26, no. 2, pp. 333-341, 2022.

[16] Kaya F., and Karagöz İ. (2007) Girdaplı Modellerin Türbülans Modellerinin Uygunluğunun İncelenmesi. Uludağ Üniversitesi Mühendislik-Mimarlık Fakültesi Dergisi, 12(1), 85-97.

[17] D. Dhande, D. Pande D, "Multiphase flow analysis of hydrodynamic journal bearing using CFD coupled Fluid-Structure Interaction considering cavitation", Journal of King Saud University-Engineering Sciences, vol. 30, pp. 345-354, 2018.

[18] Yang L., Yang L., Lowe R. (2021) A viscoelasticity model for polymers: Time, temperature, and hydrostatic pressure dependent Young's modulus and Poisson's ratio across transition temperatures and pressures. Mechanics of Materials, vol. 157, pp. 103839.

[19] Barney C., Helgeson M., and Valentine M. (2022) Network structure influence bulk modulus of nearly incompressible filled silicone elastomers, Extreme Mechanics Letters, vol. 52, pp. 101616.

SAKARYA ÜNİVERSİTESİ
FEN BİLİMLERİ ENSTİTÜSÜ DERGİSİ

Sakarya University Journal of Science
SAUJS

ISSN 1301-4048 e-ISSN 2147-835X Period Bimonthly Founded 1997 Publisher Sakarya University
http://www.saujs.sakarya.edu.tr/

Title: Bi Doped TiO2 as a Photocatalyst for Enhanced Photocatalytic Activity

Authors: İlknur ALTIN

Recieved: 2022-11-17 00:00:00

Accepted: 2023-03-30 00:00:00

Article Type: Research Article

Volume: 27
Issue: 3
Month: June
Year: 2023
Pages: 670-679

How to cite
İlknur ALTIN; (2023), Bi Doped TiO2 as a Photocatalyst for Enhanced Photocatalytic Activity . Sakarya University Journal of Science, 27(3), 670-679,
DOI: 10.16984/saufenbilder.1206303
Access link
https://dergipark.org.tr/en/pub/saufenbilder/issue/78131/1206303

Sakarya University Journal of Science 27(3), 670-679, 2023

Bi Doped TiO_2 as a Photocatalyst for Enhanced Photocatalytic Activity

İlknur ALTIN[1*]

Abstract

This study is based on the preparation of TiO_2 and bismuth doped TiO_2 (Bi-TiO_2) nanoparticles by surfactant-assisted sol-gel approach. The physiochemical characteristics of prepared samples were examined by X-ray diffraction technique (XRD), Fiel emission scanning electron microscopy-energy dispersive analysis (FESEM-EDS), and UV-visible diffuse reflectance spectroscopy (UV-vis DRS). The XRD patterns revealed that the anatase crystal phase was only formed with high crystallinity. The band gap energies were measured to be of 3.11 eV for TiO_2-2 and 3.02 eV for Bi-TiO_2 by ultraviolet (UV)-visible diffuse reflectance spectroscopy, revealing that doping Bi improves the efficient interactive relation of the catalyst with visible light. Also, EDS results confirm that Bi particles are immobilized on the surface of TiO_2 successfully. The activities of the catalysts were tested by photocatalytic degradation of methylene blue (MB) under the visible light. Bi-TiO_2 photocatalyst could achieve the best MB degradation percentage of 70.2% after 180 min. of visible irradiation. Additionally, effect of some experimental parameters such as effect of humic acid (HA) and pH has been evaluated as much as reusability of catalyst. The characterization results confirmed the successful and desired preparation of the catalysts. The Bi-TiO_2 presented significant visible light response photocatalytic activity for the degradation of MB.

Keywords: Bi-TiO_2, photocatalysis, surfactant assisted sol-gel, visible light

1. INTRODUCTION

Many of organic dyes and their industrial effluents are toxic and carcinogenic, possing a threat for aquatic ecosystems and human health. Due to their hazard even at low concentration levels, it is necessary to improve cost effective technologies for the removal of these organic pollutants so as to minimize contamination risks and ensure the safety of environment [1-4]. These effluents are treated by many methods such as coagulation/flocculation, adsorption, ion-exchange and membrane filtration [5, 6]. However, these methods cause a secondary pollution by transferring the pollutants from the liquid phase to the solid phase and require further treatment methods [7, 8].

The photodegradation of the organic pollutants by catalysts is known as photocatalysis. Heterogeneous photocatalysis method has attracted much consideration for the degradation of dye pollutants due to its cost effective, soft reaction conditions and no secondary contamination [9, 10]. In

*Corresponding author: ilknurtatlidil@ktu.edu.tr (İ. ALTIN)
[1]Karadeniz Technical University
ORCID: https://orcid.org/0000-0002-9859-3611

photocatalysis, reactive oxygen species (ROS) such as ·OH, $O_2^{\cdot-}$ and H_2O_2 are formed on the surface of TiO_2 by absorbing UV radiation. These ROS species are responsible for the decomposition of organic compounds, including dye pollutants, present in waste water [11, 12].

Recently, TiO_2 based photocatalysis is the most popular candidate for waste water treatment, because it is non-toxic material, highly efficient and stable photocatalyst under UV light irradiation [13-15]. However, its photoactivity is relatively insufficient, because of the quick recombination of electron-hole (e^--h^+) pairs and large band gap energy (~3.2 eV), especially under the visible light. Many efforts are being made to develop economical and effective methods that work in sunlight or visible light for effective photocatalytic methods. Several methods have been proposed to enhance the photocatalytic efficiency of TiO_2 [16-21], such as modification with metal ions [16], non-metals [17], coupling with other semiconductors [18, 19] and dye sensitization [20, 21]. To increase catalytic activity of TiO_2, some researchers put their effort in doping TiO_2 with metals. Doping of TiO_2 photocatalyst can help in tuning the band gap energy, extend its photocatalytic reaction from the UV light range to visible light range and decrease the recombination of charge carries [16-21].

Bismuth has d^{10} electronic configuration. Bi-doped TiO_2 shifts the spectral range of TiO_2 to the visible light region and minimizes electron-hole recombination, and therefore it is widely used for degradation of organic pollutants, antibacterial application and photocathode for fuel cell, etc. has been extensively studied. However, it is rarely used in photocatalytic oxidation reactions due to its more complex reaction mechanism [22]. According to Ma et al. [22], Bi doped TiO_2 catalyst displays visible light driven photoactive properties for oxidation of methanol to methyl formate, increasing the surface hydroxyls and decreased the band gap energy. Li et al. [23] showed that by doping Bi into TiO_2, TiO_2 created a new intermediate energy level below its conduction band edge, thus prolonging the absorption in the visible region and increased their photocatalytic efficiency. Xu et al. [24] prepared Bi-doped TiO_2 nanofibers with different Bi content by an electrospinning method. They reported that Bi^{3+} ions were successfully incorporated into TiO_2 and extended the absorption of TiO_2 into the visible light region. They evaluated the catalytic activity of the Bi-doped TiO_2 nanofibers against the degradation of Rhodamine B (RhB, 1×10^{-5} M) under visible light irradiation of a 500W Xe lamp with a 420 nm cut-off filter. They indicated that almost all of the dye was degraded after 90 minutes of photocatalytic processing. Sood et al. [25] succesfully synthesized Bi doped TiO_2 photocatalyst by a facile sol-gel process. They proved that the incorporation of Bi^{3+} into TiO_2 lattice expanding of TiO_2 spectral response into visible region. The authors achieved that more than 80% degradation of Alizarin red S dye (ARS) with the prepared Bi-doped catalysts under visible light (philips bulb 150 W)

To the best of my knowledge, this study is the first in which Bi-TiO_2 was prepared via a surfactant-assisted (CTAB) sol-gel procedure. The main importance of this study is that the photocatalytic removal of MB was achieved with Bi-loaded TiO_2 under reduced cost and ambient conditions by using a very low-energy lamp and higher efficiency was obtained compared to the control group. Surfactant plays an important role in reducing surface tension and keeping particles apart during gel treatment, promoting steric and/or electrostatic interactions and preventing agglomeration. Thus, surfactant assisted sol-gel method might be used to get better photocatalytic activity with TiO_2 based catalyst [26].

In this study, TiO_2 catalyst was prepared by both pure sol gel method (TiO_2-1) and the surfactant assisted sol gel method (TiO_2-2). To improve the photocatalytic activity of

TiO_2-2 for the removal of methylene blue under visible light irradiation, TiO_2-2 was modified with the combination of Bi doping (Bi-TiO_2) using surfactant supported sol gel procedure. The morphology of nanocomposites was characterized by field emission scanning electron microscopy (FE-SEM), energy dispersive spectroscopy (EDS), X-ray diffractometry (XRD), UV-vis spectroscopy. Finally, the photocatalytic performances of synthesized nanoparticles were evaluated for removal of the methylene blue (MB) by visible light exposure ($\lambda \geq 400$ nm, 300 $\mu W/cm^2$) under ambient conditions. This photocatalyst displayed good performance in photocatalytic removal of MB under visible light. Thus, this approach may be used an important way for the secondary treatment of industrial wastewater.

2. MATERIAL AND METHOD

2.1. Material

Titanium (IV) isopropoxide (99%), $Bi(NO_3)_3.5H_2O$, HCl (36.5%) and Cetyltrimethylammonium bromide (CTAB ≥ %99) and absolute ethanol were purchased from Sigma-Aldrich. Deionized water was used for solution preparation and dilution.

2.2. Synthesis of nanoparticles

The pure TiO_2 nanoparticles were synthesized in two different ways, including both sol-gel and surfactant assisted sol-gel method [27]. 8.4 mL titanium (IV) isopropoxide was added into 140 mL absolute ethanol (Solution A). After stirring for 2 h, a solution that contained 0.22 mL HCl (concentrated) and 0.50 mL deionized water (Solution B) was added to Solution A, and the resulting mixture was stirred for 24 h to get a wet gel.

The resulting wet-gel was dried for 24 h at 80 ^oC. Finally, the final powder was calcined at 450 ^oC for 4 h. The as-prepared catalyst was defined as TiO_2-1.

The same TiO_2 catalyst was synthesized in the presence of Cetyltrimethylammonium bromide (CTAB). Initially, CTAB was added into absolute ethanol then titanium (IV) isopropoxide was added and the mixture was kept stirring for 2 h. The as-prepared catalyst was denoted as TiO_2-2. For the synthesis of Bismuth doped TiO_2 (Bi-TiO_2) catalyst in the presence of CTAB, absolute ethanol (10 mL) containing 0.1787 g $Bi(NO_3)_3.5H_2O$ (which is equal to 3% of TiO_2 mass) seperately added into the above solution under the same conditions. Given the photocatalytic results, bismuth was loaded on the best yielding TiO_2-2 catalyst.

2.3. Characterization of catalyst

The characteristic properties of the photocatalysts were examined by different techniques. X-ray diffraction (XRD) patterns were obtained by a PANanalytical Empyrean diffractometer with CuKα radiation in the 2θ range from 20^o to 80^o. Surface morphologies were analyzed by field emission scanning electron microscopy (FE-SEM, QUANTA 400F), UV-vis diffused reflectance spectra were recorded on a UV-VIS-NIR spectrophotometer (Shimadzu UV-3600 Plus).

2.4. Photocatalytic experiments

Methylene blue (MB) was prefered as a model dye contaminant to determine activity of the prepared catalyst in the photocatalytic duration. LED lamp ($\lambda \geq 400$ nm, 300 $\mu W/cm^2$) was used as the visible light source. For photocatalytic degradation, aqueous MB (50 mL, 10 mg/L) and 50 mg catalyst were added to the reaction cell and stirred first for 30 min, in the dark, to equilibrate adsorption process.

After the time, the reaction cell was then illuminated for 180 min of photocatalytic degradation. 5 mL of solution was taken from the reaction solution, centrifuged and analyzed using UV-VIS spectrofotometer (λ_{max} = 668 nm). The control tests were

performed out in the absence of light or without photocatalysts to investigate MB photolysis.

To simulate more realistic water, the influence of humic acid presence was evaluated on the degradation yield. The pH of the reaction solution was adjusted with 0.01 M NaOH or 0.01 M HCl solutions and the degradation efficiency was studied.

3. RESULTS AND DISCUSSION

3.1. Characterization

XRD pattern TiO_2-1 nanoparticles synthesized by sol-gel method and TiO_2-2 and Bi-TiO_2 synthesized by surfactant assisted sol-gel method is indicated in Figure 1. All materials exhibited reflections at 2θ=25.3°, 37.8°, 48.0°, 54.0°, 55.0°, 62.7°, 68.9°, 70.3° and 75.1° characteristic of the (101), (004), (200), (105), (211), (204), (116), (220) and (211) planes respectively of anatase TiO_2 (JCPDS card No. 21-1272) [25]. There was also no observable shift and additional peak in any of the titania reflections following Bi addition due to the relatively low amount of doped Bi.

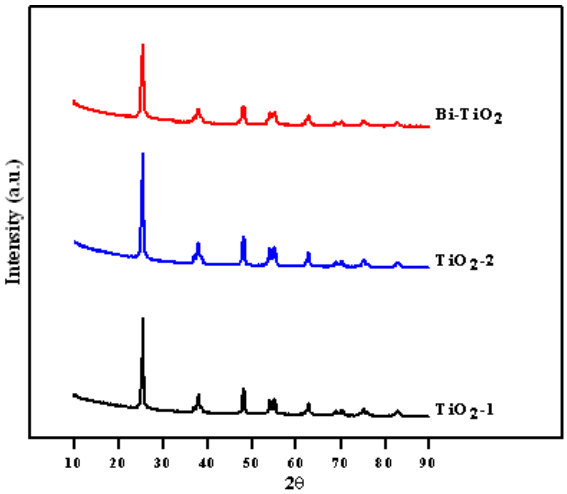

Figure 1 XRD patterns of TiO_2-1, TiO_2-2 and Bi-TiO_2 photocatalysts

The average crystallite sizes of the prepared samples were calculated by Debye Scherrer's formula:

$$D = K\lambda/\beta\cos\theta \quad (1)$$

D is the crystallite size, K=0.9 is a correction factor which accounts for the particle shape, λ is the wavelength of Cu target (0.15406 nm), β is the line width at half maximum height, and θ is the Bragg's angle [21]. Found that the average crystallite sizes of the TiO_2-1, TiO_2-2 and Bi-TiO_2 were 17.65, 16.06 and 13.09 nm, respectively.

The diffuse reflectance UV-vis spectra of the catalysts are shown in Figure 2. Figure 2 shows shift in the absorption peak of Bi-TiO_2 compared to TiO_2-2, absorption edges are found to be 411.1 nm and 398.7 nm respectively. The band gap energies can be calculated by the following equation

$$Eg=1240/\lambda_g \quad (2)$$

Where Eg is the band gap energy, and λ_g is the absorption edge of the catalyst [28]. Hence, the band gap was found out to be 3.11 eV for TiO_2-2, 3.02 eV for Bi-TiO_2. This shows that by doping Bi the efficient interactive relation of the catalyst with visible light is allowed. In addition, this reduction in band gap leads to the formation of additional energy levels induced by Bi-doping above the valence band (VB) of TiO_2, shifting its absorption into the visible region. Compared to TiO_2, Bi-TiO_2 shows a red shift in absorption wavelength favoring the successful incorporation of Bi into the TiO_2 lattice. Furthermore, compared to pristine TiO_2, the absorption in the visible region is enhanced for the Bi-TiO_2 photocatalyst.

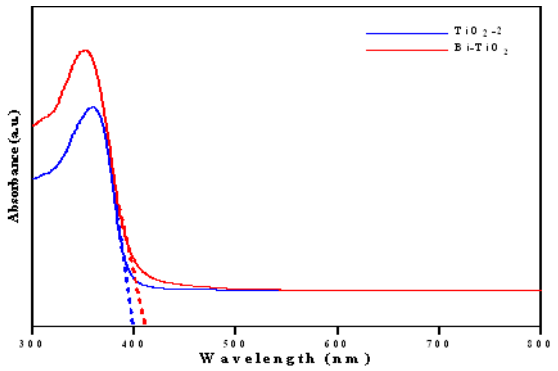

Figure 2 Optical band gap energies of TiO_2-2 and Bi-TiO_2

The morphology of the catalysts was studied by FESEM. The results are shown in the Figure 3 (a-d) shows FE-SEM images both Bi-TiO_2 and TiO_2-2 catalysts which indicates irregular oval shapped particles.

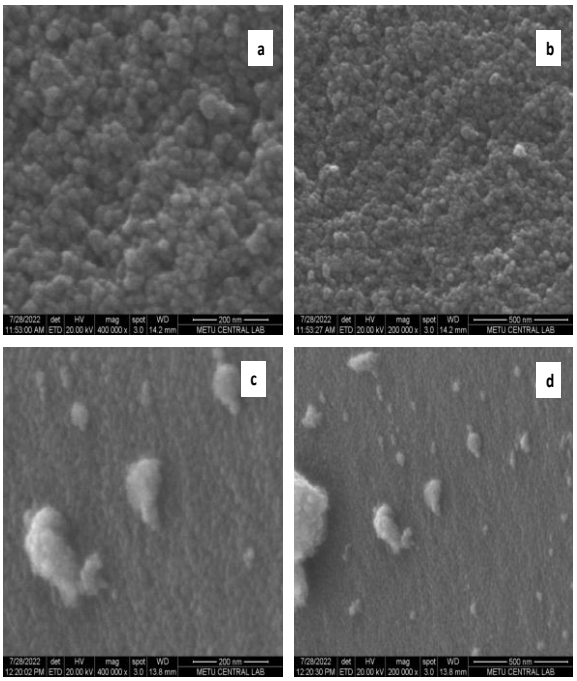

Figure 3 FE-SEM images of TiO_2-2 (a-b) and Bi-TiO_2 (c-d)

Figure 4 and Figure 5 shows the EDS spectra of the TiO_2-2 and Bi-TiO_2, respectively. The EDS spectra could also support that Bi was succesfully immobilized in the TiO_2 catalyst because of the presence bismuth, oxygen, and titanium signals. Also, the EDS data confirmed that catalysts are pure and not having any impurities.

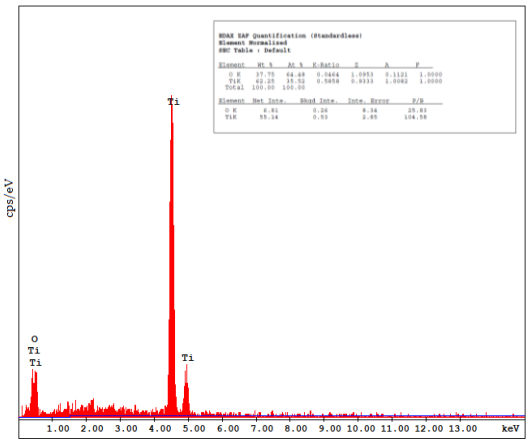

Figure 4 EDS spectra of TiO_2-2

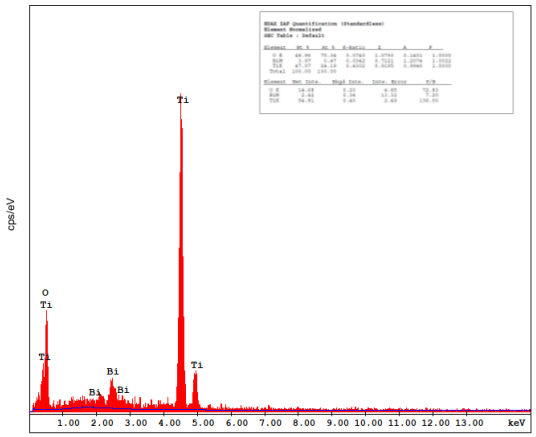

Figure 5 EDS spectra of Bi-TiO_2

3.2. Photocatalytic activity

The photocatalytic degradation percentage of MB in the presence of the prepared catalysts is given in Figure 6. Initially, the efficiency of MB degradation, in the absence of photocatalyst, only is around 1% after 180 min visible light irradiation. It can be seen that the degradation of MB with Bi-TiO_2 (70.2%) is higher than that reached with TiO_2-1 (24.3%) or TiO_2-2 (32.0%) after 180 min irradiation under the visible light. The high catalytic of Bi-TiO_2 is attributed to presence of Bi which provides a synergetic effect on MB photodegradation and results in better catalytic efficiency. Procedures for improving the photocatalytic degradation of MB due to the resistance of MB to degradation; (i) the use of CTAB as a surfactant in the process is to control aggregation, allow the surfactant to act as a surface-directing agent, lower the surface tension and increase the solubility of the reaction mixture, and act as an excellent medium for nucleation and crystal growth. Thus, the quantum efficiency may be increased, (ii) recombination of electron hole types can be inhibited by formation the heterojunction composition of Bi and TiO_2 together [26,27].

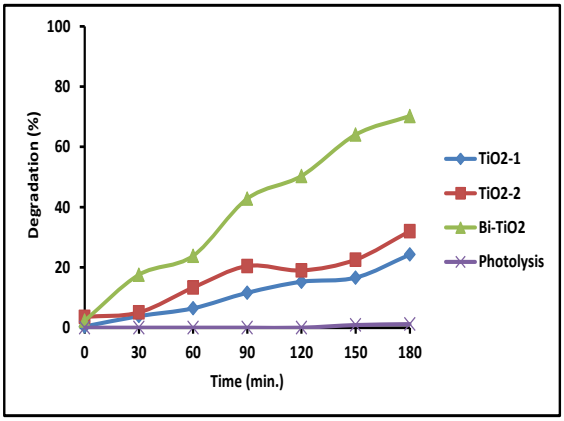

Figure 6 Photocatalytic degradation of MB under visible light irradiation [C_0=10 mg/L; Catalyst amount= 1g/L; pH 6.12]

As shown in Figure 7, the adsorption removal efficiencies of MB over the TiO_2-1, TiO_2-2 and Bi-TiO_2 (experiments in the without light) were 15.2%, 22.1% and 24.5% respectively. Although there was no significant difference between the adsorption removal of the catalysts, Bi-TiO_2 exhibited better adsorption activity.

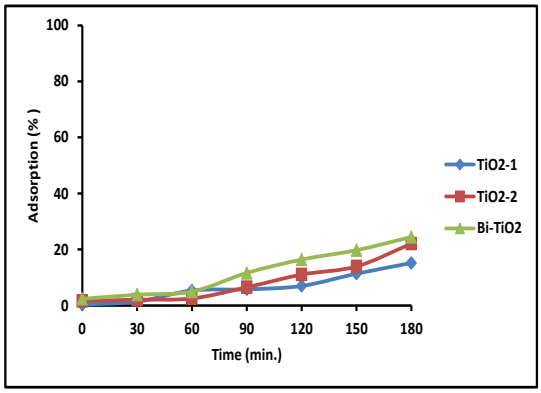

Figure 7 Adsorption removal of MB in the absence of light [C_0=10 mg/ L; Catalyst amount= 1g/L; pH 6.12]

The effect of experimental conditions on the degradation of MB such as the presence of humic acid (HA) and pH was examined on the best photocatalyst (Bi-TiO_2). Also, the reusability tests of the Bi-TiO_2 were investigated for the degradation of MB.

As seen from Figure 8, it is clear that the removal of MB was significantly reduced at acidic pH (3.04). The removal results of MB at neutral pH 6.12 did not show a significant difference from the removal results at pH 8.02 or pH 12.06. It is seen as an advantage since no additional pH arrangement is required in the removal processes of MB [29].

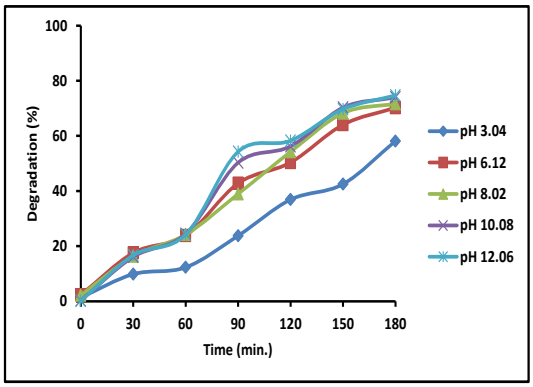

Figure 8 The effect of pH on photocatalytic removal [C_0=10 mg/ L; Bi-TiO_2= 1g/L]

HA, an important natural organic component (NOM), is typically surface water and can adversely affect the physical and chemical properties of water [30]. Humic acid (HA) solution was used in this study to simulate the reaction solution in real water. Chemical degradation reactions can be negatively affected due to the interactions of HA with ROS (Reactive Oxygen Species), which are responsible for the degradation of MB and are expected to be generated during photocatalysis removal processes.

Considering that HA concentration usually ranges from 2 mg/L to 10 mg/L in surface natural water, 5 mg/L or 8 mg/L HA was added to the reaction solution and its effect on the removal of MB was studied. As shown in Figure 9, the presence of HA in the reaction solution slightly affected the photocatalytic degradation of MB. In detail, 5 mg/L HA and 8 mg/L HA were added to the reaction solution and the degradation rate decreased from 70.2% to 67.3% and 64.3%, respectively. This slight decrease in activity may be due to: (i) competitive adsorption of HA with MB on the catalyst surface which delays the photocatalytic oxidation process interfering with the ROS and, (ii) reduced light penetration in suspension. Based on the above experimental results involving HA, the

degradation of photocatalytic MB is expected to be slower in real water samples [27,31,32].

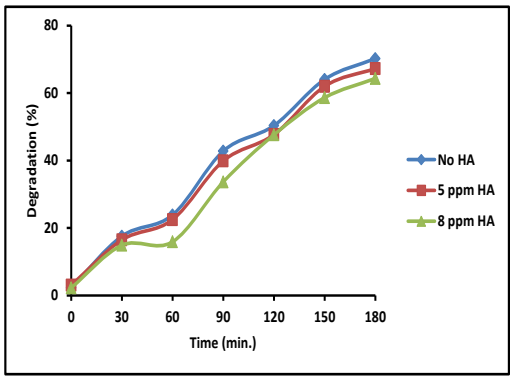

Figure 9 Photocatalytic removal of MB in the presence of different concentrations of HA [C_0=10 mg/ L; Bi-TiO_2 = 1g/L; pH 6.12]

The reusability tests of the Bi-TiO_2 were investigated for the MB. After the first 180 min. treatment the catalyst was simply washed with water and reused in a new treatment at the same pollutant concentration. Since the amount of catalyst decreased slightly before each use, fresh Bi-TiO_2 was added as much as the decreasing amount.

The degradation percentages obtained after 5 times usage for MB are shown in Figure 10. As shown in Figure 10, Bi-TiO_2 activity decreased nearly 20% for MB removal after 5 cycles. It was clear that Bi-TiO_2 was still effective but dye removal rates were lower. The degradation rate may have decreased due to the irreversible adsorption of the dye on the catalyst surface [29].

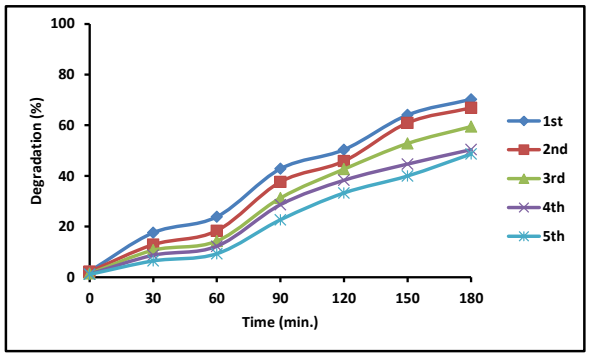

Figure 10 The recycling tests of Bi-TiO_2 [C_0=10 mg/ L; Bi-TiO_2 = 1g/L; pH 6.12]

4. CONCLUSION

In summary, in this study, bismuth doped TiO_2 (Bi-TiO_2) photocatalyst succesfully prepared using a surfactant assisted sol-gel method. It was found that Bi-TiO_2 catalyst had anatase crystal structure with non-impurity. According to the results of photocatalytic studies, Bi-TiO_2 catalyst presented on improved catalytic activity in degradation for MB and showed extention in the spectral response range shifted to the visible region. MB degradation in the presence of Bi-TiO_2 after 180 min visible light irradiation was reached 70.2%. No significant reduction in the MB catalytic activity was observed during five cycles in the reusability test, showing that the Bi-TiO_2 catalyst remains stable and performance in time and can be applied in scale-up processes. Also, the presence of HA in the reaction solution slightly affected the photocatalytic degradation of MB. This study could be a hopeful base for applicability of visible or solar light water remediation process especially those containing dye pollutants.

Funding
The author has no received any financial support for the research, authorship or publication of this study.

The Declaration of Conflict of Interest/ Common Interest
No conflict of interest or common interest has been declared by the author.

The Declaration of Ethics Committee Approval
This study does not require ethics committee permission or any special permission.

The Declaration of Research and Publication Ethics
The author of the paper declare that she complies with the scientific, ethical and quotation rules of SAUJS in all processes of the paper and that she does not make any falsification on the data collected. In addition, she declares that Sakarya University Journal

of Science and its editorial board have no responsibility for any ethical violations that may be encountered, and that this study has not been evaluated in any academic publication environment other than Sakarya University Journal of Science.

REFERENCES

[1] J. Singh, A. Arora, S. Basu, "Synthesis of coral like WO_3/g-C_3N_4 nanocomposites for the removal of hazardous dyes under visible light", Journal of Alloys and Compounds, vol. 808, Article No: 151734, 2019.

[2] M.M.J. Sadiq, U.vS. Shenoy, D.vK. Bhat, "$NiWO_4$-ZnO-NRGO ternary nanocomposite as an efficient photocatalyst for degradation of methylene blue and reduction of 4- nitro phenol", Journal of Physics and Chemistry of Solids, vol. 109, pp. 124-133, 2017.

[3] M. Shekofteh-Gohari, A. Habibi-Yangjeh, M. Abitorabi, A. Rouhi, "Magnetically separable nanocomposites based on ZnO and their applications in photocatalytic processes: a review", Critical Reviews in Environmental Science and Technology, vol. 48, pp. 806-857, 2018.

[4] İ. Altın, M. Sökmen, Z. Bıyıklıoğlu, "Quaternized zinc(II) phthalocyanine-sensitized TiO_2: surfactant-modified sol-gel synthesis, characterization and photocatalytic applications", Desalination and Water Treatment, vol. 57, pp. 1-12, 2016.

[5] Y.vM. Hunge, A.vA. Yadav, V.vL. Mathe, "Ultrasound assisted synthesis of WO_3-ZnO nanocomposites for brilliant blue dye degradation", Ultrasonics Sonochemistry, vol. 45, pp. 116-122, 2018.

[6] C.vB. Anucha, I. Altin, E. Bacaksiz, V. N. Stathopoulos, I. Polat, A. Yasar, Ö. F. Yüksel, "Silver doped zinc stannate (Ag-$ZnSnO_3$) for the photocatalytic degradation of caffeine under UV irradiation", Water, vol. 13(9), 1290, 2022.

[7] V. Homem, L. Santos, "Degradation and removal methods of antibiotics from aqueous matrices - a review", Journal of Environmental Management, vol. 92, pp. 2304-2347, 2011.

[8] M. B. Ahmed, J. L. Zhou, H. H. Ngo, W. Guo, "Science of the total environment adsorptive removal of antibiotics from water and wastewater : progress and challenges", Science of the Total Environment, vol. 532, pp. 112-126, 2015.

[9] J. L. White, M. F. Baruch, J. E. Pander, Y. Hu, I. C. Fortmeyer, J. E. Park, T. Zhang, K. Liao, J. Gu, Y. Yan, T. W. Shaw, E. Abelev, A. B. Bocarsly, Light-driven heterogeneous reduction of carbon dioxide: photocatalysts and photoelectrodes, Chemical Reviews, vol. 115, pp. 12888-12935, 2015.

[10] S. J. Alyani, A. E. Pirbazari, F. E. Khalilsaraei, N. A. Kolur, N. Gilani, "Growing Co-doped TiO_2 nanosheets on reduced graphene oxide for efficient photocatalytic removal of tetracycline antibiotic from aqueous solution and modeling the process by artificial neural network", Journal of Alloys and Compounds, vol. 799, pp. 169-182, 2019.

[11] C. Karunakaran, V. Rajeswari, P. Gomathisankar, "Optical, electrical, photocatalytic, and bactericidal properties of microwave synthesized nanocrystalline Ag-ZnO and ZnO", Solid State Sciences, vol.13, pp. 923-928, 2011.

[12] X. Hu, G. Li, J.C. Yu, "Design, fabrication, and modification of nanostructured semiconductor materials for environmental and energy applications", Langmuir, vol. 26, pp. 3031-3039, 2010.

[13] J. Schneider, M. Matsuoka, M. Takeuchi, J. Zhang, Y. Horiuchi, M. Anpo, D. W.Bahnemann, "Understanding TiO_2 photocatalysis: mechanisms and materials", Chemical Reviews, vol. 114, pp. 9919-9986, 2014.

[14] S. Y. Lee, S. J. Park, "TiO_2 photocatalyst for water treatment applications", Journal of Industrial and Engineering Chemistry, vol. 19, pp. 1761-1769, 2013.

[15] P. V. Laxma Reddy, B. Kavitha, P. A. Kumar Reddy, K. H. Kim, "TiO_2-based photocatalytic disinfection of microbes in aqueous media: a review", Environmental Research, vol. 154, pp. 296-303, 2017.

[16] Y. Li, M. Ma, W. Chen, L. Li, M. Zen, "Preparation of Ag-doped TiO_2 nanoparticles by a miniemulsion method and their photoactivity in visible light illuminations", Materials Chemistry and Physics, vol. 129, pp. 501-505, 2011.

[17] D. Sannino, V. Vaiano, O. Sacco, P. Ciambelli, "Mathematical modelling of photocatalytic degradation of methylene blue under visible light irradiation", Journal of Environmental Chemical Engineering, vol. 1(1-2), pp. 56-60, 2013.

[18] Y. J. Kim, B. Gao, S. Y. Han, M. H. Jung, A. K. Chakraborty, T. Ko, C. Lee, W. I. Lee, Heterojunction of $FeTiO_3$ Nanodisc and TiO_2 Nanoparticle for a Novel Visible Light Photocatalyst, Journal of Physical Chemistry C, vol. 113, pp. 19179-19184, 2009.

[19] C. B. Anucha, I. Altin, E. Bacaksiz, I. Degirmencioglu, T. Kucukomeroglu, S. Yılmaz, Vassilis N Stathopoulos, "Immobilized TiO_2/ZnO sensitized copper (II) phthalocyanine heterostructure for the degradation of ibuprofen under UV irradiation", Separations, vol. 24, pp. 1-21, 2021.

[20] S. Neccaroğlu Işık, G. Gümrükçü Köse, O. Avcıata, "New phthalocyanine-TiO_2 nanocomposites with photocatalyst properties", Research on Chemical Intermediates, vol. 49, pp. 1629-1648, 2023.

[21] İ. Altın, M. Sökmen, Z. Bıyıklıoğlu, "Sol gel synthesis of cobalt doped TiO_2 and its dye sensitization for efficient pollutant removal", Materials Science in Semiconductor Processing vol. 45, pp. 36-44, 2016.

[22] Y. Ma, X. Yang, G. Gao, Z. Yan, H. Su, B. Zhang, "Photocatalytic partial oxidation of methanol to methyl formate under visible light irradiation on Bi doped", RSC Advances, vol. 10, pp. 31442-31452, 2020.

[23] J.-J. Li S.-C. Cai, Z. Xu, X. Chen, J. Chen, H.-P. Jia, J. Chen, "Solvothermal syntheses of Bi and Zn co-doped TiO_2 with enhanced electron-hole separation and efficient photodegradation of gaseous toluene under visible-light", Journal of Hazardous Materials, vol. 325, pp 261-270, 2017.

[24] J. Xu, W. Wang, M. Shang, E. Gao, Z. Zhang, J. Ren, "Electrospun nanofibers of Bi-doped TiO_2 with high photocatalytic activity under visible light irradiation", Journal of Hazardous Materials, vol. 196 pp. 426-430, 2011.

[25] S. Sood, S. Kumar Mehta, Ahmad Umar, S. Kumar Kansal, "The visible light-driven photocatalytic degradation of Alizarin red S using Bi-doped TiO_2 nanoparticles", New Journal of Chemistry, vol. 38, pp. 3127-3136, 2014.

[26] T. N. Ravishankar, M. de O. Vaz , S. R. Teixeira, "The effect of surfactant on sol-gel synthesis of CuO/TiO_2 nanocomposites for the photocatalytic activities under UV-Visible and visible light illuminations", New Journal of Chemistry, vol. 44, pp. 1888-1904, 2020.

[27] I. Altin, "$CuO-TiO_2$/graphene ternary nanocomposite for highly efficient visible-light-driven photocatalytic degradation of bisphenol A", Journal of Molecular Structure, vol. 1252, Article No: 132199, 2022.

[28] L. Xu , L. Yang , E. M. J. Johansson , Y. Wang, P. Jin Photocatalytic activity and mechanism of bisphenol a removal over TiO_{2-x}/rGO nanocomposite driven by visible light, Chemical Engineering Journal, vol. 350, pp. 1043-1055, 2018.

[29] İ. Altın, M. Sökmen, "Preparation of TiO_2-polystyrene photocatalyst from waste material and its usability for removal of various pollutants", Applied Catalysis B: Environmental, vol. 144, pp. 694-701, 2014.

[30] C. Wang, L. Zhu, M. Wei, P. Chen, G. Shan, "Photolytic reaction mechanism and impacts of coexisting substances on photodegradation of bisphenol A by Bi_2WO_6 in water", vol. 46, pp. 845-853, Water Research, 2012.

[31] M. Antonopoulou, C. G. Skoutelis, C. Daikopoulos, Y. Deligiannakis, I. K. Konstantinou, "Probing the photolyticephotocatalytic degradation mechanism of DEET in the presence of natural or synthetic humic macromolecules using molecular-scavenging techniques and EPR spectroscopy", Journal of Environmental Chemical Engineering, vol. 3, pp. 3005-3014, 2015.

[32] I. Altin, X. Ma, V. Boffa, E. Bacaksız, G.Magnacca, "Hydrothermal preparation of B-TiO_2-graphene oxide ternary nanocomposite, characterization and photocatalytic degradation of bisphenol A under simulated solar irradiation", Materials Science in Semiconductor Processing, 123, Article No: 105591.

SAKARYA ÜNİVERSİTESİ
FEN BİLİMLERİ ENSTİTÜSÜ DERGİSİ

Sakarya University Journal of Science
SAUJS

ISSN 1301-4048 e-ISSN 2147-835X Period Bimonthly Founded 1997 Publisher Sakarya University
http://www.saujs.sakarya.edu.tr/

Title: The Effect of Anisotropic Gaussian Schell-Model Sources in Generalized Phase Space Stokes Parameters

Authors: Serkan ŞAHİN

Recieved: 2022-08-13 00:00:00

Accepted: 2023-04-02 00:00:00

Article Type: Research Article

Volume: 27
Issue: 3
Month: June
Year: 2023
Pages: 680-686

How to cite
Serkan ŞAHİN; (2023), The Effect of Anisotropic Gaussian Schell-Model Sources in Generalized Phase Space Stokes Parameters . Sakarya University Journal of Science, 27(3), 680-686, DOI: 10.16984/saufenbilder.1161702
Access link
https://dergipark.org.tr/en/pub/saufenbilder/issue/78131/1161702

Sakarya University Journal of Science 27(3), 680-686, 2023

The Effect of Anisotropic Gaussian Schell-Model Sources in Generalized Phase Space Stokes Parameters

Serkan ŞAHİN *1

Abstract

Phase-space transforms describe spatial and angular information about light sources where one example is the Wigner functions in wave optics. Stokes parameters, on the other hand, supply information about the polarization of light beams. The generalized phase space Stokes parameters of 2D stochastic electromagnetic beams are already developed. In this article, the application of anisotropic light sources in generalized phase space Stokes parameters is theoretically investigated and numerically analyzed. There are several different ways of studying electromagnetic light beams depending on the spatial domain. But, most measure of the polarization of random light fields is carried out within the Stokes parameters context. In this account we study the electromagnetism, Stokes parameters, phase space, and the anisotropy properties of random light beams at once. We find here that when an anisotropy introduced in phase space then the cross terms of the Wigner matrix depart from the diagonal terms, which is not the same in configuration space. As a result, anisotropy has a different effect in Phase space, i.e. an anisotropic source introduces a phase and a variance change only in the cross terms of Wigner matrix. This is due to the use of anisotropy in the shifted kernel of Wigner transform.

Keywords: Optical coherence, phase space, Stokes parameters, Wigner function, physical optics

1. INTRODUCTION

A quasi-probability distribution is the Wigner distribution function (WDF) which was introduced in 1932 [1, 2] to attach quantum perspectives to classical statistical mechanics. Since then it is applied to many areas including optics. WDF has been extensively employed in both the classical and quantum regimes to characterize the spatial and temporal statistics of optical fields. The concept of the Wigner distribution function is not restricted to deterministic fields, it can be applied to stochastic fields as well [2]. The Wigner function has a number of noteworthy benefits for optical studies. One of them is its use in imaging where one can obtain a simplified WDF of image wave field in a partially coherent microscope [3]. Another one is its utilization in signal processing where one can obtain amplitude and phase retrieval, signal recognition and such easily via Wigner distribution function [4, 5]. Additional insight into the Wigner distribution can be one can achive wave field propagation through graded index media by means of Wigner distribution function [6]. In an experimental viewpoint, the Wigner

* Corresponding author: serkan.sahin@tedu.edu.tr (S. SAHIN)
[1] TED University
ORCID: https://orcid.org/0000-0002-5241-1632

distribution function helps in the measurements of optical field correlations [7]. Thus, the Wigner function is studied in optics in detail especially in connection with radiometry and partial coherence [8].

On the other hand, the use of random light beams can be favourable in graded index media where periodicity of the statistical properties of beams takes place [9]. As another option, it is known that the use of random light beams can improve the performance of free space laser communications across atmospheric turbulence [10, 11]. Main reason for these applications is the reduction in coherent interference, which is found to lower the intensity fluctuation (scintillation) at the receiver.

This paper focuses on anisotropic random light beams of spatially partially coherent, and we analyze its phase space through Wigner distribution function. The derivations pertain to the source plane. Following sections represent the organization of this paper's material. First we supply necessary information on the beam field and its propagation in the phase space context and then derive the Wigner transform of anisotropic Schell-model Gaussian beam. We obtain the generalized phase space Stokes parameters of anisotropic Gaussian Schell-model beam and finally compare it with configuration space generalized Stokes parameters.

2. MATERIAL AND METHOD

To develop the approach of anisotropic beams in phase space, we start with the two-point electric correlation matrix of the beam which is given in the form [12]

$$\overleftrightarrow{W}(\mathbf{r}_1,\mathbf{r}_2,\omega)=\begin{pmatrix} W_{xx}(\mathbf{r}_1,\mathbf{r}_2,\omega) & W_{xy}(\mathbf{r}_1,\mathbf{r}_2,\omega)\\ W_{yx}(\mathbf{r}_1,\mathbf{r}_2,\omega) & W_{yy}(\mathbf{r}_1,\mathbf{r}_2,\omega)\end{pmatrix}, \quad (1)$$

whose elements are $W_{ij}(\mathbf{r}_1,\mathbf{r}_2,\omega)=\langle E_i^*(\mathbf{r}_1,\omega)E_j(r_2,\omega)\rangle$, $(i,j=x,y)$. $E_x(\mathbf{r},\omega)$ and $E_y(\mathbf{r},\omega)$ are the elements of suitably constructed stationary, at least in the wide sense, statistical ensembles. $\mathbf{r}$ represents the two dimensional position vector on $\mathbf{r_1}$, $\mathbf{r_2}$ plane, ω is the temporal frequency and asterisk indicates the complex conjugate. We assume that the component of the electric field along z axis is neglected and only the two transverse field components $E_{x,y}(\mathbf{r},\omega)$ are necessary (and propagating on *z* axis).

The Wigner distribution function depends in conjunction on the canonical conjugate phase space variables, which for light beams are the transverse position vector $\mathbf{r}$ and the angular (spatial frequency) vector $\mathbf{k}$, and for optical pulses are the time variable t and temporal frequency ω. The Wigner function which depends on both $(\mathbf{r},\mathbf{k},t,\omega)$ can also be constructed [5]. We shall describe the Wigner phase space matrix by the integral of the shifted electric correlation matrix [2]

$$F_{ij}(\mathbf{r},\mathbf{k},\omega)=\int W_{ij}\left(\mathbf{r}+\frac{\mathbf{r}'}{2},\mathbf{r}-\frac{\mathbf{r}'}{2},\omega\right)e^{-i\mathbf{r}'\cdot\mathbf{k}}d\mathbf{r}', \quad (2)$$

which can be easily written in the matrix notation as

$$\overleftrightarrow{F}(\mathbf{r},\mathbf{k},\omega)=\begin{pmatrix} F_{xx}(\mathbf{r},\mathbf{k},\omega) & F_{xy}(\mathbf{r},\mathbf{k},\omega)\\ F_{yx}(\mathbf{r},\mathbf{k},\omega) & F_{yy}(\mathbf{r},\mathbf{k},\omega)\end{pmatrix}. \quad (3)$$

Equation [2] integrates the shifted electric correlation matrix Equation [1]. i throughout the paper represents the imaginary unit $\sqrt{-1}$. But in the subscripts $i,j=x,y$.

In the configuration (or parametric) space, the stokes parameters can be constructed by linear combinations of the electric correlation matrix [12]. In the same manner we build the phase space stokes parameters as given [13]

$$S_0(\mathbf{r},\mathbf{k},\omega)=F_{xx}(\mathbf{r},\mathbf{k},\omega)+F_{yy}(\mathbf{r},\mathbf{k},\omega), \quad (4)$$

$$S_1(\mathbf{r},\mathbf{k},\omega)=F_{xx}(\mathbf{r},\mathbf{k},\omega)-F_{yy}(\mathbf{r},\mathbf{k},\omega), \quad (5)$$

$$S_2(\mathbf{r},\mathbf{k},\omega)=F_{xy}(\mathbf{r},\mathbf{k},\omega)+F_{yx}(\mathbf{r},\mathbf{k},\omega), \quad (6)$$

$$S_3(\mathbf{r},\mathbf{k},\omega)=i\left[F_{yx}(\mathbf{r},\mathbf{k},\omega)-F_{xy}(\mathbf{r},\mathbf{k},\omega)\right], \quad (7)$$

Based on these equations, positional and directional intensities of the electromagnetic beams are the following (see [2] for scalar beams)

$$\mathrm{I_p}(\mathbf{r},\mathbf{r},\omega) = \int \mathrm{S_0}(\mathbf{r},\mathbf{k},\omega)\mathrm{d}\mathbf{k}, \tag{8}$$

$$I_d(\mathbf{k},\mathbf{k},\omega) = \int \mathrm{S_0}(\mathbf{r},\mathbf{k},\omega)\mathrm{d}\mathbf{r}, \tag{9}$$

noting that they both depend on the first stokes parameter $\mathrm{S_0}(\mathbf{r},\mathbf{k},\omega)$.

We will now consider the paraxial propagation of the WDF. The paraxial [2] propagation (see [14] for non-paraxial propagation), from an incident flat surface to a surface at z, corresponds to a linear transformation of the wigner function's initial argument, i.e. paraxial propagation reads

$$S_l(\mathbf{r},\mathbf{k},\mathrm{z},\omega) = S_l\left(\mathbf{r} - \frac{\lambda z}{2\pi}\mathbf{k},\mathbf{k},0,\omega\right), \tag{10}$$

for l ranges from 0 to 3. The constant involved is the wavelength λ. Another way of propagation analysis can be seen by assuming the medium is a first order optical system (with its ray transfer matrix), under this condition the WDF at plane z becomes [14]:

$$S_l(\mathbf{r},\mathbf{k},\mathrm{z},\omega) = S_l(\mathrm{A}\mathbf{r} + \mathrm{B}\mathbf{k}, \mathrm{C}\mathbf{r} + \mathrm{D}\mathbf{k}, 0, \omega), \tag{11}$$

where the components of the ray transfer matrix ABCD are A, B, C, and D, and $\mathrm{A} = 1$, $\mathrm{B} = -\frac{\lambda z}{2\pi}$, $\mathrm{C} = 0$, $\mathrm{D} = 1$ in free space as an example. WDF describes optical signals concurrently in spatial frequency and space. Geometrical optics' concepts of position and angle are analogous to this idea. This characteristic allows us to use the ray transfer matrix, often known as the ABCD matrix, to propagate light in phase space [15].

For an application of the theory we consider the general expression of the well known electromagnetic anisotropic Gaussian Schell-model beam (AGSMB) as given

$$\mathrm{W_{ij}}(\mathbf{r_1},\mathbf{r_2},\mathrm{z}=0,\omega) = \left(\mathrm{A_iA_j}\right)^{\frac{1}{2}}\mathrm{B_{ij}}\exp\left[-\frac{\mathbf{r_1^2}}{4\sigma_\mathrm{i}^2}\right]\exp\left[-\frac{\mathbf{r_2^2}}{4\sigma_\mathrm{j}^2}\right]\exp\left[-\frac{(\mathbf{r_2}-\mathbf{r_1})^2}{2\delta_\mathrm{ij}^2}\right] \tag{12}$$

In Equation [12] the parameters $\mathrm{A_i}$, $\mathrm{A_j}$, $\mathrm{B_{ij}}$, σ_i, σ_j, and δ_ij are independent of location but they might depend on temporal frequency. The magnitudes of the electric field-vector components are $\mathrm{A_i}$, $\mathrm{A_j}$. σ_i^2 , σ_j^2 are the variances of the intensity dispersion through the source coordinates and the variances of the correlations between the elements of the electric field vector are δ_ij^2. Besides, the parameters Bij must satisfy the realizability conditions [16]: $\mathrm{B_{ii}} = \mathrm{B_{jj}} = 1$, $\mathrm{B_{ij}} = \mathrm{B_{ji}^*} = \mathrm{B}\exp[\mathrm{i}\theta]$. The phase difference between two orthogonal electric field components is θ , and B is used for the modulus of correlation parameter.

Use of Equation [12] as a model beam first in Equation [2] then in Equations [4]-[7] constructs the phase space stokes parameters of anisotropic Gaussian Schell-model beams (we dropped the ω dependence for brevity):

$$S_0(\mathbf{r},\mathbf{k},0) = \mathrm{A_x}\mathrm{B_{xx}}\frac{\pi}{\Lambda_{\mathrm{xx}}}\exp\left[-\left(\frac{\mathbf{r}^2}{2\sigma_\mathrm{x}^2}+\frac{\mathbf{k}^2}{4\Lambda_{\mathrm{xx}}}\right)\right] + \mathrm{A_y}\mathrm{B_{yy}}\frac{\pi}{\Lambda_{\mathrm{yy}}}\exp\left[-\left(\frac{\mathbf{r}^2}{2\sigma_\mathrm{y}^2}+\frac{\mathbf{k}^2}{4\Lambda_{\mathrm{yy}}}\right)\right], \tag{13}$$

$$S_1(\mathbf{r},\mathbf{k},0) = \mathrm{A_x}\mathrm{B_{xx}}\frac{\pi}{\Lambda_{\mathrm{xx}}}\exp\left[-\left(\frac{\mathbf{r}^2}{2\sigma_\mathrm{x}^2}+\frac{\mathbf{k}^2}{4\Lambda_{\mathrm{xx}}}\right)\right] - \mathrm{A_y}\mathrm{B_{yy}}\frac{\pi}{\Lambda_{\mathrm{yy}}}\exp\left[-\left(\frac{\mathbf{r}^2}{2\sigma_\mathrm{y}^2}+\frac{\mathbf{k}^2}{4\Lambda_{\mathrm{yy}}}\right)\right], \tag{14}$$

$$S_2(\mathbf{r},\mathbf{k},0) = \left(\mathrm{A_xA_y}\right)^{1/2}\mathrm{B_{xy}}\frac{\pi}{\Lambda_{\mathrm{xy}}}\exp\left[-\left(\frac{\mathbf{r}^2}{\Omega_{\mathrm{xy}}}+\frac{2\mathrm{i}}{4\Lambda_{\mathrm{xy}}}\left(\frac{1}{4\sigma_\mathrm{y}^2}-\frac{1}{4\sigma_\mathrm{x}^2}\right)\mathbf{r}\cdot\mathbf{k}+\frac{\mathbf{k}^2}{4\Lambda_{\mathrm{xy}}}\right)\right] + \left(\mathrm{A_xA_y}\right)^{1/2}\mathrm{B_{yx}}\frac{\pi}{\Lambda_{\mathrm{yx}}}\exp\left[-\left(\frac{\mathbf{r}^2}{\Omega_{\mathrm{yx}}}+\frac{2\mathrm{i}}{4\Lambda_{\mathrm{yx}}}\left(\frac{1}{4\sigma_\mathrm{x}^2}-\frac{1}{4\sigma_\mathrm{y}^2}\right)\mathbf{r}\cdot\mathbf{k}+\frac{\mathbf{k}^2}{4\Lambda_{\mathrm{yx}}}\right)\right], \tag{15}$$

$$S_3(\mathbf{r},\mathbf{k},0) = \mathrm{i}\left[\left(\mathrm{A_xA_y}\right)^{1/2}\mathrm{B_{yx}}\frac{\pi}{\Lambda_{\mathrm{yx}}}\exp\left[-\left(\frac{\mathbf{r}^2}{\Omega_{\mathrm{yx}}}+\frac{2\mathrm{i}}{4\Lambda_{\mathrm{yx}}}\left(\frac{1}{4\sigma_\mathrm{x}^2}-\frac{1}{4\sigma_\mathrm{y}^2}\right)\mathbf{r}\cdot\mathbf{k}+\frac{\mathbf{k}^2}{4\Lambda_{\mathrm{yx}}}\right)\right] - \left(\mathrm{A_xA_y}\right)^{1/2}\mathrm{B_{xy}}\frac{\pi}{\Lambda_{\mathrm{xy}}}\exp\left[-\left(\frac{\mathbf{r}^2}{\Omega_{\mathrm{xy}}}+\frac{2\mathrm{i}}{4\Lambda_{\mathrm{xy}}}\left(c-\frac{1}{4\sigma_\mathrm{x}^2}\right)\mathbf{r}\cdot\mathbf{k}+\frac{\mathbf{k}^2}{4\Lambda_{\mathrm{xy}}}\right)\right]\right], \tag{16}$$

where Λ_{ij} and Ω_{ij} are

$$\Lambda_{\mathrm{ij}} = \frac{1}{16\sigma_\mathrm{i}^2}+\frac{1}{16\sigma_\mathrm{j}^2}+\frac{1}{2\delta_\mathrm{ij}^2}, \tag{17}$$

$$\frac{1}{\Omega_{ij}} = \frac{1}{4\sigma_i^2} + \frac{1}{4\sigma_j^2} - \left[\frac{1}{(4\sigma_i^2)^2} + \frac{1}{(4\sigma_j^2)^2} - \frac{1}{8\sigma_i^2\sigma_j^2}\right]\frac{1}{4\Lambda_{ij}}, \quad (18)$$

We note that, for isotropic ($\sigma_i = \sigma_j = \sigma$) Gaussian Schell-model beams our Equations [13-18] simplify to Equations [14-18] of refence [13].

This allows one to investigate the evolution of the generalized phase space Stokes vector $S_l(\mathbf{r}, \mathbf{k}, z, \omega)$ through out free space. We believe such methodologies developed for phase space in the optical coherence theory can be adopted to investigate the change of the statistical states of light beams in free space and atmospheric scenarios.

The study of the phase space characteristics of random electromagnetic beams is quite widespread recently. The statistical condition of an electromagnetic beam has long been satisfactorily described using the standard Stokes parameters. When used to characterize both the coherence and the polarization characteristics of electromagnetic fields, recently proposed generalized phase space Stokes parameters, which are thought of as a two-direction extension of the typical Stokes parameters, can be written in terms of the correlations between electric field components at two directions. The acquired results make it easier to handle the phase space transformation's propagation behavior.

3. THE RESEARCH FINDINGS AND RESULTS

We first notice that Equations [15]-[16] are different than Equations [13]-[14] in the sense that there is an additional phase introduced. And they are different from the parameters obtained in [13] for isotropic Gaussian-Schell model beams. A similar case is seen in the complex Gaussian representation of partially coherent sources on propagation [17]. Second, this is not the case in the configuration space, i.e.

$$S_0(\mathbf{r}_1, \mathbf{r}_2, \omega) = W_{xx}(\mathbf{r}_1, \mathbf{r}_2, \omega) + W_{yy}(\mathbf{r}_1, \mathbf{r}_2, \omega), \quad (20)$$

$$S_1(\mathbf{r}_1, \mathbf{r}_2, \omega) = W_{xx}(\mathbf{r}_1, \mathbf{r}_2, \omega) - W_{yy}(\mathbf{r}_1, \mathbf{r}_2, \omega), \quad (21)$$

$$S_2(\mathbf{r}_1, \mathbf{r}_2, \omega) = W_{xy}(\mathbf{r}_1, \mathbf{r}_2, \omega) + W_{yx}(\mathbf{r}_1, \mathbf{r}_2, \omega), \quad (22)$$

$$S_3(\mathbf{r}_1, \mathbf{r}_2, \omega) = i\left[W_{yx}(\mathbf{r}_1, \mathbf{r}_2, \omega) - W_{xy}(\mathbf{r}_1, \mathbf{r}_2, \omega)\right], \quad (23)$$

are all having the same functional forms (form of Equation [12] in this case) and same scalings [12]. Thirdly, Equations [15]-[16] have modified variances across the position vector r only, which is to say the position variance is rescaled. As a fourth notice, this rescaled variance has the imprint of the correlations δij. To compare $S_0(\mathbf{r}, \mathbf{k}, 0)$and $S_2(\mathbf{r}, \mathbf{k}, 0)$, we plot Equation [13] and Equation [15] in Figure 1.

Since S_1 and S_3have the similar results their figuration is not presented for brevity. In the passage from Figure 1 (a) to Figure 1 (b) we see that the variance changes in **r** dimension. This is not very well pronounced in S_2 and S_3 which is because S_2 and S_3 are more symmetric in variances comparing to S_0 and S_1. In the analysis of the parts of Figure 1 we see that there is a rise in the variance with respect to the increment of anisotropy ratio α. In the numerical calculations it is worth mentioning that the phase space Stokes parameters might take negative values, since the Wigner functions are purely real, but they are not always positive [18]. The reason of the asymmetry between

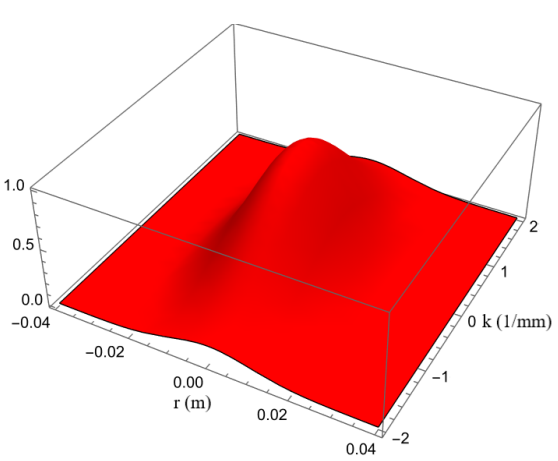

(a) S_0 for $\alpha = 1$.

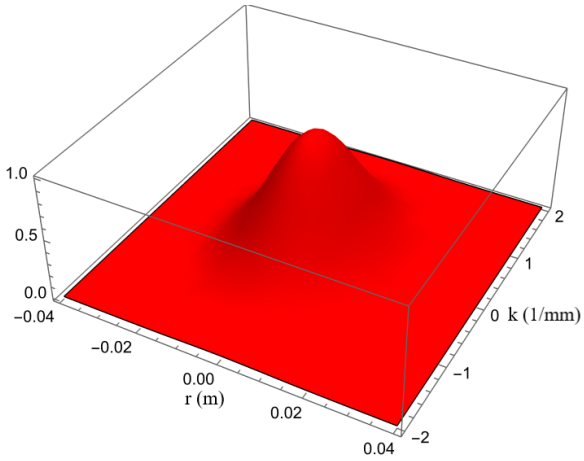

(b) S_2 for $\alpha = 1$.

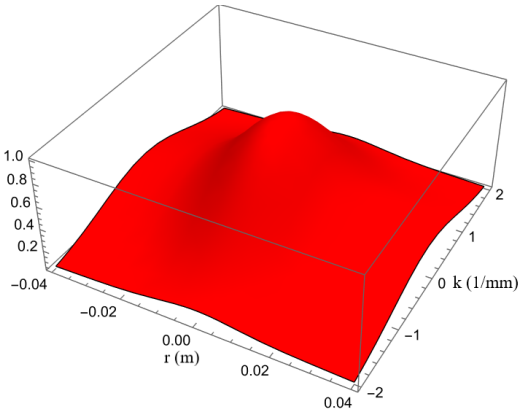

(c) S_0 for $\alpha = 4$.

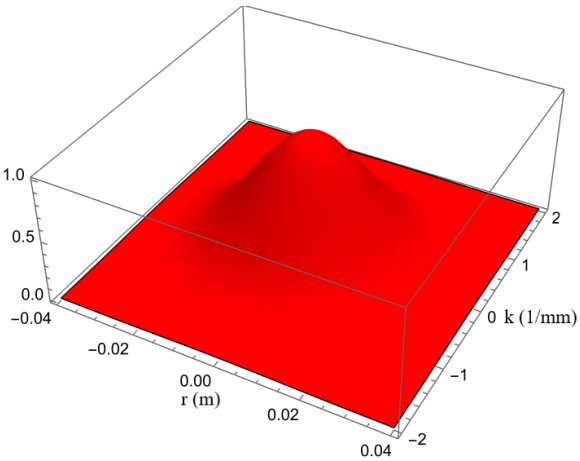

(d) S_2 for $\alpha = 4$.

Figure 1 Changes in the generalized phase space Stokes parameters S_0 and S_2, calculated from Equation 14 and Equation 16, of anisotropic electromagnetic Gaussian Schell-model beams. The parameters are taken as: $A_x = A_y = 1$, $B_{xx} = B_{yy} = 1$, $B_{yx} = B_{xy} = 0.8$, $\theta = 0$, $\sigma_y = 1$ mm, $\sigma_x = \alpha\sigma_y$, $\delta_{xx} = \delta_{yy} = 1$ mm, $\delta_{xy} = \delta_{yx} = 1.5$ mm.

Equations [13]-[14] and Equations [15]-[16] is; we now introduced an anisotropy in the kernel (shifted electric correlation matrix) of Wigner transform which causes a phase and a rescaling in the cross terms F_{xy}, F_{yx} and so in S_2, S_3. Lastly, note that the coherence widths along x and y directions are taken as equal in this study, they can be taken differently as well and would be a place of another study. In such a case, we would expect an extra variance scalings on the direction of seperate fields.

4. DISCUSSION

With the help of derived analytics we have studied the spectral changes of anisotropic Gaussian Schell-model sources in generalized phase space Stokes parameters. On comparing Figure 1 (a) and Figure 1 (c) we see that the effect of anisotropy ratio on S_0 is more noticeable, however the comparison of Figure 1 (b) and 1 (d) shows us that the effect of anisotropy ratio on S_2 is dim. The main comparison, i.e., Figure 1 (a) vs Figure 1 (b), shows a profound change because of the phase and the variance in the obtained generalized phase space Stokes parameters. Therefore, the results demonstrate that the changes in the statistical properties can be influenced by the phase space transform.

Consideration of the complete statistics, i.e. amplitude, phase and polarization, is necessary for full field description of the light field. This is because the first Stokes

parameter, S_0, is a measure of the total intensity of the light incident on the detectors. The second and third Stokes parameters, S_1 and S_2, provide information about the linear polarization state of the incident light. The fourth Stokes parameter, S_3, provides information about the circular polarization state of the incident light.

5. CONCLUSION

In this paper, generalized phase space Stokes parameters of anisotropic Gaussian Schell-model sources are derived. Effect of the anisotropy ratio α is plotted and analyzed. The Wigner transform results in different ways in the four Stokes parameters because of the shift in the transform. Based on the formulas obtained we see that the anisotropy of the source causes a modified variance in the last two Stokes parameters. The calculations show that the variance changes in r dimension in the Stokes parameters S_2 and S_3. And also, we have found that the modified variance has the imprint of correlations. Some areas of interest where this theory can be efficiently used are partially coherent imaging systems [3], optical heterodyne imaging [19], and tomography [20].

Funding
The author (s) has no received any financial support for the research, authorship or publication of this study.

The Declaration of Conflict of Interest/ Common Interest
No conflict of interest or common interest has been declared by the authors.

The Declaration of Ethics Committee Approval
This study does not require ethics committee permission or any special permission.

The Declaration of Research and Publication Ethics
The authors of the paper declare that they comply with the scientific, ethical and quotation rules of SAUJS in all processes of the paper and that they do not make any falsification on the data collected. In addition, they declare that Sakarya University Journal of Science and its editorial board have no responsibility for any ethical violations that may be encountered, and that this study has not been evaluated in any academic publication environment other than Sakarya University Journal of Science.

REFERENCES

[1] E. Wigner, "On the quantum correction for thermodynamic equilibrium," Physical Review, vol. 40, no. 5, pp. 749-759, 1932.

[2] M. J. Bastiaans, "Application of the Wigner distribution function to partially coherent light," Journal of the Optical Society of America A, vol. 3, no. 8, pp. 1227-1238, 1986.

[3] S. B. Mehta, C. J. R. Sheppard, "Partially coherent microscope in phase space," Journal of the Optical Society of America. A, Optics, image science, and vision, vol. 35, no. 8, pp. 1272-1282, 2018.

[4] D. Dragoman, "Applications of the Wigner distribution function in signal processing," EURASIP Journal on Advances in Signal Processing, vol. 10, pp. 1520–1534, 2005.

[5] D. Mendlovic, Z. Zalevsky, H. M. Ozaktas, "Wigner-related phase spaces for signal processing and their optical implementation," Journal of the Optical Society of America A; vol. 17, no. 12, pp. 2339-2354, 2000.

[6] D. Mendlovic, H. M. Ozaktas, A. W. Lohmann, "Graded-index fibers, Wigner-distribution functions, and the fractional Fourier transform," Applied Optics, vol. 33, no. 26, pp. 6188-6193, 1994.

[7] K. A. Sharma, T. G. Brown, M. A. Alonso, "Phase-space approach to lensless measurements of optical field correlations," Optics Express, vol. 24, no. 14, pp. 16099-16110, 2016.

[8] A. Walther, "Radiometry and coherence," Journal of the Optical Society of America, vol. 58, no. 9, pp. 1256-1259, 1968.

[9] S. Sahin, M. Zhang, Y. Chen, Y. Cai, "Transmission of a polychromatic electromagnetic multi-Gaussian Schellmodel beam in an inhomogeneous gradient-index fiber," Journal of the Optical Society of America A, vol. 35, no. 9, pp. 1604-1611, 2018.

[10] O. Korotkova, L. C. Andrews, R. L. Phillips, "Model for a partially coherent Gaussian beam in atmospheric turbulence with application in Lasercom," Optical Engineering, vol. 43, no. 2, pp. 330-341, 2004.

[11] J. C. Ricklin, F. M. Davidson, "Atmospheric turbulence effects on a partially coherent Gaussian beam: implications for free-space laser communication," Journal of the Optical Society of America A, vol. 19, no. 9, pp. 1794-1802, 2002.

[12] E. Wolf, "Introduction to the Theory of Coherence and Polarization of Light," 1st. Edition, Cambridge, UK: Cambridge University Press, 2007.

[13] S. Sahin, "Generalized Stokes parameters in phase space," Optics Letters, vol. 35, no. 10, pp. 1704-1706, 2010.

[14] S. Cho, J. C. Petruccelli, M. A. Alonso, "Wigner functions for paraxial and nonparaxial fields," Journal of Modern Optics, vol. 56, no. 17, pp. 1843-1852, 2009.

[15] M. Testorf, B. Hennelly, J. Ojeda-Castaneda, "Phase-Space Optics: Fundamentals and Applications," 1st. Edition, New York, US: The McGraw-Hill companies, 2010.

[16] F. Gori, M. Santarsiero, R. Borghi, V. Ramirez-Sanchez, "Realizability condition for electromagnetic Schell-model sources," Journal of the Optical Society of America A, vol. 25, no. 5, pp. 1016-1021, 2008.

[17] H. Mao, Y. Chen, C. Liang, L. Chen, Y. Cai, S. A. Ponomarenko, "Self-steering partially coherent vector beams," Optics Express; vol. 27, no. 10, pp. 14353-14368, 2019.

[18] T. Ari, A. T. Friberg, "Phase-space methods for partially coherent wavefields," in AIP Conference Proceedings, Ensenada, Mexico, 1980, pp. 313-331.

[19] A. Wax, J. E. Thomas, "Optical heterodyne imaging and Wigner phase space distributions," Optics Letters, vol. 21, no. 18, pp. 1427-1429, 1996.

[20] A. C´amara, J. A. Rodrigo, T. Alieva, "Optical coherenscopy based on phase-space tomography," Optics Express, vol. 21, no. 11, 13169-13183, 2013.

SAKARYA ÜNİVERSİTESİ
FEN BİLİMLERİ ENSTİTÜSÜ DERGİSİ

Sakarya University Journal of Science
SAUJS

ISSN 1301-4048 e-ISSN 2147-835X Period Bimonthly Founded 1997 Publisher Sakarya University
http://www.saujs.sakarya.edu.tr/

Title: Tailoring the Porosity and Breathability of Nanofiber Webs with Mesh Size of the Deposition Material

Authors: Çiğdem AKDUMAN, Nida OĞLAKÇIOĞLU

Recieved: 2023-02-22 00:00:00

Accepted: 2023-04-03 00:00:00

Article Type: Research Article

Volume: 27
Issue: 3
Month: June
Year: 2023
Pages: 687-696

How to cite
Çiğdem AKDUMAN, Nida OĞLAKÇIOĞLU; (2023), Tailoring the Porosity and Breathability of Nanofiber Webs with Mesh Size of the Deposition Material. Sakarya University Journal of Science, 27(3), 687-696, DOI: 10.16984/saufenbilder.1254690
Access link
https://dergipark.org.tr/en/pub/saufenbilder/issue/78131/1254690

Sakarya University Journal of Science 27(3), 687-696, 2023

Tailoring the Porosity and Breathability of Nanofiber Webs with Mesh size of the Deposition Material

Cigdem AKDUMAN *[1], Nida OĞLAKCIOĞLU[2]

Abstract

Nano and micro-pores of the electrospun webs present good moisture vapor transmission rate, while it maintains resistance to pressured air and resistance to liquid for some type of clothing. Laminating a nanofiber web to any textile structure could improve the desired resistance to air permeability with providing excellent breathability. In the present study, hydrophobic thermoplastic polyurethane (TPU) and hydrophilic poly (vinyl alcohol) (PVA) nanofiber webs were produced onto three different chromium sieve wires and then laminated to an interlining fabric and compared in means of pore size, breathability, and air permeability. Mesh count of the wires affected the pore size and smallest pore size are belong to 90 mesh wire. The water vapor permeability of the samples varied between 80% and 90% as well as providing relatively low air permeability values. With increasing nanofiber amount, air permeability decreased dramatically.

Keywords: Nanofibers, mesh count, porosity, water vapor permeability, air permeability

1. INTRODUCTION

Nanofibers are the fibers with diameters in the nanometer range and could be produced from different polymer with various additives. Thus, they have different physical and chemical properties, along with diverse application potentials [1-3]. Electrospinning is the mainly used method to generate nanofibers because of the easy and plain setup, the ability to produce continuous nanofibers from polymers, and the capability to generate nanofibers with controllable diameters, compositions, and orientations [4]. In an electrospinning setup, a static or a moving collector is made of conductive material which is electrically grounded are used for fiber deposition [5]. Thus, a stable potential difference between the source and the deposition area (collector) is achieved. With different collector designs various fiber patterns could be achieved [6]. The porosity and the character of the collector have an effect on the deposited fibers. Nanofiber membrane that are collected onto porous collector such as paper and metal mesh had a lower packing density than smooth surfaces such as aluminum foil. There is faster evaporation of residual fibers at a porous

* Corresponding author: cakduman@pau.edu.tr (C. AKDUMAN)
[1] Pamukkale University
[2] Ege University
E-mail: nida.gulsevin@ege.edu.tr
ORCID: https://orcid.org/0000-0002-6379-6697, https://orcid.org/0000-0002-5085-7606

target, due to higher surface area while smooth surfaces may cause an accumulation of solvents around the fibers because of slow evaporation rate [7]. Liu et al selected copper mesh, aluminum foil and water, and paper as target materials. Fibers collected on paper showed smooth surfaces and few defects, fibers on water are more densely packed. On a nonconductive collector, the presence of electrostatic charges caused fibers to repel each other and gave a more loosely packed fibrous network. The packing density of fibers determines the overall porosity of the fibrous membranes. They observed that fiber packing was much less dense when collected on porous targets, such as paper and copper mesh, than on water and aluminum foil due to the differential diffusion and evaporation of solvents from nanofibers [8]. Sattary et al. used a flat plate and a novel rotating disc collector. Both a rotating disc and disc rotation speed affected fiber morphology and pore size. Due to the special geometry of the disc collector, which exposed the charged fibers in sediment, high-density nanofibers were collected on the copper wires, while low-density nanofibers were collected between them [9]. Wang et al. used a stainless-steel mesh with a wire diameter of 0.254 mm, and a wire spacing of 0.381 mm as a template collector for electrospun nanofibers. Produced Polycaprolactone (PCL) nanofiber meshes showed similar topological structures to the mesh collector. When compared with the randomly arranged electrospun nanofiber mats, this PCL nanofiber meshes with tailored architectures and patterns exhibited improved tensile strength with tensile modulus [10].

Electrospun nanofiber webs show controllable high porous character with high interconnectivity [11]. These nano and micro-pores of the electrospun webs provide good moisture vapor transmission rate, while it maintains resistance to pressured air and resistance to liquid for some type of clothing [12]. On the other hand, several conventional microporous membranes are already used for this purpose. Nevertheless, nanofiber webs show the advantage of better breathability, controllable air permeability, possibility to functionalization.

Although, conventional waterproof and breathable fabric structures include high-density woven fabrics, coated and laminated fabrics [13], the potential of using electrospun nanofibrous webs for waterproof, breathable, wind resistant textile application has been widely investigated. Yoon and Lee developed layered fabric structures by laminating mass produced electrospun polyurethane nanofiber webs that have a web density of 5.2 g/ m^2, to different substrates and produced layered structure, then investigated the breathability and waterproof characteristics [14] Sumin et al measured the water transfer properties of waterproofness and vapor permeability as well as the thermal transfer properties of warm/cool feeling and thermal conductivity of laminated nanofibers before and after laundering [15].

Gibson et al. pioneered using nanofibers in application of protective clothing. They produced polyurethane electrospun nanofibers for protective clothing and compared them with a wind-proof breathable membrane, ie, Goretex™ [16]. Gorji et al. produced polyurethane and poly (2-acryloylamido-2-methylpropanesulfonic acid)-graphene oxide nanofibers for protective clothing. They evaluated the nanofibrous membrane performance with their tensile strength, water vapor permeability, and contact angle and developed a dual-mode behavior on two opposite faces [17]. Sadighzadeh et al. studied waterproof-breathable fabric development by applying electrospun polyurethane, polyacrylonitrile, and polyethersulfone directly onto the substrate fabric. They compared the air permeability, water vapor transport rate, and resistance to water penetration for produced membranes with Goretex [18]. Oglakcioglu et al. used nanofibers to overcome the low air resistance of conventional weft knitted fabrics to develop windoproof textile surfaces even

open structures are in case. Thermoplastic nanofibers laminated between two single jersey fabrics and the effect of the nanofiber amount on the air resistance performance and breathability of the multilayered structure were investigated [12].

Air permeability is defined as the rate of airflow passing perpendicularly through a known area under a prescribed air pressure differential between the two surfaces of a material. Since a pressurized air is used in measurement, small pores of nanofibers can block the air but still allow water vapour to diffuse for breathability. So, body can still transfer the sweat from skin to environment while protecting from wind and prevent heat loss. Producing nanofibers directly onto a textile material or a deposition material are the options for combining nanofibers with textiles. When electrospinning is directly carried out onto textiles, a glue or a binder should be applicated prior to electrospinning process, then an additional layer may be laminated over nanofiber coated material. In case of using a deposition material such as mass production of standard membrane production, a silicone applied paper, or a similar material could be used as a carrier since nanofiber membranes are more fragile than conventional membranes. Then these membranes could be transferred and laminated to a textile material. Since deposition material has a significant effect on the porosity character of the nanofiber membrane, present study investigates the mesh size effect of the deposition material for mass production methods and aims to tailor the breathability.

Polyurethanes have been widely used to produce smart membranes because of several desirable properties, such as prominent elasticity, good abrasive resistance, and excellent hydrolytic stability [13]. Poly (vinyl alcohol) (PVA) nanofibers have diverse application areas when they are crosslinked [18-22].

In present study, hydrophobic thermoplastic polyurethane (TPU) and hydrophilic PVA nanofiber webs were produced onto three different chromium sieve wires with 90, 40 and 20 mesh and then, nanofiber webs were transferred to a knitted interlining in order to analyze the effect of mesh count on the pore sizes. Besides, for comparing the effect of nanofiber amount, nanofibers were produced with different deposition times ranging from 1 hour to 10 hours onto 90 mesh wire sieves. Nanofiber transferred interlinings' water vapor and air permeability were determined for both a hydrophobic and a hydrophilic structure.

2. MATERIAL AND METHOD

In this study commercial Pellethane 2103-80AE (Velox (Lubrizol Advanced Materials) was used as TPU Polymer. It was based on 4,4-methylene bisphenylene isocyanate, polytetramethyleneoxide and 1,4 butanediol. For hydrobhobic polymer PVA was supplied with average molecular weight of ~125,000 g/mol. A polycarboxylic acid 1,2,3,4 butanetetracarboxylic acid (BTCA), and it cataysyst sodium hypophosphite monohydrate ($NaPO_2H_2.H_2O$) were used for crosslinking. Dimethylformamide (DMF) was used as solvent for TPU and was supplied from Sigma Aldrich Chemical Company. Chromium wire sieves were used as deposition material. 90, 40 and 20 mesh sieves were purchased from Akyol Sanayi Malzemeleri. Vilene AP08 (Freudenberg), 100% polyester (PES) interlining was received from Gamateks.

TPU solutions were prepared by dissolving 10% (w/w) of TPU granulates in DMF. PVA solutions were prepared by dissolving again 10% (w/w) PVA powder in distilled water at 100°C. BTCA as crosslinking agent, was added to the PVA solutions in the ratio of 10% ($w/w_{polymer}$) with sodium hypophosphite monohydrate as catalyst in ratio of 2:1 (w/w) PVA solutions were further stirred for 10-15 min.

TPU and PVA solutions were electrospun at a voltage of 13 kV and 18 kV respectively and a tip-to-collector distance of 18 cm with a feeding rate of 0.5 ml/h were used. Rotating metal drum collector covered by chromium wire sieve and was grounded to achieve negative potential in order to travel nanofibers to the depostion area. Produced TPU and PVA nanofibers were coded with their collection sieve and period and given in Table 1. For PVA nanofibers different fixation methods can be used [23]. In this study a polycarboxylic acid, BTCA was used, thus after electrospinning, PVA nanofibers were heat set at 130ºC for 20 min in an oven to enhance the crosslinking reaction. Each nanofiber web was transferred onto PES interlining by a heat transfer machine to simulate combining these layers with textiles.

Table 1 Collection parameters and coding of TPU and PVA nanofibers

Parameters	***TPU Coding***	***PVA Coding***
1h collection onto 90 mesh	TPU1	PVA1
3h collection onto 90 mesh	TPU2	PVA2
5h collection onto 90 mesh	TPU3	PVA3
10h collection onto 90 mesh	TPU4	PVA4
5h collection onto 40 mesh	TPU5	PVA5
5h collection onto 20 mesh	TPU6	PVA6

In order to characterize the surface morphology of TPU and PVA nanofibers scanning electron microscopy (SEM, FEI Quanta 250FEG) images were taken. A thin film of gold was coated onto the nanıfibers. EMITECH K550X ion sputtering device was used for coating.

Air permeability measurement was carried out according to EN ISO 9237 with FX3300 (Textest, Switzerland). 5 cm^2 measurement area and 200 Pa pressure drop were used for the measurement. It is the rate of air flow passing through a known area under a prescribed air pressure differential between the two surfaces [24]. The air is drawn through the specimen into a closed chamber and out through an orifice that measures the flow.

Water vapor permeability measurements were carried out of Permetest (Sensora Company, Liberec, Czech Republic) in accordance with ISO 11092. The instrument works according to the principle of heat flux sensing. The temperature of the measuring head is kept at room temperature for isothermal conditions. Some heat is lost after the water flows into the measuring head. This instrument measures the heat loss from the measuring head due to the evaporation of water in bare state (without a sample) and covered with sample [25, 26].

Relative water vapour permeability of the textile sample P_{wv} determined from the equation (1):

$$P_{wv}\ [\%] = 100\ U_s / U_o \quad (1)$$

Here, U_s means the instrument reading without a sample (heat loses of the free wet surface), and U_s presents the heat loses of the wet measuring head (skin model) with a sample [27].

3. RESULTS AND DISCUSSION

In Figure 1 and Figure 2, the representative SEM images with two magnifications were given. Bead free smooth TPU and PVA nanofibers were electrospinned. Fiber diameter of TPU and PVA nanofibers were measured as 966 nm and 320 nm, respectively. Mesh structure of the wire sieve could be better seen at TPU nanofibers. Since PVA nanofibers were thinner, mesh structure disappeared at longer collections.

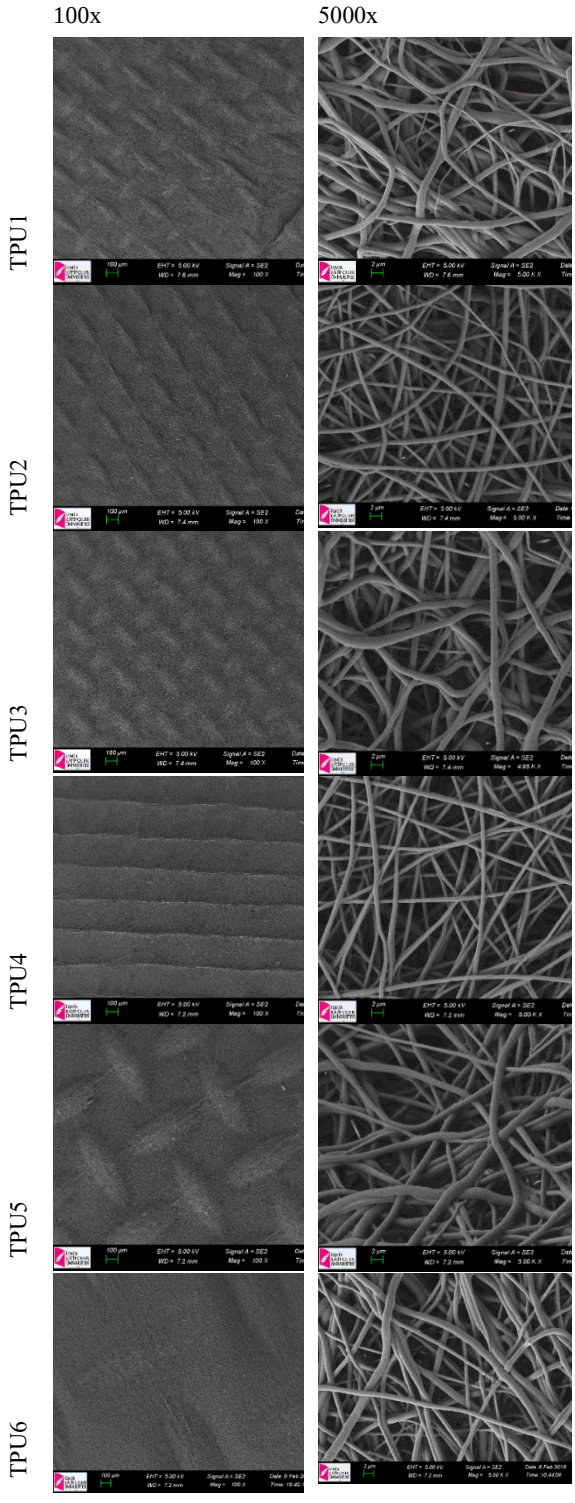

Figure 1 SEM images TPU nanofibers with 100x and 5000x magnification

The pores of the nanofiber membranes are caused by the entanglement of the nanofibers. When nanofiber diameter is constant, more nanofiber covering a specific area would result in narrower pore size distribution along with smaller pores [28]. Thus, with increasing collection period mean flow pore size (MFP) of TPU nanofiber decreased to 2.28 from 3.45µm (Table 2). Sparse mesh resulted in 3.09 µm of MFP for 20 mesh, 2.78 for 40 mesh and 2.69 for 90 mesh for same amount of nanofiber. For PVA nanofibers, due to thinner nanofiber diameter, all PVA webs had smaller pore sizes. Similar to TPU nanofibers, with increasing collection period MFP of PVA nanofiber webs decreased to 1.06 from 1.85 µm. MFP of PVA nanofibers was 1.73 for 20 mesh, 1.56 for 40 mesh and 1.44 µm for 90 mesh. That showed pore size of the nanofibers could be controlled with mesh count of deposition material.

Table 2 Pore size of TPU and PVA nanofiber webs

Nanofibers	***Biggest Bubble Point (µm)***	***Mean Flow Pore Size (µm)***	***Smallest Pore Size (µm)***
TPU1	6.67	3.45	2.43
TPU2	6.32	2.89	1.65
TPU3	4.82	2.69	1.87
TPU4	4.82	2.28	1.71
TPU5	6.03	2.78	1.69
TPU6	6.51	3.09	1.74
PVA1	2.72	1.85	1.51
PVA2	2.05	1.60	1.30
PVA3	2.22	1.44	1.44
PVA4	1.90	1.06	0.64
PVA5	2.08	1.56	1.40
PVA6	2.35	1.73	1.16

Understanding of the relation between mesh structure of the deposition material and transport properties of electrospun nanofibrous membrane will help to design tailored comfortable nanofiber laminated fabrics. Figure 3 and 4. present the water vapor and air permeability of nanofiber samples.

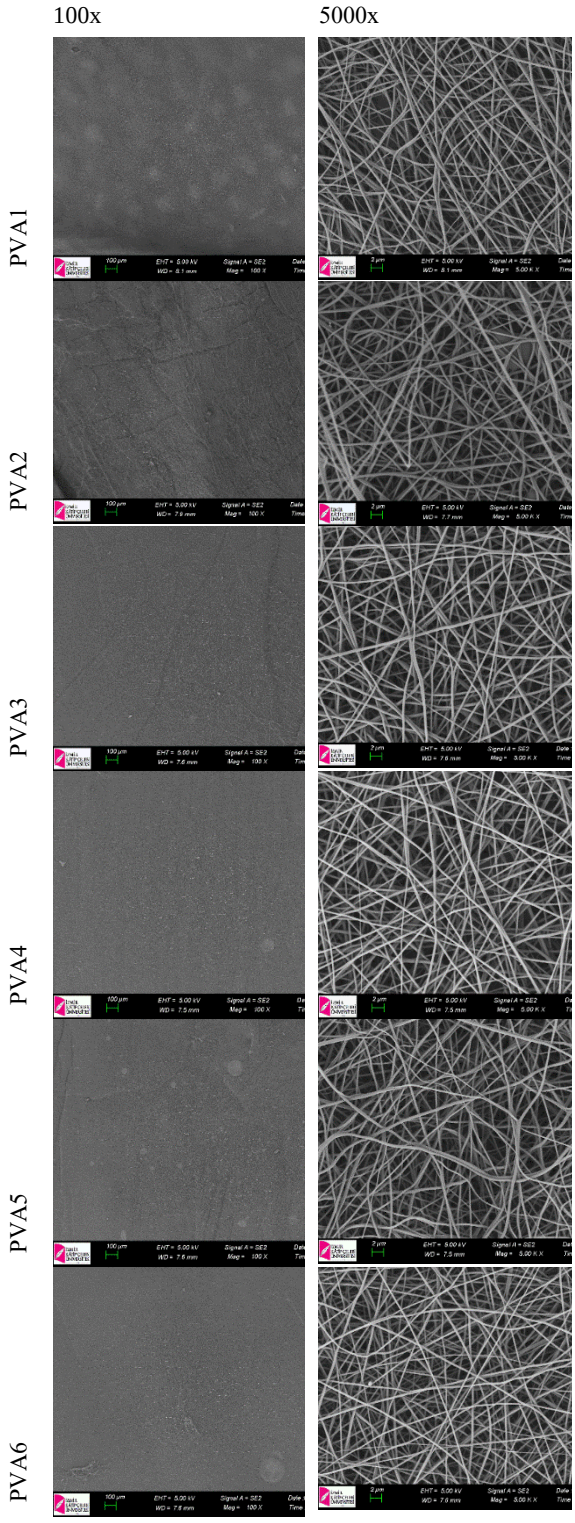

Figure 2 SEM images PVA nanofibers with 100x and 5000x magnification

Similar to the study of Gibson et al., this interconnected nanofiber webs present minimum resistance to moisture vapor diffusion [29]. The water vapor permeability of the TPU and PVA nanofiber webs varied between 80% and 90% as well as providing relatively high air resistance values. It was observed that the mesh count and different nanofiber amount caused by different deposition time significantly changed the permeability properties and it is possible to achieve good breathable structures with different air permeability characteristics. Water vapor permeability values were not much affected from the hydrophilic or hydrophobic character of the polymer, because both 1 h collected nanofibers water vapor permeability values are about 90%. Even the densest coatings of 10 h collections showed 81.1 and 82.9% for TPU and PVA nanofibers, respectively. Highly porous structure allowed water vapor passing through the nanofiber membranes. These results indicate that not only the nanofiber diameter, but deposition material mesh structure/design may also contribute to the porosity of the final composite material, and hence, the water vapor transport performance of the material.

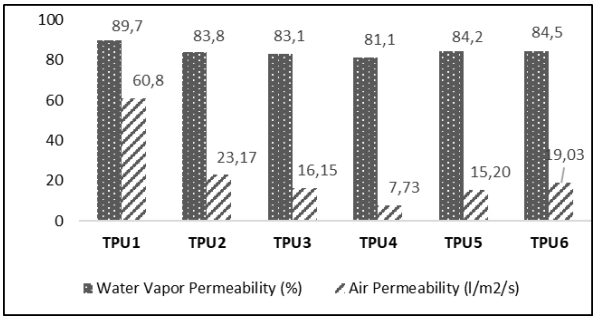

Figure 3 Water vapor and air permeability results of TPU nanofibers

In case of air permeability, significant difference could be seen at minimum amount of nanofiber (1h collection), thinner TPU nanofiber web had the highest air permeability value. Since the pore size of the TPU nanofiber membrane had the biggest (3.45 μm) MFP, it allowed higher pressured air penetration. On the other hand, with finer PVA nanofibers 1h collection onto 90 mesh, air permeability was about half of the TPU nanofiber web as 29.07 l/m2/s and it was close to the 5 h collection onto 20 mesh. Since the difference of the pore size was more significant at TPU nanofibers because of the thicker nanofiber diameter, the air

permeability results showed significant differences. It was seen that the air permeability properties of the nanofiber webs could be controlled by the character of the deposition material and finer nanofibers were much affected from the character of deposition material. Air permeability of the PVA nanofibers which were collected for 5 hours onto 90 mesh was 10.11 and 25.6 l/m2/s for 20 mesh, while they were 16.15 and 19.03 l/m2/s for TPU nanofibers. Besides, finer PVA nanofibers of 1h collection onto 90 mesh was similar to the 5 h collection onto 20 mesh.

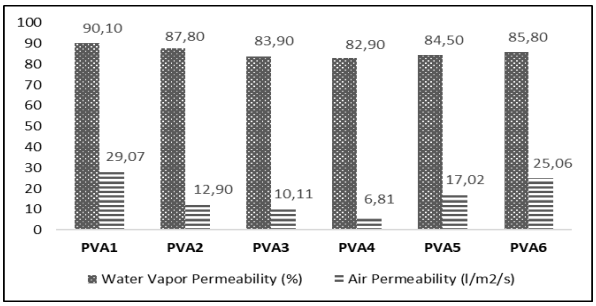

Figure 4 Water vapor and air permeability results of PVA nanofibers

4. CONCLUSIONS

Electrospun nanofiber webs have high porous character with nano and micro-pores. These nano and micro-pores of the electrospun webs provide good moisture vapor transmission rate, while it maintains resistance to pressured air and resistance to liquid for some type of clothing and may be controlled with the feature of the collector.

When stainless steel wire meshes were used as a deposition material, by changing the mesh count, it is possible to modify the porosity of the produced nanofiber membrane.

After the production of nanofibers onto a deposition material, common mass production practice is transferring it onto a textile material for waterproof and breathable fabrics. In this study, TPU nanofiber webs are investigated because of its several commercial applications as hydrophobic and breathable textile membrane and compared with hydrophilic PVA nanofiber webs. Nanofibers were densely deposited on the wires and sediment to the gaps; thus, mesh structure of wire could be easily seen. However, because of the thinner nanofiber diameter of PVA nanofibers (320 nm), at longer collection periods, mesh structures disappeared. When collection period is increased at same mesh count, pore size of TPU membranes decreased to 2.28 μm. 20 mesh count resulted in largest pore size of 3.09 μm for TPU nanofibers. Since PVA nanofibers are significantly thinner than TPU nanofibers, its pore sizes are smaller. Nevertheless, the mesh count of the wires affected the pore size, and the smallest pore size belongs to 90 mesh wire.

In order to evaluate the water vapor and air permeability, the nanofiber webs are transferred onto an interlining and that also simulates lamination process and combine nanofiber web with a textile material. The water vapor permeability of the samples varied between 80% and 90% as well as providing relatively low air permeability values. Significant difference is seen at minimum amount of thicker TPU nanofiber web (1h collection), which has the highest air permeability value. With increasing nanofiber amount, air permeability decreased dramatically. In case of air permeability, finer nanofibers are much affected from the character of deposition material.

Authors' Contribution

The authors contributed equally to the study.

The Declaration of Conflict of Interest/ Common Interest

No conflict of interest or common interest has been declared by the authors.

The Declaration of Ethics Committee Approval

This study does not require ethics committee permission or any special permission.

The Declaration of Research and Publication Ethics

The authors of the paper declare that they comply with the scientific, ethical and quotation rules of SAUJS in all processes of the paper and that they do not make any falsification on the data collected. In addition, they declare that Sakarya University Journal of Science and its editorial board have no responsibility for any ethical violations that may be encountered, and that this study has not been evaluated in any academic publication environment other than Sakarya University Journal of Science.

REFERENCES

[1] T. Subbiah, G.S. Bhat, R.W. Tock, S. Parameswaran, and S. S. Ramkumar, "Electrospinning of nanofibers", Journal of Applied Polymer Ccience, vol. 96 no. 2, pp. 557-569, 2005.

[2] S. Ramakrishna, K. Fujihara, W.E. Teo, T. Yong, Z. Ma, and R. Ramaseshan, "Electrospun nanofibers: solving global issues," Materials Today, vol. 9 no. 3, pp. 40-50, 2006.

[3] Ü. Kurtan, "Carbon nanofibers fabricated from electrospun nano-sized boron oxide/polyacrylonitrile nanofibers as electrode for supercapacitors," Sakarya University Journal of Science, vol. 25 no.5, pp. 1180-1188, 2021.

[4] I. Alghoraibi, S. Alomari, "Different Methods for Nanofiber Design and Fabrication" In Handbook of Nanofibers, A. Barhoum, M. Bechelany, A. Makhlouf, Springer International Publishing, Cham, Switzerland, 2018, 1170p.

[5] W. E. Teo, and S. Ramakrishna, "A review on electrospinning design and nanofibre assemblies," Nanotechnology, vol.17, no.14, pp. 1878-184, 2006.

[6] M. A. A. De Prá, R. M. Ribeiro-do-Valle, M. Maraschin and B. Veleirinho, "Effect of collector design on the morphological properties of polycaprolactone electrospun fibers," Materials Letters, vol. 193, pp. 154-157, 2007.

[7] S. Ramakrishna, K. Fujihara, W. Teo, T. Lim, and Z. Ma, "Electrospinning Process" In An Introduction to Electrospinning and Nanofibers, World Scientific Publishing Co. Pte. Ltd., Singapore, 2005, 382p.

[8] H. Liu and Y. L. Hsieh, "Ultrafine fibrous cellulose membranes from electrospinning of cellulose acetate," Journal of Polymer Science Part B: Polymer Physics, vol.40, no.18, pp. 2119-2129, 2002.

[9] M. Sattary, M. Rafienia, M. T. Khorasani and H. Salehi, "The effect of collector type on the physical, chemical, and biological properties of polycaprolactone/gelatin/nano-hydroxyapatite electrospun scaffold," Journal of Biomedical Materials Research Part B: Applied Biomaterials, vol. 107, no.4, pp. 933-950, 2019.

[10] Y. Wang, G. Wang, L. Chen, H. Li, T. Yin, B. Wang, J.C. Lee and Q. Yu, "Electrospun nanofiber meshes with tailored architectures and patterns as potential tissue-engineering scaffolds," Biofabrication, vol. 1, no.1, 015001, 2009.

[11] C. Akduman, N. Oğlakcıoğlu, P. A. Akcakoca Kumbasar, and Sarı, B. "Investigation of thermal comfort properties of electrospun nanofiber mats," Journal of Fashion Technology and Textile Engineering, , vol.S4, no. 015, pp.1-3, 2018.

[12] N. Oğlakcıoğlu, C. Akduman, and B. Sarı, "Investigation of thermal comfort

properties of electrospun thermoplastic polyurethane fiber coated knitted fabrics for wind-resistant clothing," Polymer Engineering and Science, vol. 61, no.3, pp.669-679, 2021.

[13] J.Sheng, J. Zhao, X. Yu, L. Liu, J. Yu, and B. Ding, "Electrospun nanofibers for waterproof and breathable clothing" In Electrospinning" In Nanofabrication and Applications, pp. 543-570, B. Ding,W. Xianfeng, Y. Jianyong (Eds), Elsevier Inc., Oxford, 2019, 806p.

[14] B. Yoon and S. Lee, "Designing waterproof breathable materials based on electrospun nanofibers and assessing the performance characteristics," Fibers and Polymers, vol. 12, no.1, pp. 57-64, 2011.

[15] L. Sumin, D. Kimura, K. H. Lee, J. C. Park and I. S. Kim, "The effect of laundering on the thermal and water transfer properties of mass-produced laminated nanofiber web for use in wear," Textile Research Journal, vol. 80, no.2, pp.99-105, 2010.

[16] P. Gibson, M. Sieber, J. Bieszczad, J. Gagne, D. Fogg and J. Fan, "A Design Tool for Clothing Applications: Wind Resistant Fabric Layers and Permeable Vents," Journal of Textiles, pp.1-7, 2014.

[17] M. Gorji, M. Karimi and S. Nasheroahkam, "Electrospun PU/P (AMPS-GO) nanofibrous membrane with dual-mode hydrophobic–hydrophilic properties for protective clothing applications," Journal of Industrial Textiles, vol.47, no.6, pp.1166-1184, 2018.

[18] A. Sadighzadeh, M. Valinejad, A. Gazmeh and B. Rezaiefard, "Synthesis of polymeric electrospun nanofibers for application in waterproof-breathable fabrics," Polymer Engineering and Science, vol. 56, no.2, pp.143-149, 2016.

[19] S. Ullah, M. Hashmi, N. Hussain, A. Ullah, M. N. Sarwar, Y. Saito, S. H. Kim and I. S. Kim, "Stabilized nanofibers of polyvinyl alcohol (PVA) crosslinked by unique method for efficient removal of heavy metal ions," Journal of Water Process Engineering, vol 33, pp. 101111, 2020.

[20] A. Çay, E. P. A. Kumbasar, Z. Keskin, Ç. Akduman and A. Ş. Ürkmez, "Crosslinking of poly (vinyl alcohol) nanofibres with polycarboxylic acids: biocompatibility with human skin keratinocyte cells," Journal of Materials Science, vol. 52, no.20, pp.12098-12108, 2017.

[21] A. Cay and M. Miraftab, "Properties of electrospun poly (vinyl alcohol) hydrogel nanofibers crosslinked with 1, 2, 3, 4-butanetetracarboxylic acid," Journal of Applied Polymer Science, vol.129, no.6, pp.3140-3149, 2013.

[22] Ç. Akduman, E. P. Akçakoca Kumbasar and I. Özgüney, "Development and Characterization of Naproxen-Loaded Poly (Vinyl Alcohol) Nanofibers Crosslinked with Polycarboxylic Acids," AATCC Journal of Research, vol. 5, no.1, pp. 29-38, 2018.

[23] A. Pakolpakçil, Effect of Glutaraldehyde Crosslinking Parameters on Mechanical and Wetting Properties of PVA/NaAlg Electrospun Mat", Sakarya University Journal of Science, vol. 26, no.5, pp 990-999, 2022.

[24] A. Patanaik and R. D. Anandjiwala, "Modelling nonwovens using artificial neural networks" In Soft Computing in Textile Engineering, pp. 246-267, Woodhead Publishing, 2011.

[25] T. Vadicherla and D. Saravanan, "Thermal comfort properties of single jersey fabrics made from recycled polyester and cotton blended yarns," Indian Journal of Fibre and Textile Research, vol.42, no.3, pp.318-324, 2017.

[26] M. Boguslawska-Baczek and L. Hes, "Effective water vapour permeability of wet wool fabric and blended fabrics," Fibres and Textiles in Eastern Europe, pp. 67-71, vol. 21, no.1(97), 2013.

[27] L. Hes. Permetest Manual, SENSORA [Online] Available:http://www.sensora.eu/PermetestManual09.pdf, 31 March 2023.

[28] Y. Liu, R. Wang, H. Ma, B. S. Hsiao and B. Chu, "High-flux microfiltration filters based on electrospun polyvinylalcohol nanofibrous membranes," Polymer, vol. 54, no.2, pp.548–556, 2013.

[29] P. Gibson, H. Schreuder-Gibson and D. Rivin, "Transport properties of porous membranes based on electrospun nanofibers," Colloids and Surfaces A: Physicochemical and Engineering Aspects, vol.187, pp.469-481, 2001.

SAKARYA ÜNİVERSİTESİ
FEN BİLİMLERİ ENSTİTÜSÜ DERGİSİ

Sakarya University Journal of Science
SAUJS

ISSN 1301-4048 e-ISSN 2147-835X Period Bimonthly Founded 1997 Publisher Sakarya University
http://www.saujs.sakarya.edu.tr/

Title: Phytochemicals and Antioxidant Activities in Methanol Extracts of Endemic Haplophyllum Species From Turkey

Authors: Cennet YAMAN

Recieved: 2022-03-21 00:00:00

Accepted: 2023-04-06 00:00:00

Article Type: Research Article

Volume: 27
Issue: 3
Month: June
Year: 2023
Pages: 697-707

How to cite
Cennet YAMAN; (2023), Phytochemicals and Antioxidant Activities in Methanol Extracts of Endemic Haplophyllum Species From Turkey. Sakarya University Journal of Science, 27(3), 697-707, DOI: 10.16984/saufenbilder.1091181
Access link
https://dergipark.org.tr/en/pub/saufenbilder/issue/78131/1091181

Sakarya University Journal of Science 27(3), 697-707, 2023

Phytochemicals and Antioxidant Activities in Methanol Extracts of Endemic *Haplophyllum* Species from Türkiye

Cennet YAMAN *1

Abstract

The aim of the current study is to determine the total flavonoids, phenolics and antioxidant activities of methanol extracts from aerial parts of four endemic *Haplophyllum* species to Türkiye (*H. myrtifolium, H. vulcanicum, H. pumiliforme*, and *H. sahinii*). There are two populations collected from different regions belonging to *H. myrtifolium* and *H. pumiliforme*. Antioxidant activities were measured by radical scavenging activity such as the 2, 2′-azino-bis-3-ethylbenzothiazoline-6-sulfonic acid (ABTS) and 2, 2-diphenyl-1-picrylhydrazyl (DPPH), and compared with synthetic standards such as trolox, ascorbic acid and butylated hydroxytoluene (BHT). The highest total bioactive contents were recorded as *H. sahinii* for total phenolic content (66.4 mg GAE/g extract) and *H. myrtifolium* for total flavonoid content (40.8 mg QE/g extract), but *H. vulcanicum* displayed the lowest amount for both contents (38.0 mg GAE/g extract and 34.5 mg QE/g extract, respectively). Among the species, *H. myrtifolium* exhibited the strongest DPPH and ABTS radical scavenging activity followed by *H. pumiliforme*, *H. sahinii* and *H. vulcanicum*. All *Haplophyllum* species showed higher antioxidant activity for these two radical scavenging activities than trolox and BHT. The phytochemicals and antioxidant activities in methanol extracts from these endemic *Haplophyllum* species is reported for the first time. The diversity of the findings is to be discussed as likely consequence of the different species and regions.

Keywords: *Haplophyllum* L, phenolic, flavonoids, DPPH, ABTS

1. INTRODUCTION

Haplophyllum, belonging to Rutaceae family, herbaceous perennial and fragrant plants is a genus containing approximately 68 species, and has the most species diversity in the flora of Türkiye and Iran in terms of its spread over the world [1]. Türkiye is an important gene center for the Haplophyllum genus which is represented in the flora of Türkiye by 17 taxa belonging to 14 species with 52% endemism [2]. Recently, two new species (*Haplophyllum sahinii and H. ermenekense*) was described by Tugay and Ulukuş, Ulukuş and Tugay [3, 4], Türkiye has 18 *Haplophyllum* taxa, 11 (58%) of which are endemic. This genus taxa are foetid perennial herbs, which grows mainly on rocky hills, steppes, slopes, rocky place on limestone, especially near pine forests, or sandy soils [2].

* Corresponding author: cennet.yaman@bozok.edu.tr (C. YAMAN)
[1] Yozgat Bozok University
ORCID: https://orcid.org/ 0000-0002-2364-8171

Members of the Rutaceae family are of great economic importance, including wood, food, cosmetic and medicinal uses [5]. *Haplophyllum* species of this family are traditionally used actively in the treatment of different diseases in many countries. It is used in the treatment of malaria, rheumatoid arthritis and gynecological diseases in Saudi Arabia [6]. The herb part is used as an antispasmodic in the treatment of allergic rhinitis and gynecological diseases, asthma and respiratory distress in Sudan [7], while its leaves are used for skin infections in Oman [8]. Infusion samples of the herbal part are used to treat gynecological problems and digestive problems such as rheumatoid arthritis as well as constipation and diarrhea [9]. Moreover, *Haplophyllum* species, analyzed in previous studies, have been reported to exhibit incredible levels of biological activities including antimicrobial [10, 11], antioxidant [12, 13], anti-inflammatory [14], and especieally anti-cancer [15-17]. The potential of these activities is based on phytochemicals in the plant. Many scientists reported that various *Haplophyllum* species contained important characteristic classes of phytochemical such as phenolics, flavonoids, flavonols, coumarins, alkaloids and important compounds of lignans [4, 15, 18].

Many compound classes or compounds with high antioxidant properties are preferred for preservative and additive purposes in industries such as food, medicine, pharmacology and cosmetics. These compounds are mostly synthetic products due to their cheapness and quick availability. As a result of the researches, it was revealed that synthetic compounds have toxic and carcinogenic effects, and instead, natural products/preparations with high antioxidant activity have become popular [19, 20]. Natural products of plant origin provide alternatives to synthetic antioxidants. Therefore, natural antioxidant products have been developed from aromatic plants, spices, and fruit powder and are still being developed [21, 22].

The biosynthesis of these phytochemicals in plant and therefore their biological activities are affected by external factors such as environmental factors (soil, light intensity and climatic conditions) [23], as well as by internal factors such as the biotype and chemo-type of the plant [24], physiological and genetic aspects [25]. Therefore, it is an important first step to identify the preparation/extract or a specific compound that can be used for commercial purposes from nature.

The high pharmaceutical effects of *Haplophyllum* species suggest that there may be species with high antioxidant activity among the species. In this context, this study aims to investigate the antioxidant activities of endemic *Haplophyllum* species to Türkiye, of which there are very few studies, and to compare them with synthetic antioxidant standards. The results of this study are important in terms of the use of *Haplophyllum* species as a potential source of natural antioxidants in food and pharmaceutical products.

2. MATERIALS AND METHODS

2.1. Material

The erial parts of *Haplophyllum* species (*H. myrtifolium, H. vulcanicum, H.pumiliform*e and *H. sahinii*) respresenting a total of 40 shoots were collected according to completely randomized design at full flowering period (Figure 1). The species were identified by Prof. Dr. Osman Tugay, Faculty of Farmacy, Department of Pharmaceutical Botany, Selçuk University, Konya, Türkiye. The locations belonging to each taxon were recorded as following (Table 1).

2.2. Extraction

The dried and finely ground samples (about 4g) of the aerial parts of *Haplophyllum* species were extracted in methanol at 40°C for 24 h. The resulting solutions were filtered through whatman paper and solvent was

separated with a rotary evaporator (Heidolph, laborota 4000), and extract yields were calculated as %. Then, extracts were dissolved in methanol. Each extraction process was repeated three times.

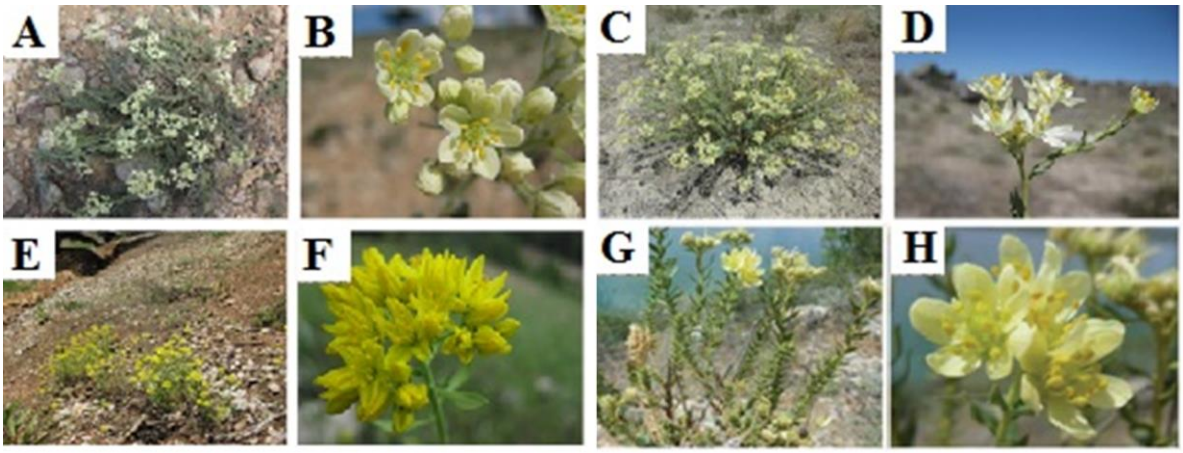

Figure 1 General view of habit and flowers of endemik *Haplophyllum* species (*H. myrtifolium* (A&B), *H. vulcanicum* (C&D), *H.pumiliforme* (E&F) and *H. sahinii* (G&H))

Table 1 Habitats of *H. myrtifolium, H. vulcanicum, H. pumiliforme* and *H. sahinii* from Türkiye

Plant Name	**Abbreviated Names**	**Hazard Category[1]**	**Altitude (m)**	**Collection Site**	**Collector Number**
Haplophyllum myrtifolium Boiss.	HM1	EN	1070	C4[2] Konya; Çumra, Apasaraycık Köyü, taşlı yerler	OT-9264-DU[3]
	HM2		1090	C4 Konya; Çumra, Apasaraycık Köyü	OT-7392-DU
Haplophyllum vulcanicum Boiss. & Heldr.	HV2	VU	1200	C4 Karaman; Karadağ	OT-9614-DU
Haplophyllum pumiliforme Hub.-Mor. & Reese	HP1	VU	1450	C3 Konya; Derebucak, Soğukoluk yolu	OT-7495-DU
	HP2		1470	C3 Konya; Derebucak	OT-7481-DU
Haplophyllum sahinii Tugay & Ulukuş	HS	EN	1090	C4 Konya; Çumra, Apasaraycık-Apa köyü, kayalık alan	OT-7410-DU

2.3. Phytochemical Contents

2.3.1. Total phenolic

Total phenolic content in the methanol extracts of *Haplophyllum* species will be measure using the Folin–Ciocalteu reagent method as described by Yaman et al. [13]. The total phenolic contents of the samples were expressed as mg gallic acid equivalent (GAE) / g extract according to the equation obtained from the standard gallic acid graph. The experiment was done in triplicates with two replicates.

2.3.2. Total flavonoid

Total flavonoid content in the methanol extracts of *Haplophyllum* species will be determine using colorimetric method as described by Yaman et al. [13]. The total flavonoid contents will be calculate from the calibration curve and express as mg quercetin equivalent (QE) / g extract according to the equation obtained from the standard quercetin graph. The experiment will be done in triplicates with two replicates.

2.4. Radical Scavenging Activity

2.4.1. DPPH free radical scavenging activity

Measurement of DPPH (2, 2-diphenyl-1-picryl-hydrazyl) radical scavenging properties of the methanol extracts from *Haplophyllum* species will be carry out according to the method described by Yaman et al. [13] with some modifications. Trolox, Ascorbic acid (AA), butylated hydroxytoluene (BHT) will be used as positive control. The experiments will be doing in triplicates with two replicates. The results of the radical scavenging activity were calculated according to the following equation as % inhibition of the DPPH radical.

$$\%\ inhibisyon = \frac{(Abscontrol - Abssample)}{Abscontrol} \times 100$$

2.4.2. ABTS radical cation scavenging activity

Measurement of ABTS (2,2′-azino-bis-3-ethylbenzothiazoline-6-sulfonic acid) radical scavenging properties of the methanol extracts from *Haplophyllum* species will be carry out according to the method described by Yaman et al. [13] with some modifications. Trolox and AA will be used as positive control. The experiments will be doing in triplicates with two replicates. Results of radical scavenging activity were denoted as % inhibition of ABTS radical. The % inhibition of ABTS radical cation scavenging activity was calculated according to the following equation:

$$\%\ inhibisyon = \frac{(Abscontrol - Abssample)}{Abscontrol} \times 100$$

2.5. Statistical Analysis

The findings were statistically analyzed using one-way ANOVA in SPSS statistical program, and comparison of the means was evaluated by Duncan's multiple range tests at a significance level of 0.05. Data were given as the mean ± standard deviation.

3. RESULTS AND DISCUSSIONS

3.1. Extract Yield

The methanol extract yields of *Haplophyllum* species used in the project were analyzed and are given in Table 2 as %.

Table 2 The methanol extract yields of endemic *Haplophyllum* species from Türkiye

Species	Extract Yield (%)	Standard Error
HM1	13.98[a]	1.54
HM2	5.54[e]	3.18
HV1	9.92[b]	2.70
HP1	6.91[d]	0.73
HP2	8.28[c]	0.51
HS	9.32[b]	2.43

HM, *H. myrtifolium*; HV, *H. vulcanicum*; HP, *H.pumiliforme*; HS, *H. sahinii*

Generally, in the extraction of plants, methanol solvent provides higher extract yield than other solvents [26, 27]. Yaman et al. [13] investigated ethanol extracts of similar species in their study, and reported their extract yields lower than the methanol extract yield in the current study.

HM1 gives the best extraction yield an average of 13.9%, while HM2 collected from a second region had the lowest yield (5.54 % on average). HV and HS had a statistically similar extract yield with 9.92% and 9.32% whereas HP from two regions was lower with 8.28% - 6.9%.

3.2. Phytochemical contents

The methanol extracts of endemic *Haplophyllum* species collected from different localities were investigated for their phytochemical contents such as total phenolic and flavonoid contents (Table 3). Results was calculated from the calibration curve (R^2 = 0.999 for total phenolic content and R^2 = 0.9997 for total flavonoid content). Differences for the species were showed in findings of this study. The great distinction between the same species collected from different regions appears due to different environmental and climatic conditions [13].

Table 3 Total bioactive contents in methanol extracts of endemic *Haplophyllum* species from Türkiye

Species	Total phenolic content (mg GAE/g extract)	Total flavonoid content (mg QE/g extract)
HM1	48.0±0.4^{d}	39.7±0.2^{b}
HM2	56.1±0.8^{c}	40.8±0.2^{a}
HV	38.0±0.3^{f}	34.5±0.1^{f}
HP1	40.1±0.2^{e}	35.3±0.1^{d}
HP2	60.1±1.0^{b}	36.1±0.2^{c}
HS	66.4±0.2^{a}	35.0±0.2^{e}

HM, *H. myrtifolium*; HV, *H. vulcanicum*; HP, *H.pumiliforme*; HS, *H. sahinii*

The results revealed that the HS is very rich in phenolic compounds with 66.4 mg of GAE/g of extract, whereas HV is lowest with 38.0 mg of GAE/g of extract (Table 2). Interestingly, Yaman et al. [14] reported that ethanol extracts of the *Haplophyllum vulcanicum* (HV) species contained higher total phenolic than other *Haplophyllum* species. HV may differ from other species in terms of phytochemical content or biosynthesis ability, or affected by environmental factors.

When Table 3 was examined, the total flavonoid amounts of extracts varied from 34.5 to 40.8 mg QE/g extract. The highest levels of the total flavonoid were found in HM2 and HM1, respectively. Yaman et al. [13] also reported a similar finding for ethanol extracts of *Haplophyllum myrtifolium* (HM).

The collection of species from different regions affected their phytochemical contents and compositions, especially total phenolic content (Table 2). Different results have been observed in populations at the different regions of one species. As a result of these differences, populations belonging to different regions of each species have ecological conditions (abiotic and biotic differentiators) and habitat (rocky, slopes etc. and diversity of flora). Such differences have also been identified by many researchers [28-31]. Rawat et al. [30] indicated that total phenol contents among the populations of *Hedychium spicatum* ranged were a significantly significant different. The present findings indicate to have a significant effect on different species and regions for total bioactive components.

3.3. Radical Scavenging Activity

Various phytochemicals (secondary metabolites) of plants such as flavonoids, polyphenols and other phenolics, tannins are the main group of components that serve as primary free radical scavengers [32, 33]. The extracts obtained from endemic *Haplophyllum* species collected from different localities were investigated for their two radical scavenging activities, namely ABTS and DPPH. Results were also expressed as % inhibition (Figure 2 and Figure 3).

The DPPH radical is largely used in the evaluation of free radical scavenger activity due to the ease of the reaction. When the DPPH radical is cleaned by a compound of antioxidant via hydrogen donation to form a stable DPPH-H molecule, the color of the solution is return from purple to yellow. All extracts in current study were determinate to reduce the stable violet DPPH radical to yellow. DPPH antioxidant activity ranged between 43.9-86.5% at a concentration of 100 µg of all the assessed extracts and standards

(Figure 2). Among extracts of *Haplophyllum* species, HP1, HP2 and HM1 exhibited maximum DPPH free radical scavenging activity and statistically the same DPPH activity with 85.0-85.1%, followed by HM2 (83.1%) and HS (71.7%) and HV (68.3%). The scavenging effect of different species on the DPPH radical for methanol solvent generally decreased in the order of HP ≥HM >HS >HV (Figure 2).

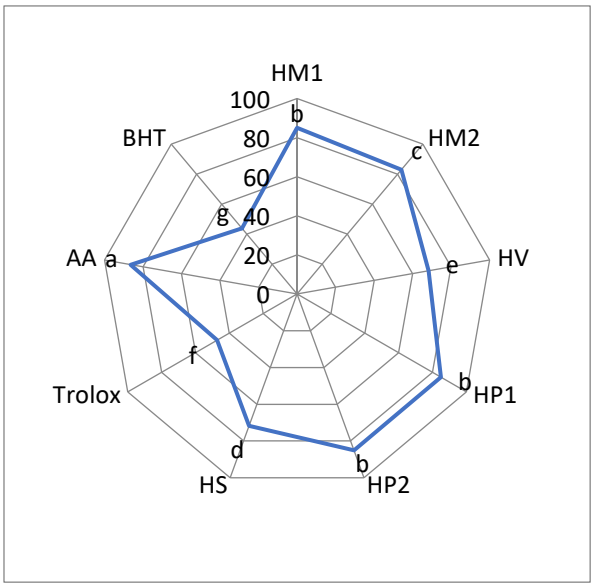

Figure 2 The DPPH free radical activities of methanol extracts of endemic *Haplophyllum* species from Türkiye (HM, *H. myrtifolium*; HV, *H. vulcanicum*; HP, *H.pumiliforme*; HS, *H. sahinii*)

The ABTS radical is blue, but transforms from blue to the colorless form through an antioxidant compound. As seen in Figure 3, ABTS radical scavenging activity ranged between 39.5%-89.9% at a concentration of 200 µg of all the assessed extracts and standards.

All values of methanol extracts from *Haplophyllum* species were statistically in different groups. Among *Haplophyllum* species, samples at both different regions of HM displayed the highest ABTS activity (HM1:76.5% and HM2:71.1%), followed by HP (HP2: 66.7%, HP1: 61.3%) and HS (56.5%) and HV (47.2%).

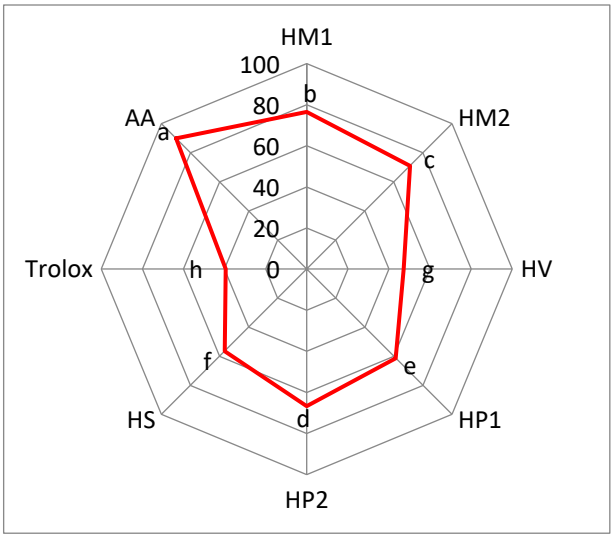

Figure 3 The ABTS free radical activities of methanol extracts of endemic *Haplophyllum* species from Türkiye (HM, *H. myrtifolium*; HV, *H. vulcanicum*; HP, *H.pumiliforme*; HS, *H. sahinii*)

Interestingly, DPPH and ABTS activities of all *Haplophyllum* species were lower than AA as the synthetic antioxidant standard, but stronger than the trolox standard. Also, DPPH activities of all *Haplophyllum* species had the higher than BHT standard. This finding indicates that the analyzed *Haplophyllum* species exhibit very powerful radical scavenging activity. In the other hand, the results between different localities of the species were close to each other.

Antioxidant activities of these *Haplophyllum* species have been reported very little in some previous studies [13, 34], but, for the first time, methanol extracts of endemic *Haplophyllum* species from Türkiye were compared among themselves and with synthetic standards in this study.

Bioactive compounds defined as secondary metabolites in plants have been taken the evidence as natural functional components, and various medicines have been developed all over the World [35, 36]. These compounds include total flavonoids, other phenolic compounds (phenolic acids, tocopherols, stilbenes, alcohols etc.) and polyphenolics (condensed and hydrolysable tannins, saponin, lignin), vitamins, terpenoids,

carotenoids, essential oils [37]. These compounds could use as a potential source of natural antioxidants [38]. Many researchers reported that found a correlation between the antioxidant activity and phenolics, in particular flavonoids [39-42]. Moreover, flavonoids are the most important and abundant polyphenols, more than 5000 reported up to today [43]. So, former studies have indicated that the amount of bioactive compounds in plants and their antioxidant activities depend on both biological factors (genetic, organ etc.) and environmental (precipitation, temperature, altitude, light intensity etc.) conditions [44]. Also, stress conditions may induce various flavonoid biosynthetic genes. The biotic and abiotic stresses such as drought, temperature, wounding, nutrient deprivation, metal toxicity and can increase the levels of flavonoids in the plants as a part of their defense strategy [45]. So, the antioxidant activity of flavonoids is principal gone on their ability to donate the electrons or hydrogen atoms [46]. The variety of phenolic and flavonoid compounds is as important as amount of the compounds, because effect of antioxidant activity of each compound is different.

4. CONCLUSIONS

Less than 10% of the world's biological diversity has been assessed for potential biological activity and there are many more natural compounds awaiting exploration to achieve this natural chemical variety. When both radical scavenging activities are taken into consideration, HM and HP have been exhibited the strongest antioxidant activity, especially the antioxidant activities of both species are very close to those of ascorbic acid. The findings suggest that these endemic species show much stronger antioxidant activities, involved significantly high levels of total phenolic and flavonoid contents, and could be a potential source of natural antioxidants. However, there is little research about antioxidant activities and total bioactive components of the species evaluated in this study. Further chemical investigations are required to isolate the elements of active phenolic and flavonoid components of the plants that show a broad spectrum of pharmacological activity.

Acknowledgments
The author thanks Prof. Dr. Osman Tugay and Assoc. Prof. Dr. Deniz Ulukuş for their contributions to the collection of plants.

Funding
This research received no external funding.

The Declaration of Conflict of Interest/ Common Interest
No conflict of interest or common interest has been declared by the authors.

The Declaration of Ethics Committee Approval
This study does not require ethics committee permission or any special permission.

The Declaration of Research and Publication Ethics
The authors of the paper declare that they comply with the scientific, ethical and quotation rules of SAUJS in all processes of the paper and that they do not make any falsification on the data collected. In addition, they declare that Sakarya University Journal of Science and its editorial board have no responsibility for any ethical violations that may be encountered, and that this study has not been evaluated in any academic publication environment other than Sakarya University Journal of Science.

REFERENCES

[1] C. C. Townsend, "*Haplophyllum* A. Juss. In: Davis, P.H (Ed.) Flora of Türkiye and the Aegean Islands. vol 2," Edinburgh University Press, Edinburgh, pp. 496–506, 1967.

[2] C. C. Townsend, "Taxonomic revision of the genus *Haplophyllum* (Rutaceae). In: Hooker's icones plantarumvol 40

parts 1," Bentham-Moxon Trustees Royal Botanical Gardens, Kew, 1986.

[3] O. Tugay, D. Ulukuş, "*Haplophyllum sahinii* (Rutaceae), a new species from Central Anatolia (Turkey),"Phytotaxa, vol. 297, No. 3, pp. 265-272, 2017.

[4] D. Ulukuş, O. Tugay. O. "*Haplophyllum ermenekense* (Rutaceae), a new species from Turkey," PhytoKeys, (111), 119, 2018.

[5] M. Debouba, B. Khemakhem, S. Zouari, A. Meskine, H. Gouia, "Chemical and biological activities of *Haplophyllum tuberculatum* organic extracts and essential oil," Journal of essential oil bearing plants, vol. 17, no. 5, pp. 787-796, 2014.

[6] M. A. Al-Yahya, A. J. Al-Rehaily, M. S. Ahmad, M. S. Al-Said, F. S. El-Feraly, C. D. Hufford, "New alkaloids from *Haplophyllum tuberculatum,"* Journal of Natural Products, vol. 55, pp. 899-903, 1992.

[7] A. H. Mohamed, M. B. Ali, A. K. Bashir, A. M. Salih, "Influence of *Haplophyllum tuberculatum* on the cardiovascular system," International Journal of Pharmacognosy, vol. 34, no. 3, pp. 213-217, 1996.

[8] J. S. Mossa, M. A. Al-Yahya, I. A. MAl-Meshal, Medical Plants of Saudi Arabia. Vol. 1, Riyadh, King Saud University Libraries, 1987.

[9] O. Said, K. Khalil, S. Fulder, H. Azaizeh, "Ethnopharmacological survey of medicinal herbs in Israel, the Golan Heights and the West Bank region," Journal of Ethnopharmacology, vol. 83, no. 3, pp. 251-265, 2002.

[10] S. A. M Abdelgaleil, M. M. G. Saad, N. R. Ariefta, Y. Shiono, "Antimicrobial and phytotoxic activities of secondary metabolites from Haplophyllum tuberculatum and *Chrysanthemum coronarium*," South African Journal of Botany, vol. 128, pp. 35-41, 2020.

[11] A. Abdelkhalek, M. Z. Salem, E. Hafez, S. I. Behiry, S. H. Qari, "The phytochemical, antifungal, and first report of the antiviral properties of Egyptian *Haplophyllum tuberculatum* extract," Biology, vol. 9, no.9, pp. 248, 2020.

[12] C. Yaman, D. Ulukuş, O. Tugay, "*Haplophyllum suaveolens* varyetelerinin antioksidan aktivitesi ve sekonder metabolitleri üzerine farklı çözücülerin etkisi,"Türkiye Tarımsal Araştırmalar Dergisi, vol. 6, no. 3, pp. 277-284, 2019.

[13] C. Yaman, D. Ulukuş, O. Tugay, "Endemik Haplophyllum A. Juss. türlerinin antioksidan aktivitesi üzerine lokasyon ve tür farkının etkisi," Journal of the Institute of Science and Technology, vol. 10, no. 1, pp. 648-657, 2020.

[14] A. Hamdi, K. Majouli, A. Abdelhamid, B. Marzouk, H. Belghith, I. Chraief, Y. Vander Heyden, "Pharmacological activities of the organic extracts and fatty acid composition of the petroleum ether extract from *Haplophyllum tuberculatum* leaves,"Journal of ethnopharmacology, vol. 216, pp. 97-103, 2018.

[15] M. Mohammadhosseini, A. Venditti, C. Frezza, M. Serafini, A. Bianco, B. Mahdavi, "The Genus Haplophyllum Juss.: Phytochemistry and Bioactivities—A Review, "Molecules, vol. 26, no. 15, pp. 4664, 2021.

[16] A. Hamdi, A. Halouani, I. Aouf, J. Viaene, B. Marzouk, J. Kraiem, Y. Vander Heyden, "Cytotoxicity and Antiviral Activities of Haplophyllum tuberculatum Essential Oils, Pure

Compounds, and Their Combinations against Coxsackievirus B3 and B4, ”Planta medica, vol. 87, no.10/11, pp. 827-835, 2021.

[17] P. Varamini, M. Doroudchi, A. Mohagheghzadeh, M. Soltani, A. Ghaderi, “Cytotoxic evaluation of four *Haplophyllum* species with various tumor cell lines, ”Pharmaceutical Biology, vol. 45, no. 4, pp. 299-302, 2007.

[18] J. M. Prieto, “*Haplophyllum* A. Juss, a rich source of bioactive natural principles. In: Bioactive Compounds: Types,” Biological Activities and Health Effects, pp. 341-380, 2012.

[19] A. Pasqualone, A. M. Bianco, V. M. Paradiso, C. Summo G. Gambacorta, F. Caponio, A. Blanco, “Production and characterization of functional biscuits obtained from purple wheat,” Food Chemistry, vol. 180, pp. 64-70, 2015.

[20] B. Narayanasamy, N. Jeyakumar, D. K. Manoharan, “Effect of natural antioxidants on the oxidation stability of methyl ester of rubber seed oil,” Journal Energy Sources, Part A: Recovery, Utilization, and Environmental Effects, vol. 40, no. 6, pp. 680-687, 2018.

[21] S, Bajaj, A, Urooj, P. Prabhasankar,” Effect of incorporation of mint on texture, colour and sensory parameters of biscuits” International Journal of Food Properties, vol. 9, pp. 691-700, 2006.

[22] M. A. Shah, S. J. Don Bosco, S. A. Mir, “Plant extracts as natural antioxidants in meat and meat products,” Meat Science, vol. 98, pp. 21-33, 2014.

[23] A. Russo, C. Formisano, D. Rigano, F. Senatore, S. Delfine, V. Cardile, S. Rosselli, M. Bruno, “Chemical composition and anticancer activity of essential oils of Mediterranean sage (*Salvia officinalis* L.) grown in different environmental conditions,” Food and Chemical Toxicology, vol. 55, pp. 42-47, 2013.

[24] A. R. Duarte, R. R. Naves, S. C. Santos, J. C. Seraphinand, P. H. Ferri, “Genetic and environmental influence on essential oil composition of *Eugenia dysenterica*,” Journal Brazilian Chemical Social, vol. 21, no.8, pp. 1459-1467, 2010.

[25] B. Li, C. Zhang, L. Peng, Z. Liang, X. Yan, Y. Zhu, Y. Liu, “Comparison of essential oil composition and phenolic acid content of selected *Salvia* species measured by GC–MS and HPLC methods,” Industrial Crops Products, vol. 69, pp. 329-334, 2015.

[26] D. H. Truong, D. H. Nguyen, N. T. A. Ta, A. V. Bui, T. H. Do, H. C. Nguyen, “Evaluation of the use of different solvents for phytochemical constituents, antioxidants, and in vitro anti-inflammatory activities of *Severinia buxifolia*, ”Journal of Food Quality, 2019.

[27] M. Barbouchi, K. Elamrani, M. El Idrissi, “A comparative study on phytochemical screening, quantification of phenolic contents and antioxidant properties of different solvent extracts from various parts of *Pistacia lentiscus* L., ”Journal of King Saud University-Science, vol. 32, no. 1, pp. 302-306, 2020.

[28] J. S. Dambolena, M. P. Zunino, E. I. Lucini, R. Olmedo, E. Banchio, P. J. Bima, J. A. Zygadlo, “Total phenolic content, radical scavenging properties, and essential oil composition of *Origanum* species from different populations,” Journal of Agricultural and Food Chemistry, vol. 58, pp. 1115-1120, 2010.

[29] R. Chirinos, R. Pedreschi, H. Rogez, Y., Larondelle, D. Campos, "Phenolic compound contents and antioxidant activity in plants with nutritional and/or medicinal properties from the Peruvian Andean region," Industrial Crops and Products, vol. 47, pp. 145-152, 2013.

[30] S. Rawat, I. D. Bhatt, R. S. Rawal, "Total phenolic compounds and antioxidant potential of *Hedychium spicatum* Buch. Ham. ex D. Don in west Himalaya, India," Journal of Food Composition and Analysis, vol. 24, pp. 574-579, 2011.

[31] C. Çırak, J. Radušıenė, V. Janulıs, L. Ivanauskas, N. Çamaş, A. K. Ayan, "Phenolic constituents of *Hypericum triquetrifolium* Turra (Guttiferae) growing in Turkey: variation among populations and plant parts," Turkish Journal of Biology, vol. 35, pp. 449-456, 2011.

[32] T. Sharma, V. Khandelwal, S. Gupta, S. Singh, "Secondary Metabolites, Boon for Plants; Their Role in Defence Mechanism and Antioxidant Activity of *Anthocephalus cadamba*," In Antioxidants in Plant-Microbe Interaction, Springer, Singapore, pp. 413-424, 2021.

[33] T. K. Patle, K. Shrivas, R. Kurrey, S. Upadhyay, R. Jangde, R. Chauhan, "Phytochemical screening and determination of phenolics and flavonoids in *Dillenia pentagyna* using UV–vis and FTIR spectroscopy, "Spectrochimica Acta Part A: Molecular and Biomolecular Spectroscopy, vol. 242, pp. 118717, 2020.

[34] G. Zengin, C. Sarikurkcu, A. Aktumsek, R. Ceylan, O. Ceylan, "A comprehensive study on phytochemical characterization of *Haplophyllum myrtifolium* Boiss. endemic to Turkey and its inhibitory potential against key enzymes involved in Alzheimer, skin diseases and type II diabetes, "Industrial Crops and Products, vol. 53, pp. 244-251, 2014.

[35] M. S. Butler, "The role of natural product in chemistry in drug discovery," Journal of Natural Products, vol. 67, pp. 2141-2153, 2004.

[36] B. B. Mishra, V. K. Tiwari, "Natural products: An evolving role in future drug discovery," European Journal of Medicinal Chemistry, vol. 46, pp. 4769-4807, 2011.

[37] M. Mazid, T. A. Khan, F. Mohammad, "Role of secondary metabolites in defense mechanisms of plants," Biology and Medicine, vol. 3, pp. 232-249, 2011.

[38] Y. Z. Cai, Q. Luo, M. Sun, H. Corke, "Antioxidant activity and phenolic compounds of 112 Chinese medicinal plants associated with anticancer," Life Sciences, vol. 74, pp. 2157-2184, 2004.

[39] V. Katalinic, M. Milos, T. Kulisic, M. Jukic, "Screening of 70 medicinal plant extracts for antioxidant capacity and total phenols," Food Chemistry, vol. 94, pp. 550-557, 2006.

[40] S. M. Cottica, A. Sawaya, M. N. Eberlin, S. L. Franco, L. M. Zeoula, J. V. Visentainer, "Antioxidant activity and composition of propolis obtained by different methods of extraction," Journal of the Brazilian Chemical Society, vol. 22, pp. 929–935, 2011.

[41] Z. A. Abbas, S. Saggu, M. I. Sakeran, N. Zidan, H. Rehman, A. A. Ansari, "Phytochemical, antioxidant and mineral composition of hydroalcoholic extract of chicory (*Cichorium intybus* L.) leaves," Saudi Journal of Biological Sciences, vol. 22, no. 3, pp. 322-326, 2015.

[42] M. J. Iqbal, S. Hanif, Z. Mahmood, F. Anwar, A. Jamil, "Antioxidant and antimicrobial activities of Chowlai (*Amaranthus viridis* L.) leaf and seed extracts," Journal of Medicinal Plants Research, vol. 6, no. 27, pp. 4450-4455, 2012.

[43] J. Dai, R. J. "Mumper, Plant phenolics: extraction, analysis and their antioxidant and anticancer properties," Molecules, vol. 15, pp. 7313-7352, 2010.

[44] M. J. Bano, J. Lorente, J. Casstillo, G. O. Benavente, J. A. Rio, A. Ortuno, K. W. Quirin, D. Gerard, "Phenolic diterpenes, flavones, and rosmarinic acid distribution during the development ofleaves, flowers, stems and roots of *Rosmarinus officinalis* antioxidant activity," Journal of Agricultural and Food Chemistry, Vol. 51, pp. 4247-4253, 2003.

[45] B. Winkel-Shirley, "Biosynthesis of flavonoids and effects of stress," Current Opinion in Plant Biology, vol. 5, pp. 218-223, 2002.

[46] X. C. Li, J. Lin, W. J. Han, W. Q. Mai, L. Wang, Q. Li, M. F. Lin, M. S. Bai, L. S. Zhang, D. F. Chen, "Antioxidant ability and mechanism of Rhizoma *Atractylodes macrocephala*. Molecules. Vol. 17, pp. 13457-13472, 2012.